

DEVELOPMENT OF A NEW HYBRID DAMPER FOR STEEL BRACING
SYSTEMS

A THESIS SUBMITTED TO
THE GRADUATE SCHOOL OF NATURAL AND APPLIED SCIENCES
OF
MIDDLE EAST TECHNICAL UNIVERSITY



BY

NEFIZE SHABAN

IN PARTIAL FULFILLMENT OF THE REQUIREMENTS
FOR
THE DEGREE OF DOCTOR OF PHILOSOPHY
IN
CIVIL ENGINEERING

DECEMBER 2017

Approval of the thesis:

DEVELOPMENT OF A NEW HYBRID DAMPER FOR STEEL BRACING
SYSTEMS

submitted by **NEFIZE SHABAN** in partial fulfillment of the requirements for the degree of **Doctor of Philosophy in Civil Engineering Department, Middle East Technical University** by,

Prof. Dr. Gülbin Dural Ünver
Dean, Graduate School of **Natural and Applied Sciences**

Prof. Dr. İsmail Özgür Yaman
Head of Department, **Civil Engineering**

Prof. Dr. Alp Caner
Supervisor, **Civil Engineering Dept., METU**

Examining Committee Members

Prof. Dr. Murat Altuğ Erberik
Civil Engineering Dept., METU

Prof. Dr. Alp Caner
Civil Engineering Dept., METU

Assoc. Prof. Dr. Eray Baran
Civil Engineering Dept., METU

Prof. Dr. Hakkı Polat Gülkan
Civil Engineering Dept., METU NCC

Asst. Prof. Dr. Gürsoy Turan
Civil Engineering Dept., İzmir Institute of Technology

Date: 27.12.2017



I hereby declare that all information in this document has been obtained and presented in accordance with academic rules and ethical conduct. I also declare that, as required by these rules and conduct, I have fully cited and referenced all material and results that are not original to this work.

Name, Last Name : Nefize SHABAN

Signature :

ABSTRACT

DEVELOPMENT OF A NEW HYBRID DAMPER FOR STEEL BRACING SYSTEMS

Shaban, Nefize

Ph.D., Department of Civil Engineering

Supervisor: Prof. Dr. Alp Caner

December 2017, 239 pages

A new hybrid energy dissipation device named as “Backbone Damper” is introduced. The device assembly is composed of two main components: a viscoelastic (VE) unit and an internal displacement amplification mechanism. Energy dissipation is generated through deformations of the VE unit and friction within the mechanism. The mechanism is designed to remain elastic.

The effectiveness of the device is verified through numerical simulations of tests of full-size prototypes.

A comprehensive three-dimensional solid model of the device is developed to produce the parts of the assembly. The manufactured prototypes are tested under reversed sinusoidal cycles of displacement inputs over a range of frequencies and displacements. The test results evidence a promising device with significant energy dissipation capacity and stable behavior. Prototype tests are used to monitor the device response under different dynamic motions to quantify the design parameters of expected prevalent effect on the Backbone damper performance.

The device demonstrates a stable hysteretic performance, satisfactory energy dissipation capacity and no damage after 100 cycles of reversed loading. Neither strength nor stiffness degradation are observed in the device performance.

Numerical simulations are performed to monitor some of the parameters that are not measured during tests. To this aim, detailed three-dimensional numerical models of a prototype are developed in ABAQUS finite element analysis software. The numerical model is verified against the test results of the device. The test results are also studied to analyze the device behavior and provide estimates for the upper and lower bound values of device modelling parameters.

Finally, the response of five buildings equipped with Backbone dampers under an ensemble of strong ground motions is analyzed. A significant improvement of structural response is recorded.

The final aim and contribution of the research can be divided in three modules: (1) introduction of a new patented passive energy dissipation device; (2) assessment of its performance and (3) setting design parameters to control its response.

Keywords: Backbone damper, hybrid damper, structural response control, amplification mechanism, re-centering capability

ÖZ

ÇELİK BAĞLANTI SİSTEMLERİ İÇİN YENİ HİBRİT BİR SÖNÜMLEYİCİ GELİŞTİRİLMESİ

Shaban, Nefize

Doktora, İnşaat Mühendisliği Bölümü

Tez Yöneticisi: Prof. Dr. Alp Caner

Aralık 2017, 239 sayfa

Bu çalışmada, “Omurga Sönümleyici” adlı yeni hibrit bir enerji sönümleyici sunulmaktadır. Sunulan cihaz iki ana bileşenden oluşmaktadır: viskoelastik (VE) birim ve büyütücü mekanizma. Enerji sönümlenmesi VE birimdeki deformasyonlardan ve mekanizma içindeki katı sürtünmeden meydana gelmektedir. Mekanizma, elastik kalacak şekilde tasarlanmıştır.

Cihazın etkinliği, tam ölçekli prototip testlerinin nümerik simülasyonları ile doğrulanmıştır.

Cihaz bileşenlerinin üretimi için üç boyutlu bir katı modeli detaylı olarak oluşturulmuştur. Üretilen prototip belirli frekans ve deplasman aralıklarında sinüsoidal deplasman girdileri için test edilmiştir. Testler sonucunda, cihazın önemli büyüklükte enerji sönümleme kapasitesi olduğu görülmüştür. Bu testlerle, cihazın davranışı ayrıntılı olarak gözlemlenmiş ve tasarım parametrelerinin Omurga sönümleyicinin performansındaki etkileri belirlenmiştir.

Üretilen cihaz 100 yükleme çevriminden sonra hasarsız kalarak, kararlı ve tatmin edici bir histeretik performans göstermiştir. Testler sonucunda, cihazın dayanımında veya rijitliğinde azalma gözlemlenmemiştir.

Testler sırasında ölçülmeyen parametrelerin de incelenmesi için nümerik simülasyonlar yapılmıştır. Bu amaçla, sonlu elemanlar analiz programı ABAQUS'te cihaz prototipinin detaylı üç boyutlu nümerik modeli oluşturulmuştur. Nümerik model test sonuçlarıyla doğrulanmıştır. Test sonuçları değerlendirilerek cihazın davranışı incelenmiş ve modelleme parametreleri için alt ve üst sınır değerleri elde edilmiştir.

Son aşamada, omurga sönümleyicilerle donatılmış beş tane binanın şiddetli yer hareketleri altındaki tepkisi incelenmiştir. Yapısal davranışta önemli ölçüde iyileşme kaydedilmiştir.

Bu araştırmanın nihai hedefi ve katkısı üç aşamada özetlenebilir: (1) yeni bir patentli pasif enerji sönümleme cihazının sunulması; (2) bu cihazın performansının değerlendirilmesi ve (3) cihaz davranışının kontrolü için tasarım parametrelerinin belirlenmesi.

Anahtar kelimeler: Omurga Sönümleyici, hibrit sönümleyici, yapısal davranış kontrolü, büyütücü mekanizma, merkezleme özelliği



To my Family

ACKNOWLEDGEMENTS

I would like to express a sincere and profound gratitude to my supervisor Prof. Dr. Alp Caner for his priceless guidance and mentoring. He has always been supporting and encouraging me, motivating me to pursue the good and the human. The time spent with him has been a source of inspiration for me and has greatly contributed to my professional and personal growth. It was really a privilege to work with him.

I would like to sincerely thank my committee members Prof. Dr. Hakkı Polat Gülkan and Assoc. Prof. Dr. Eray Baran for their very valuable advice, comments and support throughout my research. They have greatly contributed to this study.

I owe special thanks to Prof. Dr. Hakkı Polat Gülkan. It was really an honor to have him on my committee.

I am grateful to Hasan Metin, İsmail Ozan Demirel, Mehmet Bakır Bozkurt, Burhan Alam, Sina Kazemzadeh Azad and Milad Bybordiani for their help and kindness which is highly appreciated.

I would like to thank the Scientific and Technological Research Council of Turkey (TÜBİTAK) for the scholarship of BİDEB 2215 Program.

My research was also financially supported by 110G093 KAMAG project, METU BAP project with the grant number BAP 03-03-2016-005, SismoLab and BridgeWiz. Their financial support is gratefully acknowledged.

I would like to further thank KCM Mühendislik and Özdekan Rubber Industry for their help in the process of prototype production.

I wish to express my indebtedness to Salih Alan for his continued support and encouragement from the day we met.

Finally, I would like to dedicate this thesis to my family and thank them for standing by me with their unconditional love and support throughout my whole life.

TABLE OF CONTENTS

ABSTRACT	v
ÖZ	vii
ACKNOWLEDGEMENTS	x
TABLE OF CONTENTS	xi
LIST OF TABLES	xvii
LIST OF FIGURES	xix
LIST OF SYMBOLS AND ABBREVIATIONS	xxx
CHAPTERS	
1. INTRODUCTION	1
1.1 Motivation	1
1.2 Aim and scope	3
1.3 Outline of the Research	5
2. LITERATURE REVIEW.....	7
2.1 Introduction	7
2.2 Passive energy dissipation devices	11
2.2.1 Motion-activated devices	11
2.2.2 Rate-independent dampers	11
2.2.2.1 Metallic dampers.....	12
2.2.2.2 Friction dampers	12
2.2.3 Rate-dependent dampers	16
2.2.3.1 Viscous dampers	16
2.2.3.2 Viscoelastic dampers.....	17
2.2.4 Hybrid dampers	20

2.2.5 Re-centering systems.....	21
2.2.6 Amplification of structural displacement.....	23
2.3 Summary.....	25
3. DEVICE MECHANISM.....	27
3.1 Introduction	27
3.2 Prototype I	29
3.2.1 DAM unit	30
3.2.2 VE unit	32
3.2.2.1 Limit design criteria for EB.....	36
3.3 Prototype II.....	38
4. EXPERIMENTAL WORK.....	43
4.1 Introduction	43
4.2 Elastomer material tests.....	43
4.2.1 Test samples and equipment	43
4.2.2 Test procedure and program.....	45
4.2.2.1 Preload.....	45
4.2.2.2 Uniaxial cyclic tension-compression tests under different velocities.....	45
4.2.3 Test results.....	46
4.3 Dynamic test set-up	48
4.3.1 Loading set-up.....	49
4.3.2 Measurement instrumentation	52
4.3.2.1 Prototype I.....	52
4.3.2.2 Prototype II.....	52
4.4 Loading Protocol	56
4.5 Investigated parameters	56
4.6 Test data processing.....	59
4.6.1 Filtering	59
4.6.2 Pull and push definition.....	60

4.7 Test results.....	60
4.7.1 Prototype I.....	60
4.7.2 Prototype II	63
4.7.2.1 A3-1 results.....	63
4.8 Summary of results.....	70
5. FINITE ELEMENT MODELLING AND ANALYSIS OF THE DEVICE.....	73
5.1 Introduction	73
5.2 Modeling details	73
5.2.1 Elastomer block numerical model.....	75
5.2.2 Modeling details for complete assembly	77
5.3 Comparison with test results	79
5.3.1 Hysteresis loop	80
5.3.2 Strain gauge readings	82
5.3.3 Elastomeric block rotations.....	83
5.4 Detailed motion study of the full assembly of Backbone damper.....	84
5.4.1 Bottom elastomeric block	85
5.4.2 Bottom driven bar	91
5.4.2.1 Force transferred from VE unit.....	93
5.4.2.2 Forces generated at the contact between driven bar and case supports.....	95
5.4.2.3 Force transferred form Pin3	98
5.4.2.4 Force balance and hysteretic response of driven bar.....	99
5.4.3 Bottom asymmetric disk	102
5.4.4 Driving bar	105
5.5 Summary and conclusions.....	109
6. EVALUATION OF DEVICE PERFORMANCE PARAMETERS	111
6.1 Introduction	111
6.2 Evaluation of performance parameters from test results.....	112
6.2.1 Energy Dissipated per Cycle (EDC)	112

6.2.1.1 Analysis of experimental data	112
6.2.1.2 Upper and lower bound estimations	116
6.2.2 Effective stiffness (<i>K_{eff}</i>)	121
6.2.2.1 Analysis of experimental data	121
6.2.2.2 Upper and lower bound estimations	122
6.3 Summary and conclusions	125
7. ANALYSIS OF A HOSPITAL BUILDING EQUIPPED WITH BACKBONE DAMPERS	127
7.1 Introduction	127
7.2 Building in analysis	127
7.3 Backbone damper installation	130
7.4 Ground motion selection	134
7.5 Analysis results	136
7.5.1 El-Centro earthquake ground motion	138
7.5.1.1 2-storey building	139
7.5.1.2 10-storey building	144
7.5.1.3 Summary of analysis results for El-Centro record	147
7.5.2 Summary of all analysis results	149
7.6 Discussions and conclusions	152
8. CONTRIBUTIONS, CONCLUSIONS AND RECOMMENDATIONS	153
8.1 Main contributions	153
8.2 Conclusions	155
8.3 Future work	156
REFERENCES	159
APPENDICES	
A. TEST RESULTS	177
A.1 A1 results	177
A.2 B1-1 results	180

A.3 B1-2 results.....	183
A.4 B3-1 results.....	186
A.5 B3-2 Results	189
A.6 B3-4 results.....	192
A.7 BRB results.....	195
B. NUMERICAL ANALYSES	199
B.1 Unfiltered and filtered results.....	199
B.2 Free-body diagrams for configuration A3-1 under 10mm at 1.0 Hz.....	200
B.2.1 Top elastomeric block.....	200
B.2.2 Top driven bar	203
B.2.3 Top asymmetric disk.....	206
C. BUILDING ANALYSES	209
C.1 Response spectrum parameters	209
C.2 El-Centro earthquake ground motion	212
C.2.1 4-storey building	212
C.2.2 6-storey building	213
C.2.3 8-storey building	215
C.3 Kobe earthquake ground motion	217
C.3.1 2-storey building	218
C.3.2 4-storey building	219
C.3.3 6-storey building	220
C.3.4 8-storey building	222
C.3.5 10-storey building	223
C.3.6 Summary	225
C.4 Landers earthquake ground motion	227
C.4.1 2-storey building	228

C.4.2 4-storey building	229
C.4.3 6-storey building	230
C.4.4 8-storey building	232
C.4.5 10-storey building	233
C.4.6 Summary	235
CURRICULUM VITAE	237



LIST OF TABLES

TABLES

Table 3-1. EB mechanical properties	33
Table 3-2. Mechanical properties of EB configurations	40
Table 4-1. List of instrumentation used for dynamic performance tests.....	53
Table 4-2. Results for Prototype I.....	62
Table 4-3. Results for A3-1.....	69
Table 6-1. Coefficients of power functions fitted to the EDC vs displacement curves from test data.....	114
Table 7-1. Records selected for the NLTHA	135
Table 7-2. Fundamental periods of investigated buildings with and without Backbone damper.....	136
Table 7-3. Change in response parameters of the 2-storey building under El-Centro earthquake record	141
Table 7-4. Change in response parameters of the 10-storey building under El-Centro earthquake record	146
Table A-1. Mechanical properties of configuration A1	177
Table A-2. Results for A1 tests	179
Table A-3. Mechanical properties of configuration B1-1	180
Table A-4. Results for B1-1 tests	182
Table A-5. Mechanical properties of configuration B1-2.....	183
Table A-6. Results for B1-2 tests	185
Table A-7. Mechanical properties of configuration B3-1	186
Table A-8. Results for B3-1 tests	188
Table A-9. Mechanical properties of configuration B3-2.....	189
Table A-10. Results for B3-2 tests	191
Table A-11. Mechanical properties of configuration B3-4.....	192
Table A-12. Results for B3-4 tests	194

Table A-13. Mechanical properties of configuration BRB 195
Table A-14. Results for BRB tests 197



LIST OF FIGURES

FIGURES

Figure 1-1. Backbone damper general view	4
Figure 2-1. Viscoelastic material properties (after [85]).....	18
Figure 2-2. Flag-shaped versus full-cycle hysteretic response (after [4]).....	22
Figure 2-3. Amplification factors for selected configurations (after [155])	24
Figure 3-1. Backbone damper idealization	27
Figure 3-2. Isometric view of the 3D SolidWorks model of Prototype I.....	30
Figure 3-3. Produced Prototype I.....	30
Figure 3-4. Geometry of (a) the asymmetric disk; (b) driven bar and (c) driving bar	32
Figure 3-5. Geometry and dimensions of laminated rubber block.....	33
Figure 3-6. Configurations of Prototype II as manufactured and installed in the dynamic test set-up.....	41
Figure 4-1. Round dog-bone test samples.....	44
Figure 4-2. MTS Servohydraulic test machine	44
Figure 4-3. A photo (a) and dimensions (b) of the special apparatus for test specimen installation.....	45
Figure 4-4. Strain vs Time curves for uniaxial cyclic tension-and-compression tests	46
Figure 4-5. Stress-strain loops of uniaxial cyclic tension-and-compression tests under different loading rates	46
Figure 4-6. Relaxation test data	48
Figure 4-7. Side view (top) and plan view (bottom) of the dynamic performance test set-up design drawings (all dimensions are in mm).....	49
Figure 4-8. A three-dimensional design drawing of the dynamic performance test set-up.....	50
Figure 4-9. Completed installation of the steel supports.....	50

Figure 4-10. Detail of connection between driving bar and actuator head	51
Figure 4-11. A general view of the completed dynamic test set-up.....	51
Figure 4-12. Strain gauges installed on a driven bar	53
Figure 4-13. Channel locations in the test set-up	55
Figure 4-14. Phase offset between the driving and driven bar responses	58
Figure 4-15. Strain time-history plot.....	59
Figure 4-16. Offset due to filtering	60
Figure 4-17. Hysteresis loops of Prototype I for (a) 0.5Hz and (b) 1.0Hz.....	61
Figure 4-18. EDC versus mean displacement for Prototype I.....	62
Figure 4-19. K_{eff} versus mean displacement for Prototype I.....	63
Figure 4-20. Hysteresis loops of configuration A3-1 at 1.0Hz frequency and different displacement amplitudes	64
Figure 4-21. All hysteresis loops of A3-1 organized by displacement amplitude	65
Figure 4-22. Device EDC vs input frequency and displacement for A3-1.....	66
Figure 4-23. Device K_{eff} vs input frequency and displacement for A3-1	66
Figure 4-24. Rotations of top EB	67
Figure 4-25. Hysteresis loops of A3-1 for increasing displacement amplitudes at 0.5Hz and 1.0Hz	67
Figure 5-1. Assembly model before (left) and after (right) simplification	75
Figure 5-2. Hyperelasticity curve.....	76
Figure 5-3. Elastomer configurations analyzed: A3-1 (left) and B3-1 (right)	77
Figure 5-4. Device hysteresis loops as obtained from ABAQUS simulations and experiments for configuration A3-1 under 10 mm amplitude at 1.0 Hz	80
Figure 5-5. Device hysteresis loops as obtained from ABAQUS simulations and experiments for configuration A3-1 under 10mm amplitude at 1.0Hz	81
Figure 5-6. Strain gauge readings from experiments and numerical analyses recorded at the bottom surface of the bottom driven bar	83
Figure 5-7. Top EB rotation readings (for the third cycle) from experiments and numerical analyses	84
Figure 5-8. Free-body diagram of bottom elastomeric block at maximum pull (with contour of U1-direction displacement)	85
Figure 5-9. Bottom elastomeric block at maximum push	86

Figure 5-10. S22 contour plot of bottom EB at maximum pull	87
Figure 5-11. Envelope curves of S22 for bottom EB.....	87
Figure 5-12. LE12 contour plot of bottom EB at maximum pull	89
Figure 5-13. S22 contour plot of bottom EB at maximum push.....	90
Figure 5-14. LE12 contour plots of bottom EB at maximum push.....	90
Figure 5-15. Envelope curves of LE12 of bottom EB	91
Figure 5-16. Bottom driven bar at maximum pull	92
Figure 5-17. Bottom driven bar at maximum push.....	93
Figure 5-18. U1-direction force components transferred from VE unit to bottom driven bar.....	94
Figure 5-19. U1-direction friction forces acting on bottom driven bar generated from its sliding on the supports.....	95
Figure 5-20. U1-direction normal forces acting on bottom driven bar generated from its sliding on the supports.....	97
Figure 5-21. U1-direction total forces acting on bottom driven bar generated from its sliding on the supports	98
Figure 5-22. U1-direction contact forces transferred from Pin3 to bottom driven bar	99
Figure 5-23. U1-direction forces acting on bottom driven bar	100
Figure 5-24. Magnitude comparison of U1-direction forces acting on bottom driven bar.....	100
Figure 5-25. Hysteretic behavior of bottom driven bar.....	101
Figure 5-26. Bottom asymmetric disk at maximum pull	102
Figure 5-27. U1-direction force components transferred from Pin1, Pin2 and Pin3 to bottom asymmetric disk	103
Figure 5-28. U1-direction forces transferred from Pin1, Pin2 and Pin3 to bottom asymmetric disk	104
Figure 5-29. Magnitude comparison of U1-direction forces acting on bottom asymmetric disk	104
Figure 5-30. Amplification ratio	105
Figure 5-31. Driving bar at maximum push.....	106

Figure 5-32. U1-direction force components transferred from top and bottom Pin2 to the driving bar	107
Figure 5-33. U1-direction total forces transferred from top and bottom Pin2 to the driving bar	107
Figure 5-34. Hysteresis loop of each force component and total force transferred from pins to the driving bar.....	108
Figure 5-35. Hysteresis loop of transferred forces and of total force on driving bar	109
Figure 6-1. EDC vs displacement for test data of prototype II	112
Figure 6-2. Power functions fitted to EDC vs displacement curves for Prototype II	114
Figure 6-3. EDC vs displacement curves for all tests including prototype I	115
Figure 6-4. Power functions fitted to EDC vs displacement curves for all tests.....	115
Figure 6-5. Candidate EDC curves normalized by (a) Kh ; (b) $Kh1.5$; (c) $Kh2$ and	117
Figure 6-6. Formulation of EDC as a function of Kh and d , with mean and standard deviation curves.....	118
Figure 6-7. Formulation of EDC as a function of Kh and d , with pow (top) and poly2 (bottom) fits for mean and standard deviation curves.....	119
Figure 6-8. Formulation of EDC as a function of Kh and d , with poly2 fits for mean and standard deviation curves	120
Figure 6-9. K_{eff} vs displacement	121
Figure 6-10. Power functions fitted to K_{eff} vs displacement curves	122
Figure 6-11. Candidate K_{eff} curves normalized by (a) Kh ; (b) $Kh1.5$; (c) $Kh2$ and	123
Figure 6-12. Formulation of K_{eff} as a function of Kh and d with pow (top) and poly2 (bottom) fits for mean and standard deviation curves.....	124
Figure 7-1. A typical urban hospital complex in Turkey	128
Figure 7-2. Moment vs rotation curve for beam end nonlinear (hysteretic) springs	129
Figure 7-3. Backbone damper force-displacement curve as idealized in LARSA4D interface.....	131
Figure 7-4. Damper installation in a typical bay	132
Figure 7-5. Analyzed building without (above) and with (below) dampers	133

Figure 7-6. Target response spectrum	135
Figure 7-7. 5%-Damped SRSS spectra of selected ground motions (scaled)	136
Figure 7-8. El-Centro earthquake record North-South (NS) and East-West (EW) components (unscaled).....	138
Figure 7-9. Roof displacement time histories in x and y directions of the 2-storey building under El-Centro earthquake record.....	139
Figure 7-10. Base shear vs roof displacement plots in x and y directions of the 2-storey building under El-Centro earthquake record.....	139
Figure 7-11. Drift ratio plots in x and y directions of the 2-storey building under El-Centro earthquake record	140
Figure 7-12. Plots of maximum damper displacement in x and y directions of the 2-storey building under El-Centro earthquake record	141
Figure 7-13. Forces in columns connected to dampers in the 2-storey building	143
Figure 7-14. Roof displacement time histories in x and y directions of the 10-storey building under El-Centro earthquake record.....	144
Figure 7-15. Base shear vs roof displacement plots in x and y directions of the 10-storey building under El-Centro earthquake record.....	145
Figure 7-16. Drift ratio plots in x and y directions of the 10-storey building under El-Centro earthquake record	145
Figure 7-17. Plots of maximum damper displacement in x and y directions of the 10-storey building under El-Centro earthquake record	146
Figure 7-18. Reduction in peak response parameters for different models under El-Centro earthquake record after Backbone damper installation	147
Figure 7-19. Maximum damper displacement for different models under El-Centro earthquake record.....	148
Figure 7-20. Reduction in peak response parameters under selected ground motions after Backbone damper installation.....	149
Figure 7-21. Reduction in maximum base shear under selected ground motions after Backbone damper installation	151
Figure 7-22. Maximum damper displacements under selected ground motions	151
Figure A-1. Device EDC vs input frequency and displacement for A1	177

Figure A-2. Hysteresis loops of configuration A1 at 1.0Hz frequency and different displacement amplitudes	178
Figure A-3. Device EDC vs input frequency and displacement for B1-1	180
Figure A-4. Hysteresis loops of configuration B1-1 at 1.0Hz frequency and different displacement amplitudes	181
Figure A-5. Device EDC vs input frequency and displacement for B1-2	183
Figure A-6. Hysteresis loops of configuration B1-2 at 1.0Hz frequency and different displacement amplitudes	184
Figure A-7. Effect of frequency and displacement on the device EDC for B3-1	186
Figure A-8. Hysteresis loops of configuration B3-1 at 1.0Hz frequency and different displacement amplitudes	187
Figure A-9. Device EDC vs input frequency and displacement for B3-2	189
Figure A-10. Hysteresis loops of configuration B3-2 at 1.0Hz frequency and different displacement amplitudes	190
Figure A-11. Device EDC vs input frequency and displacement for B3-4	192
Figure A-12. Hysteresis loops of configuration B3-4 at 1.0Hz frequency and different displacement amplitudes	193
Figure A-13. Device EDC vs input frequency and displacement for BRB	195
Figure A-14. Hysteresis loops of configuration BRB at 1.0Hz frequency and different displacement amplitudes	196
Figure B-1. Comparison of ABAQUS result (unfiltered) against test result for A3-1, 10 mm 1.0 Hz	199
Figure B-2. S22 contour plot of top EB at maximum pull	200
Figure B-3. S22 contour plot of top EB at maximum push.....	200
Figure B-4. Envelope curve of S22 of top EB	201
Figure B-5. LE12 contour plot of top EB at maximum pull	201
Figure B-6. LE12 contour plot of top EB at maximum push.....	202
Figure B-7. Envelope curve of LE12 of top EB.....	202
Figure B-8. U1-direction force components transferred from VE unit to top driven bar	203
Figure B-9. U1-direction friction forces acting on top driven bar generated from its sliding on the supports.....	203

Figure B-10. U1-direction normal forces acting on top driven bar generated from its sliding on the supports	204
Figure B-11. U1-direction total forces acting on top driven bar generated from its sliding on the supports	204
Figure B-12. U1-direction contact forces transferred from Pin3 to top driven bar..	205
Figure B-13. U1-direction forces acting on top driven bar	205
Figure B-14. Magnitude comparison of U1-direction forces acting on top driven bar	206
Figure B-15. U1-direction force components transferred from Pin1, Pin2 and Pin3 to top asymmetric disk	206
Figure B-16. U1-direction forces transferred from Pin1, Pin2 and Pin3 to top asymmetric disk	207
Figure B-17. Magnitude comparison of U1-direction forces acting on top asymmetric disk	207
Figure C-1. “ S_S Risk-Targeted Maximum Considered Earthquake (MCE_R) [174]..	210
Figure C-2. “ S_I Risk-Targeted Maximum Considered Earthquake (MCE_R) [174]..	210
Figure C-3. Response spectra for analyses	211
Figure C-4. Roof displacement time histories in x and y directions of the 4-storey building under El-Centro earthquake record.....	212
Figure C-5. Base shear vs roof displacement plots in x and y directions of the 4-storey building under El-Centro earthquake record.....	212
Figure C-6. Drift ratio plots in x and y directions of the 4-storey building under El-Centro earthquake record	213
Figure C-7. Plots of maximum damper displacement in x and y directions of the 4-storey building under El-Centro earthquake record.....	213
Figure C-8. Roof displacement time histories in x and y directions of the 6-storey building under El-Centro earthquake record.....	213
Figure C-9. Base shear vs roof displacement plots in x and y directions of the 6-storey building under El-Centro earthquake record.....	214
Figure C-10. Drift ratio plots in x and y directions of the 6-storey building under El-Centro earthquake record	214

Figure C-11. Plots of maximum damper displacement in x and y directions of the 6-storey building under El-Centro earthquake record	214
Figure C-12. Roof displacement time histories in x and y directions of the 8-storey building under El-Centro earthquake record	215
Figure C-13. Base shear vs roof displacement plots in x and y directions of the 8-storey building under El-Centro earthquake record	215
Figure C-14. Drift ratio plots in x and y directions of the 8-storey building under El-Centro earthquake record	216
Figure C-15. Plots of maximum damper displacement in x and y directions of the 8-storey building under El-Centro earthquake record	216
Figure C-16. Kobe earthquake record North-South (NS) and East-West (EW) components.....	217
Figure C-17. Roof displacement time histories in x and y directions of the 2-storey building under Kobe earthquake record	218
Figure C-18. Base shear vs roof displacement plots in x and y directions of the 2-storey building under Kobe earthquake record	218
Figure C-19. Drift ratio plots in x and y directions of the 2-storey building under Kobe earthquake record	218
Figure C-20. Plots of maximum damper displacement in x and y directions of the 2-storey building under Kobe earthquake record	219
Figure C-21. Roof displacement time histories in x and y directions of the 4-storey building under Kobe earthquake record	219
Figure C-22. Base shear vs roof displacement plots in x and y directions of the 4-storey building under Kobe earthquake record	219
Figure C-23. Drift ratio plots in x and y directions of the 4-storey building under Kobe earthquake record	220
Figure C-24. Plots of maximum damper displacement in x and y directions of the 4-storey building under Kobe earthquake record	220
Figure C-25. Roof displacement time histories in x and y directions of the 6-storey building under Kobe earthquake record	220
Figure C-26. Base shear vs roof displacement plots in x and y directions of the 6-storey building under Kobe earthquake record	221

Figure C-27. Drift ratio plots in x and y directions of the 6-storey building under Kobe earthquake record	221
Figure C-28. Plots of maximum damper displacement in x and y directions of the 6-storey building under Kobe earthquake record	221
Figure C-29. Roof displacement time histories in x and y directions of the 8-storey building under Kobe earthquake record.....	222
Figure C-30. Base shear vs roof displacement plots in x and y directions of the 8-storey building under Kobe earthquake record.....	222
Figure C-31. Drift ratio plots in x and y directions of the 8-storey building under Kobe earthquake record.....	223
Figure C-32. Plots of maximum damper displacement in x and y directions of the 8-storey building under Kobe earthquake record	223
Figure C-33. Roof displacement time histories in x and y directions of the 10-storey building under Kobe earthquake record.....	223
Figure C-34. Base shear vs roof displacement plots in x and y directions of the 10-storey building under Kobe earthquake record	224
Figure C-35. Drift ratio plots in x and y directions of the 10-storey building under Kobe earthquake record	224
Figure C-36. Plots of maximum damper displacement in x and y directions of the 10-storey building under Kobe earthquake record	224
Figure C-37. Reduction in peak displacement for different models under Kobe earthquake record	225
Figure C-38. Reduction in max. IDR for different models under Kobe earthquake record.....	225
Figure C-39. Reduction in peak acceleration for different models under Kobe earthquake record	226
Figure C-40. Maximum damper displacement for different models under Kobe earthquake record	226
Figure C-41. Landers earthquake record North-South (NS) and East-West (EW) components	227
Figure C-42. Roof displacement time histories in x and y directions of the 2-storey building under Landers earthquake record.....	228

Figure C-43. Base shear vs roof displacement plots in x and y directions of the 2-storey building under Landers earthquake record.....	228
Figure C-44. Drift ratio plots in x and y directions of the 2-storey building under Landers earthquake record	228
Figure C-45. Plots of maximum damper displacement in x and y directions of the 2-storey building under Landers earthquake record	229
Figure C-46. Roof displacement time histories in x and y directions of the 4-storey building under Landers earthquake record.....	229
Figure C-47. Base shear vs roof displacement plots in x and y directions of the 4-storey building under Landers earthquake record.....	229
Figure C-48. Drift ratio plots in x and y directions of the 4-storey building under Landers earthquake record	230
Figure C-49. Plots of maximum damper displacement in x and y directions of the 4-storey building under Landers earthquake record	230
Figure C-50. Roof displacement time histories in x and y directions of the 6-storey building under Landers earthquake record.....	230
Figure C-51. Base shear vs roof displacement plots in x and y directions of the 6-storey building under Landers earthquake record.....	231
Figure C-52. Drift ratio plots in x and y directions of the 6-storey building under Landers earthquake record	231
Figure C-53. Plots of maximum damper displacement in x and y directions of the 6-storey building under Landers earthquake record	231
Figure C-54. Roof displacement time histories in x and y directions of the 8-storey building under Landers earthquake record.....	232
Figure C-55. Base shear vs roof displacement plots in x and y directions of the 8-storey building under Landers earthquake record.....	232
Figure C-56. Drift ratio plots in x and y directions of the 8-storey building under Landers earthquake record	232
Figure C-57. Plots of maximum damper displacement in x and y directions of the 8-storey building under Landers earthquake record	233
Figure C-58. Roof displacement time histories in x and y directions of the 10-storey building under Landers earthquake record.....	233

Figure C-59. Base shear vs roof displacement plots in x and y directions of the 10-storey building under Landers earthquake record.....	233
Figure C-60. Drift ratio plots in x and y directions of the 10-storey building under Landers earthquake record	234
Figure C-61. Plots of maximum damper displacement in x and y directions of the 10-storey building under Landers earthquake record.....	234
Figure C-62. Reduction in peak displacement for different models under Landers earthquake record	235
Figure C-63. Reduction in max. IDR for different models under Landers earthquake record.....	235
Figure C-64. Reduction in peak acceleration for different models under Landers earthquake record	236
Figure C-65. Maximum damper displacement for different models under Landers earthquake record.....	236

LIST OF SYMBOLS AND ABBREVIATIONS

α	exponent
γ_0	shear strain
$\dot{\gamma}(t)$	shear strain rate
γ_0	peak shear strain
γ_a	shear strain caused by axial load
γ_r	shear strain caused by rotation
γ_s	shear strain caused by shear displacement
δ	lag angle
Δ	lateral displacement
Δ_t	time step
ε_1	normal strain component in x-direction
ε_a	average axial strain
η	loss factor
θ^+	rotation at d^+
θ^-	rotation at d^-
θ_s	design rotation angle of elastomer
μ	coefficient of friction
μ_k	coefficient for kinetic friction
μ_s	coefficient for static friction
$\mu\varepsilon$	microstrain
ξ	equivalent damping ratio
ξ_{eff}	effective damping
σ	standard deviation
σ_s	average compressive stress
σ_{hyd}	hydrostatic stress
σ_L	effective yield stress of lead
$\tau(t)$	shear stress
τ_0	peak shear stress

ω	frequency
a	displacement amplitude
a_R	amplification ratio
a_R^+	amplification ratio for maximum pull position
a_R^-	amplification ratio for maximum push position
acc	acceleration
A	plain elastomer
A	area
A_L	area of lead core
A_R	bonded rubber area
B	laminated rubber
BRB	ball-rubber bearing
B_a	dimensionless coefficient
C	arbitrary constant
C	damping coefficient
C3D6	continuum three dimensional tetrahedral element
C3D6R	continuum three dimensional tetrahedral element, reduced
C3D8	continuum three dimensional brick element
C3D8R	continuum three dimensional brick element, reduced
c_{DAM}	damping of DAM
c_{EB}	damping of EB
Ch1	channel 1
d	displacement input
d	input interstory drift
d^+	maximum positive test displacement
d^-	maximum negative test displacement
d_p^+	maximum displacement recorded at Ch7 at pull
d_p^-	maximum displacement recorded at Ch7 at push
d_{ave}^r	average of displacements measured by Ch1- Ch4 either at d_p^+ or d_p^-
d_{max}	damper displacement capacity
deg	degree
disp	displacement
D	diameter

D_{ave}	average of the absolute values of displacements d^+ and d^-
D_r	dimensionless coefficient
DAD	Damage Avoidance Design
DAM	displacement amplification mechanism
DCLs	damage control limit state
EB	elastomeric block
EDC	Energy Dissipation per Cycle
EDR	Energy Dissipating Restraint
E_b	bending modulus
E_c	compression modulus
E_{cycle}	energy dissipated per unit volume and per cycle of oscillation
EW	east-west
f	frequency
F	damper force
F^+	positive force at d^+
F^-	negative force at d^-
F_f	frictional force
$F_{spi,surf}$	total force developed on the contact surface
$F_{spi,surf}^{FR}$	total force due to frictional stress developed on the contact surface
$F_{spi,surf}^N$	total force due to contact pressure developed on the contact surface
F_{VE}	resistance force generated by a single elastomer block
F_d^{VE}	contribution of a single elastomer block to the total damper force
F_{VE}^{FR}	force generated by the contact friction between Pin4 and driven bar
F_{VE}^N	force generated by the contact pressure between Pin4 onto driven bar
F_x	column shear force in global x direction in the original structure
$F_{x,d}$	column shear force in global x direction in the protected structure
F_y	column shear force in global y direction in the original structure
$F_{y,d}$	column shear force in global y direction in the protected structure
F_z	column axial force in the original structure
$F_{z,d}$	column axial force in the protected structure
FEA	finite element analysis
G	shear modulus of elastomer
G'	storage shear modulus

G''	shear loss modulus
h	total height of laminated rubber block
HDNR	high-damping natural rubber
i	pin number
I	area moment of inertia
IDR	interstory drift ratio
k	constant related to the hardness of the rubber
k	elastic stiffness
k_{DAM}	stiffness of DAM
k_{EB}	stiffness of EB
k_{eff}	effective stiffness
K	rubber bulk modulus
K_2	post-yield stiffness
K_h	horizontal stiffness
K_R	rotational stiffness
K_{R0}	rotational stiffness under shear strain $\gamma = 0$
K_v	vertical stiffness
K_{v0}	initial vertical stiffness
K_{eff}	effective horizontal stiffness
LDD	Low Damage Design
LE	strain
LE12	shear strain component between x- and y-directions
LVDT	linear variable differential transformer
M_x	column bending moment in global x direction in the original structure
$M_{x,d}$	column bending moment in global x direction in the protected structure
M_y	column bending moment in global y direction in the original structure
$M_{y,d}$	column bending moment in global y direction in the protected structure
MDOF	multi degree of freedom
n	number of elastomer layers
N	normal force
NS	north-south
NLTHA	nonlinear time history analysis
PE	plastic strain

PGA	peak ground acceleration
Q_d	characteristic strength
r	radius
rs	R-square
rms	root-mean-square
R	radius
std	standard deviation
<i>surf</i>	considered surface
S	shape factor
S_i	shape factor of the i^{th} elastomer layer
S	stress
S_{22}	normal stress component in y-direction
SMA	shape memory alloy
SRSS	square root of sum of squares
t	time
t_i	thickness of i^{th} internal elastomer layer t
t_r	total rubber height
t_s	steel shim thickness
T_{1x}	fundamental period in x-direction
T_{1y}	fundamental period in y-direction
TMD	Tuned-Mass Damper
$u^i(t)$	deformation at element i
U1	displacement in x-direction
U2	displacement in y-direction
v	velocity
V_B	base shear
vel	velocity
V	volumen
VCD	viscoelastic coupling damper
VDW	viscous damping wall
VPD	visco-plastic device
VE	viscoelastic
W	system weight

CHAPTER 1

INTRODUCTION

1.1 Motivation

Earthquakes are unpredictable events that can result in large-scale catastrophic devastations. Tools for earthquake mitigation have been developed from ancient times and are still being upgraded in line with the evolution of modern science and society. Today, socio-economic expectations dictate an improved seismic performance of civil engineering structures and a higher level of control on the seismic risk.

The real cost of seismic damage is being reevaluated in light of past earthquakes and seismic risk is nominated as an economical decision variable. A structure designed to meet higher performance levels can be proven more feasible, especially considering that the cost of the structure is significantly smaller than the cost of downtime and lost equipment and properties. Therefore, minimizing the damage to structural and non-structural elements even under high levels of seismic intensity is a design objective in modern earthquake engineering. However, this cannot be achieved by the conventional ductile design targeting at life safety but not at damage prevention. The desired plasticity is limited to appropriately designed locations of the lateral load-resisting system, causing damage in structural and non-structural members. Herein, the objective of high performance structures yields to need for the development of innovative technologies and solutions achievable at reasonable costs.

Earthquake damage can be minimized by reducing the demand imposed on the lateral load-resisting system either through (a) absorbing the seismic input energy by supplemental energy dissipation devices or (b) uncoupling the structure from the ground shaking by seismic isolation.

Seismic isolation systems, usually located between the structure and the foundation, consist of structural elements with low lateral stiffness that deflect the earthquake energy by a shift to long periods and thus limit the transfer of seismic forces to the structure. Major displacements develop at the isolation level and the system is usually called base isolation.

Supplemental damping systems protect the primary structural members by absorbing a portion of the input seismic energy. They can be classified in two categories: (a) passive control devices and (b) active and semi-active devices. Active and semi-active energy dissipation devices need an external power supply and a robust control algorithm. On the other hand, passive devices do not require a power source and are activated by the relative motion between their points of attachment. This makes them more simple, reliable, cheaper, also more available and preferable.

Passive dampers can be further divided into two main categories: displacement-dependent (rate-independent) and velocity-dependent (rate-dependent). The displacement-dependent dampers dissipate energy through yielding (metal dampers) or solid friction (friction dampers). They exhibit large energy dissipation capacity, add stiffness to the structure, do not provide a restoring force and are activated under moderate and high level excitations. The rate-dependent devices absorb energy per principles of viscoelasticity; they can provide a restoring force and are activated under all magnitudes of excitation.

The potential of these two categories is combined in hybrid dampers which couple the displacement-activated and velocity-activated devices in terms of mechanism and characteristics. Thereby, they can be qualified as devices with enhanced performance.

A special class within the response control systems are the devices with re-centering capability. They minimize or even eliminate the residual drifts which significantly impair the structural safety, serviceability and post-event performance. Therefore, re-centering property is an essential attribute for earthquake resilience. On the other hand, the proposed re-centering systems require major interventions to the structural system, have a complicated design or are considerably expensive.

The effectiveness of passive control systems is dependent on the magnitude of structural response and the bracings used for the installation of dampers. For structures

that respond with small drifts and use the most common bracings (diagonal or chevron), the dampers may turn out to be ineffective in improving the structural performance. This issue can be engineered through methods for amplifying the displacement input to the damper. To date, the desired magnification is achieved through the configuration of bracing geometry and is used mainly for viscous dampers. The proposed configurations successfully amplify the structural drift but the provided amplification ratio may be affected by the stiffness of bracing members. Also, the configurations increase the cost of supplemental damping and insert an additional design parameter for the damper performance.

The state-of-the-art of modern earthquake engineering suggests that the next-generation passive control device for the resilient community would be welcomed if hybrid, re-centering and drift-amplifying at an affordable cost. A device synthesizing all these features within a practical capsule is truly appealing and challenging, and has not yet been launched. The damper on the focus of this doctoral thesis is proposed as a successful design to take the challenge.

1.2 Aim and scope

The aim of this research is the development and validation of a novel passive supplemental damping device named as “Backbone damper”. It combines multiple advantages and innovations within a single device with mechanically simple design that can be produced and installed at relatively low cost. The innovations introduced with the Backbone damper are:

- Engineering of a large-magnitude frictional force proportional to displacement;
- Displacement-dependent amplification of structural drift within the device mechanism;
- Providing all notable attributes (hybrid, self-centering, drift-amplifying and cost-effective) in a single unit.

The proposed device provides damping and stiffness through viscoelastic material deformation and solid friction, which makes it hybrid. Also, the device has an internal amplification mechanism that increases its energy absorption capacity, drift sensitivity

and the level of reliability in predicting the device performance. In addition, the amplifier develops the friction component of supplemental damping and stiffness. The generated frictional force is proportional to the input displacement, and so is the viscoelastic force. The device is designed in such a way that the viscoelastic and the frictional components are simultaneously activated. Within a vibration cycle, they reach their peaks at the same time and pass through the zero force-zero displacement point in tandem, which results in a re-centering hysteretic response.

In the device assembly, the viscoelastic material is concentrated in two separate symmetric blocks, connected in series to the amplifier. The “Backbone damper” is shown in Figure 1-1 and described in detail in Chapter 3.

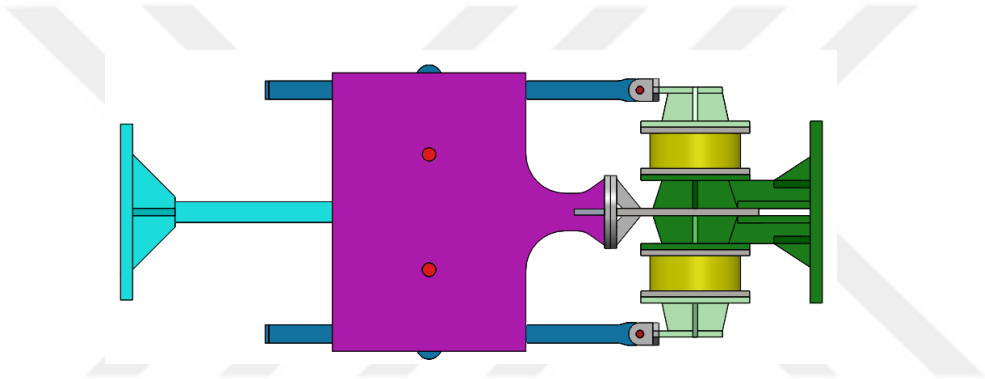


Figure 1-1. Backbone damper general view

The Backbone damper does not suffer any damage while absorbing energy. Thereby, it does not need any repair or replacement after a possible event and keeps its operational capability during following excitations and aftershocks. It has a simple design which allows for easy production and installation without any major intervention in the integrity of the housing structural system. It can be implemented both in new construction and retrofitting projects. All these features are achieved by the proper combination of material, geometry and delicate prediction of working mechanism.

In this scope, full-scale prototypes of the damper have been designed, manufactured and tested under dynamic harmonic motions. The experimental results have been verified against results from simulations with the device numerical model. The damper

has been implemented into a structural model to measure the change in seismic response of five different buildings.

The Backbone damper patent application has been filed under patent reference number P15/442.

1.3 Outline of the Research

Chapter 2 covers a literature review to provide a general technical background. It includes high-performance design concept, structural protection technologies, typologies of passive energy dissipation devices, elastomer material properties and friction laws and models.

Chapter 3 provides a detailed description of the device including geometry and operational mechanism.

Chapter 4 introduces the experimental work. It includes the material tests, the detailed description of the full-size prototypes, the test-set-up, the loading protocol, and test results and discussions.

Chapter 5 presents the detailed finite element analysis of the Backbone damper. The numerical simulations performed in ABAQUS software are used to validate the test results.

Chapter 6 covers the investigation of device performance parameters. The derivation of formulations to predict the device performance parameters using the experimental results is presented.

Chapter 7 includes the global analysis of hospital buildings with 2, 4, 6, 8 and 10 stories equipped with a selected configuration of the Backbone damper under an ensemble of strong ground motions scaled to a design-based earthquake level. The analyses are performed on LARSA4D structural analysis program.

Finally, the results and conclusions are summarized in Chapter 8. Recommendations for future research are presented.

CHAPTER 2

LITERATURE REVIEW

2.1 Introduction

Earthquakes are disastrous events that may result in many casualties and collapse of building inventory. Even if casualties can be minimized, the damages can leave the structures unserviceable and a significant amount of human and financial resources would be needed for rescue and recovery activities. The cost could reach ten times that for the countermeasures [1]. Experience from past earthquakes has documented that it is usually not feasible to repair a ductile building that has survived a major seismic event [2], [3].

Post-earthquake structural resilience is a determinant metric of modern society. Post-disaster functionality of critical infrastructure such as schools, hospitals, fire stations and transportation facilities is an imperative and therefore of primary concern to governments. Private sector companies also require uninterrupted operation even after moderate-intensity earthquakes considering the cost of downtime. For example, if every day or hour of post-earthquake downtime can amount to a significant financial loss for a business, it would clearly benefit from an “immediate occupancy” level of performance, aimed even under very rare levels of seismic hazard [4]. Therefore, high-performance structural design is preferred due to its socio-economic benefits.

In this light, advanced design methods have been proposed to upgrade the performance of urban infrastructure. The new approach termed either Damage Avoidance Design (DAD) or Low Damage Design (LDD) proposes the design of innovative earthquake-resistant systems that can survive even a catastrophic earthquake with no damage or damage limited to easily replaceable elements. Thus, the costs of expensive downtime and/or demolition can be removed or reduced. Projects to this aim were launched in

Japan [5], the US [3] and New Zealand [2]. The concept has in fact been considered for a long time [3], [6].

A damage control limit state (DCLs) introduced by Priestley et al. [7] is included as a performance limit state in the assessment of a building with low damage design systems. It allows for a certain amount of repairable damage as long as the cost of repair is considerably less than the one of replacement. The members of the low damage structure remain elastic and resume their initial positions after an earthquake. The objectives of low damage design are uninterrupted post-earthquake operation and minimal financial loss due to downtime, repair, and replacement. The efficiency of low damage design systems can be assessed with the following criteria: (i) damage mitigation, (ii) reparability, (iii) self-centering ability, (iv) non-structural damage and (v) affordability.

Damage mitigation is the key feature in the design of high-performance seismic-resistant structures. Hysteretic energy dissipation is no more acceptable for resisting earthquakes, since it is achieved at the cost of structural damage. Modern systems for structural control are available under three categories: (1) seismic isolation; (2) semi-active and active control; and (3) passive energy dissipation [8]–[11], [12]–[14].

The concept of seismic isolation has been developed into a practical technology widely implemented in seismically active areas. Its basic principle is set on uncoupling the structure from the damaging action of an earthquake, thereby reducing the forces transmitted to the structure. Typically, the isolation system employs structural elements with low horizontal stiffness usually placed at the foundation level. Thus, the structure's fundamental frequency is reduced and its corresponding dynamic mode involves displacement only at the isolation level. The higher modes do not contribute to the structural motion and, consequently, do not transfer energy to the structure. The structural protection is achieved not by absorption but rather through deflection of the input energy using the dynamics of the system. The net result is a decrease in the energy dissipation demand on the structure, while the displacement is concentrated in the isolation system. The concept is applicable and effective both for buildings and bridges [8]–[10], [15].

Active and semi-active control systems reduce the structural response by means of controllers, processing response information in real time, integrated with force generators that apply counteracting control forces. In the active control methods, the counteracting forces are applied by actuators and provided by a large power source, while in the semi-active control systems such forces are generated by reactive devices with controllable dynamic (damping and/or stiffness) properties. The power supply for semi-active control devices is typically orders of magnitude smaller compared with the one required for active control methods. Usually, the large control forces required by these methods can limit their practical application, especially for large and massive structures [16]–[18].

Contrary to semi-active and active systems, passive energy dissipation devices do not require an external supply of power. Furthermore, compared to seismic isolation, these devices can provide an effective protection against both earthquake and wind loads. The exceptional highlight should be made for bridges with high piers and long-period long-duration earthquake ground motions, the set of conditions that make the seismic base isolation inadequate and insufficient and the active control methods unaffordable. Thus, incorporation of passive energy dissipation devices comes out to be a modern and innovative approach for economical and safer structural design. These dampers purely dissipate energy during structural movements to maintain movements at permissible levels.

Passive devices are activated by the structural drift. It deforms the energy dissipating material within the damper. In general, all engineering materials absorb energy under cyclic deformations. A metric for the energy absorption capacity of a given material is the area enclosed by its hysteresis loop. This loop is the stress-strain curve obtained under cyclic loading of the material. Common structural materials have a very thin hysteresis loop in the elastic range, except for viscoelastic materials, which have very large the hysteretic loops.

As a result, passive dampers increase the total damping of the protected structure and consequently, mitigate the effect of dynamic excitations. Studies report that the damping ratio of buildings is generally less than 10% and decreases with the increase in height [19].

Along with damage mitigation, the structural control systems are expected to also provide the self-centering ability which is given a special importance for high-performance structures. Self-centering is the property of a structure to arrive at its original position after surviving a seismic event, i.e. not to lean. Recent studies have shown that the amount of lean of a building after an earthquake is a critical parameter for its residual capacity to sustain aftershocks [20], [21], [22]. The lean is generally termed as residual drift and caused by the nonlinearity of the yielding components in the system. McCormic et al. [23] concluded that for structures with more than 0.5% residual interstory drift, replacement is less costly than repair. The threshold for the residual drift was determined considering human comfort, building functionality and safety. Straightening, which can be a repair option, may not be applicable in many cases because of technical difficulties and high cost. Therefore, a residual drift of no more than 0.5% need to be targeted in the design of new buildings. A study by Erochko et al. [24] shows that even design-level earthquakes can cause more than 0.5% residual drifts in structures with ductile steel yielding systems.

The likely permanent drift can be limited by designing for the post-yield stiffness of the whole structure to be at least 5% – 10% of the initial elastic stiffness [25]. Residual drifts can also be effectively controlled or even completely eliminated through the employment of systems with self-centering capability.

The effectiveness of response control strategies has been validated during recent very severe earthquakes like the 2011 Tohoku-Oki earthquake [26]. For buildings without dampers the responses were recorded to not decay fast enough, and the number of large cycles was considerably large [26]. On the other hand, the buildings with supplemental damping did not suffer any significant damage. Furthermore, the added damping reduced the response acceleration and the fear of building occupants, which was significant in the 2011 Tohoku-Oki earthquake.

The effective performance of a certain passive energy dissipation device depends on the peculiar features of the original structure, the properties of the implemented device, and the characteristics of the ground motion. Considering the large variability in each of these parameters, a comprehensive series of analyses is a requisite to conclude about the particular passive energy dissipation system which is appropriate for a given case.

2.2 Passive energy dissipation devices

Passive control devices are generally grouped in two categories: displacement-dependent (displacement-activated) and velocity-dependent (velocity-activated). They are also addressed as rate-independent and rate-dependent, respectively. The classification can be further enhanced to include the motion-activated devices that cover the mass dampers. It need also be noted that some devices, such as viscoelastic dampers can be both displacement- and velocity-dependent.

2.2.1 Motion-activated devices

A motion-activated device transfers a portion of the input energy to a supplemental vibrating system. Representatives of this category are the tuned mass dampers (TMDs). In its simplest form, a TMD is a secondary mass-spring-dashpot system attached to the structure. The frequency of this system is tuned to the fundamental frequency of the protected structure. In this way the TMD is activated together with the structure but vibrates out of phase with it, and energy is dissipated through the inertia forces. These systems are typically installed on the roofs and used mainly for protection against wind-induced vibrations in high-rise buildings. Effectiveness of TMDs against ground motion pulses has been studied in [27].

2.2.2 Rate-independent dampers

Displacement-dependent dampers absorb energy through the relative displacement between their attachment points. Their performance is generally not affected by the frequency of motion. The forces these devices develop and transfer to the primary structural elements are usually in phase with the internal forces resulting from structural deformation. Therefore, within each cycle of oscillation, the maxima of both the damper forces and the internal forces occur at peak structural deformations and add up to larger force demands.

The reduction in ductility demand is provided through both an increased system stiffness and hysteretic energy dissipation. Typical representatives of this category are metallic and friction dampers. Metallic dampers develop a smooth hysteretic behavior while friction dampers follow an essentially bilinear hysteretic pattern with very high

initial stiffness [26], [28]–[30]. There are also hybrid dampers combining friction and yielding mechanism [31], [32].

2.2.2.1 Metallic dampers

Energy absorption mechanism of metallic dampers relies on inelastic deformation of metals, which can be categorized as one form of internal friction. Within the dampers, metals are usually deformed under shear or bending to reach plastic strains. The advantages of these dampers are the large energy dissipation, stable hysteretic behavior, long term reliability and relatively low cost.

Over the past 30 years, a number of innovative hysteretic steel dampers with high energy dissipation capacity have been proposed and tested. TADAS device [33]–[35], ADAS device [34], HADAS damper [36], honeycomb damper [37], shear panel [38], combined steel and aluminium damper [39], shear panel from low-yield-strength steel [40], dual-function DFMD [41], slit damper [42], [43], buckling restrained braces [44]–[48], tube-in-tube damper [47], circular plate damper [49] and U-shaped steel damper [50] are just some of the available variety of configurations.

Lead dampers [51] possess very good energy dissipation capacity since the yield stress is low and lead recrystallizes at room temperature after being subjected to many inelastic cycles. However, cracks are reported to form in these dampers due to frequent small deformations under wind loading [26] which compromises their performance under seismic actions.

2.2.2.2 Friction dampers

Friction dampers have been preferred for their high energy dissipation capacity, behavior that is relatively less affected by the excitation frequency and maintenance-free operation.

2.2.2.2.1 Basic principles of dry solid friction

The source of energy dissipation generated within friction dampers is the dry friction that develops across the interface between two solid bodies sliding relatively to each other. The basic theory of dry friction between two sliding bodies is founded upon the

following three hypotheses that have been experimentally validated for planar sliding ([12], [9]):

- The total frictional force is independent of the apparent area of contact.
- The total frictional force is proportional to the total normal force acting across the sliding interface.
- For the case of sliding with low relative velocities, the total frictional force does not depend on that velocity.

These assumptions are employed to define a general formulation for the frictional force either before slippage or during sliding as

$$F_f = \mu N \quad (1)$$

where F_f and N are the frictional and normal forces, respectively, and μ is the coefficient of friction. Since the coefficient of friction is observed to be higher immediately before slippage than during sliding, separate coefficients for static (μ_s) and kinetic (μ_k) friction are introduced [12].

The basics of dry friction theory expressed with Equation (1) is commonly referred to as Coulomb friction. In practice, the Coulomb theory is an approximate formulation of the more complex frictional phenomena. Identification of the true contact area, the bonding mechanisms involved in the interfacial sliding and the localized inelastic deformations are key items in the examination of frictional phenomena. These have been investigated in detail in [52] and [53].

The coefficient of friction is often idealized as a constant for a selected pair of materials. In practice, this is not the case. The coefficient of friction depends on the normal pressure, sliding velocity, temperature, load dwell, corrosion of mating surfaces, contamination and travel length [9].

It has been experimentally evidenced that the sliding coefficient of friction decreases with the increase in normal pressure [52]. Also, the sliding coefficient of friction changes with the increase in the number of deformation cycles.

At very low sliding velocities the sliding coefficient of friction is low. The coefficient is increased with a further increase in the velocity, but at very high velocities the coefficient of friction is reduced [54].

The heat flux across the faying surfaces is influenced by the apparent pressure and the sliding velocity. It increases with the increase in the velocity and pressure. Thereby, similarly to the effect of sliding velocity, when the heat flux is small the sliding coefficient of friction increases whereas the large heat flux results in a decrease in the friction coefficient [54].

A phenomenon commonly observed at a sliding interface is the stick-slip motion. It is due to the static coefficient of friction being greater than the kinetic coefficient of friction. During the change in the direction of motion, a momentary stop occurs followed by a motion in the reverse direction. At the onset of the motion in the reversed direction, the static frictional force is mobilized. It is usually larger than the sliding friction force and this causes a pulse in the developed friction force.

Another phenomenon to be considered in dry sliding friction is the wear. It is quantified with the amount of material removed from the sliding surfaces. The wear is universal in almost all sliding systems and can be reduced, but not eliminated. It is proportional to both the normal force and the travel length.

The clamping force between the surfaces is designed so as to allow for a slippage at a pre-defined friction force, commonly referred to as the slip load of the damper. In a family of friction dampers where the clamping force is provided through a bolt preload, the normal force is not uniformly distributed across the sliding interface. This results in a change in the slip resistance and consequently in unstable hysteresis loops [9].

2.2.2.2 Existing friction dampers

Most of the friction dampers are characterized with rectangular hysteresis loops which indicates behavior similar to the Coulomb theory.

The Pall friction damper introduced by Pall and Marsh [55] is a pioneering device for the employment of friction mechanism for energy dissipation under extreme events. The Pall damper consists of braces connected with horizontal and vertical link elements which dissipate energy when slippage occurs. Tests of the device have

evidenced significant amount of energy absorption [56] and [57]. A proposed recent improvement to the Pall friction damper is presented in [58].

Slotted Bolted Connections is another popular friction damper [59], [60] experimentally established to reduce the structural response to ground shaking.

The Sumitomo-type friction damper is characterized by a more complicated mechanism [61], [62]. Similar to Pall friction dampers, Sumitomo dampers reduce the structural displacements. The reductions, however, depend on the ground motion because friction dampers are not activated under small excitations (dampers do not slip and thus do not dissipate energy for forces smaller than the slip load) [61]. The installation of the friction dampers did not have a significant influence on the base shear.

A new configuration of friction damper called Energy Dissipating Restraint (EDR) was developed and tested by Nims et al [63]. Its design is similar to the Sumitomo's friction damper but uses steel and bronze wedges. The main elements of the damper are internal springs, friction wedges, compression wedges, stops and a cylinder. The EDR is not characterized by a rectangular loop and generating a force proportional to displacement. Thereby, in contrast to other frictional dampers, it gets activated under small levels of excitation and has a re-centering capability. However, according to shaking table tests performed by Nims and Kelly, the maximum force provided by the device is only 3kN which is far below the needs of practical applications in engineering structures. Both the output force and the stroke of the EDR need to be enhanced. Researchers have later investigated the possibilities for such an enhancement but it has been very difficult to provide a spring that has a large output force as well as deformation capacity [64]. Therefore, an EDR cannot be designed to fit the application in practical structures. Furthermore, many passive devices have been analyzed to produce an effect similar to an active variable stiffness system, but none of these efforts has yielded a successful result.

Another frictional device characterized with self-centering capability is developed by Karr et al. [65], [66]. However, it is expensive to construct and does not scale easily to the force capacity needed in structural applications [67], [68].

Over the years, a lot more configurations of friction dampers have been developed [69]–[73].

2.2.3 Rate-dependent dampers

A velocity-activated damper absorbs energy through the relative velocity across the device. Thereby, its behavior depends on the frequency of motion. The damper forces are usually out of phase with the internal forces in the connected structural members that arise in resisting a seismic input. Hence, the maximum forces developed within the dampers do not add to the peak member internal forces, which ends up with lower design forces for the parent structure, including the foundations.

Representatives of rate-dependent passive devices are viscous dampers and viscoelastic solid dampers. Viscoelastic solid dampers affect the structural stiffness and thus the fundamental natural frequency while viscous fluid dampers do not. The latter provide a reduction in ductility demand and structural response as a result of supplemental damping only.

2.2.3.1 Viscous dampers

Viscous dampers dissipate energy through the deformation of highly viscous fluids. The most common design is a piston moving within a cylindrical tube and thus forcing the fluid inside the tube to flow through orifices around or through the piston head [74], [75]. This process results in a difference in pressures on the two sides of the piston head, which actually generates the damper force.

A mathematical model to represent the behavior of viscous dampers has been derived using experimental results [76]. The model can be formulated as follows:

$$F = C \text{sign}(v) |v|^\alpha \quad (2)$$

where F is the damper force, C is a damping coefficient, v is the relative velocity between damper ends, α is an exponent, and $\text{sign}(\ast)$ is the signum function.

For $\alpha = 1.0$, the viscous damper is linear and has an elliptical hysteresis loop under harmonic motion. The major advantage of linear viscous dampers is the phase difference between the damper forces and structural drifts. However, the maximum

damper force is not limited and may exceed the capacity of connected structural members. When α approaches zero, the hysteresis loop expands to an almost rectangular shape which provides for a significantly larger energy dissipation per cycle compared to linear dampers. Their disadvantage is that they are relatively more complicated to manage and model. Dampers with $\alpha > 1.0$ are not commonly used in practice. The effect of linear and nonlinear viscous dampers on structural response is examined in detail in [77]–[80].

In an alternative design, perhaps more effective, the piston is replaced with a steel plate and the tube – with a narrow steel container. The plate named as a viscous damping wall (VDW) is moving within the container filled with the viscous fluid [81], [82]. The wall is fixed to the upper floor and the container to the bottom one.

2.2.3.2 Viscoelastic dampers

Viscoelastic dampers typically consist of a solid viscoelastic material sandwiched between rigid steel plates. Energy absorption is provided through large shear strains in the viscoelastic material.

Under a sinusoidal load with frequency ω , the shear strain $\gamma(t)$ and the shear stress $\tau(t)$ oscillate at the same frequency ω but in general out-of-phase. They can be expressed by [83], [84], [12]

$$\gamma(t) = \gamma_0 \sin \omega t \quad (3)$$

$$\tau(t) = \tau_0 \sin(\omega t + \delta) \quad (4)$$

where γ_0 and τ_0 are the peak shear strain and the peak shear stress, respectively, and δ is the lag angle.

The shear stress can also be written as

$$\tau(t) = \gamma_0 [G'(\omega) \sin \omega t + G''(\omega) \cos \omega t] \quad (5)$$

where

$$G'(\omega) = \frac{\tau_0}{\gamma_0} \cos \delta \quad (6)$$

and

$$G''(\omega) = \frac{\tau_0}{\gamma_0} \sin \delta \quad (7)$$

Therefore, the stress-strain relationship can be expressed as

$$\tau(t) = G'(\omega)\gamma(t) \pm G''(\omega)[\gamma_0^2 - \gamma^2(t)]^{1/2} \quad (8)$$

Which defines an ellipse as shown in Figure 2-1, whose area gives the energy dissipated by the viscoelastic material per unit volume and per cycle of oscillation

$$E_{cycle} = \pi\gamma_0^2 G''(\omega) \quad (9)$$

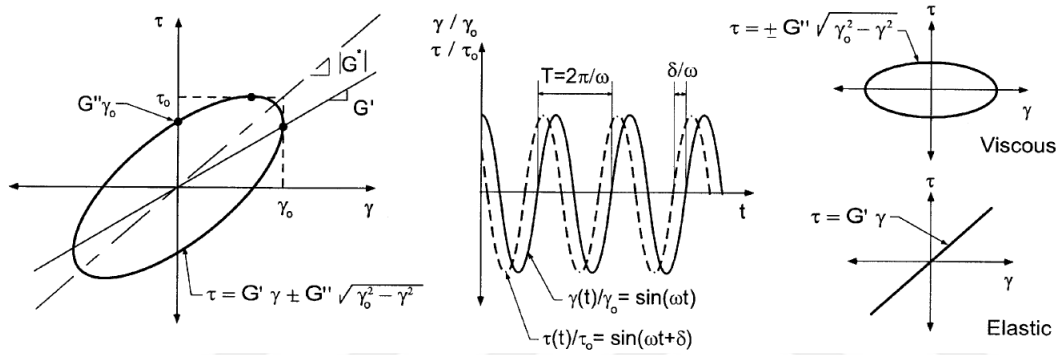


Figure 2-1. Viscoelastic material properties (after [85])

It is seen from Equation (8) that the first term of the shear stress is the in-phase portion with $G'(\omega)$ representing the elastic stiffness. The second term is the out-of-phase portion and represents the energy dissipation component.

Implementation of viscoelastic dampers causes a small increase in structural stiffness due to the inherent storage stiffness of the viscoelastic material. One of the primary advantages of the viscoelastic dampers is that they dissipate energy under all levels of ground motion. This is seen more clearly when Equation (4) is written in the form

$$\tau(t) = G'(\omega)\gamma(t) + \frac{G''(\omega)}{\omega}\dot{\gamma}(t) \quad (10)$$

Which is valid under harmonic motion since in that case $\dot{\gamma}(t) = \gamma_0\omega \cos \omega t$. The quantity $G''(\omega)/\omega$ is the damping coefficient of the damper material. The equivalent damping ratio is

$$\xi = \frac{G''(\omega)}{\omega} \left(\frac{\omega}{2G'(\omega)} \right) = \frac{G''(\omega)}{2G'(\omega)} \quad (11)$$

Accordingly, $G''(\omega)$ is defined as the shear storage modulus of the viscoelastic material, which is a measure of the energy stored and recovered per cycle; and $G'(\omega)$ is defined as the shear loss modulus, which gives a measure of the energy dissipated per cycle. The loss factor, η , defined by

$$\eta = \frac{G''(\omega)}{G'(\omega)} = \tan \delta \quad (12)$$

is also often used as a measure of energy dissipation capacity of viscoelastic material.

It is seen that the two moduli, $G'(\omega)$ and $G''(\omega)$, or $G'(\omega)$ and η , determine the dynamic behavior of the linear viscoelastic material in shear under harmonic excitation. These moduli depend on (i) excitation frequency, (ii) ambient temperature, (iii) shear strain level and (iv) the variation of internal temperature within the material during deformation.

Chang et al. [84] summarized test results on dynamic cyclic shear response of three types of viscoelastic materials. For the tested configurations, the shear storage modulus and the energy dissipated per cycle are observed to decrease with increasing ambient temperature but the loss factor η remains fairly constant for all temperatures.

The dynamic response of steel and concrete frame structures equipped with viscoelastic dampers has been investigated both analytically and experimentally and results proved the damping effect of the dampers [83]–[90], [91].

Viscoelastic dampers in various configurations have been used to reduce both wind and earthquake vibrations in tall building applications. Over 10000 VE dampers were installed in each of the twin towers in the World Trade Center, a total of 260 VE dampers were installed in the Columbia SeaFirst building in Seattle and a total of 16 large VE dampers were also installed in the Two Union Square building [12]. The viscoelastic dampers have been shown to increase the inherent damping of these tall buildings [92].

Christopoulos et al. [93] and Montgomery et al. [92] proposed and tested a new viscoelastic damper to be installed in lieu of coupling beams.

Gong et al. [94], [95] proposed a new type of VE damper with strong nonlinear characteristics. The new VE damper is characterized with stable performance, almost independent of frequency; improved capacity and larger stiffness.

VE damper combined with other types of units were also researched and used in order to obtain an improved performance, such as metallic yielding component [96] and lead elements [97].

With the invention of high-damping natural rubber (HDNR) [98], the damping of viscoelastic materials was increased to values between 10 and 20% at 100% shear strain. The material is nonlinear at shear strains less than 20% and demonstrates higher stiffness and damping. Between 20 and 120% shear strains, the modulus is low and constant. Under large strains, the modulus and the energy dissipation increase. This behavior can be beneficial for implementations in structural control. HDNR was then used for seismic isolators [99] and dampers [100]–[102].

Research on the development of new VE materials is going on. Xu et al. [103] developed several types of VE materials based on nitrile butadiene rubber matrix and silicone rubber matrix; the results show that VE materials based on nitrile butadiene rubber matrix have great capacity of energy dissipation, whereas those based on silicone rubber matrix have stable performance under various conditions.

2.2.4 Hybrid dampers

The primary performance advantage of displacement-dependent dampers is their large energy absorption capacity. Upon activation (either yielding or slip) of the damper, the area enclosed by the hysteresis loop enlarges and the maximum force is capped off. However, the threshold for activation is usually reached under moderate and high levels of excitation. This makes the hysteretic dampers ineffective under both wind loading and lower-intensity seismic events. Under minor earthquakes, the dampers increase the overall structural stiffness without providing any damping, which results in an increase in both the forces and accelerations.

On the other hand, rate-dependent dampers provide damping for all magnitudes of deformation, i.e. their drift-sensitivity is enhanced. They are activated even under wind disturbances and minor earthquakes and are effective throughout the excitation

duration from its very onset. This behavior is highly beneficial and desirable, especially when designing for an improved performance under both wind and earthquake loading and over a wide range of hazard levels. Also, it needs to be considered that both wind storms and low-intensity earthquakes are more frequent than severe seismic events.

To exploit the strengths of both categories of passive devices and minimize their shortcomings, combinations of passive devices into hybrid systems have been studied [104], [105], [106]. Vargas and Bruneau [105] reported an improvement in structural performance, although the viscous fluid dampers, installed together with yielding dampers, reduced the effectiveness of the latter. The simple combination of damping units into a hybrid supplemental damping system resulted in response reduction, but did not fully use the potential of coupled devices. This motivated the further investigation of the concept and eventually hybrid dampers were developed to more efficiently combine the advantages of rate-dependent and rate-independent devices. The Visco-Plastic Device (VPD) [29], Visco-Hyperelastic Device [107], Viscoelastic Coupling Damper (VCD) [93] and [108]–[111] are some recently proposed hybrid dampers.

2.2.5 Re-centering systems

Hysteretic dampers, that are the most commonly used devices for structural control, dissipate a substantial amount of energy but cannot prevent the residual drifts which are a critical measure for the safety, serviceability and economical feasibility of the structure. Therefore, the design of supplemental damping tools has further evolved so as to control the residual deformations, and re-centering systems have been developed to this end. These systems are characterized with a flag-shaped hysteretic behavior, shown in Figure 2-2. They absorb less amount of energy compared to the full-cycle hysteretic dampers but re-center the structure after each vibration cycle and eliminate any residual displacements. Furthermore, they are as effective as full-cycle hysteric devices in reducing the peak structural response [112]–[115].

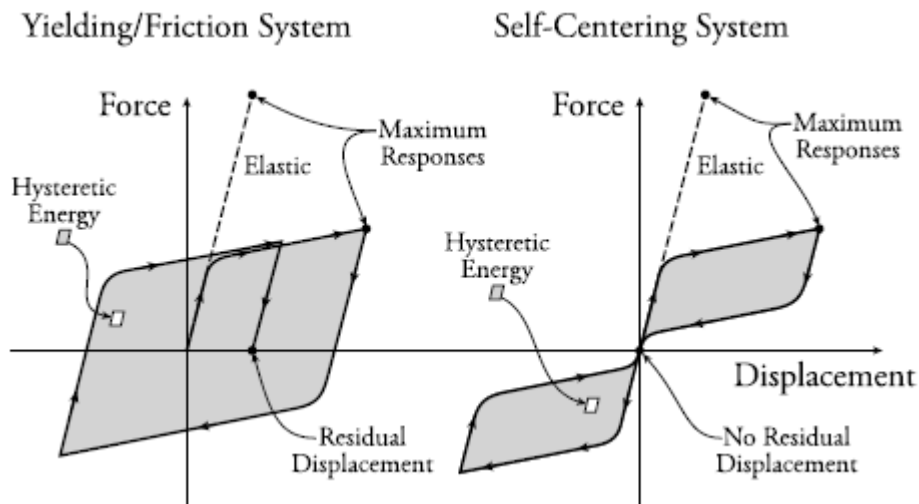


Figure 2-2. Flag-shaped versus full-cycle hysteretic response (after [4])

Another prominent advantage of self-centering systems is their capability to eliminate the progressive collapse resulting from P-Delta effects. Researchers report that P-Delta effects may cause residual drifts after each cycle that accumulate in the same direction throughout the successive cycles [116], [117]. The re-centering systems protect the structure against collapse by preventing residual drifts that can otherwise accumulate in one direction and result in progressive collapse. Such a mechanism of progressive collapse may be experienced especially under long-duration subduction fault earthquakes [4].

Considering the benefits of self-centering capability, it has been an area of extensive research and different designs have been proposed to yield the flag-shaped hysteresis loop. Many of the available re-centering systems require significant interventions to the structural system. For example, rocking-wall systems [118]–[121] and rocking frame systems [122]–[129] need elaborate detailing to allow for the rocking at the base and the vertical displacement of walls/frames at each floor level. The self-centering systems applied at the connections of frame systems ([123], [130]–[134]) also require consideration of issues related to the device installation and integration in the global structure.

Re-centering capability is a characteristic of a special class of materials named shape memory alloys (SMAs) that exhibit a flag-shaped stress-strain curve. Other beneficial

properties of SMAs are their fairly good energy dissipation capacity, recovery after large elastic strains and high fatigue resistance. Therefore, they have been studied for use in re-centering damping systems [135]–[142]. Fully re-centering dampers with SMAs have been tested by Dolce et al. [138]. The experiments have evidenced that the SMA braces can improve the structural response as much as steel braces can do. However, SMAs are still an expensive technology.

Other re-centering dampers [68], [143], [4] are using pre-tensioning tendons combined with an energy dissipation mechanism.

2.2.6 Amplification of structural displacement

The passive supplemental damping devices are activated by either the relative velocity or relative displacement between their attachment points. Thereby, the magnitude of these parameters is essential for the amount of dissipated energy. On the other hand, the magnitude is determined by both the structural response and the brace configuration used for the installation of dampers. The most common installation configurations are the diagonal and chevron bracing due to their popularity in steel structures. These configurations, however, reduce the interstory drift transferred to the damping devices. For structures that respond with small deformations, the drifts are further reduced before reaching the dampers, which makes them ineffective in controlling the response.

The challenge is solved by installing the dampers in special configurations that amplify the structural drift. The most popular of these are the toggle [144] and Scissor-Jack [145] configurations. Other available amplification mechanisms are presented in [16], [18], [146]–[154]. The most recent ones can be found in [155], [156]–[159].

Some of the mentioned configurations and the amplification ratios they provide can be seen in Figure 2-3.

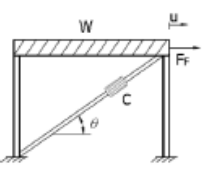
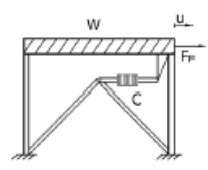
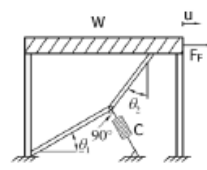
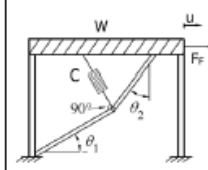
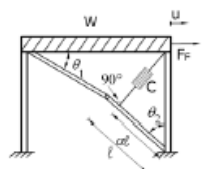
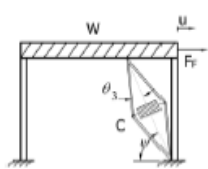
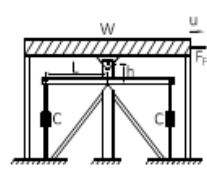
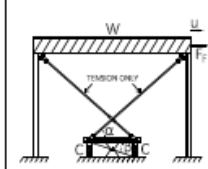
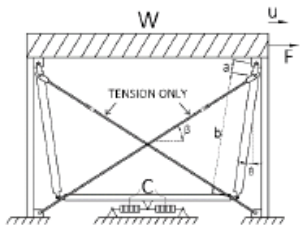
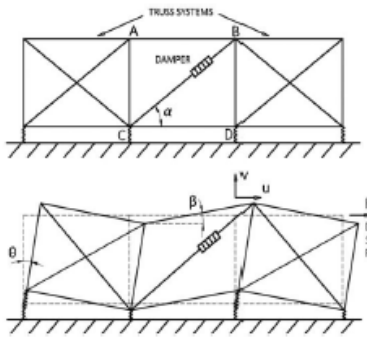
Diagonal	Chevron	Lower Toggle	Upper Toggle
 $f = \cos\theta$	 $f = 1.00$	 $f = \frac{\sin\theta_2}{\cos(\theta_1 + \theta_2)}$	 $f = \frac{\sin\theta_2}{\cos(\theta_1 + \theta_2)} + \sin\theta_2$
Reverse Toggle	Scissor-Jack	Lever-Arm	Seesaw
 $f = \frac{\alpha \sin\theta_1}{\cos(\theta_1 + \theta_2)} - \cos\theta_2$	 $f = \frac{\cos\psi}{\tan\theta_3}$	 $f = \frac{L}{h}$	 $f = \frac{\cos\alpha \cos\beta}{\sin(\alpha + \beta)}$
Eccentric Lever-arm System		Coupled Truss and Damping Mechanism	
 $f = \frac{a + b \cos\theta \cos\beta}{a \cos(\beta + \theta)} - 1$		 $u_D = u \cos\alpha + v \sin\alpha$ $f = \frac{u_D}{u}$	

Figure 2-3. Amplification factors for selected configurations (after [155])

The large and rapidly increasing amount of research on the topic once again demonstrate the importance of amplifying the structural drift for the effectiveness of passive energy dissipation devices.

All the mentioned amplification systems are installation configurations for the dampers. The behavior of a damper when installed in a given configuration cannot be predicted just on the basis of the performance tests of the damper, but needs testing of the damper within the configuration. This obviously is an additional item for both the design and implementation.

2.3 Summary

The aimed high-performance structural design needs high-performance seismic protection tools. These would be hybrid and re-centering dampers integrated into a displacement amplifying configuration. Also, the advanced device needs to be easily scaled to project-specific performance targets and produced at affordable cost. The combination of these within a single device has not yet been achieved. The Backbone damper introduced in this doctoral thesis is proposed as a successful combination of the above mentioned properties and is investigated throughout the thesis to validate the proposal.



CHAPTER 3

DEVICE MECHANISM

3.1 Introduction

The damper assembly has two main subassemblies: a viscoelastic unit (VE unit) and a displacement amplification mechanism (DAM). They are connected in series, each assigned a specific function in the device performance, to create a hybrid damper. The device is hybrid in all of its performance parameters, having two sources of energy dissipation and stiffness: viscoelasticity and friction. The viscoelastic source is generated by the VE unit while the friction part is developed by the DAM. The schematic representation of the damper is given in Figure 3-1.

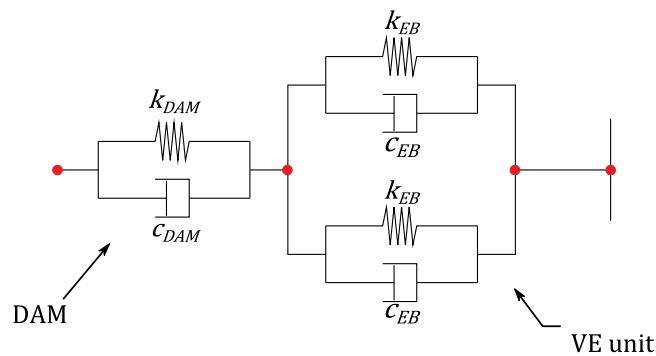


Figure 3-1. Backbone damper idealization

In Figure 3-1

k_{EB} = stiffness of EB

c_{EB} = damping of EB

k_{DAM} = stiffness of DAM

c_{DAM} = damping of DAM

The part on the left-hand side in Figure 3-1 is the DAM and the one on the right is the VE unit composed of a group of elastomeric blocks (EB). The input to activate the damper is the relative displacement between its points of attachment that are actually the two end points in the scheme. The DAM is to be connected to the structural element expected to displace more while the free end of the VE unit need to be connected to a fixed element or the one expected to displace less.

The VE unit has a certain stiffness and energy dissipation capacity while the DAM unit does have neither of them. In the complete assembly, the VE unit connected to the DAM provides the shear resistance necessary for the development of friction within the DAM. Friction is to supply the energy dissipation ability and stiffness within the DAM unit.

The DAM unit magnifies the displacement demand within the damper and transfers it to the VE unit. The damper is a dynamically activated system and its properties are dependent on structural displacement demand, i.e. the larger the displacement, the higher the damper efficiency. Thereby, the damper is kept active by the response it aims to reduce. The engineering solution manifests into manipulating the structural drift to differentiate the demand from the response. The structural response reduced by the damper can be amplified before being inserted back to the device. Also, the amplification of structural drift makes the damper active under small drifts and effective for all levels of structural response, i.e. increases the drift-sensitivity of the device.

In the device assembly, the two subassemblies support and complement each other and successfully combine to create a device with enhanced effectiveness both in terms of energy dissipation capacity and stiffness compared to the performance of each component taken alone.

The DAM unit is made of hinged steel parts and designed so as to remain elastic during a possible dynamic event. The integration of this mechanism enhances the device effectiveness and also provides the friction component of device performance parameters. The contact pressure to produce the friction is defined by the lateral and

rotational stiffness of the EB. Thus, the design parameters of the VE unit control both the viscoelastic and the frictional component of damper parameters.

The VE unit includes a group of symmetrically placed elastomeric blocks (EB) provided with a central fixed part in between and adapters to enable their connection to the DAM. The EBs can be plain elastomer, laminated rubber, lead rubber or ball rubber composite. The EBs dissipate energy through dynamic straining of the viscoelastic material and at the same time provide the stiffness necessary for the development of friction forces within the amplification mechanism. In doing so, they can sustain many cycles of reversed loading without experiencing any damage. The EB's shear, rotational and coupled shear-rotational stiffness values control the magnitude of friction forces developed within the amplifier. Therefore, the EB's mechanical properties can be tuned to the pre-defined device performance targets (energy dissipation capacity and stiffness).

Two prototypes of the device are designed, subsequently produced and their dynamic performance tests performed. The 3D solid models of the prototypes are developed in SolidWorks software to better understand the motion characteristics of the assembly. The two prototypes differ in the design of both the VE unit and the amplification mechanism. The displacement capacity of both prototypes is 45mm, corresponding to 1.5% interstory drift of a 3m-high frame.

3.2 Prototype I

Prototype I is designed with only one configuration of the VE unit. The VE unit is composed of two adapters and two laminated rubber blocks, mounted symmetrically on a central steel support to be fixed to the parent structural member by an anchor plate (Figure 3-2). The adapter is designed to provide the connection between the DAM and the EB. Its height determines the moment arm between the two components and regulates the shear strain due to rotation developed within the EB. The higher the adapter, the larger the shear strain due to rotation. The produced Prototype I is shown in Figure 3-3.

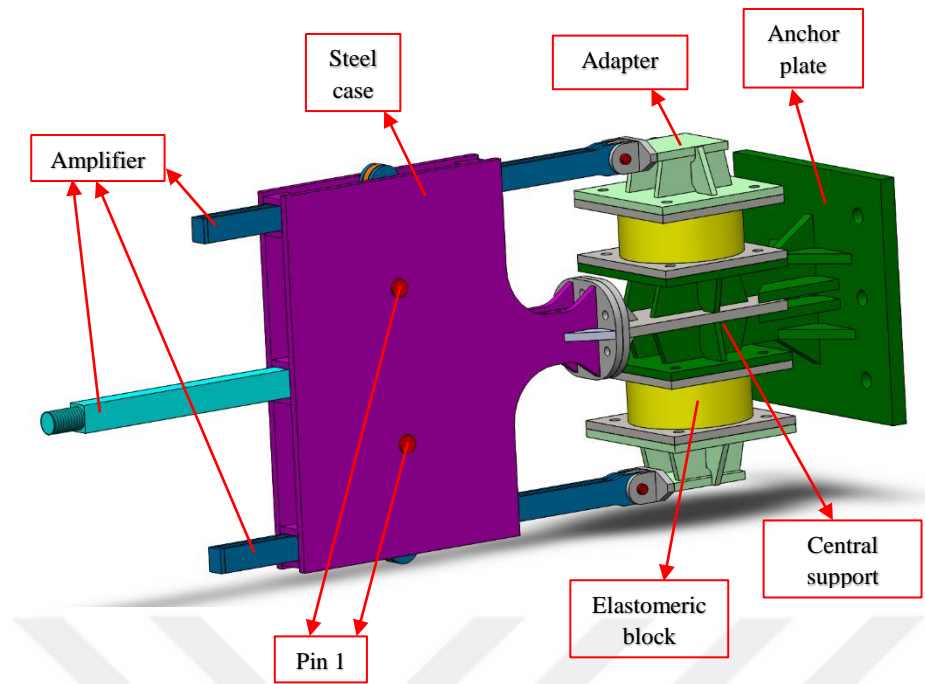


Figure 3-2. Isometric view of the 3D SolidWorks model of Prototype I

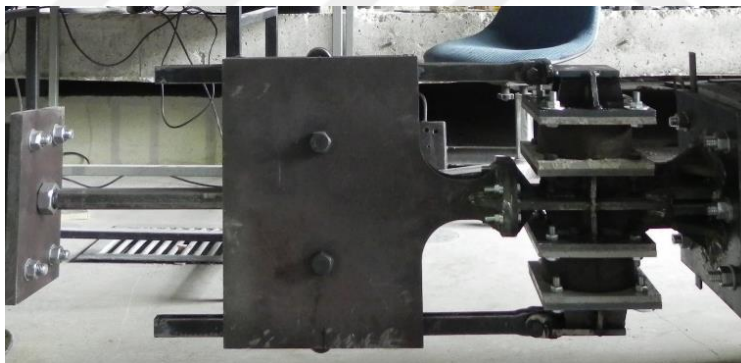


Figure 3-3. Produced Prototype I

3.2.1 DAM unit

The DAM unit consists of an amplifier and a steel case housing the amplifier. The steel case is rigidly connected to the central support of the VE unit. Thus, the fixed parts of the device are the central support and the steel case.

The case housing the amplifier is made of two steel plates, welded into a rigid box with small steel parts in between. It serves several functions:

1. supports the pivot point (Pin 1) of the amplification mechanism;
2. limits the rotation of the driving and the driven bars;
3. generates the friction component of energy dissipation while resisting the rotation of the driven bars under the forces developed by the VE unit;
4. ensures the out-of-plane stability of the amplifier.

The DAM has three components connected with pins. It magnifies the displacements on the principle of lever mechanism, having hinged steel elements.

The amplifier components and their functions are as:

1. **Central driving bar.** This part is attached at its free end to the connector brace. Thus, it is the application point of the input interstory drift d and the bar is the component activating the damper, therefore called “driving” bar (Figure 3-4 c).
2. **Driven bar.** There are two of them. One end of each is free and the other one is connected to the VE unit with pins. This bar transfers the amplified interstory drift to the VE unit, being “driven” by the central bar and the asymmetric disk (Figure 3-4 b).
3. **Asymmetric disk.** There are two of them. They connect the driving bar with the driven bars and provide the relation between the structural response d and the demand. The asymmetric disk is actually the lever of the mechanism and the amplification ratio, a_R , is defined by the geometrical proportions of the spacings between its pin holes. The “fulcrum” is Pin 1 and the two arm lengths are the distance from Pin 3 to Pin 1, and the distance from Pin 2 to Pin 1, respectively (Figure 3-4 a). The amplification ratio a_R is set to 2.0 for the current design.

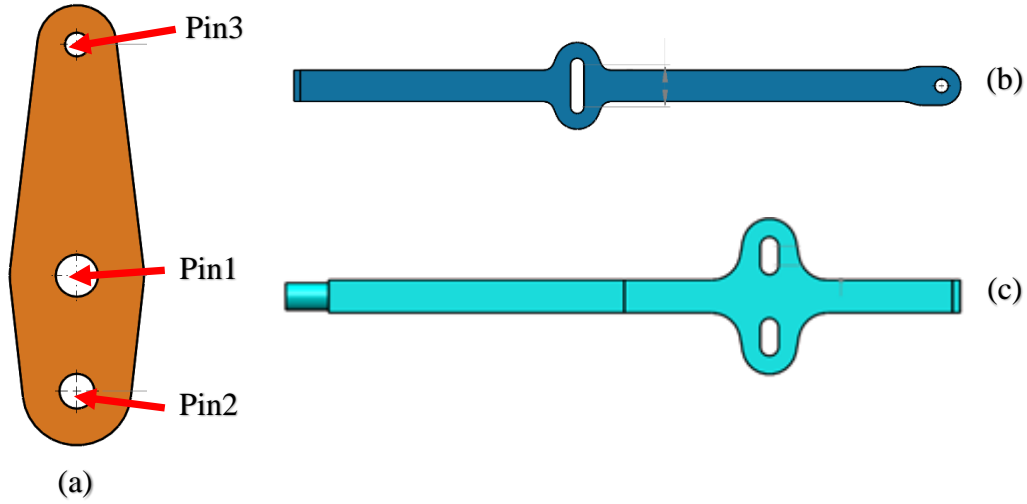


Figure 3-4. Geometry of (a) the asymmetric disk; (b) driven bar and (c) driving bar

The lever mechanism should be considered for the force path as well. The elastomeric block of the VE unit generates a resistance force F_{VE} dependent on the amplified displacement. This force is acting through the driven bar and is transferred as $a_R F_{VE}$ to the driving bar connected to the shorter arm of the lever. Consequently, the total benefit from the amplification mechanism, in terms of just the elastomer force contribution and essentially its shear component, can be estimated as:

$$F_{VE} = a_R d K_h \quad (13)$$

$$F_d^{VE} = a_R F_{VE} = a_R^2 d K_h \quad (14)$$

where

F_{VE} is the resistance force generated by a single elastomer block.

F_d^{VE} is the contribution of a single elastomer block to the total damper force.

3.2.2 VE unit

The driven bars transfer the amplified displacement to the VE unit and its EBs deform under shear and rotation. Their dynamic straining generates the viscoelastic component of total dissipated energy and a re-centering force due to the elastomer

storage stiffness. The geometry of the laminated rubber blocks of the VE unit is presented in Figure 3-5.

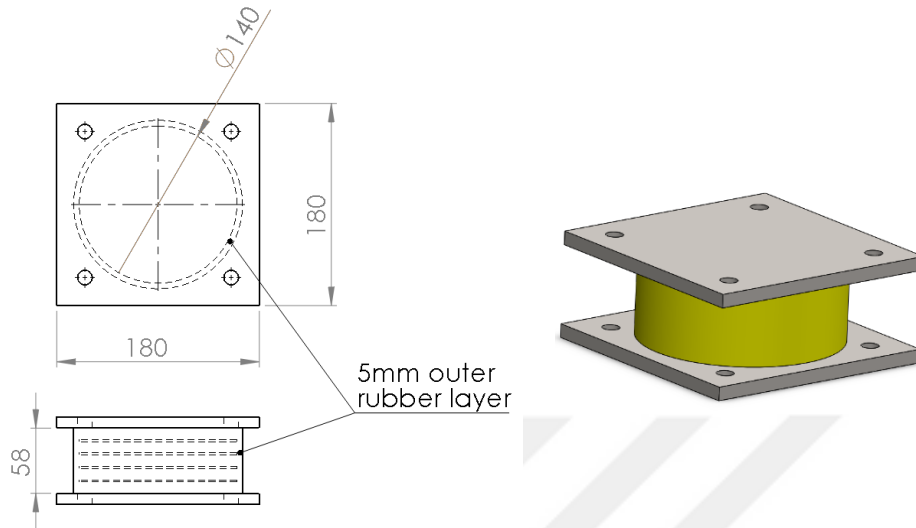


Figure 3-5. Geometry and dimensions of laminated rubber block

During the device operation, each elastomeric block is subjected to dynamic straining under combined shear and rotation. Therefore, its horizontal, vertical and rotational stiffness values are important input design parameters. The EB's mechanical properties are summarized in Table 3-1.

Table 3-1. EB mechanical properties

G , [MPa]	K_h , [kN/m]	E_c , [MPa]	$K_{\nu 0}$, [kN/m]	K_{ν} , [kN/m]
0.8	282.74	65.22	23051.31	3042.34

where

t_r = total rubber height, [mm]

t_i = thickness of i^{th} internal elastomer layer t, [mm]

S = shape factor

$$S = \frac{\text{loaded area}}{\text{area free to bulge}} \quad (15)$$

For a circular pad of radius R and thickness t_i

$$S = \frac{R}{2t_i} \quad (16)$$

n = number of elastomer layers

h = total height of laminated rubber block, [mm]

t_s = steel shim thickness, [mm]

G = shear modulus of elastomer, [MPa]

K_h = horizontal stiffness, [kN/m]

$$K_h = \frac{GA}{t_r} \quad (17)$$

A = full cross-sectional area (which may differ from the area of the reinforcing shims), [mm²]

E_c = compression modulus, [MPa]. As derived by Chalhoub *et al.* [160]

$$E_c = 6GS^2 \left(1 - \frac{8GS^2}{K} \right) \quad (18)$$

where

$K = 2000\text{MPa}$ is the rubber bulk modulus. This is the value most commonly used in the reference literature [161], [162], [163].

As reported by Warn *et al.* [164], vertical stiffness decreases with increasing lateral displacement and the vertical stiffness at a lateral displacement Δ , K_v , is estimated as

$$K_v = K_{v0} \frac{1}{\left[1 + \frac{3}{\pi^2} \left(\frac{A\Delta^2}{I} \right) \right]} \quad (19)$$

For a solid circular pad of radius R , the above equation can be simplified as

$$K_v = K_{v0} \frac{1}{\left[1 + \frac{12}{\pi^2} \left(\frac{\Delta}{R}\right)^2\right]} \quad (20)$$

where

Δ = lateral displacement [mm]

K_{v0} = initial vertical stiffness (with no lateral displacement), [kN/m]

$$K_{v0} = \frac{E_c A}{t_r} \quad (21)$$

The value of vertical stiffness in Table 3-1 is estimated for

$$\Delta = a_R d_{max} = 2 * 45 = 90mm$$

where

$d_{max} = 45mm$ is the damper displacement capacity.

EB's rotational stiffness is also affected by the lateral displacement. He *et al.* [165] conclude that the rotational stiffness of rubber bearings decreases dramatically with the increase in shear strain. They propose the following formulation for estimating the rotational stiffness of elastomeric bearings considering the effect of shear strain γ

$$K_R = K_{R0} \left(1 - \left|\frac{\Delta}{D}\right|^{\frac{1}{1+\gamma^2}}\right) \quad (22)$$

where

$D = 2R$ = bearing diameter

K_{R0} = rotational stiffness under shear strain $\gamma = 0$

$$K_{R0} = \frac{E_b I}{t_r} \quad (23)$$

For a solid circular pad of radius R , the above equation can be simplified as

$$K_{R0} = \frac{E_b I}{t_r} = \frac{\pi R^4 E_b}{4 t_r} \quad (24)$$

Here

E_b = bending modulus, [MPa].

The bending modulus E_b can be estimated using the following relations referenced in [166]:

$$E_c = \frac{E(1 + 2kS^2)K}{E(1 + 2kS^2) + K} \quad (25)$$

$$E_b = \frac{E \left(1 + \frac{2}{3}kS^2\right) K}{E \left(1 + \frac{2}{3}kS^2\right) + K} \quad (26)$$

where E , K and k are the Young's modulus, the bulk modulus and a constant related to the hardness of the rubber, respectively, and S is the shape factor.

In the above formulations, the effect of rubber compressibility is included. This effect increases with the increase in shape factor and has a more dramatic influence on the response of EB to axial load and rotation.

3.2.2.1 Limit design criteria for EB

The limit design criteria describe the limit states of EBs. The criteria are the maximum shear strain and peak tensile stress.

3.2.2.1.1 Shear strain

Critical parameter in the design of EBs is the shear strain in the elastomer at its interface with the steel plates. When the shear strain reaches a large value it may cause either debonding of elastomer and steel plate or shear failure of elastomer. To avoid such failures, shear strains need to be limited. Shear strains can be caused by axial load, shear displacement and rotation.

The limit on shear strains under combined compression, rotation and shear specified in Section 14.7.5.3.3 of [167] can be used. It includes both static and cyclic loading components, but since the damper is designed to operate under dynamic excitation, the static contribution is neglected and the modified equation reduces to

$$1.75(\gamma_a + \gamma_r + \gamma_s) \leq 5.0 \quad (27)$$

where

γ_a = shear strain caused by axial load

γ_r = shear strain caused by rotation

γ_a = shear strain caused by shear displacement

Since the Backbone damper EBs are not subjected to axial load, $\gamma_a = 0$.

For a circular geometry, the shear strain caused by rotation is calculated as

$$\gamma_r = D_r \left(\frac{D}{t_i} \right)^2 \frac{\theta_s}{n} \quad (28)$$

in which

$D_r = 0.375$ = dimensionless coefficient used to determine shear strain due to rotation

θ_s = design rotation angle of elastomer

The shear strain due to shear displacement is given by

$$\gamma_s = \frac{\Delta}{t_r} \quad (29)$$

3.2.2.1.2 Tensile stress

In Backbone damper, EBs have external plates bonded to the outer elastomer layers. One of the plates (the one connected to the bottom adapter) is fixed and the other one is partially restrained due to its guided motion. During rotation or lateral displacement combined with rotation of the guided plate (the one connected to the top adapter), an upward movement of its part can cause internal rupture due to hydrostatic tension. Considering this failure mode, the hydrostatic tension in elastomer body, with its peak value expected at the interface with the external plates, need not exceed the limit value as specified in [167]

$$\sigma_{hyd} \leq 2.25G \quad (30)$$

The hydrostatic stress can be calculated following the procedure proposed by [168] and used in [167]

$$\sigma_{hyd} = 3GS_i^3 \frac{\theta_s}{n} C_\alpha \quad (31)$$

$$C_\alpha = \frac{4}{3} \left[\left(\alpha^2 + \frac{1}{3} \right)^{1.5} - \alpha(1 - \alpha^2) \right] \quad (32)$$

$$\alpha = \frac{\varepsilon_a n}{S_i \theta_s} \quad (33)$$

$$\varepsilon_a = \frac{\sigma_s}{3B_a G S_i^2} \quad (34)$$

where

θ_s = design rotation angle of elastomer multiplied by 1.75

S_i = shape factor of the i^{th} elastomer layer

B_a = dimensionless coefficient used to determine peak hydrostatic stress

For circular geometry

$B_a = 1.6$ = dimensionless coefficient used to determine peak hydrostatic stress

ε_a = average axial strain multiplied by 1.75, taken as positive for compression

σ_s = average compressive stress multiplied by 1.75

3.3 Prototype II

The amplification ratio of Prototype II is variable depending on the relative displacement between the attachment points. It is designed to be equal to 2.62 at the initiation of motion and equal to 2.00 at 45mm displacement applied on the driving bar. This displacement-dependent amplification ratio is designed with the objective of increasing the device drift-sensitivity and energy dissipation capacity even further at the onset of earthquake excitation so as to refrain accumulation of strains in the parent structure. The gradual decrease in the amplification ratio, reaching its minimum design value at the ultimate displacement capacity of the device, is conscientiously pre-defined to limit the damper forces to be transferred to supporting structural members. These forces increase in parallel with the displacements. Thereby coupling a smaller amplification ratio with larger displacements keeps a constant level of design forces,

thus optimizing the sizing and design of the damper components and supporting members.

Avoiding stress concentration and facilitating even distribution and smooth flow of forces have been considered and aimed in the detailing and dimensioning of the device parts and the design has been performed accordingly. These are all considered in defining the geometry of parts.

The device steel case is again made of two plates, but this time not welded; instead connected by bolts with case supports in between. These supports are bedding the driving and driven bars of the amplifier throughout their sliding in translation.

The amplifier operates on the same principle as for Prototype I, just the geometry and dimensions of its components are changed to generate and accommodate the desired displacement-dependent amplification ratio.

Three different types of elastomeric block are designed for the VE unit of Prototype II. These are the plain elastomer, laminated rubber and ball rubber composite. Their mechanical properties summarized in Table 3-2. All the configurations have a circular cross-section. The major test parameter is the EB's shear stiffness.

Top adapter is the part connecting the EB with the driven bar and the bottom adapter is the one connecting it to the central support. Thereby, motion is transferred through the top adapter while the bottom adapter represents a support for the EB. Every EB configuration comes with its adapters that enable its integration into the device assembly.

The elastomer shear modulus is $G = 0.8 \text{ MPa}$ and the steel shim thickness is $t_s = 2 \text{ mm}$ for all configurations.

Table 3-2. Mechanical properties of EB configurations

Configuration	K_h , [kN/m]	E_c , [MPa]	K_{v0} , [kN/m]	K_v , [kN/m]
A1	279.25	1.48	516.75	260.22
A3-1	281.65	2.24	788.22	319.61
B1-1	241.53	98.40	3300.92	1542.61
B1-2	279.25	112.80	4374.96	2203.08
B3-1	241.94	66.91	3372.60	1245.98
B3-2	281.65	77.43	4543.59	1842.38
B3-4	362.29	98.40	5988.20	2634.45
BRB	327.25	-	-	-

The configuration notation is as follows:

Type (A, B or BRB) - shear strain level at damper displacement capacity (1, 2 or 3) - horizontal stiffness level (1, 2 or 3)

where

“A” = plain elastomer

“B” = laminated rubber

“BRB” = Ball-Rubber Bearing

Shear strain levels are:

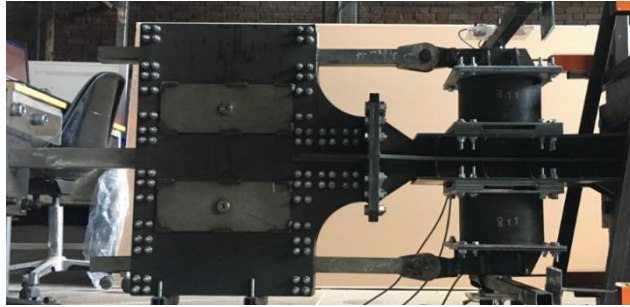
- “1” = 100% rubber shear strain at $d_{max} = 45mm$ ($t_r = 90mm$)
- “2” = 125% rubber shear strain at $d_{max} = 45mm$ ($t_r = 72mm$)
- “3” = 150% rubber shear strain at $d_{max} = 45mm$ ($t_r = 60mm$)

d_{max} = damper displacement capacity

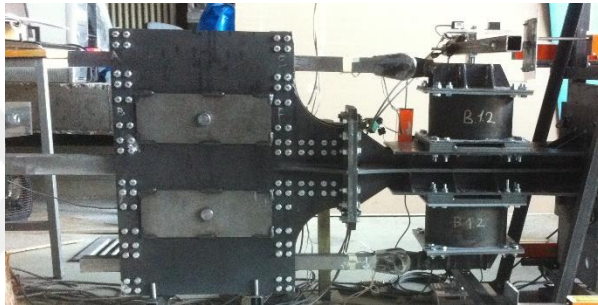
Horizontal stiffness levels are again in an increasing order (from 1 to 3) with the values given in Table 3-2.

The BRB design parameters are per [169]. For 100% shear strain the steel balls do not provide any supplementary stiffness and the horizontal stiffness is calculated as for a regular annular laminated rubber composite.

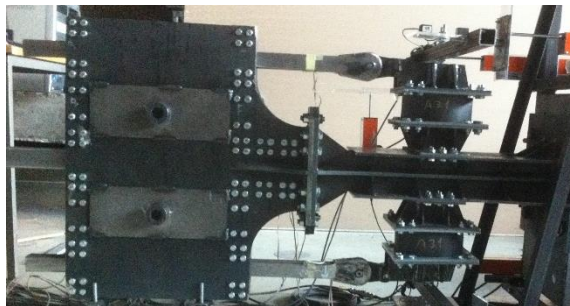
Each time a different configuration is tested, just the top and bottom adapters are changed. Photos of the test-ready prototype for three different configurations are shown in Figure 3-6.



(a) B1-1



(b) B1-2



(c) A3-1

Figure 3-6. Configurations of Prototype II as manufactured and installed in the dynamic test set-up

CHAPTER 4

EXPERIMENTAL WORK

4.1 Introduction

The experimental investigation of the Backbone damper covers dynamic characterization tests of full-scale prototypes. In addition, the elastomer material used for the EBs was also tested. The test results were later introduced into the device numerical model to realistically represent the material behavior. Procedures and results of the experiments are explained below.

4.2 Elastomer material tests

Elastomer material test are needed for properly defining the elastomer material in the device numerical model. Thereby, elastomer material of the EBs was tested for its elastic and damping properties.

4.2.1 Test samples and equipment

Investigation of the material properties of EBs' elastomer was realized through a series of material tests. The test program included uniaxial cyclic and relaxation tests under different loading velocities and the analysis of test results enabled the identification of viscoelastic and plastic behavior in the elastic and nonlinear range and how this balance is affected by loading rate and cycling.

The elastomer used in VE units is rubber reinforced with carbon black. The stress-strain curves obtained from tests are needed to create the three-dimensional constitutive relations governing the material behavior and determine the material parameters. Thereby, 'round dog-bone' test samples that essentially satisfy the

prerequisite of homogeneous deformation distribution are used. The test sample is shown in Figure 4-1 (a) and its dimensions given in Figure 4-1 (b).

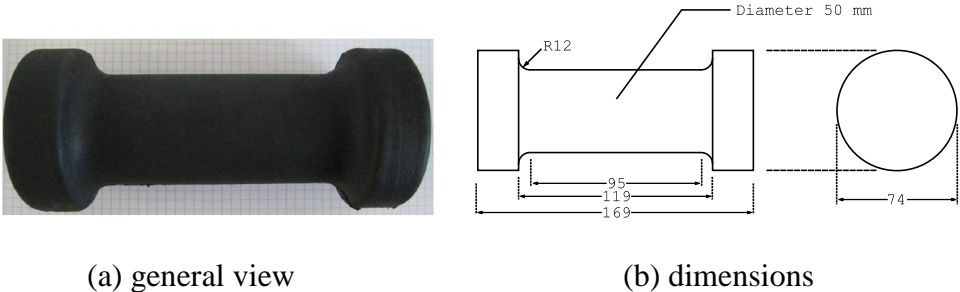


Figure 4-1. Round dog-bone test samples

The tests were performed on the MTS Servohydraulic testing machine of 250kN loading capacity. A photo of the testing machine located in the Structural Materials Laboratory of Civil Engineering Department is presented in Figure 4-2.

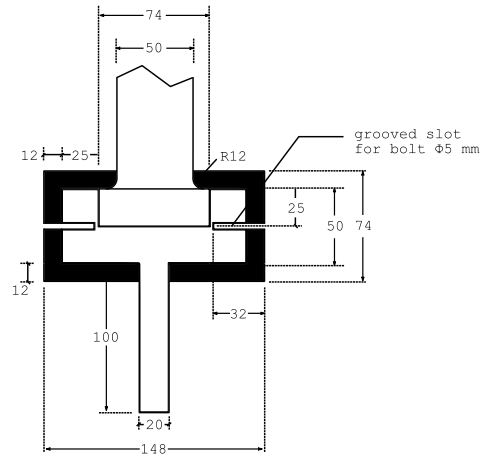


Figure 4-2. MTS Servohydraulic test machine

A special apparatus for the installation of the specimens, designed to avoid any slippage between the test specimens and the tension grips of the machine, was used for the tests. The apparatus and its dimensions can be seen in Figure 4-3 (a) and Figure 4-3 (b), respectively.



(a)



(b)

Figure 4-3. A photo (a) and dimensions (b) of the special apparatus for test specimen installation

4.2.2 Test procedure and program

4.2.2.1 Preload

During vulcanization included in manufacturing process, weak secondary connections are formed in elastomer. To eliminate their effect, all test specimens were subjected to initial pre-load before the tests. The pre-load amplitude was kept within the planned test parameters' limits. After applying the pre-load, each specimen was uninstalled from the testing machine and put to rest for two hours of relaxation so that its microstructure can recover its balanced state.

4.2.2.2 Uniaxial cyclic tension-compression tests under different velocities

To evaluate the material sensitivity to loading rate, the specimens were subjected to displacement-controlled cyclic tension-and-compression tests under four different cross-head velocities (0.1mm/s, 1mm/s, 5mm/s and 10mm/s). Assuming that the deformation is homogeneous at the specimen gauge length, these loading rates correspond to 0.001 s^{-1} , 0.01 s^{-1} , 0.05 s^{-1} and 0.11 s^{-1} strain rates, respectively. During the tests, the specimens were subjected to cyclic displacements changing between strain amplitudes of -0.3 and 1 (-30% and 100) as shown in Figure 4-4.

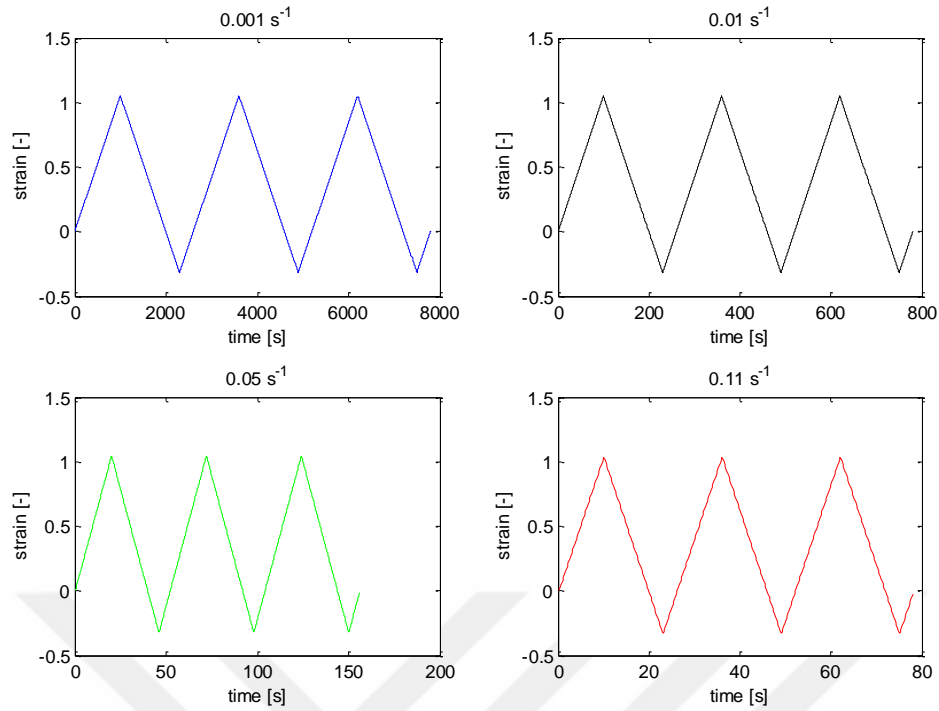


Figure 4-4. Strain vs Time curves for uniaxial cyclic tension-and-compression tests

4.2.3 Test results

The stress-strain loops obtained from the uniaxial cyclic tension-and-compression tests are given in Figure 4-5.

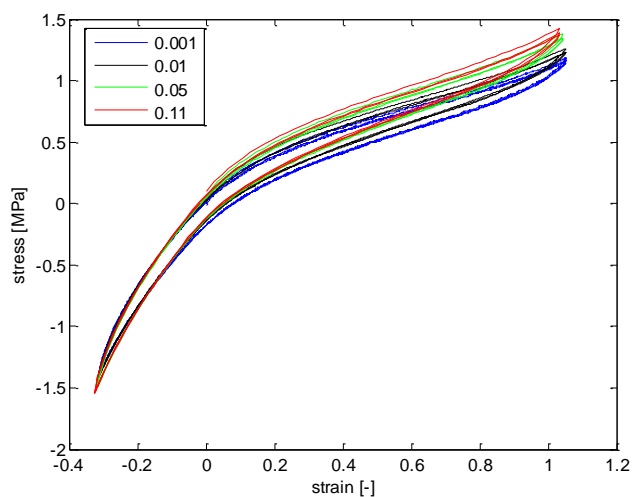


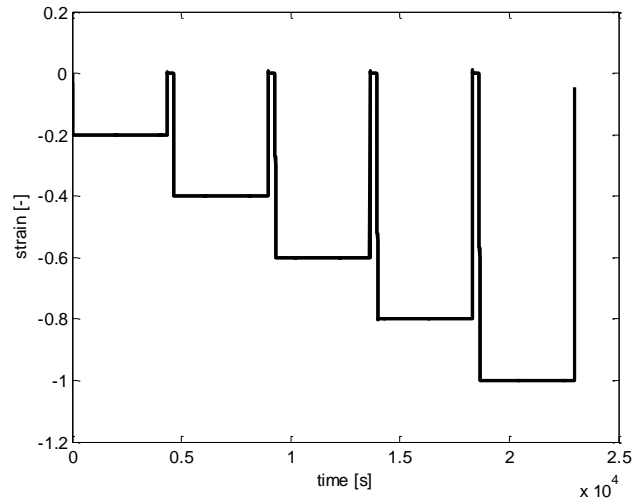
Figure 4-5. Stress-strain loops of uniaxial cyclic tension-and-compression tests under different loading rates

The following observations and conclusions can be drawn upon analyzing the loops of Figure 4-5:

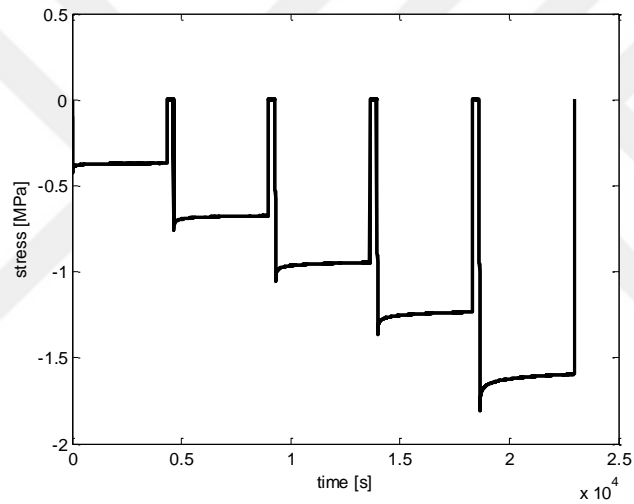
- After the first loading cycle, the stress-strain loops are essentially repeated.
- The stiffness of the tested elastomer increases with an increase in loading rate, as expected from a viscoelastic material. Therefore, a higher stress value is observed for a higher velocity under the same strain. The increase is more pronounced under tension rather than compression.
- The area of the hysteresis loop, enclosed between the loading and unloading curves, slightly increases with an increase in loading rate which translates into increase in energy dissipation. Yet, this increase is negligibly small.

These results are consequently considered in analyzing the global behavior of the Backbone damper.

The time-dependent properties of elastomer are examined through relaxation tests. In the test, the displacement is kept constant for a certain time and the change in applied force is recorded. The tests are performed for five different shear strain levels starting from 20% and reaching up to 100% with 20% increase for consecutive tests. The graphs of recorded displacement and force through time are shown in Figure 4-6.



(a) time-history plot of strain



(b) time-history plot of stress

Figure 4-6. Relaxation test data

4.3 Dynamic test set-up

A set-up for the dynamic performance tests of the device prototypes was designed and subsequently built up in the Structural Mechanics Laboratory of METU Civil Engineering Department. The design, components, features and construction stages of the set-up are explained next.

4.3.1 Loading set-up

The test set-up for the dynamic performance tests of the prototypes was installed at the Structural Mechanics Laboratory of Civil Engineering Department. The set-up design drawings are shown in Figure 4-7 and Figure 4-8. The set-up includes two steel supports, a hydraulic actuator and steel fillers placed between the prototype fixed end and the support. The same test set-up was used for both prototypes by just changing the fillers to adjust the set-up to the prototype length.

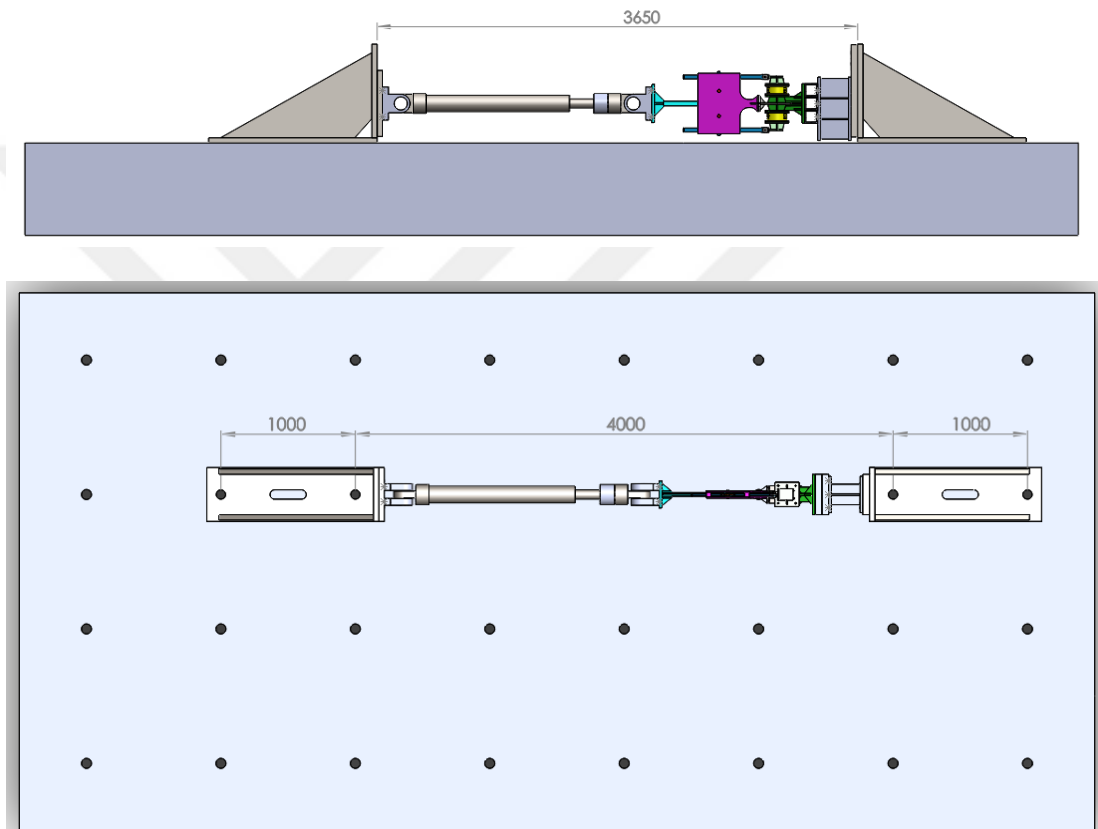


Figure 4-7. Side view (top) and plan view (bottom) of the dynamic performance test set-up design drawings (all dimensions are in mm)

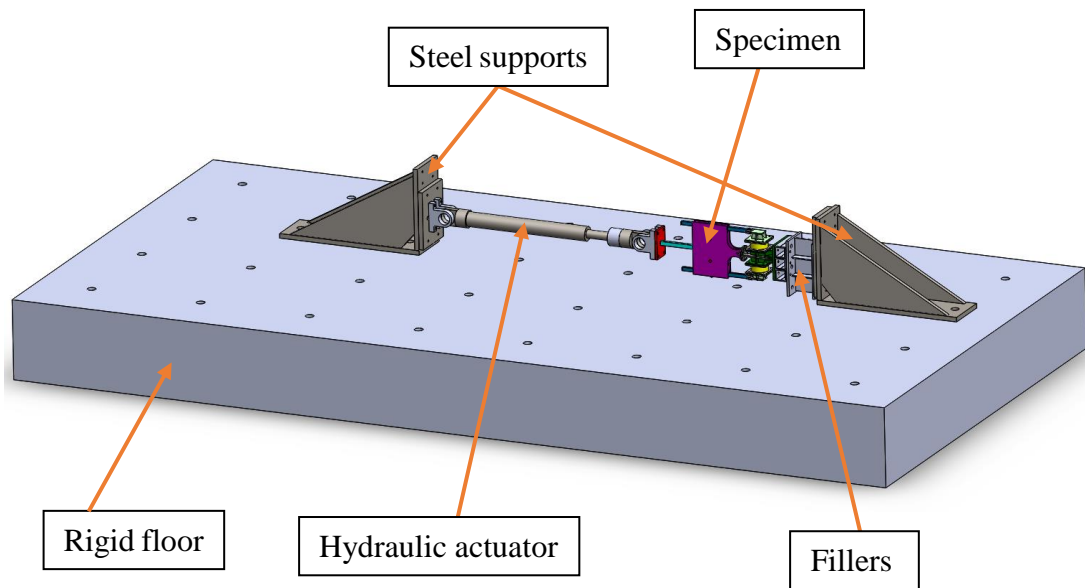


Figure 4-8. A three-dimensional design drawing of the dynamic performance test set-up

The 70cm-thick rigid floor of the laboratory has 7cm-diameter cylindrical openings drilled every 1m in both directions. Accordingly, each steel support has two holes on the support surface, 1m apart to meet the rigid floor. Each support was fixed to the floor by two stud bolts, each pre-stressed with 225kN. The completed installation of the supports is shown in Figure 4-9.

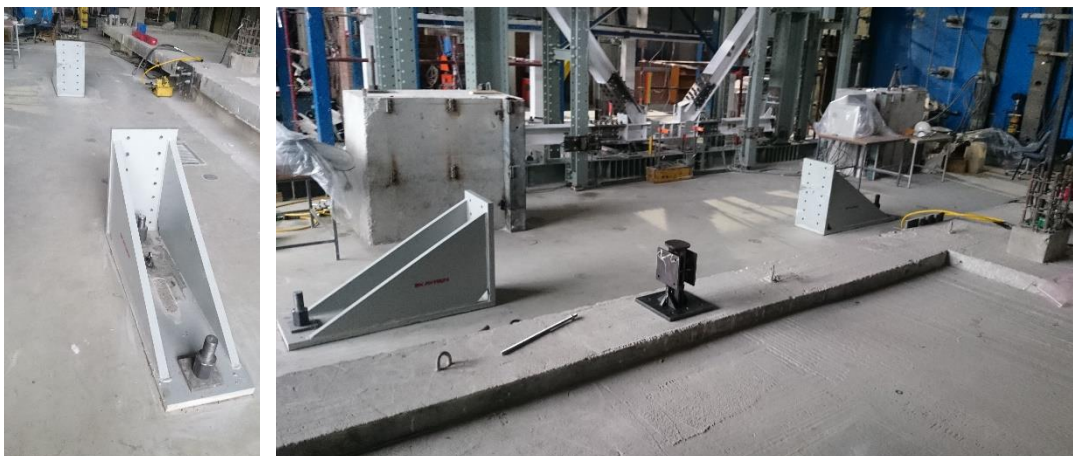


Figure 4-9. Completed installation of the steel supports

The hydraulic actuator to apply the dynamic loading has a load capacity of 150kN, a displacement stroke of $\pm 15\text{cm}$ and can reach a velocity up to 250mm/s. The actuator control system allows for both displacement- and force-controlled tests. The actuator was fixed to one of the steel supports and the piston rod was connected to the device driving bar.

The driving bar of the prototype was connected to the hydraulic actuator rod with the detail shown in Figure 4-10. First, the driving bar was fastened to two steel plates, each 10mm thick, with vibration-resistant washer and nut. Then, the plates were bolted to the connection at the actuator rod. The other end of the damper was fixed to the other steel support through its anchor plate. The completed set-up is as presented in Figure 4-11.



Figure 4-10. Detail of connection between driving bar and actuator head

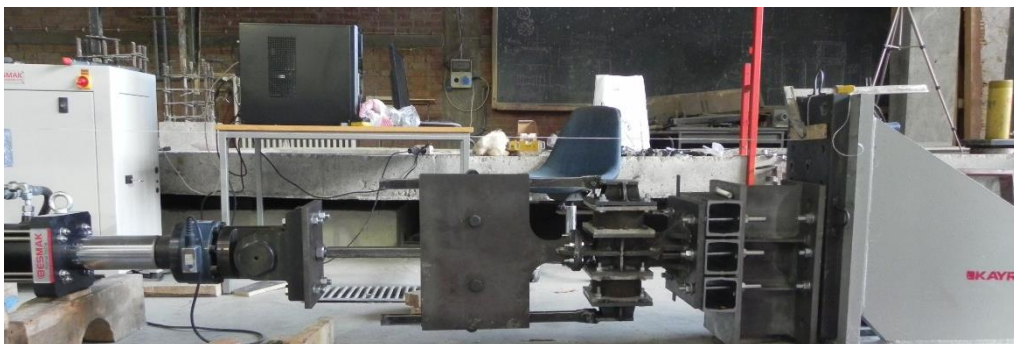


Figure 4-11. A general view of the completed dynamic test set-up

4.3.2 Measurement instrumentation

4.3.2.1 Prototype I

The test set-up for the dynamic performance tests of Prototype I is shown in Figure 4-11. The force and displacement measurements were recorded by the hydraulic actuator control software that samples 1000 data points per second.

4.3.2.2 Prototype II

Measurements from 17 channels were recorded during the tests. The list of used instrumentation is provided in Table 4-1. Displacement of each EB at top adapter level was recorded in two locations (at both ends of the EB). Also, longitudinal and transverse rotations of both EBs were measured through tiltmeters. For the sake of redundancy and cross-check, the rotation of the top EB was also measured with two LVDTs, spaced 12cm apart. The displacement of the driving bar is recorded both with an LVDT and by the hydraulic actuator control software. This redundancy and cross-check minimize the possibility of any mistakes in measurements. Also, recording the displacements of each EB at two locations serves the purpose of redundancy and eliminates possible outliers. Thereby, the first step in the data processing procedure following the experiment, was performing checks to validate the experiment as successful. These checks include the comparison of redundant data. If the experiment is not successful, it was repeated once again.

The mean of two (either Ch1 and Ch3 or Ch2 and Ch4) readings was then used in processing the test results.

Table 4-1. List of instrumentation used for dynamic performance tests

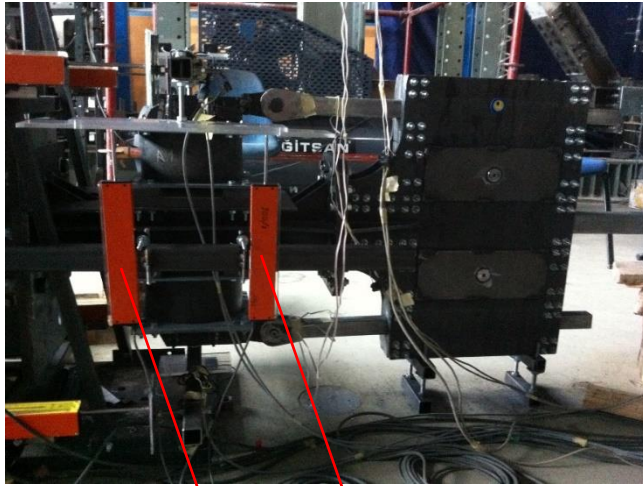
Channel	Instrument	Measured quantity	Unit	Parent element	Location
Ch1	LVDT	displacement	mm	Upper Top filler	right
Ch2	LVDT	displacement	mm	Lower Top filler	left
Ch3	LVDT	displacement	mm	Upper Top filler	right
Ch4	LVDT	displacement	mm	Lower Top filler	left
Ch5	LVDT	displacement	mm	Actuator support	-
Ch6	LVDT	displacement	mm	Damper support	-
Ch7	LVDT	displacement	mm	Actuator rod tip	-
Ch8	Strain gauge	strain	$\mu\epsilon$	Top driven bar	Top surface
Ch9	Strain gauge	strain	$\mu\epsilon$	Top driven bar	Bottom surface
Ch10	Strain gauge	strain	$\mu\epsilon$	bottom driven bar	Top surface
Ch11	Strain gauge	strain	$\mu\epsilon$	bottom driven bar	Bottom surface
Ch12	LVDT	displacement	mm	Upper top filler	Piston side
Ch13	LVDT	displacement	mm	Upper top filler	Support side
Ch14	tiltmeter	rotation	deg	Upper top filler	longitudinal
Ch15	tiltmeter	rotation	deg	Upper top filler	transverse
Ch16	tiltmeter	rotation	deg	lower top filler	longitudinal
Ch17	tiltmeter	rotation	deg	lower top filler	transverse

To estimate the force generated by the EB, strain gauges were installed on the top and bottom surfaces of each driven bar, to serve as local load cells. They give a reading in units of microstrain ($\mu\epsilon$). The strain gauges were installed with adhesive as shown in Figure 4-12.

The data sampling rate for all the channels was again 1000 data points per second.

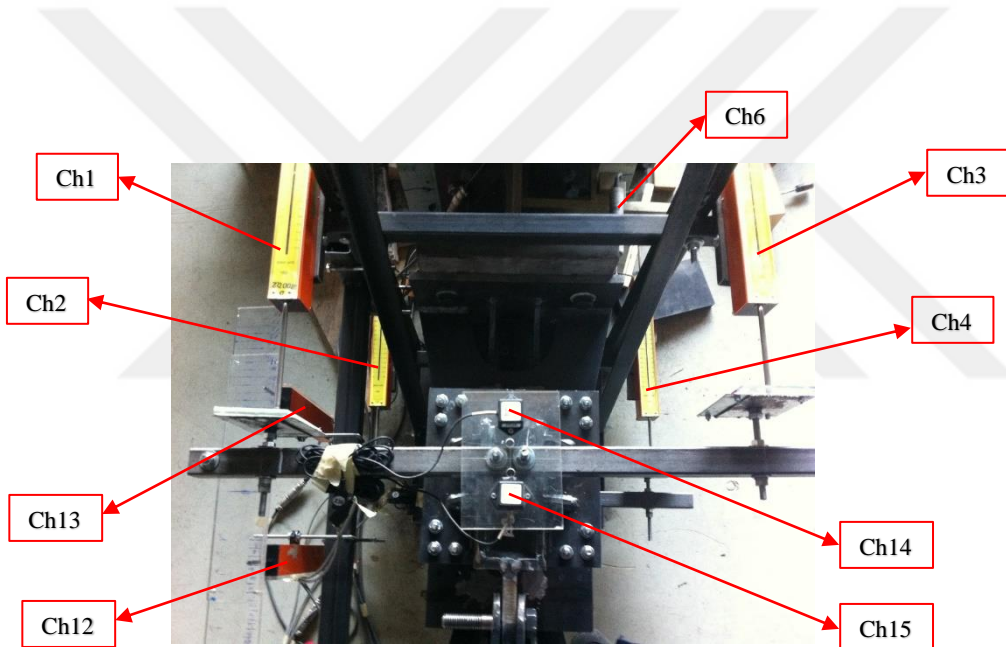


Figure 4-12. Strain gauges installed on a driven bar



Ch13

Ch12



Ch1

Ch2

Ch13

Ch12

Ch6

Ch3

Ch4

Ch14

Ch15



Ch5

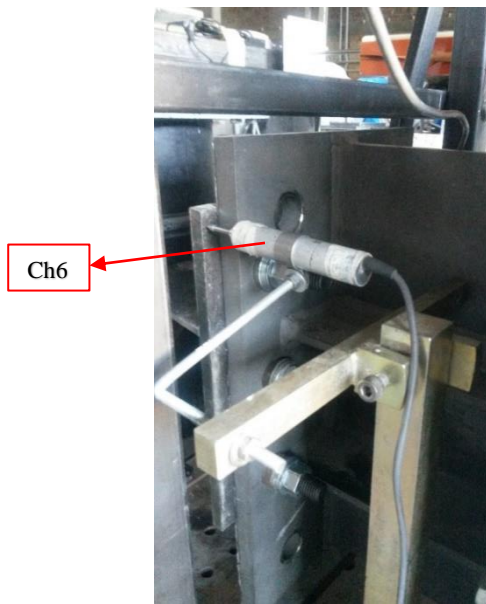
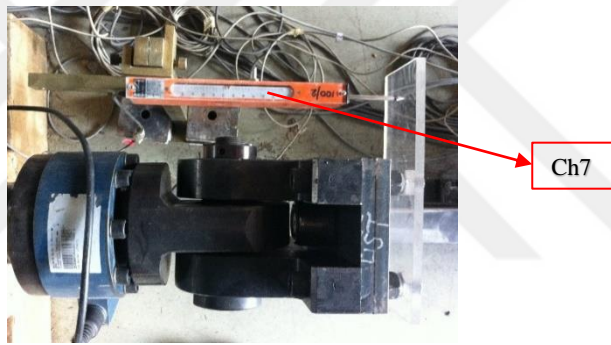
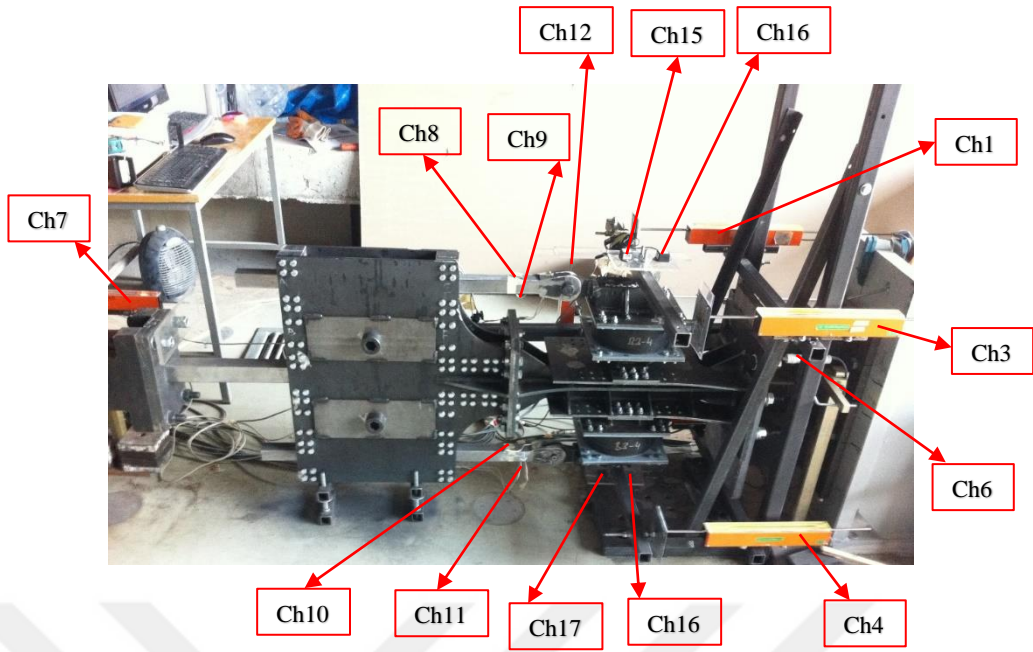


Figure 4-13. Channel locations in the test set-up

4.4 Loading Protocol

A series of sinusoidal harmonic displacement-controlled tests are performed. The test program is the same for both prototypes. The input parameters are the sine wave amplitude in mm and frequency in Hz. The displacement input can be expressed with Equation (35)

$$d(t) = a * \sin(2\pi ft) \quad (35)$$

f = sine wave frequency, [Hz]

The input frequency range is from 0.5Hz to 5.0Hz and the displacement amplitude changes between 5mm and 25mm with an increment of 5mm. The possible inputs are confined by the hydraulic actuator force and velocity limitations and change depending on the EB horizontal stiffness. For instance, tests covering the whole range of input variables are applied for the less stiff configuration A1, whereas only those up to 15mm under 1.0Hz can be applied for the stiffer B3-4.

4.5 Investigated parameters

Since the Backbone damper is a hybrid one and its energy dissipation capacity is provided by both viscoelastic and friction mechanisms, it involves the characteristics of both displacement-dependent and velocity-dependent damping systems. Thereby, the response parameters defined for both types of systems need to be investigated and estimated.

Elastomer has a markedly higher stiffness during the first cycle than during the subsequent cycles of motion. The initial stiffness characterizes the unscragged state of the elastomer. During deformation, molecules within the elastomer stretch and fracture and thus the material reaches the scragged state with stable properties. It has been accepted in the past that the elastomer cannot resume its virgin state. So that the initial high stiffness was disregarded in the analysis. However, recent experimental findings [54], [170] evidenced that recovery occurs within a short time. Thompson et al. [170]

also concluded that significant differences between unscragged and scragged properties are likely in elastomers with low shear modulus.

In the light of these findings, for each consecutive test the elastomer is expected to be involved into motion in the unscragged state and estimating the damper performance parameters from the third cycle's records is justified.

The equations in [171] both for displacement-dependent and velocity-dependent devices can be used for determination of force-deformation characteristics:

$$K_{eff} = \frac{|F^+| + |F^-|}{|d^+| + |d^-|} \quad (36)$$

where

d^+ = maximum positive displacement of driving bar (in pull direction);

d^- = maximum negative displacement of driving bar (in push direction);

F^+ and F^- are the positive and negative forces at d^+ and d^- , respectively.

The device damping coefficient is estimated from the equation in FEMA 450 [171] for the solid viscoelastic devices:

$$C = \frac{EDC}{\pi\omega D_{ave}^2} \quad (37)$$

where

ω_1 = angular frequency

$$\omega_1 = 2\pi f \quad (38)$$

D_{ave} = the average of the absolute values of displacements d^+ and d^- .

EDC = Energy Dissipation per Cycle = the area enclosed by one complete cycle of the force-displacement response of the device.

The effective damping, ξ_{eff} , can be estimated from:

$$\xi_{eff} = \frac{2}{\pi} \left[\frac{EDC}{K_{eff}(|d^+| + |d^-|)^2} \right] \quad (39)$$

where the energy dissipated per cycle of loading, EDC , and the effective stiffness, K_{eff} , shall be based on peak test displacements of d^+ and d^- .

Some parts in the DAM of Prototype II are produced with tolerances larger than those prescribed by the design. The diameter of the hole for Pin3 in the top asymmetric disk is measured to be 1mm bigger than the diameter by design. Also, the clearance of case supports for the top driven bar is 1.5mm larger than the design value. These increased production tolerances combined with the tolerances by design create a slip in the system that reflects into offsets between the input displacement and the displacement measured at top adapter level. This effect can be recognized from the plots in Figure 4-14. The displacement input applied at the driving bar is transferred with a certain delay to the driven bar. The production tolerances described above are introduced into the numerical model of the device assembly to realistically simulate the experiment.

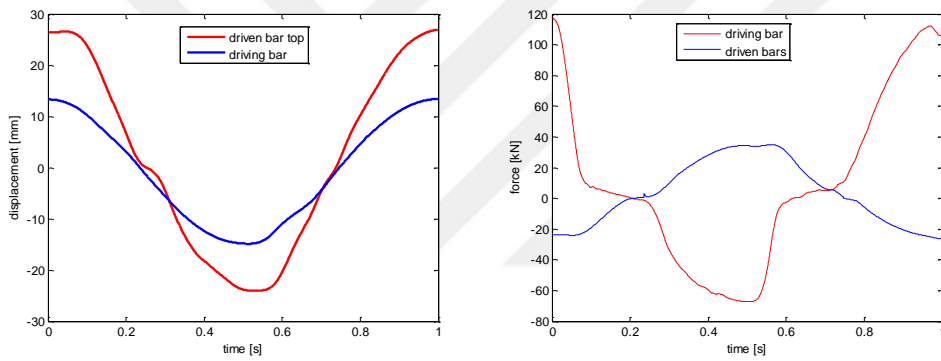


Figure 4-14. Phase offset between the driving and driven bar responses

The amplification ratio is estimated for the maximum pull and maximum push positions of the tests as follows:

$$a_R^+ = \frac{d_{ave}^r}{d_p^+} \quad (40)$$

$$a_R^- = \frac{d_{ave}^r}{d_p^-} \quad (41)$$

where

d_p^+ = maximum displacement recorded by Ch7 at pull

d_p^- = maximum displacement recorded by Ch7 at push

d_{ave}^r = average of displacements measured by Ch1- Ch4 either at d_p^+ or d_p^-

4.6 Test data processing

4.6.1 Filtering

Figure 4-15 shows a plot of the strain time-history recorded on the top driven bar. Examining closely, a certain noise is observed in all the recorded data. The sources of the experimental noise may be generated by both the test set-up environment and measurement instrumentation.

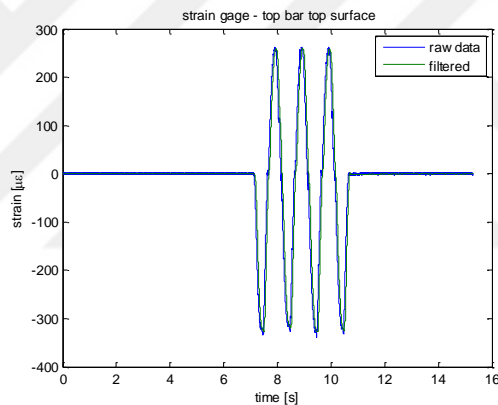


Figure 4-15. Strain time-history plot

To eliminate the noise, a fourth order Butterworth low-pass filter with 10 Hz cut-off frequency was applied to all the sampled data including all the channels. The applied filter offsets the sampled data on the horizontal axis as shown in Figure 4-16. Since the same filter is applied to all the data, the filtering shift effect is the same in all data and thus eliminated.

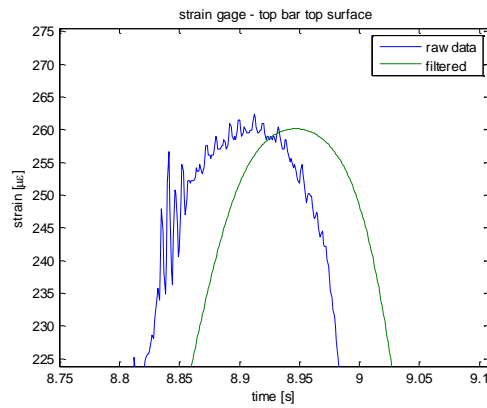


Figure 4-16. Offset due to filtering

4.6.2 Pull and push definition

A clear understanding of expected behavior is needed to properly investigate the device response using test results. The device response changes depending on whether it is in the pull or push position. In the pull position of the device, the driving bar is under compression while the driven bars are in tension and vice versa.

4.7 Test results

The test results for both Prototype I and Prototype II are summarized and discussed below.

4.7.1 Prototype I

Analyzing the hysteresis loops of Prototype I given in Figure 4-17, the following conclusions can be made:

- The device effective stiffness in the loading branch reduces under increasing input displacements. This reduction is more pronounced for displacements larger than 25mm.
- For displacements larger than 15mm the hysteresis loop has markedly sharp corners and stiffening is observed in the loading branch. Thereby, for

displacements up to 15mm the device backbone curve can be idealized as bilinear while a trilinear curve better fits larger displacements.

- The hysteresis loops are not symmetric, exhibiting a higher stiffness in the pull direction. This can be attributed to different deformation states of EBs for the pull and push positions. In pull position the elastomeric blocks of the VE unit can rotate, while in push position their rotation is restricted due to the connection detail of the top adapter to the driven bar. The rotation of the EBs is associated with vertical forces in the driven bars, which generate friction during sliding of the bars against the case beddings. This effect is investigated in more detail with the tests of Prototype II where EB rotations and driven bar forces are also recorded.

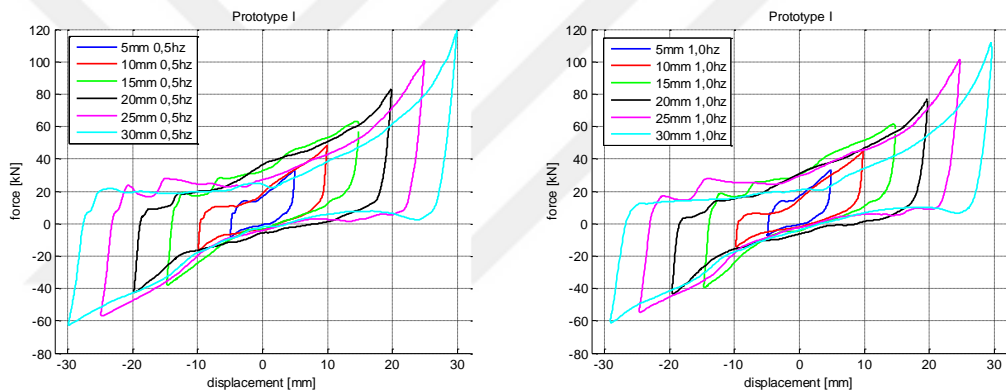


Figure 4-17. Hysteresis loops of Prototype I for (a) 0.5Hz and (b) 1.0Hz

Prototype stiffness and energy dissipation parameters are estimated from the loops and summarized in Table 4-2.

Table 4-2. Results for Prototype I

d [mm]	f [Hz]	d ⁺ [mm]	d ⁻ [mm]	F ⁺ [kN]	F ⁻ [kN]	EDC [kNm]	k _{eff} [kN/m]	c _{eq} [kNs/m]	ξ _{eff}
5	0.5	4.967	-4.974	32.91	-8.21	0.173	4136.63	0.709	0.27
5	1	4.905	-4.916	32.64	-7.08	0.167	4044.5	0.351	0.273
5	1.5	4.886	-4.883	31.32	-7.1	0.156	3933.03	0.22	0.264
5	2	4.873	-4.866	31.7	-6.91	0.15	3964.06	0.161	0.254
5	2.5	4.876	-4.861	28.57	-7.18	0.14	3670.9	0.12	0.255
5	3	4.919	-4.882	29.05	-7.74	0.14	3753.8	0.099	0.246
10	0.5	9.919	-9.932	48.15	-16.85	0.453	3274.85	0.466	0.224
15	0.5	14.838	-14.777	57.67	-37.04	1.148	3198.24	0.531	0.26
15	1	14.819	-14.753	55.57	-38.67	1.116	3186.84	0.259	0.254
15	1.5	14.883	-14.698	56.05	-39.3	1.057	3223.34	0.163	0.236
15	2	14.752	-14.598	58.71	-39.39	1.038	3342.24	0.122	0.227
20	0.5	19.848	-19.801	82.15	-41.85	1.672	3127.52	0.431	0.216
20	1	19.745	-19.617	76.64	-43.38	1.505	3049.16	0.197	0.201
20	1.5	19.719	-19.58	75.14	-43.07	1.667	3007.89	0.146	0.227
20	2	19.707	-19.422	76.84	-44.33	1.579	3096.61	0.104	0.209
25	0.5	24.888	-24.924	100.78	-56.34	2.306	3154.35	0.377	0.188
25	1	24.762	-24.649	101.61	-54.53	2.23	3159.96	0.185	0.183
25	1.5	24.647	-24.335	101.1	-53.39	2.16	3154	0.122	0.179
30	0.5	29.888	-29.895	119.87	-62.49	2.692	3050.45	0.305	0.157
30	1	29.662	-29.097	109.6	-59.43	2.316	2876.61	0.136	0.146

In Figure 4-18 and Figure 4-19 the damper EDC and K_{eff} are plotted versus the mean input displacement. Curves are fitted to the test data to better assess the dependence of the device parameters on the input displacement. It is clearly observed that, in contrast to K_{eff}, the EDC increases with the increase in displacement.

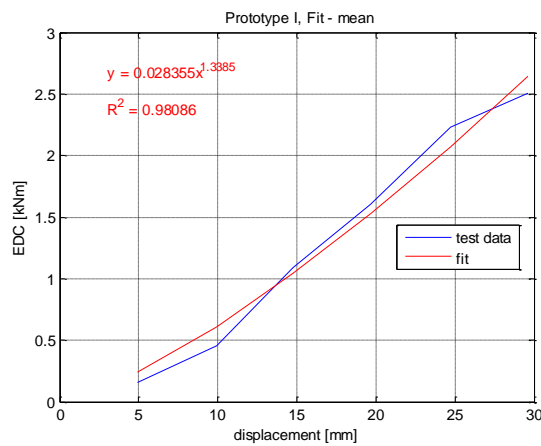


Figure 4-18. EDC versus mean displacement for Prototype I

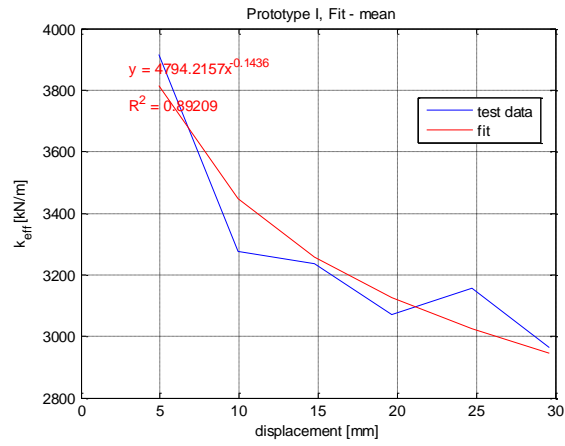


Figure 4-19. K_{eff} versus mean displacement for Prototype I

4.7.2 Prototype II

In this section, detailed results for configuration A3-1 only are presented. The results for the other configurations are given in Appendix A.

4.7.2.1 A3-1 results

At least three cycles of reversed sinusoidal displacement loading are applied during each test. The obtained loops are summarized in Figure 4-20 and Figure 4-21.

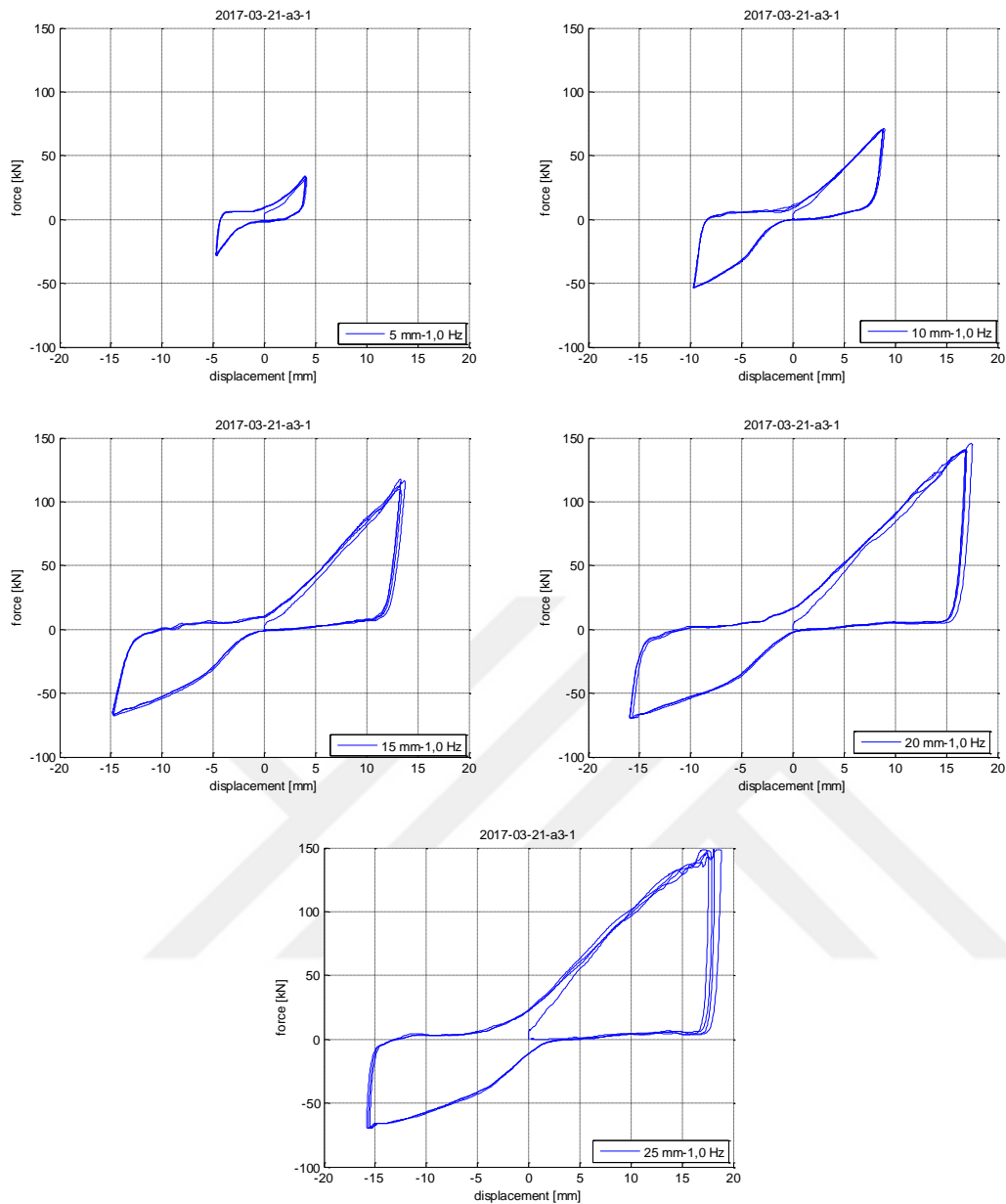


Figure 4-20. Hysteresis loops of configuration A3-1 at 1.0Hz frequency and different displacement amplitudes

The damper hysteresis loops plotted in Figure 4-20 indicate a stable device behavior. Within each test, the loops of consecutive cycles overlap.

The displacement inputs for the last two graphs of Figure 4-20 are 20mm and 25mm, respectively. However, the hydraulic actuator's force and velocity capacities did not allow for applying the maximum displacement inserted in the control system.

The hysteresis loops obtained for the same displacement but varying frequencies are plotted in Figure 4-21.

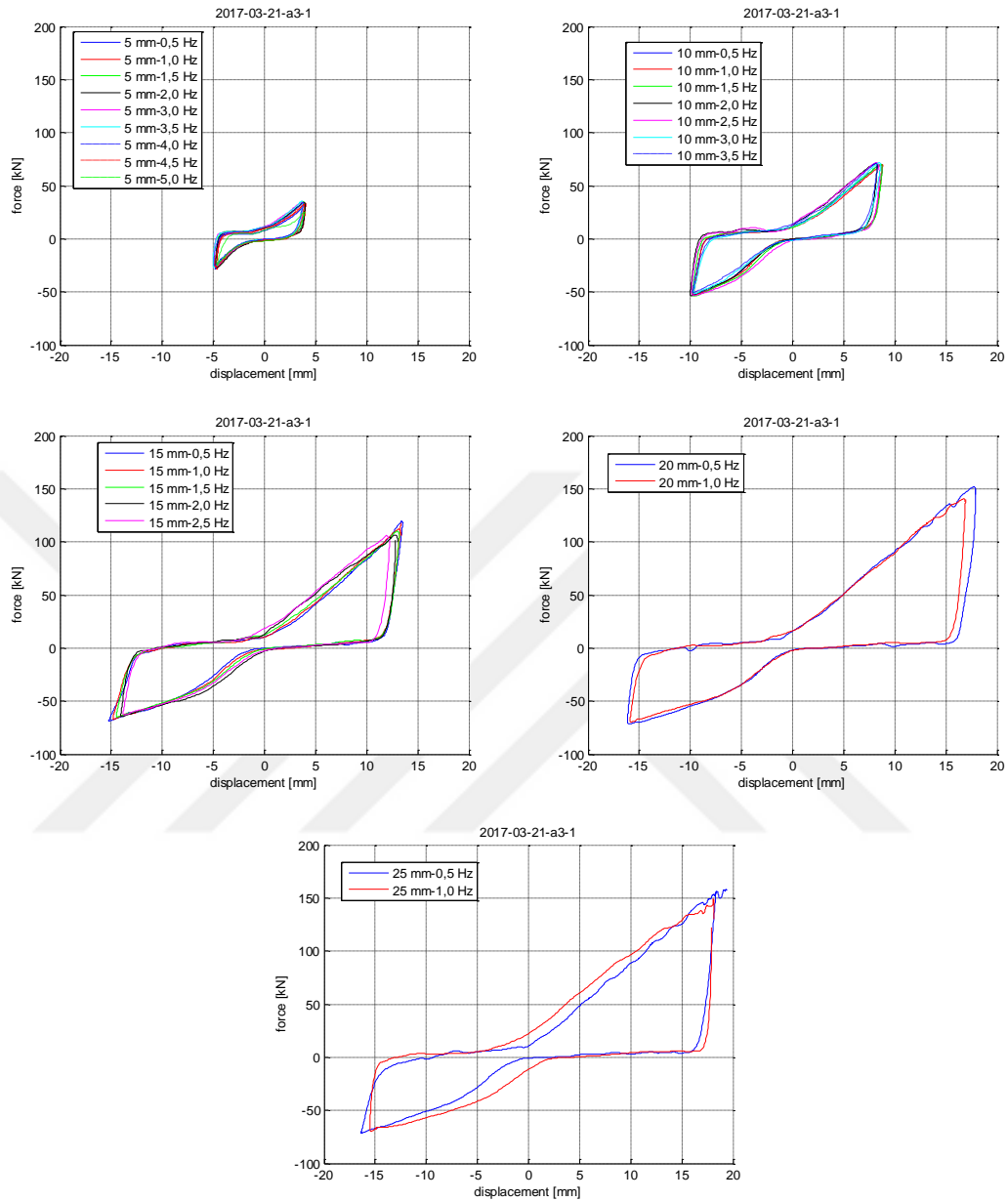


Figure 4-21. All hysteresis loops of A3-1 organized by displacement amplitude

The plots of Figure 4-21 show that the loops obtained for different frequencies of the same amplitude just slightly differ. The effect of increasing frequency can be observed in just slightly smoothing the hysteresis loops including their sharp peaks as well.

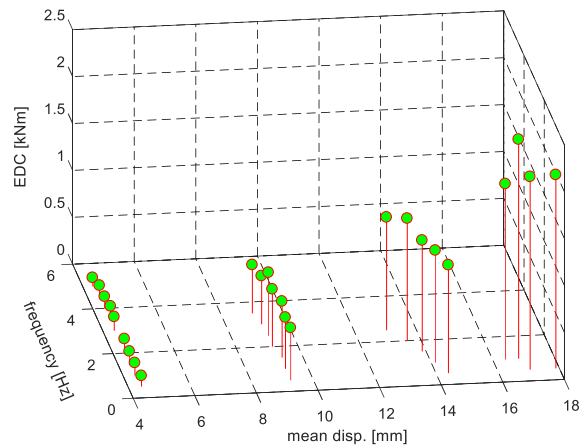


Figure 4-22. Device EDC vs input frequency and displacement for A3-1

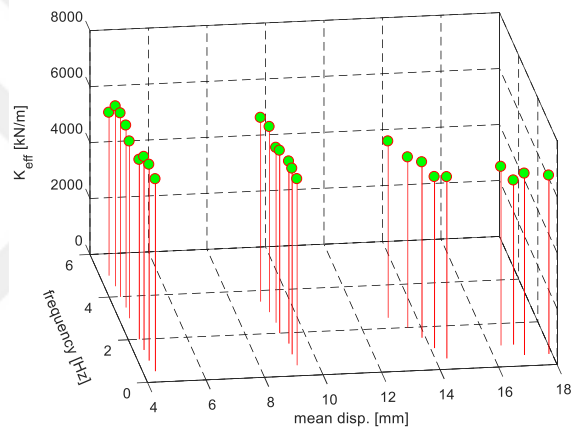


Figure 4-23. Device K_{eff} vs input frequency and displacement for A3-1

In Figure 4-22 and Figure 4-23, the estimated EDC and K_{eff} values are plotted against the test inputs. Analyzing the figures, it can be concluded that both the effective stiffness and the energy dissipation capacity of the device are essentially independent of frequency and at the same time displacement-dependent.

Rotations of elastomeric blocks are an important parameter necessary for the motion analysis of the device. The rotations of top EB measured under 0.5Hz frequency are given in Figure 4-24.

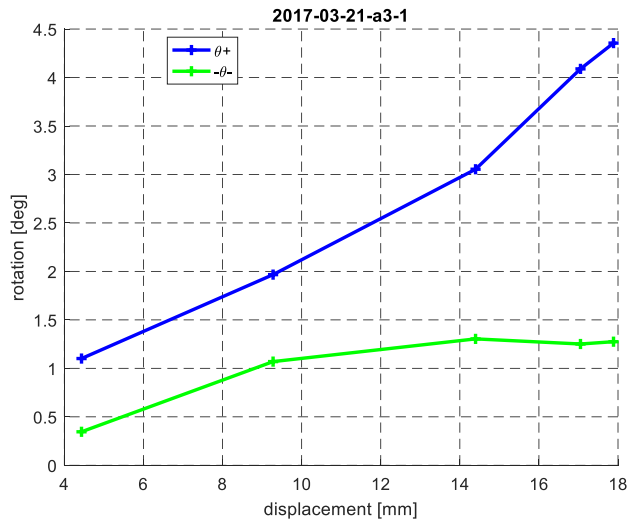


Figure 4-24. Rotations of top EB

Here

θ^+ = rotation at d^+

θ^- = rotation at d^-

It is observed from Figure 4-24 that the magnitude of rotation at maximum pull is bigger than at maximum push. θ^+ steadily increases with the increase in displacement but θ^- does not increase after 14mm. This results in consistent increase in the difference between two rotations which causes asymmetry in device hysteretic behavior.

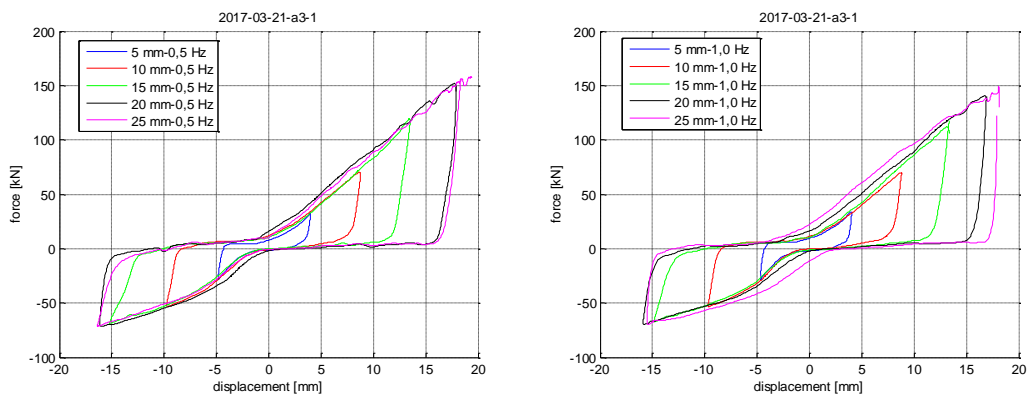


Figure 4-25. Hysteresis loops of A3-1 for increasing displacement amplitudes at 0.5Hz and 1.0Hz

The hysteresis loops of Figure 4-25 indicate that under increasing displacements the device hysteretic behavior follows the same pattern. No strength and stiffness degradation are observed.

The hysteresis loops are asymmetric, i.e. loop area in pull is bigger than in push. It is caused by asymmetry in the rotational restraints of elastomeric blocks. Due to the detailing of the top adapter connection, the EB can rotate in pull while in push its rotation is rather limited. The difference in rotation generates difference in both shear strains and axial stresses developed within the elastomer body which consequently creates a difference in stiffness and force. The asymmetry increases with increasing input displacements because the rotation in pull is increasing in line with the displacement but the rotation in push just slightly changes and thus, the difference between the two is building up. As a result, under increasing displacements, the pull branch consistently increases while the push branch does not enlarge.

This asymmetry in device motion has a projection on its performance parameters. The smaller stiffness in push results in reduced K_{eff} and EDC of the device. If the push branch were fattened as the pull one, then both the EDC and K_{eff} would be considerably larger.

The asymmetry can be cancelled out by changing the top adapter connection detailing and designing one that enables equal amount of rotation in both directions. Then, both the EDC and K_{eff} can be significantly improved. For the current design, with the increase in displacement the ratio of force at maximum pull to the one at maximum push rises and reaches up to 2.0 for 15mm input amplitude as can be seen from Table 4-3. This suggests that if the two forces were equal, then the EDC and K_{eff} could be increased by a ratio of 1.33 for the considered case. By implication, the ratio is expected to be higher for larger displacements.

From the hysteresis loops of Figure 4-20, Figure 4-21 and Figure 4-25, re-centering is observed in pull direction, but not in push direction. That is, an asymmetry in re-centering capability is observed as well. The residual displacement in pull is less than 5mm for all hysteresis loops. The one in push varies with input displacement and changes between 4mm and 13mm recorded at 5mm and 25mm input, respectively.

Table 4-3. Results for A3-1

d [mm]	f [Hz]	d ⁺ [mm]	d ⁻ [mm]	F ⁺ [kN]	F ⁻ [kN]	EDC [kNm]	k _{eff} [kN/m]	c _{eq} [kNs/m]	ξ _{eff}	AR at d ⁺	AR at d ⁻
5	0,5	4.00	-4.87	32.39	-28.51	0.115	6866.74	0.593	0.17	1.99	0.93
5	1,0	4.05	-4.72	33.54	-27.89	0.134	7006.06	0.353	0.19	1.65	1.15
5	1,5	3.91	-4.84	33.97	-26.40	0.138	6903.06	0.244	0.21	1.70	1.12
5	2,0	3.98	-4.77	32.28	-23.88	0.151	6417.73	0.200	0.24	1.67	1.16
5	3,0	3.78	-4.96	33.35	-21.80	0.149	6312.74	0.131	0.26	1.85	1.13
5	3,5	3.78	-5.05	34.28	-23.08	0.142	6498.25	0.105	0.24	1.90	1.11
5	4,0	3.83	-4.94	34.06	-23.44	0.126	6555.50	0.083	0.21	2.01	1.02
5	4,5	3.92	-4.85	31.40	-24.91	0.125	6423.22	0.073	0.20	2.01	1.00
5	5,0	4.01	-4.64	25.17	-25.13	0.090	5815.80	0.049	0.15	1.99	0.91
10	0,5	8.79	-9.77	70.62	-52.72	0.557	6647.10	0.655	0.17	2.11	1.74
10	1,0	8.81	-9.74	69.55	-53.60	0.549	6641.34	0.323	0.17	2.06	1.72
10	1,5	8.78	-9.87	68.88	-52.61	0.600	6513.57	0.233	0.19	2.06	1.66
10	2,0	8.31	-10.04	67.20	-52.48	0.612	6524.32	0.184	0.22	2.20	1.61
10	2,5	8.52	-9.90	64.70	-50.37	0.670	6244.38	0.160	0.24	2.10	1.66
10	3,0	8.63	-9.68	70.23	-50.81	0.516	6611.18	0.104	0.17	2.22	1.67
10	3,5	8.28	-9.75	68.89	-49.43	0.516	6561.42	0.092	0.18	2.26	1.51
15	0,5	13.56	-15.23	118.03	-68.64	1.152	6482.86	0.563	0.15	2.15	1.78
15	1,0	13.41	-14.87	106.00	-67.03	1.193	6118.16	0.302	0.17	2.19	1.83
15	1,5	13.21	-14.54	109.33	-64.82	1.184	6275.60	0.208	0.17	2.16	1.82
15	2,0	13.01	-14.10	100.36	-64.60	1.303	6085.40	0.180	0.20	2.18	1.73
15	2,5	12.23	-13.87	101.64	-62.64	1.204	6296.29	0.143	0.20	2.21	1.73
20	0,5	17.93	-16.18	149.83	-71.40	2.055	6487.22	0.716	0.16	2.17	1.74
20	1,0	16.91	-15.92	139.60	-69.75	1.869	6377.60	0.351	0.16	2.17	1.77
25	0,5	19.37	-16.41	155.94	-71.34	2.064	6380.49	0.659	0.14	2.18	1.76
25	1,0	18.15	-15.53	129.81	-67.94	2.337	5870.83	0.417	0.19	2.12	1.77

It is observed from Table 4-3 that the amplification ratio at maximum pull is bigger than the one at maximum push. Also the difference is greater for smaller displacements and decreases with the increase in displacements. This can be explained with tolerances in the production of the prototype, the initial shift of 1mm in pull direction and the larger input displacement in push. These together have a greater influence on the amplification ratio under smaller displacement amplitudes because their magnitude makes up a bigger percentage of the input. The same factors explain the measured amplification ratio being smaller than the design value.

During each test, the prototype was subjected to a total of 100 fully reversed sinusoidal cycles in average. Since the same amplification mechanism was connected to all the configurations, it was subjected to around 800 reversed cycles. During and after all

these cycles, no change in the damper behavior was measured. Also, no damage in the EBs and in the amplification mechanism was observed, although the latter is the part susceptible to performance changes due to repeated friction.

The experimental observations for the device performance are further investigated with the numerical simulations presented in Chapter 5.

The experimental results from all configurations are analyzed together and design equations for predicting the damper performance are proposed in Chapter 6.

4.8 Summary of results

Two prototypes of the Backbone damper have been designed, produced and tested in a laboratory set-up. Prototype I has been designed for only one configuration of the EB while Prototype II – for eight different configurations differing in type and mechanical properties. All the configurations have been subjected to a series of displacement controlled dynamic performance tests to experimentally investigate the Backbone damper behavior and evaluate its performance parameters. The experimental investigation indicates that Prototype II is the one with a more successful design and production. Thereby, it is planned to be the backbone for further investigation and optimization of the device and hereby its test results are addressed as the findings from the experimental program. Eventually, the overall results from the experimental study can be summarized within the following conclusions:

1. The Backbone damper has a stable hysteresis loop without any sign of degradation neither in strength nor in stiffness.
2. The damper EDC increases with increase in input displacement.
3. The effective viscous damping ratio exceeds 0.15 in all the tests.
4. Both the energy dissipation capacity and the effective stiffness of the damper are essentially independent of frequency.
5. The behavior does not change and the device does not experience any damage after a total of 100 fully reversed sinusoidal cycles in average for each EB and 800 cycles for the amplification mechanism.

6. Asymmetry is observed in the device hysteresis loops and the effect of asymmetry increases with the increase in displacements. The reason for this asymmetry is considered to be the asymmetry in the rotation of the EB. EB rotates in unequal amounts in both directions due to the top adapter connection detailing. The asymmetry can be eliminated with a change in the top adapter connection detailing. This is expected to also considerably improve the device performance parameters.
7. Re-centering is observed in pull direction, but not in push direction. That is, an asymmetry in re-centering capability is observed as well. This may be due to the experimental set-up being less than perfect and need to be further investigated. The change in top adapter connection detailing is expected to improve device re-centering behavior as well.

CHAPTER 5

FINITE ELEMENT MODELLING AND ANALYSIS OF THE DEVICE

5.1 Introduction

The FEA is a key step in the investigation of the device. It can be used to verify the experimentally measured values. FEA also allows for a more comprehensive analysis and monitoring of parameters that cannot be experimentally measured. Furthermore, numerical simulations provide the opportunity of performing a parametric study and predicting the device behavior without the need for experimental testing.

In the course of the experimental investigation, Prototype II is proposed as a more successful design and subsequently proven so by the test results. Therefore, a numerical model of the complete assembly is prepared for detailed analyses of the motion study performed exclusively for Prototype II.

Since the procedure of modelling and analysis follows the same routine for all configurations of Prototype II, the simulation is performed for only one configuration of the EB, namely A3-1. This analysis provides sufficient data to perform the motion study of the device. Once the model of A3-1 is verified, it can be used to reliably analyze other configurations as well, by just changing the EB and its adapter connections.

5.2 Modeling details

The thing to keep in mind in the process of modelling is that the model is a mathematical idealization with a physical equivalent. Simulating the physical system response need to be in focus. Including the smallest details may just overload the

model, increase the possibility for likely errors and multiply the computational cost without adding any significant contribution to capturing system realistic response that may be worth the extra effort. This issue becomes crucial especially in the case of complex systems to model.

All the strengths and capabilities of the ABAQUS software package are mobilized in simulating the damper response. The main challenges posed by device modelling can be resumed in three modules: (i) properly and efficiently modeling elastomer material capturing both its hyperelastic and viscous properties, (ii) modeling the many contact conditions to cover the interactions between instances and (iii) the complexity of the total assembly.

A multi-level step-by-step structuring technique is applied in creating the numerical model and running the simulations. The numerical model of the whole assembly is built up incrementally and verification is performed at each step. The steps are as follows:

- First, the elastomeric block of the prototype is modelled. Its shear, vertical and rotational stiffness values are numerically evaluated and verified against the design values predicted with the analytical equations given in Chapter 3.
- Then, the top adapter connection, the bottom driven bar and its case supports are added to the verified numerical model of the EB and a simulation for a selected reference input case (10mm at 1.0Hz) is run. The forces obtained at the strain gauge locations are compared with the test readings.
- Finally, the FE model of the whole device assembly is created and simulations run for a selected reference input case (10mm at 1.0Hz).

All the analyses are three-dimensional. The three-dimensional solid model created in SolidWorks is imported in ABAQUS and the finite element model is developed following the program modules. For simplicity of numerical analysis, insignificant details, such as bolts and nuts, circlips and circlip holes, are removed from the model. In Figure 5-1, imported geometry before simplification is shown against the simplified model. The simplification is applied to all the modelling levels to reduce the computational cost by removing secondary elements that do not have an effect on the device overall response but just overload the computations. The assumption for the

negligible contribution of these elements on device behavior is confirmed with the test observations.

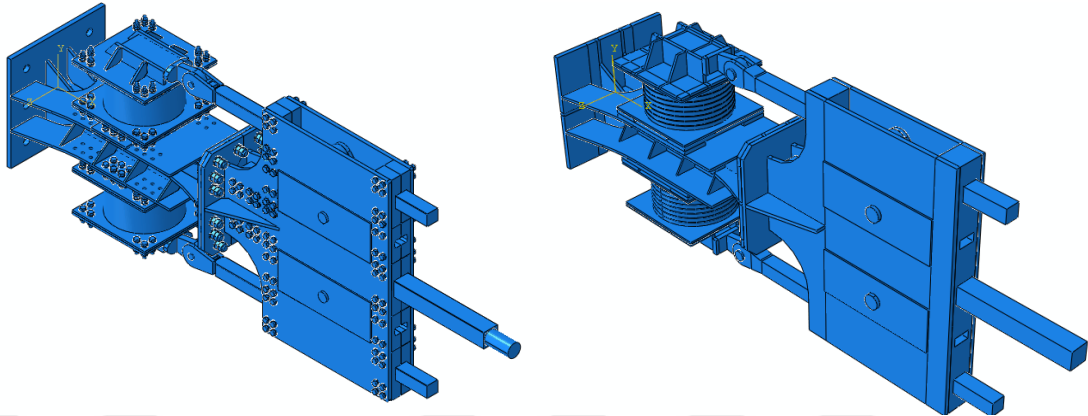


Figure 5-1. Assembly model before (left) and after (right) simplification

In all the steps, the stresses and strains on the boundary surface between elastomer body and its boundary plates, that cannot be experimentally measured, are numerically estimated and checked against their limit values pre-defined in the prototype design process.

The notation for the results analyzed below is as follows: displacement in x direction (U1), displacement in y-direction (U2), maximum principal stress component (S max principal), maximum principal strain component (LE max principal), maximum principal plastic strain component (PE max principal), normal stress component in y-direction (S22), shear stress component between x and y-directions (LE12).

5.2.1 Elastomer block numerical model

The geometry of the elastomeric block is imported from SolidWorks and the dimensions are kept in mm. The units are mm for length, N for load and MPa for stress.

Elastomer hyperelasticity is modelled using the test data given in Chapter 4. The test loops are averaged and the curve of Figure 5-2 is obtained. This uniaxial test data is introduced and Mooney-Rivlin model is assumed as a strain energy potential to model elastomer hyperelasticity. For volumetric response definition, Poisson's ratio is defined to be 0.47. Elastomer material density is defined as 1200 kg/m³.

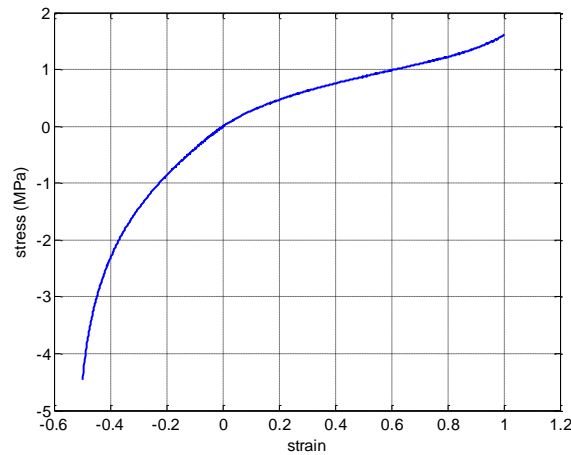


Figure 5-2. Hyperelasticity curve

Time-dependent properties of elastomer are modelled using the relaxation test data introduced again in Chapter 4. The relaxation test is performed for different shear strain levels. Since the inputs of the reference case for numerical analysis are 10mm amplitude and 1.0Hz frequency, and the amplification ratio is expected to be around 2.0, the data corresponding to this case is normalized and introduced in ABAQUS interface.

Shear stiffness, vertical stiffness and rotational stiffness values of EB configurations are estimated by their ABAQUS models. Two EB configurations are analyzed: A3-1 and B3-1, shown in Figure 5-3. Bottom surface of lower boundary plate is fixed. Z-symmetry is implemented as in the assembly model and the loading is symmetric along z-direction.

Steel shims are the most critical elements, as they have the smallest element dimensions along thickness. Large plastic deformations on these disks resulted in failure in the analyses. Finer meshes of the circular section provided reasonable plastic deformations and stable analyses.

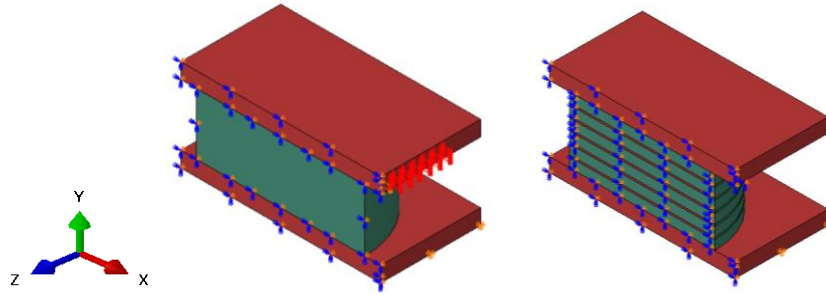


Figure 5-3. Elastomer configurations analyzed: A3-1 (left) and B3-1 (right)

5.2.2 Modeling details for complete assembly

The below explanations of the model and analysis follow the sequence of program modules.

Modeling in ABAQUS begins with model import from SolidWorks. Dimensions are expressed in mm while importing the simplified solid assembly model in ABAQUS. The units used in FE model and analyses are mm for length, N for load and MPa for stress.

Five different materials are defined in the model: one material for elastomer and four different materials for steel parts of different steel grades. Mass density of 7800kg/m^3 is used for all steel materials. Young's modulus is assigned as $210\text{e}3\text{MPa}$, and Poisson's ratio as 0.3. Plasticity region is defined in the plastic strain range between 0 and 0.15.

Five different solid sections are defined with these five material models. Elastomer section is applied for the elastomer of VE units. Steel 10.9 section is applied for all the pins. Steel St52 section is assigned for the driving bar and driven bars of the amplification mechanism. Asymmetric discs of the amplifier are modeled with steel 1040 section. All other steel parts, including the steel shims inside elastomer, are assigned St37 section.

As the model and loading are both symmetric around z axis, symmetric boundary condition is implemented to reduce computational time.

The loading is applied in a dynamic explicit step and time period covering up to five cycles is set for the analysis. Nonlinear geometry is toggled on as large deformations

are expected during the analyses. Automatic time incrementation is selected and no mass scaling is defined. An initial fixed boundary condition is assigned on the anchor plate and the displacement input is applied on the projecting surface of the driving bar. The displacements in x and z directions of the input surface are nulled.

The displacement input in time is defined with a periodic amplitude of circular frequency ω . Field output requests for stress, strain, displacement and forces are defined for 0.01s time steps in the analysis. History output requests are selected for displacement, reaction forces, strain, stress and contact force distributions for a time step of 0.001s. The displacement and the reaction forces are recorded for the projecting surface of the driving bar, where the driving bar is controlled by the hydraulic actuator during the tests. Displacements of top adapters are also recorded to compare with test measurements at these locations. Stress and strain components on elements of the driven bars are requested to compare with the strain gage readings of the test data.

In interaction module, contact pairs are found for separation tolerance of 1 mm. Contact pairs without relative motion during device motion are tied and 42 tie constraints are defined. An interaction property is defined for contact pairs with relative motion. Tangential behavior model with penalty friction formulation of 0.5 friction coefficient is used. This friction model is introduced between the parts in relative motion: parts in the pin connections and the parts in sliding contact (driving end bars and case supports).

Three dimensional solid elements are used for meshing the assembly model. These are the C3D8 and C3D8R brick elements, and the C3D6 and C3D6R tetrahedral elements. Brick elements dominate the meshes, while tetrahedral elements are used only if ABAQUS gives analysis warning for mesh with brick elements, specifically for elastomer mesh in laminated rubber. C3D8 is fully integrated at eight points, whereas C3D8R is labeled as reduced integration with only one integration point. Shear locking phenomenon is reported to happen, if a single element is meshed along the thickness of a part. There are some thin parts in the model, such as disks in elastomers, support plates and case plates. Disks in elastomers are critical elements in the analyses; therefore possible shear locking may compromise solution. When reduced elements are used in the mesh, shear locking problem is solved; however some other numerical

drawbacks may occur. Therefore, two or three elements per thickness are recommended.

In the analyses, the stable time increment is defined by the instance with minimum ratio of element size to dilatational wave speed. Wave speed is not applicable for elastomer material, while it has a unique value for all steel materials. Therefore, the instance with minimum mesh size is the critical one. For the model with single element per thickness, pins are critical instances while for three elements per thickness model, steel shims in elastomer are the critical ones. Stable time increments on these elements are in the range of $1e-7$ to $3e-7$ seconds. Hence, for an explicit analysis of 1 to 5 seconds, more than one million time increments are needed.

Pin instances and contact surfaces are studied for mesh improvement and further refined. Pins are meshed with an adequately small element size to model the interaction in holes accurately.

5.3 Comparison with test results

In this section, numerical results obtained from ABAQUS simulations are compared with test measurements. Comparison is made for parameters that are both monitored during tests and reported from simulations. These are the device hysteresis loop, strain gauge readings and EB rotations. The response of configuration A3-1 under harmonic input excitation with 10mm amplitude and 1.0Hz frequency is selected as the reference case for comparison. All the parameters are compared for the third cycle of either test or simulation.

(ABAQUS loops have some slight oscillations. These oscillations are based on numerical solution with explicit dynamic analysis. Hereafter, all the numerical results reported from ABAQUS are filtered with the same cut-off frequency to keep to the consistency and so as to be able to compare the parameters without introducing any shift due to the filter. The numerical oscillations do not affect the validity and reliability of FEA results. The comparison of filtered and unfiltered ABAQUS results and discussions on the effect of filter against the character of the observed “chatter”

are given in Appendix B. In summary, in this section the filter is proven to have no effect on the validity of numerical solution.)

5.3.1 Hysteresis loop

The ABAQUS simulation is run for three complete cycles of harmonic displacement input, pretty much the same like the experimental program. The hysteresis loops of all the three cycles, shown in Figure 5-4, are stable and repeat themselves as was also observed from experiments.

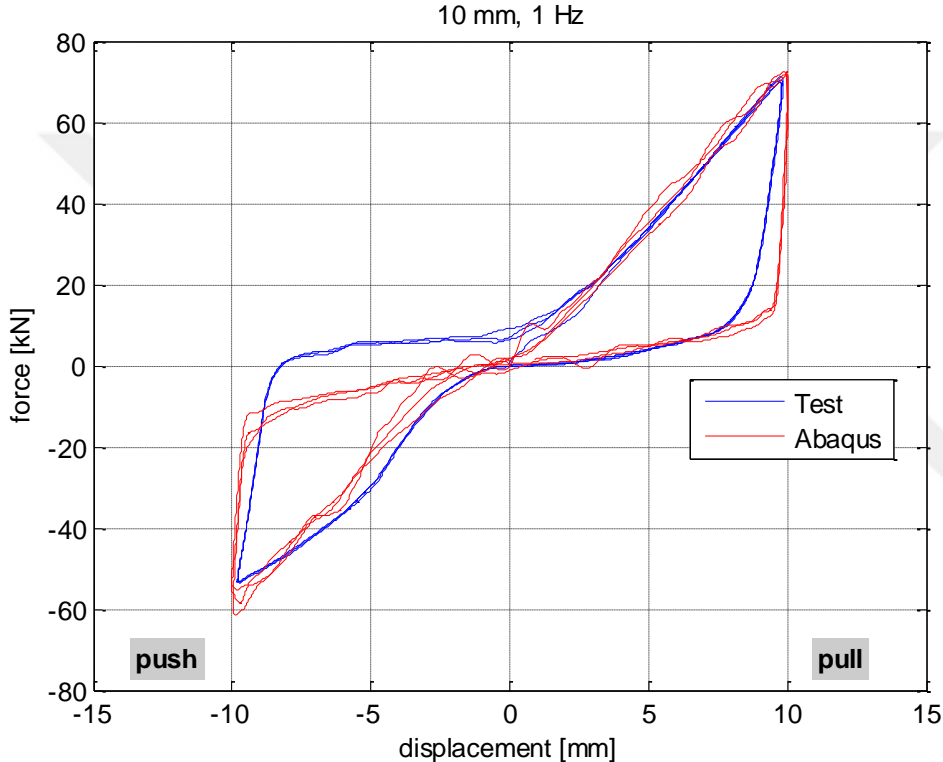


Figure 5-4. Device hysteresis loops as obtained from ABAQUS simulations and experiments for configuration A3-1 under 10 mm amplitude at 1.0 Hz

Comparison of hysteresis loops for configuration A3-1 under a 10 mm displacement amplitude at 1.0 Hz input is presented in Figure 5-4 and Figure 5-5. In Figure 5-5, only the loop of the third cycle is presented and its EDC value is estimated. As can be seen from the figures, loops obtained from ABAQUS simulation fairly well follow the test loops. A very good match is observed for both the pull and push branches of the loop except for the unloading branch in the push direction. Possible reasons for this

difference are commented in the following paragraph. The EDC values of Figure 5-5 are computed for the hysteresis loops of the third cycles. The difference between the EDC values of the two curves is 7%, which can be accepted as a reasonable margin. The numerical solution catches the peak forces of the test hysteresis loop very successfully. The peak forces at maximum pull and maximum push reported by ABAQUS are just slightly bigger (around 1%) than the test measurements because ABAQUS strictly follows the input displacement function and applies 10mm in either push or pull, but the hydraulic actuator of the test set-up applies the inserted displacement command with a lower precision and thus does not apply exactly 10mm. It applies 8.81mm in pull and 9.74mm in push as given in Table 4-3.

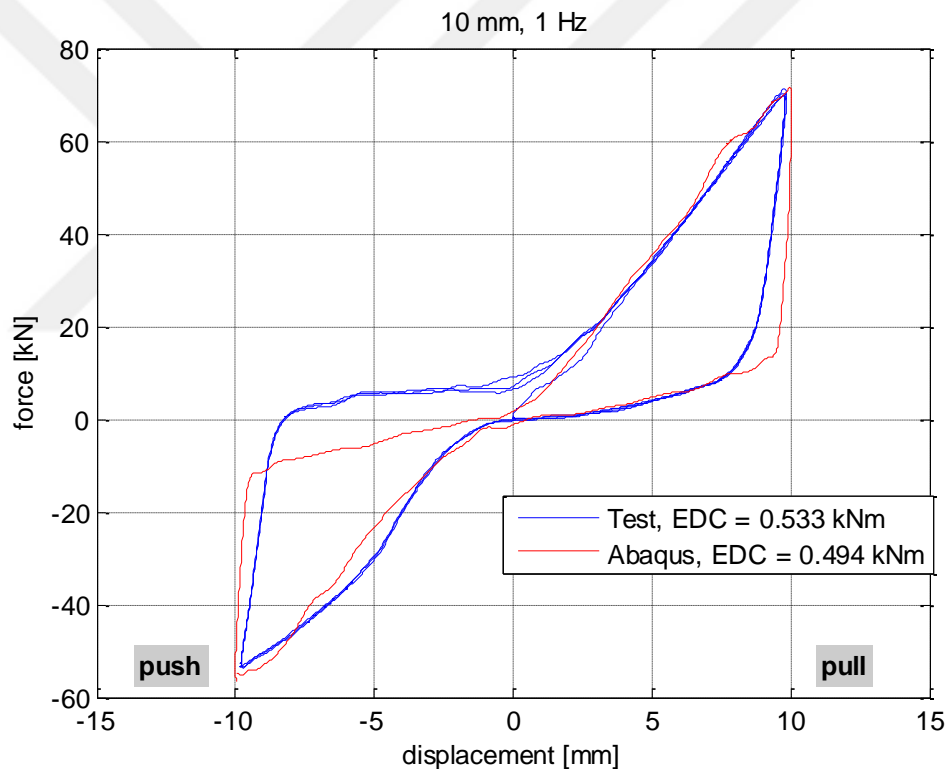


Figure 5-5. Device hysteresis loops as obtained from ABAQUS simulations and experiments for configuration A3-1 under 10mm amplitude at 1.0Hz

The experimentally obtained hysteresis loop is verified for both the pull and push directions except for the unloading branch of push direction. This branch of the experimental hysteresis loop is typical of hysteretic dampers. Possible reasons for this

difference in results may be (i) either an additional source of friction in the test set-up that is not included in the numerical model or (ii) a mismatch in the force measurement calibration of the hydraulic actuator used for the tests. The hysteresis loop from test data plots a residual displacement in the push direction. If a residual displacement is to be present in the device behavior, it is expected to be observed in both directions, i.e. both in pull and in push. The component that would cause this residual displacement is the friction developed within the DAM. This component, however, is governed by the VE unit force which is proportional to displacement, i.e. it is expected to become zero at zero displacement, if no plastic strains are present in the EB. Even if plastic strains are present, they are expected to be very small and may be neglected without compromising the precision satisfactory for the engineering practice. Therefore, when approaching zero displacement, both the elastomer and friction force are expected to fade, thus leaving no residual displacement. This is valid both under pull and push. Consequently, the device is expected to have a hysteresis loop typical of re-centering dampers.

The loops reported from ABAQUS characterize a re-centering damper, reporting less than 0.5mm residual displacement in both pull and push directions. This loop is the one expected by the damper design.

5.3.2 Strain gauge readings

In the experimental program, strain gauges are installed on the top and bottom surfaces of each driven bar, as shown in Figure 4-12 and Figure 4-13, and readings from four strain gauges in total are recorded during the tests. 1000 records per second are collected during the tests. In the numerical model, strains are reported at the integration points of all the seven elements along the width (dimension in U1 direction) of each driven bar. The corresponding elements are placed at the strain gauge locations and again 1000 strain values are reported per second. For all the strain gauge readings, the experimental measurements are compared against the numerical results. The agreement between the two curves is of the same character for all the four strain gauges. Thereby, only one representative case, the comparison for the bottom-surface strain gage of the bottom driven bar, is discussed herein, the results being valid for the rest, too. The corresponding curves are plotted in Figure 5-6.

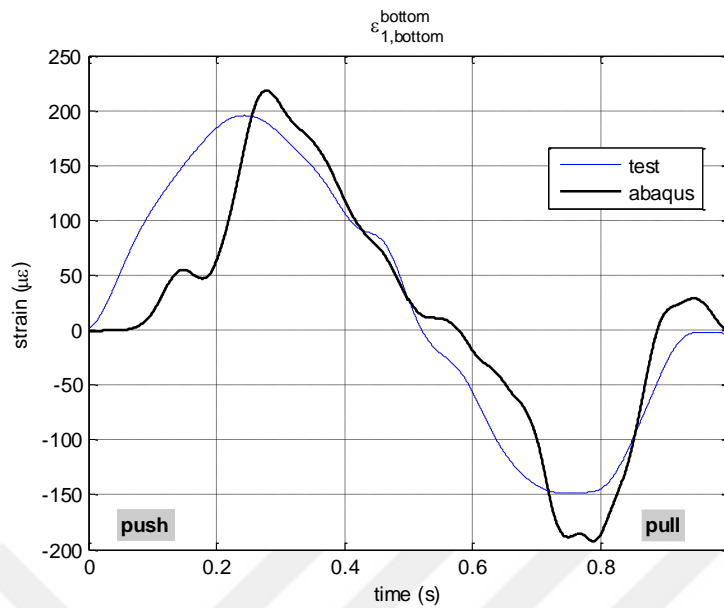


Figure 5-6. Strain gauge readings from experiments and numerical analyses recorded at the bottom surface of the bottom driven bar

The two curves of Figure 5-6 have essentially the same character, though the measured strain curve is smoother. The experimentally measured peak values are closely identified (overestimated with 10% difference in push and 15% in pull) by the numerical model. The numerical results are reported for the integration point which is 2.5mm away from the element surface. This is a reason for the difference in curves.

A 0.03s time lapse between peak values is observed in push direction. Similarly, there is a 0.05s-long zero-strain plateau in both curves. The length of the zero-strain plateau corresponds to the time needed for the gap closing. In the experimental curve, this zone is at its end. In the numerical result, however, it is in the beginning. This is because the experiment starts in pull direction but the simulation in push.

5.3.3 Elastomeric block rotations

In the tests, rotation time-history is measured for both the top and the bottom EB. The rotation of the latter is compared with its counterpart reported from numerical simulations and the two graphs are plotted in Figure 5-7. Herein, rotation in counterclockwise direction is taken as positive.

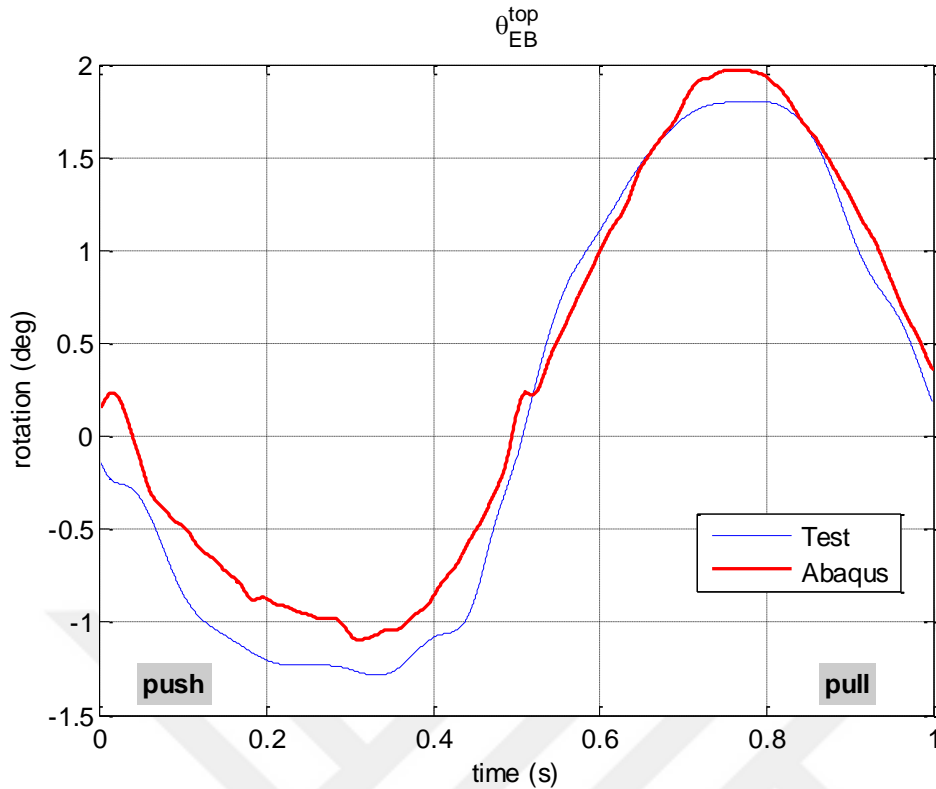


Figure 5-7. Top EB rotation readings (for the third cycle) from experiments and numerical analyses

The ABAQUS curve smoothly follows the test measurement and effectively captures its character. The magnitude of peak rotation in push is underestimated by 15% while in pull direction it is overestimated by 9%. The same as in the test, rotation of larger magnitude is registered in pull direction. The rotation in pull direction is measured to be 1.4 times the rotation in push. The same value is reported as 1.8 from FEA.

5.4 Detailed motion study of the full assembly of Backbone damper

Every component in the device assembly is assigned a specific function and has a corresponding contribution to device performance parameters. In the full assembly, the interaction and contact between system parts defines the load generation and transfer. To track this process and analyze the device mechanism, the force balance for each component is investigated through free-body diagrams.

5.4.1 Bottom elastomeric block

The top boundary plate of the EB is fixed and the bottom one displaces laterally and rotates under the motion transferred from the bottom driven bar. The field of displacements in U1-direction corresponding to maximum pull and maximum push are presented in Figure 5-8 and Figure 5-9, respectively.

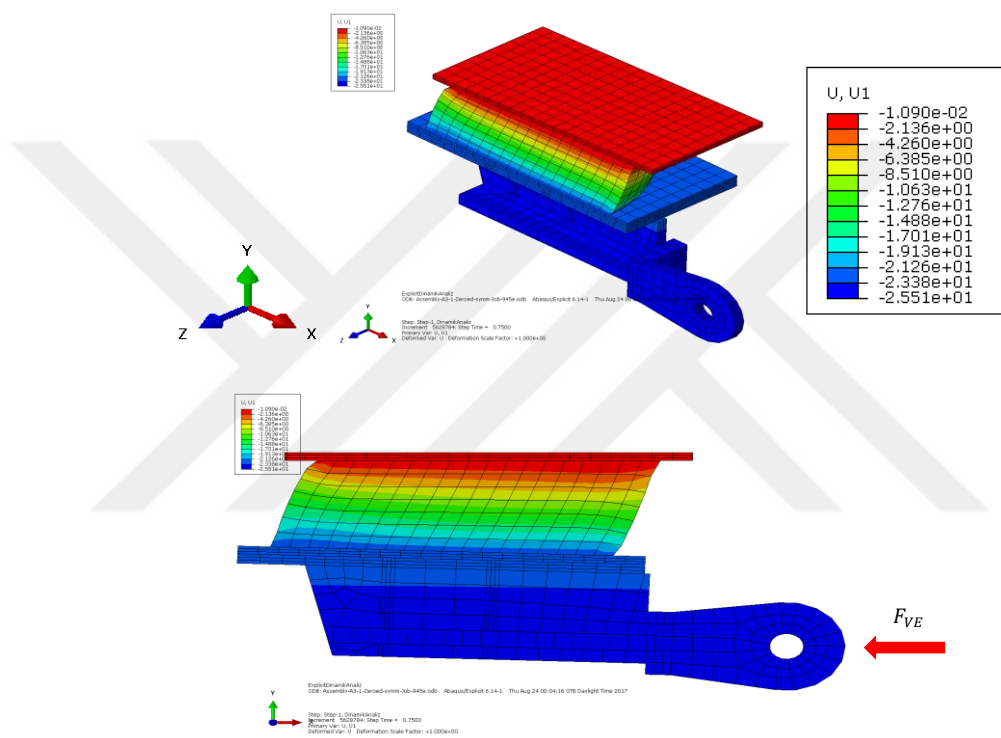


Figure 5-8. Free-body diagram of bottom elastomeric block at maximum pull (with contour of U1-direction displacement)

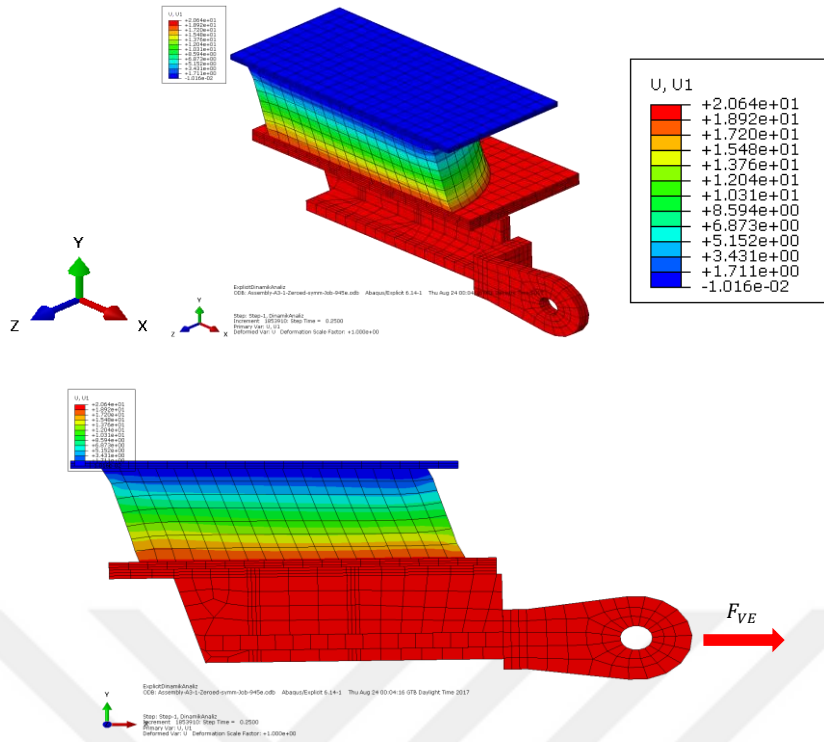


Figure 5-9. Bottom elastomeric block at maximum push

The deformed shape of the EB at maximum pull and maximum push and the force applied to the top adapter connection by the driven bar are also shown in Figure 5-8 and Figure 5-9, respectively.

Contour plot of the axial stresses at maximum pull is presented in Figure 5-10. In this position, the maximum compressive stress plotted with blue color in the figure reaches 1.35 MPa and is concentrated at the outer edge of the fixed elastomer surface. The maximum tensile stress which is a more critical parameter as already described in Chapter 3, is observed on the opposite side of the same interface. It is also observed from the contour plot that larger part of the elastomer body is under compression. Compressive forces develop in the central part while tension is concentrated in two opposite locations at the edges.

The field of axial stresses and shear strains developed in elastomer body under this dynamic straining are presented in Figure 5-10 and Figure 5-12.

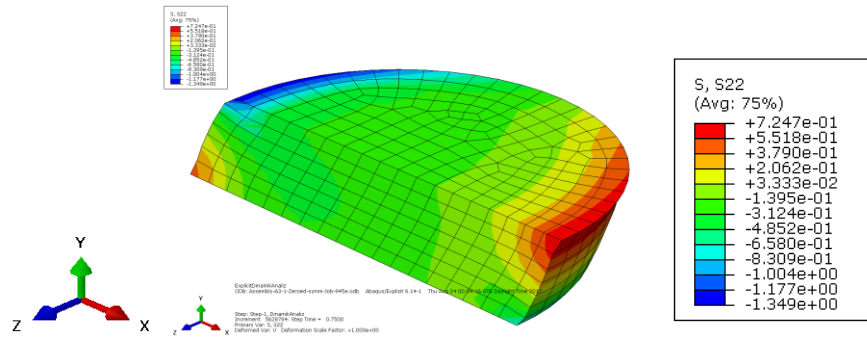


Figure 5-10. S22 contour plot of bottom EB at maximum pull

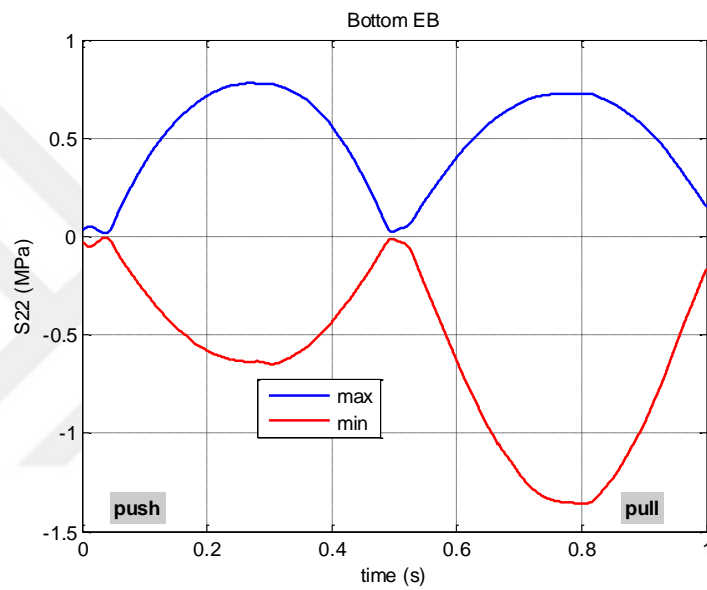


Figure 5-11. Envelope curves of S22 for bottom EB

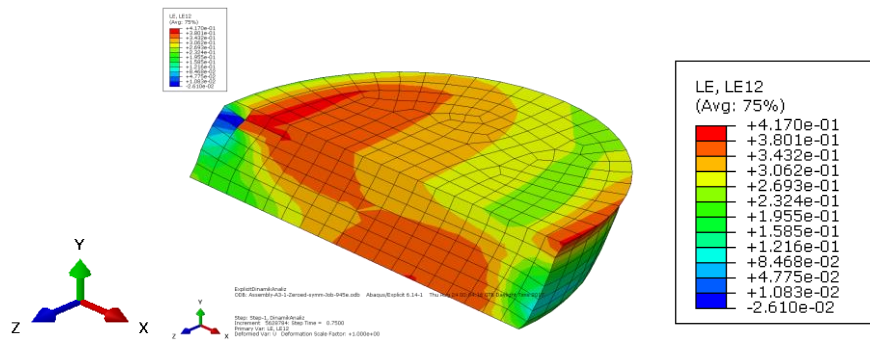
The envelope curves of true stresses in U2 direction (Y) are plotted in Figure 5-11. All the stress values developed within the elastomer body during the third cycle of simulations are enclosed between the curves. It is observed from the figure that in push direction peak tensile stresses reach slightly higher values than compressive ones, i.e. tension is dominant.

In pull direction, the tensile stresses are slightly smaller than in push. The peak compression stress is almost twice the peak tension stress, i.e. compression is much more pronounced.

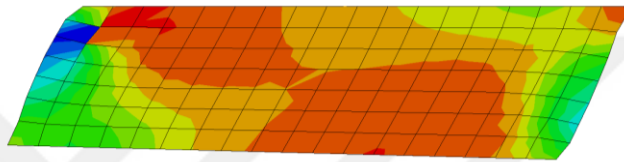
The tension peak in push is slightly larger than in pull, but the compression peak in pull is more than twice the one in push. This can be related to the larger rotations in pull. Rotation in pull which is predicted to be 1.4 times the one push has more than doubled the compression stresses, although slightly reduced the peak tension. This is actually beneficial because the compression capacity of elastomer body is not limiting while the tensile stresses are critical because of debonding. Also, the tensile stress does not exceed the 1.8MPa limit specified in Chapter 3. Therefore, the rotation is not recorded to challenge the EB's integrity and device performance. Hereby, the initial design has been validated as successful.

The shear strains are the second checkpoint for the EB. Their contour plot at maximum pull and push are presented in Figure 5-12 and Figure 5-14.

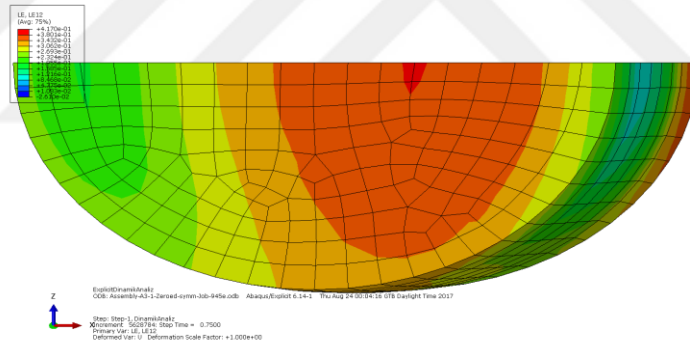




(a) 3D view the top visible surface being the boundary surface with the bottom adapter



(b) Diametric surface (X-Y)



(c) Boundary surface with top adapter (X-Z)

Figure 5-12. LE12 contour plot of bottom EB at maximum pull

The top surface is the fixed one. From Figure 5-12, the maximum magnitude of shear strain is predicted to be 0.42 and the minimum one 0.011.

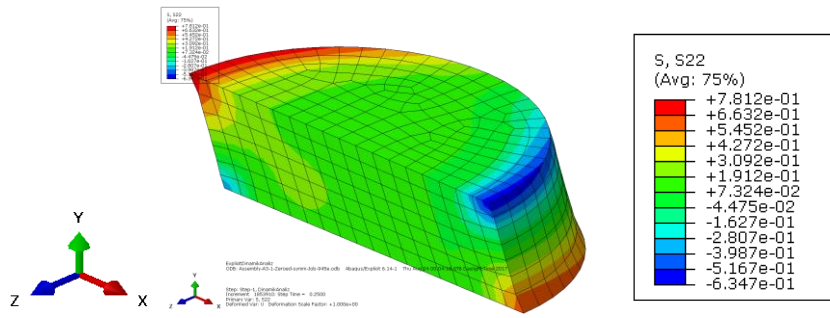
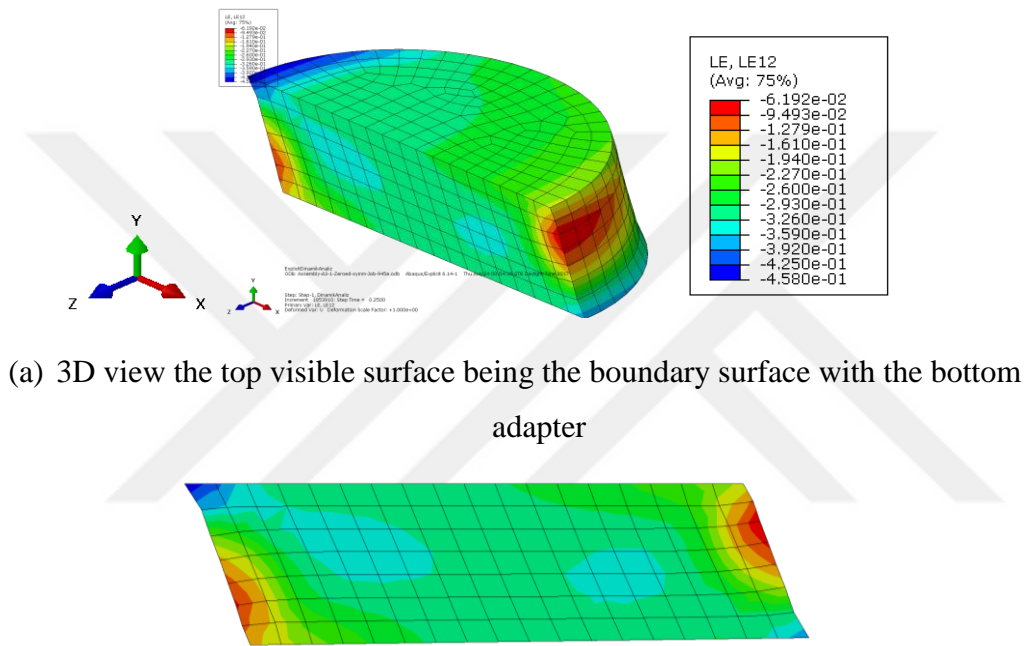
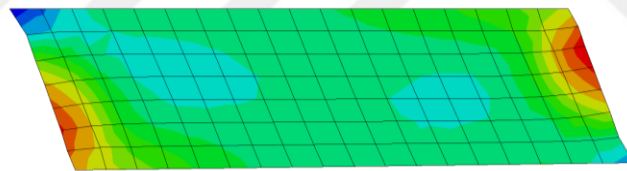


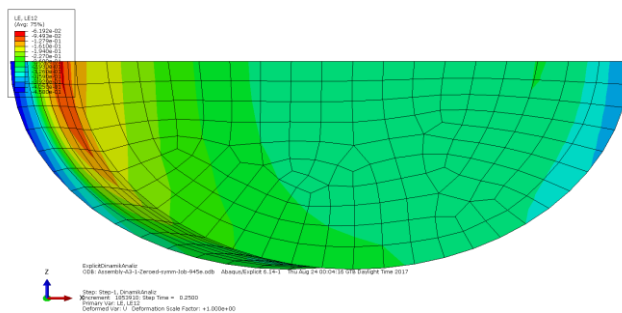
Figure 5-13. S22 contour plot of bottom EB at maximum push



(a) 3D view the top visible surface being the boundary surface with the bottom adapter



(b) Diametric surface (X-Y)



(c) Boundary surface with top adapter (X-Z)

Figure 5-14. LE12 contour plots of bottom EB at maximum push

From Figure 5-14, the maximum and minimum magnitudes of shear strain as predicted as 0.46 and 0.062, respectively. The other important observation from the same contour plot is that the shear strains are of the same sign all over the elastomer body and the boundary surfaces, unlike the result in pull where a zone of opposite sign shear strains is predicted. When compared to Figure 5-12, in pull the magnitudes are bigger.

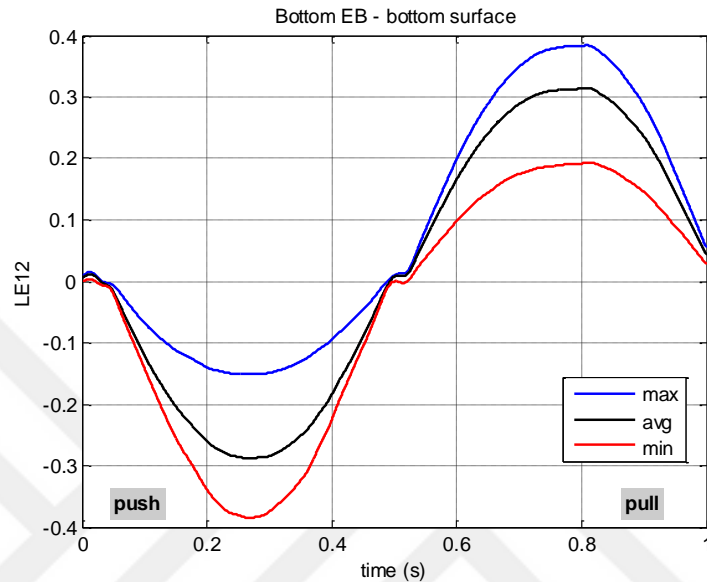


Figure 5-15. Envelope curves of LE12 of bottom EB

The shearing strains in elastomer at the surfaces with the boundary plates are between the envelope curves of Figure 5-15. The lower bound is slightly higher in pull.

5.4.2 Bottom driven bar

The amplifier was designed to remain elastic during the damper motion. Hereby, it is checked for plastic strains and none is predicted by the model.

The displaced shape of the bottom driven bar at maximum pull and maximum push with the forces acting on it in either direction are presented in Figure 5-16 and Figure 5-17, respectively.

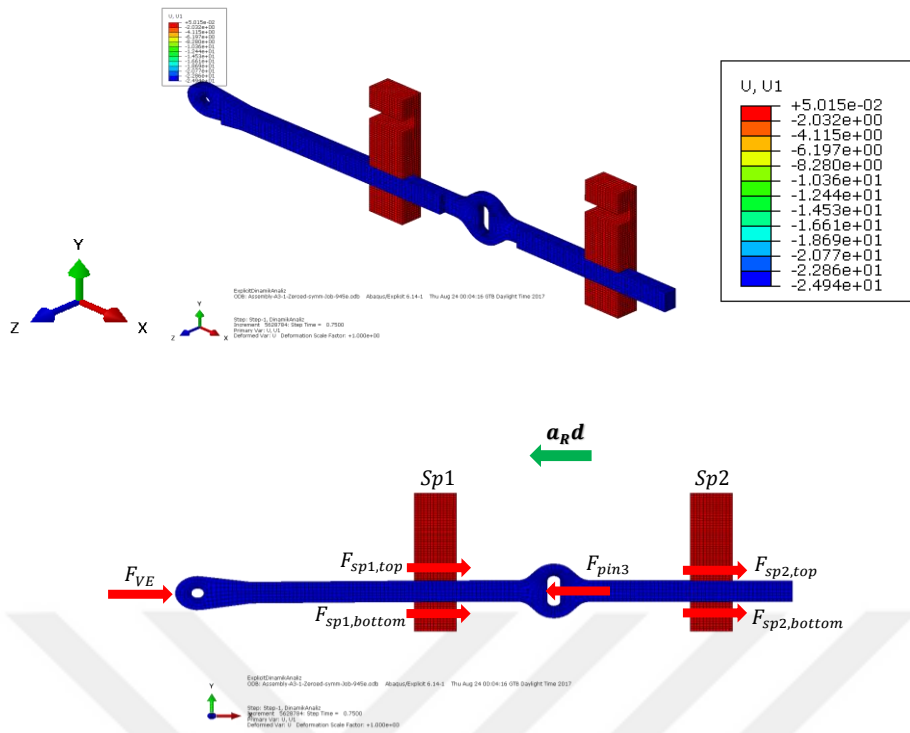


Figure 5-16. Bottom driven bar at maximum pull

In pull, the motion of the driving bar is in positive X unlike the driven bars; and vice versa in push. The driven bar is moving in direction opposite to the driving bar, conforming to the initial design. Every time this is considered in the analysis of the figures and in the equations used to track the transfer of forces.

As shown in Figure 5-16 and Figure 5-17, the forces acting on the top driven bar are generated from its contact with three parts during its motion: (1) VE unit, (2) Pin3 and (3) case supports. The contribution and source of each is investigated and discussed next, along with its effect on the force balance.

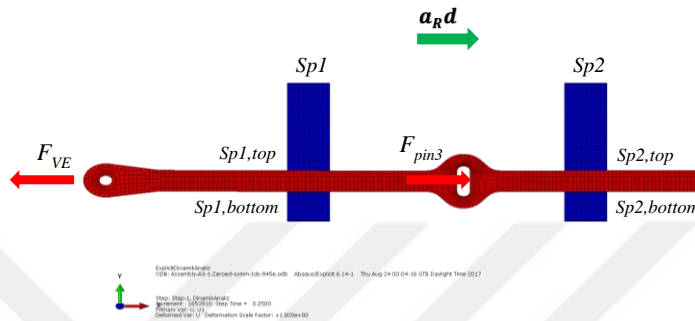
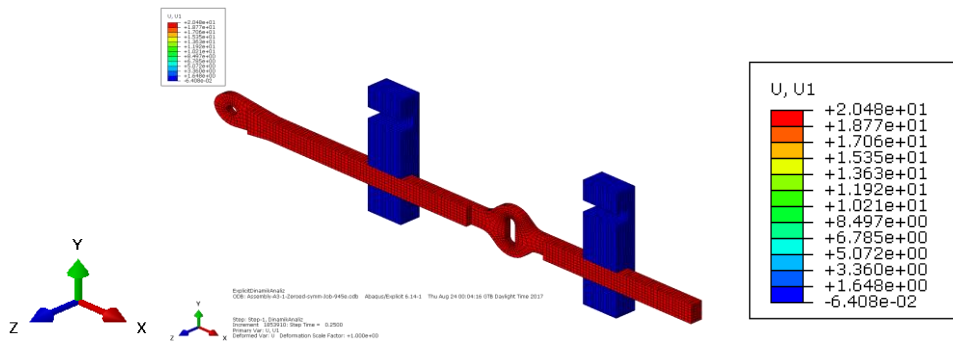


Figure 5-17. Bottom driven bar at maximum push

5.4.2.1 Force transferred from VE unit

The force generated by the EB of VE unit and acting on the driven bar has two components as expressed by Equation (42)

$$F_{VE} = F_{VE}^{FR} + F_{VE}^N \quad (42)$$

Here

F_{VE}^{FR} = the force generated by the contact friction between Pin4 and the driven bar

F_{VE}^N = the force generated by the contact pressure applied by Pin4 onto the driven bar

The time histories of all the three forces are plotted in Figure 5-18.

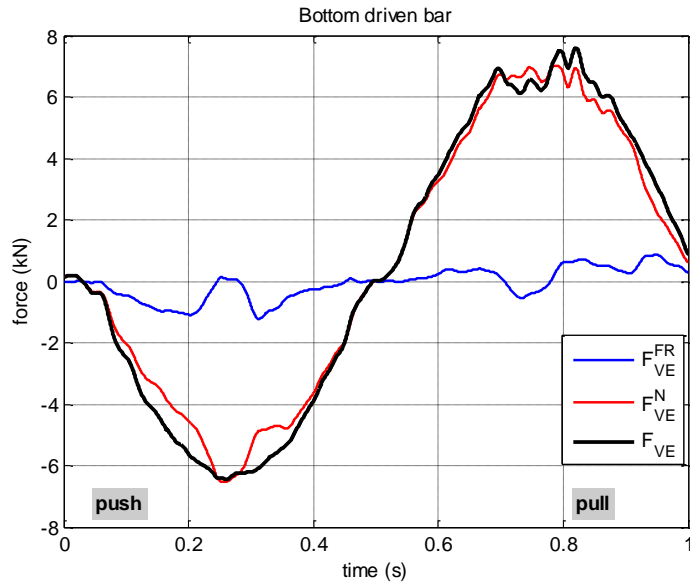


Figure 5-18. U1-direction force components transferred from VE unit to bottom driven bar

As seen from the figure, F_{VE}^N is the main component, i.e. the friction between Pin4 and the driven bar has an insignificant contribution to the total force effect coming from the VE unit. F_{VE}^{FR} is small in magnitude and has some observable oscillations. They are caused by the contact conditions that are changing during the motion. The more pronounced fluctuations are predicted at the point of maximum displacement in both directions, because there the velocity is first zeroed and then changes its direction, and so does the friction force. The oscillations of this force are reflected in the total force as well, which can be observed again in Figure 5-18.

An important observation from the same figure is that the normal component, as well as the total force F_{VE} , are larger in pull direction. Although this difference is not so big (around 15% of the force at maximum push), it increases when transferred to the driving bar and the device total force, which contributes to the asymmetry of device hysteresis loop. This difference in forces can be explained with the stresses and strains developed in EB in pull and push. Looking at Figure 5-11 and Figure 5-14, the shear strains that dominate over a larger area of boundary surface with top adapter are higher in pull than in push, i.e. the average of shear strains in pull is bigger. The time history of average shear strains is plotted in Figure 5-15. Analyzing the graphs, it is seen that

the average shear strains at the boundary surface with the top adapter are closer to the maximum envelope all the time and the value at maximum pull is 1.15 times the corresponding value in push. This is due to the larger rotations in pull that cause shear strains. And this difference in shear strains explains F_{VE} and F_{VE}^N being bigger in pull than in push, later reflected in the asymmetry of device hysteresis loop.

5.4.2.2 Forces generated at the contact between driven bar and case supports

Frictional stresses and contact pressure develop on each mating surface. Therefore, for each surface, being either top or bottom for either support 1 or support 2, the resultant force developed at the support equals

$$F_{spi,surf} = F_{spi,surf}^{FR} + F_{spi,surf}^N \quad (43)$$

where

$surf$ = considered surface, either top or bottom

$F_{spi,surf}$ = total force developed on the contact surface

$F_{spi,surf}^{FR}$ = total force due to frictional stress developed on the contact surface

$F_{spi,surf}^N$ = total force due to contact pressure developed on the contact surface

The time-history plots of forces due to frictional stress are given in Figure 5-19.

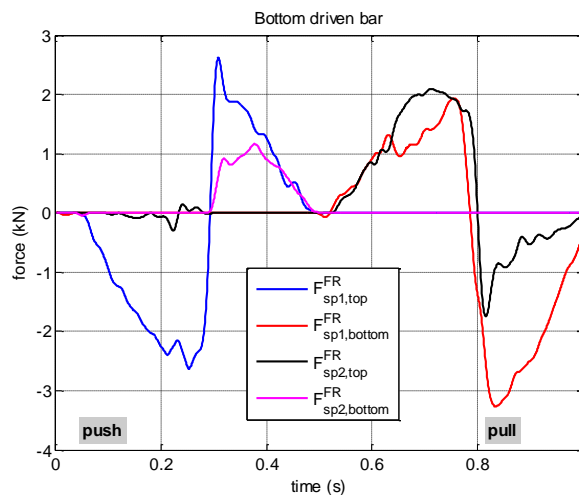


Figure 5-19. U1-direction friction forces acting on bottom driven bar generated from its sliding on the supports

There are two parameters defining the shape of the friction forces' curves shown in Figure 5-19: the direction and magnitude of displacement. The displacement indirectly includes the amplification ratio because the displacement of the driven bar is the one under consideration. The shape of the friction forces' curves in Figure 5-19 follows the change in the direction of motion. The jumps corresponding to the change in sign of the friction force are due to the change in the direction of motion. On the other hand, the friction force changes sign but not magnitude. Because the magnitude is determined by the magnitude of displacement. The displacement magnitude determines the axial strains and stresses in U2 direction (seen from the plots of Figure 5-11). Their resultant is the force in vertical direction that is the normal force needed for the friction. Therefore, under the same displacement the friction force magnitude is the same, just the sign is changed with the change in motion direction.

Then, the friction forces gradually decrease with the reduction in displacement magnitude following the change in S22 of the EB. After that, it gradually increases in line with the displacement and thus the "valley" in the middle is formed.

Again, the conclusion that the pull forces are larger than push ones implies that not only the displacement but also the deformed state is important. This is so because the rotation in pull direction changes the deformation state which is naturally reflected onto the stresses and their resultant forces. Here, the detailing also comes into play.

At 0.5 s, i.e. zeroed position, the motion has the highest velocity and the curves are smoother compared to other time instances.

Looking at Figure 5-19, an observation on the inclusion of each support surface in the generation of friction forces can be made. This observation can be further used to predict the effect of eventual changes in the design and detailing on the device performance. Therefore it is useful for future optimization also. For example, the bottom surface of support 2 has a contribution only during the motion from maximum pull till the initial position. Therefore, changing the properties of this surface will have an effect only in this branch and this effect will be smaller compared to a similar change in the top surface of support 1. Analogous discussions can be made for the other surfaces as well. Also, it can be clearly observed that support 1 is more prominent.

During the contact between bottom driven bar and case supports, forces due to contact pressure are developed and transferred as well. The time histories of U1-direction components of these forces developed at both supports are given in Figure 5-20. As seen from the plots, these forces are very small compared to the forces resulting from frictional stress presented in Figure 5-19 and can be neglected without any loss of accuracy.

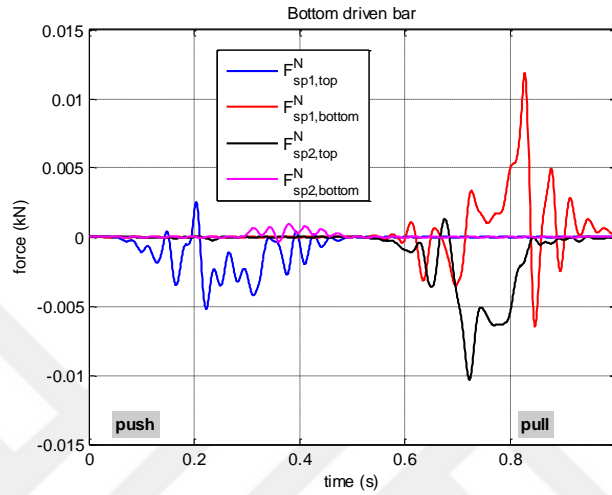


Figure 5-20. U1-direction normal forces acting on bottom driven bar generated from its sliding on the supports

The total forces are estimated with the following equations:

$$\sum F_{sp}^{FR} = \sum_{i=1}^2 (F_{spi,top}^{FR} + F_{spi,bottom}^{FR}) \quad (44)$$

$$\sum F_{sp}^N = \sum_{i=1}^2 (F_{spi,top}^N + F_{spi,bottom}^N) \quad (45)$$

$$\sum F_{sp} = \sum F_{sp}^{FR} + \sum F_{sp}^N \quad (46)$$

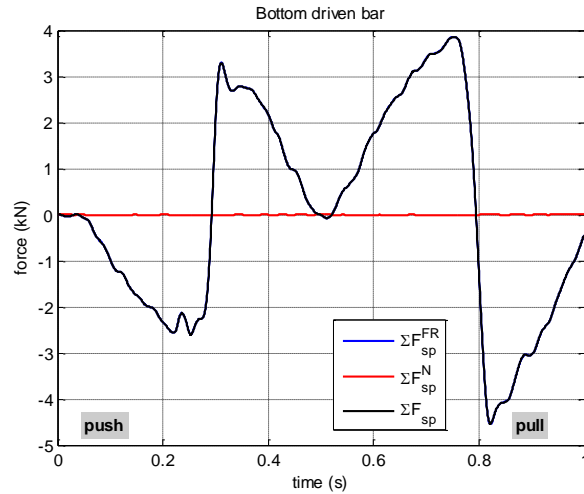


Figure 5-21. U1-direction total forces acting on bottom driven bar generated from its sliding on the supports

Looking at both Figure 5-19 and Figure 5-20, it is seen that total forces due to contact pressure are much smaller (orders of magnitude smaller) than the resultant forces due to frictional stress. Thereby, in Figure 5-21 the forces generated at the supports almost overlap with the sum of frictional forces. The peak forces in pull are larger than in push due to the larger rotation in this direction which creates additional shear strains.

5.4.2.3 Force transferred form Pin3

The force to put in motion the driven bar is the one applied by Pin3. Again, during the motion the contact between the pin and the driven bar creates both contact pressure and frictional stresses. Their resultants, as well as the total force in Pin3 expressed with (47), are plotted in Figure 5-22.

$$F_{pin3} = F_{pin3}^{FR} + F_{pin3}^N \quad (47)$$

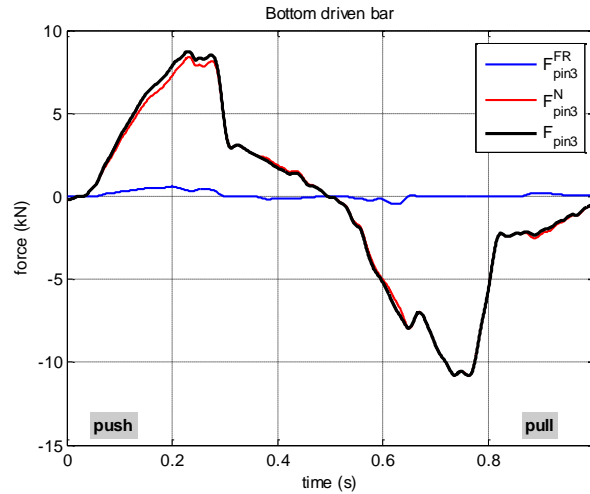


Figure 5-22. U1-direction contact forces transferred from Pin3 to bottom driven bar

Here, the force due to contact pressure is dominant while friction has a negligible contribution, i.e. the total force in Pin3 almost coincides with normal force at contact.

5.4.2.4 Force balance and hysteretic response of driven bar

Considering Figure 5-16 and Figure 5-17, the force balance of the driven bar can be expressed with the following equation (48)

$$F_{VE} + F_{sp} - F_{pin3} = 0 \quad (48)$$

or

$$F_{VE} + F_{sp} = F_{pin3} \quad (49)$$

Time-history plots of these forces are given in Figure 5-23.

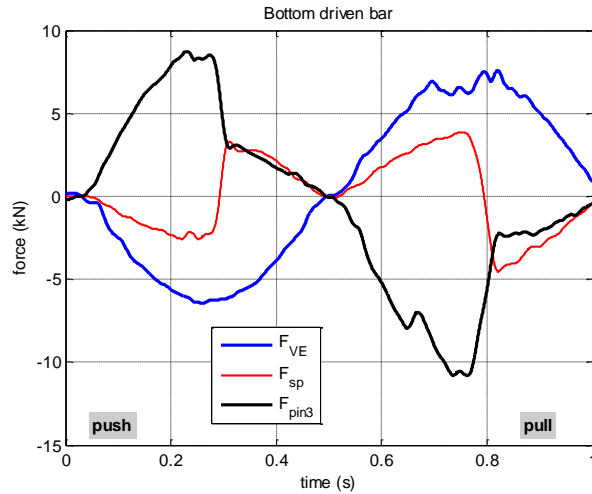


Figure 5-23. U1-direction forces acting on bottom driven bar

Equation (49) expresses equality in magnitudes of the left-hand side and right-hand side components. Each side is plotted in Figure 5-24. The two curves of the graph overlap, except for some minor differentiations at the peak displacement in either direction. The reason for this difference is considered to be the inertial forces which are not included in the force balance equation because their effect is assumed as minimal.

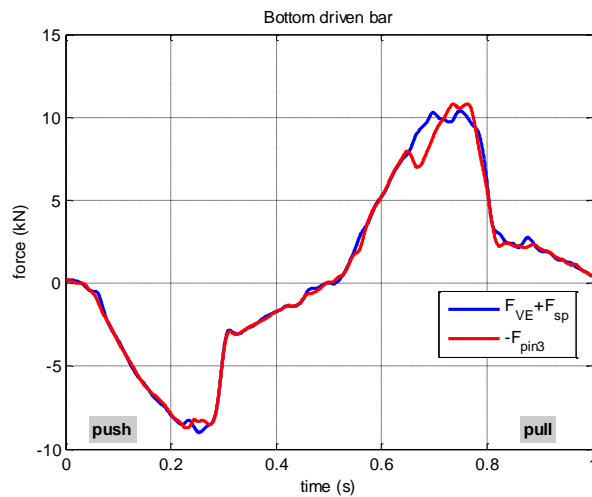


Figure 5-24. Magnitude comparison of U1-direction forces acting on bottom driven bar

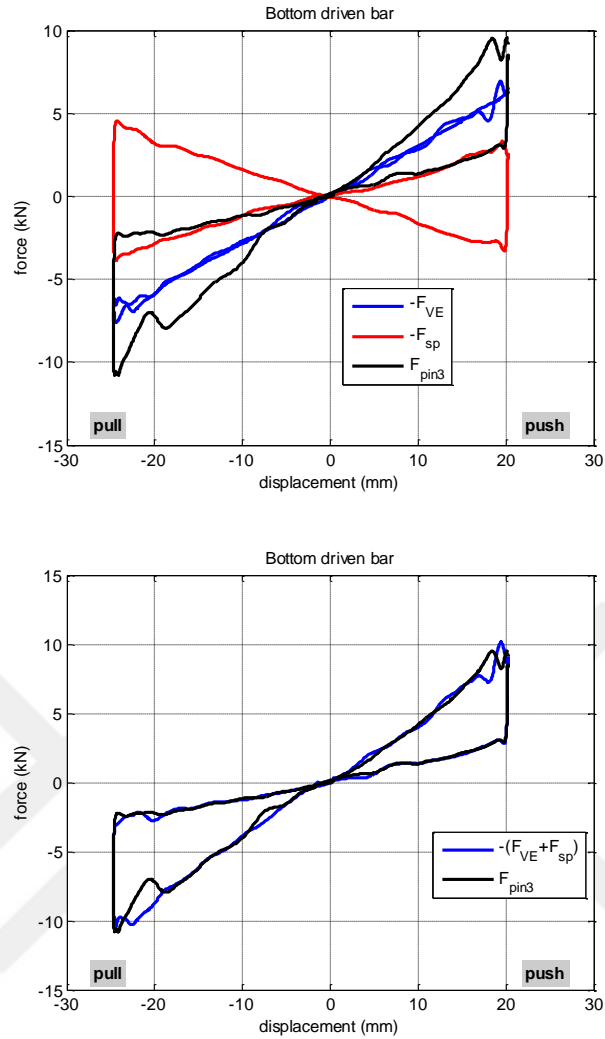


Figure 5-25. Hysteretic behavior of bottom driven bar

The bigger the difference between the loading and unloading branches of the hysteresis loop, the larger the EDC. In Backbone damper, till reaching the maximum displacement in either pull or push direction (i.e. in the loading branches), both F_{VE} and F_{Sp} are in the same direction and sum up to increase the loading branch slope and consequently its force. Thus, they complement in increasing K_{eff} . When peak displacement is reached, F_{Sp} also reaches its maximum value and then changes direction but its magnitude remains the same. These two characteristics in the behavior are equally important for improving the device performance. This sudden change in the sign of F_{Sp} is reflected as the sudden force jump from the loading to the unloading branch of the total hysteresis loops in Figure 5-25. Exactly this jump creates the

difference between the loading and unloading branches and causes the “fattening” of the hysteresis loop. The amount of this jump is as much as the magnitude of F_{Sp} . Therefore, both the action of the jump and the amount of the jump are important in increasing the device EDC.

If there were not any F_{Sp} , the hysteresis loop would be just the thin one of blue color in Figure 5-25, i.e. with very small EDC. If there were only F_{Sp} without F_{VE} , the hysteresis loop would be the red one, characterized with large EDC but the effective stiffness would be just one third of the stiffness of the hybrid device. In conclusion, the viscoelastic and friction mechanisms combine and complement each other to create a device with an increased energy dissipation capacity and effective stiffness.

5.4.3 Bottom asymmetric disk

The asymmetric disk at maximum pull with the forces acting on it is shown in Figure 5-26. The directions of the acting forces are reversed with the change in the direction of motion.

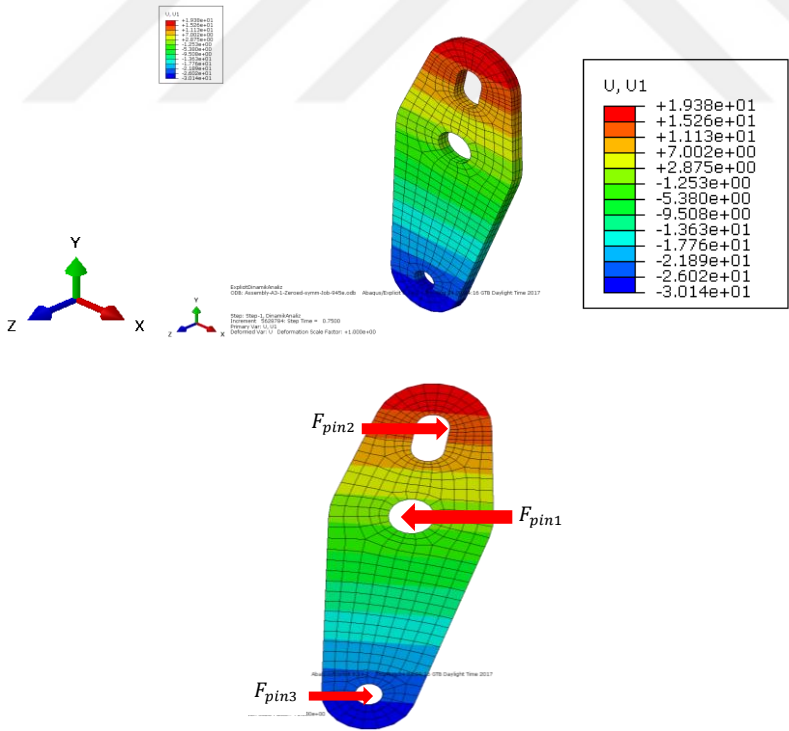


Figure 5-26. Bottom asymmetric disk at maximum pull

Analyzing the above figure, the force balance of the asymmetric disk is expressed with Equations (50) and (51):

$$F_{pin2} + F_{pin3} - F_{pin1} = 0 \quad (50)$$

or

$$F_{pin2} + F_{pin3} = F_{pin1} \quad (51)$$

The force in each pin has two components as:

$$F_{pini} = F_{pini}^{FR} + F_{pini}^N \quad (52)$$

Where

$i = \{1; 2; 3\} = \text{pin number}$

The two components for all the three pins are plotted together in Figure 5-27.

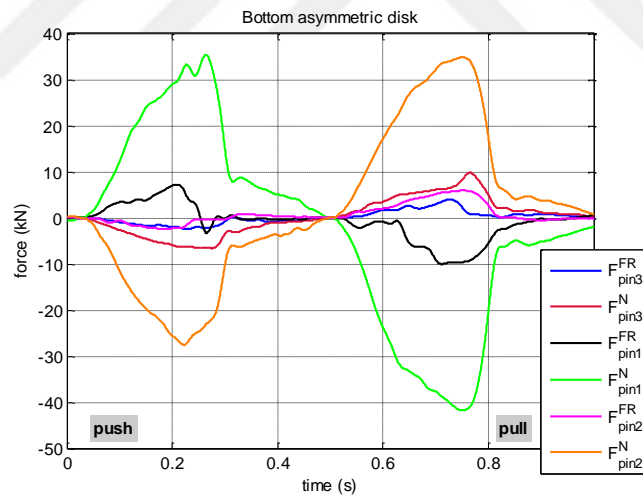


Figure 5-27. U1-direction force components transferred from Pin1, Pin2 and Pin3 to bottom asymmetric disk

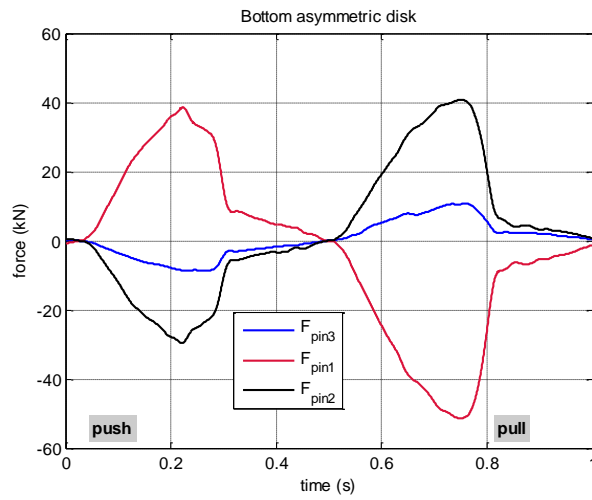


Figure 5-28. U1-direction forces transferred from Pin1, Pin2 and Pin3 to bottom asymmetric disk

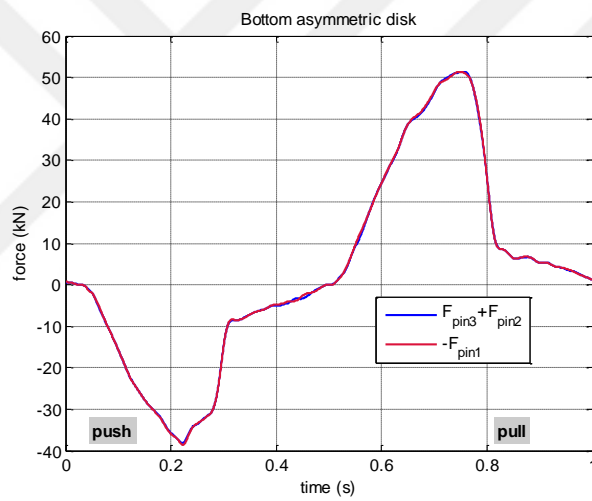


Figure 5-29. Magnitude comparison of U1-direction forces acting on bottom asymmetric disk

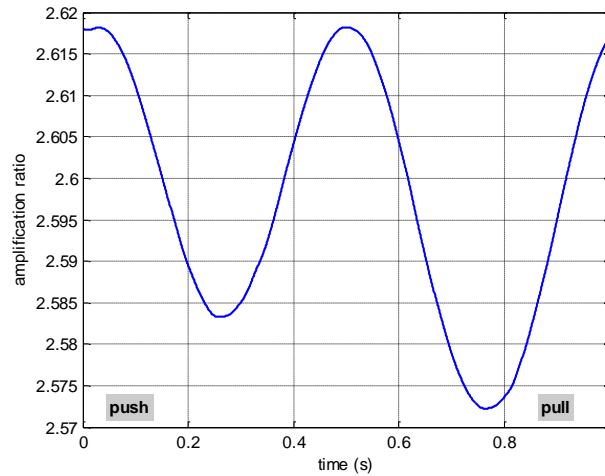


Figure 5-30. Amplification ratio

The estimated amplification ratio is plotted in Figure 5-30. Both the pattern and the values of the curve agree with the performance expected by the design. The amplification ratio at maximum push is slightly smaller than its push counterpart. This is due to the initial shift of 1mm in pull direction. The same difference between pull and push is observed from test readings but the experimentally measured difference is bigger.

5.4.4 Driving bar

The forces acting on the driving bar at maximum push are shown in Figure 5-31. At maximum pull, all the directions are reversed.

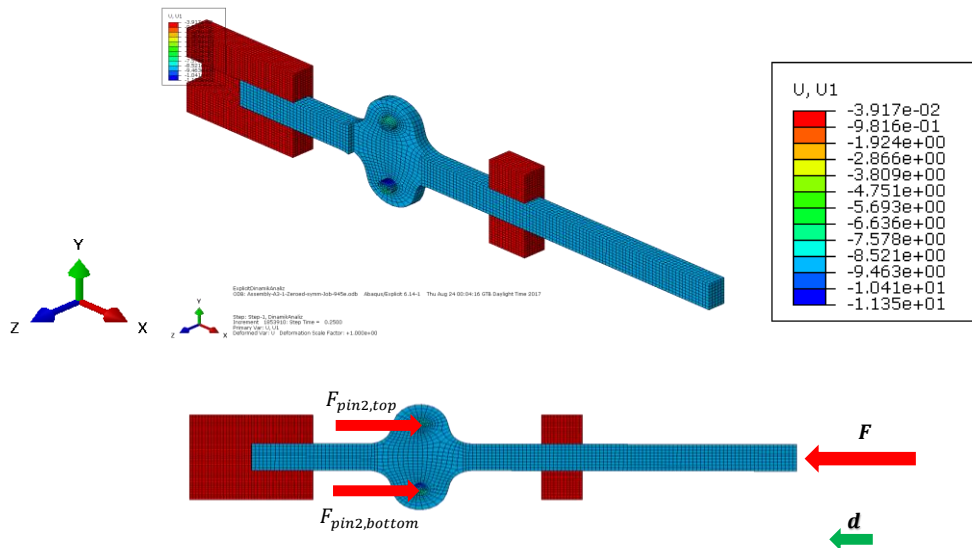


Figure 5-31. Driving bar at maximum push

The force balance of the driving bar is expressed with Equation (53)

$$F = F_{pin2,top} + F_{pin2,bottom} \quad (53)$$

The components of the pin forces in the above equation are plotted in Figure 5-32. It is seen from the plots that the forces transferred from the bottom pin are larger than the forces of top Pin2. This is because the case supports of the top driven bar are 1mm looser than their bottom counterparts. This gap causes both a reduction in the normal component of the contact force and a delay in time.

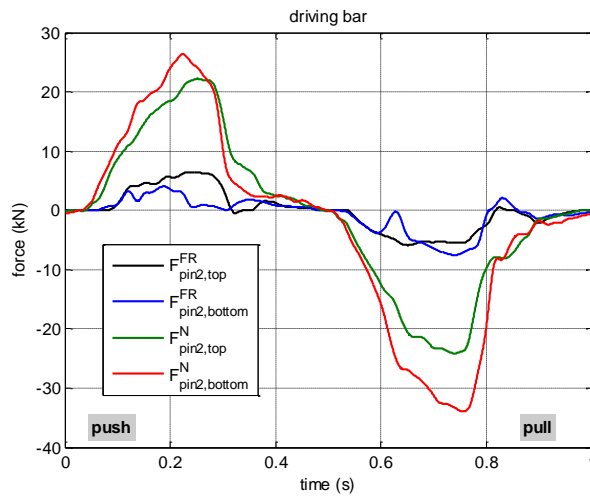


Figure 5-32. U1-direction force components transferred from top and bottom Pin2 to the driving bar

The time-history plots of the total forces due to frictional stress and due to contact pressure are given in Figure 5-33. The forces due to contact pressure are recorded to be determinant while contribution of the friction generated by rotation of the pins is much smaller.

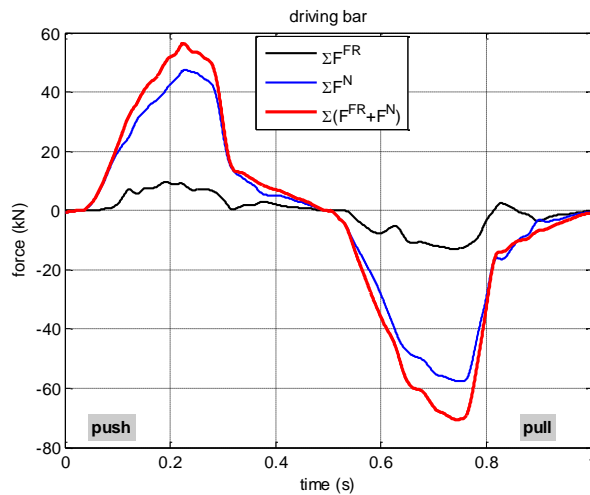


Figure 5-33. U1-direction total forces transferred from top and bottom Pin2 to the driving bar

When the forces of Figure 5-33 are plotted with respect to the displacement of the driving bar, the hysteresis loops of Figure 5-34 are obtained. Comparing the area enclosed by each loop, it can be again concluded that the device EDC is determined by the contact pressure.

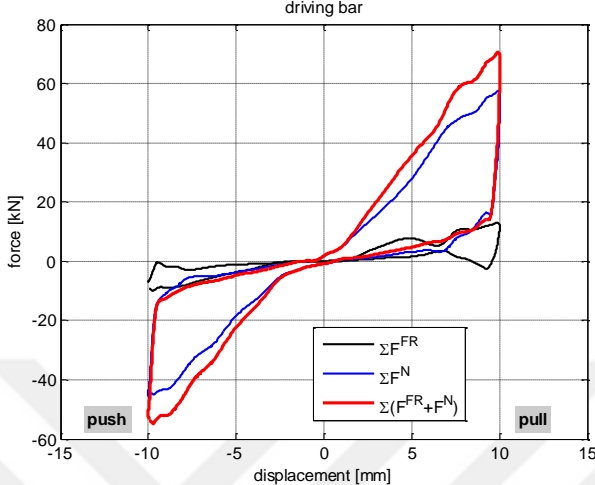


Figure 5-34. Hysteresis loop of each force component and total force transferred from pins to the driving bar

Finally, the device hysteresis loop can be compared against the loop obtained from total forces transferred from pins. The two loops presented in Figure 5-35 overlap. This demonstrates that the flow of forces and the device mechanism are effectively tracked and inertia forces do not have an effect on the force balance.

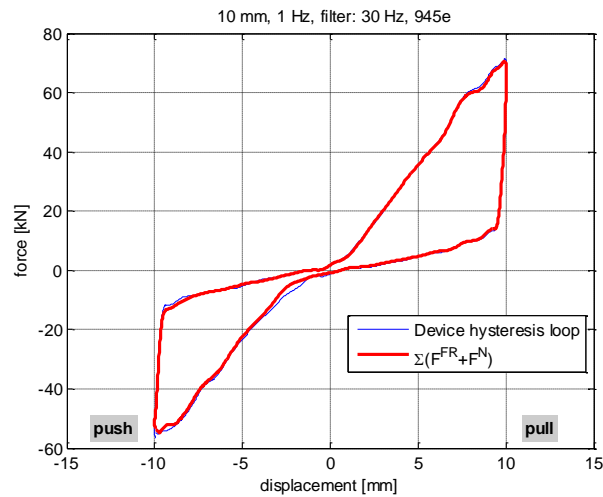


Figure 5-35. Hysteresis loop of transferred forces and of total force on driving bar

5.5 Summary and conclusions

A comprehensive numerical model of the complete assembly of Backbone damper has been created in ABAQUS environment. Considering the complexity of the detailed assembly, the model has been built up step by step and validation performed at each step to avoid possible errors. The main challenges in modelling, excluding the complexity of the whole device, can be outlined as proper modelling of elastomer material behavior exhibiting both hyperelastic and viscous properties and contact interactions between assembly parts.

The damper response under harmonic displacement inputs has been simulated through dynamic explicit analyses. The results from numerical simulations are compared against test measurements for all the monitored parameters, thus the numerical model has been verified. A detailed motion study of the device full assembly has been performed.

The assembly FE model in ABAQUS is very successful in simulating the device behavior and can be used to further investigate Backbone damper performance.

CHAPTER 6

EVALUATION OF DEVICE PERFORMANCE PARAMETERS

6.1 Introduction

The proposed device has already been experimentally tested and the test results verified against the numerical simulations. In this chapter, the relationships between performance parameters and the independent control parameters are investigated with the analysis of experimental data.

The performance parameters of Backbone damper are:

- EDC
- K_{eff}

The independent design parameters and inputs affecting these two performance parameters are

- Input displacement d
- Type of EB (plain, laminated or ball included)
- EB horizontal stiffness K_h
- EB vertical stiffness K_v

Rotation of EB is an indirect parameter that affects the performance parameters, and it depends on EB rotational stiffness and input displacement.

6.2 Evaluation of performance parameters from test results

6.2.1 Energy Dissipated per Cycle (EDC)

6.2.1.1 Analysis of experimental data

To observe the trend in Backbone damper *EDC* with change in displacement, the mean *EDC* values are plotted against mean displacements of test data.

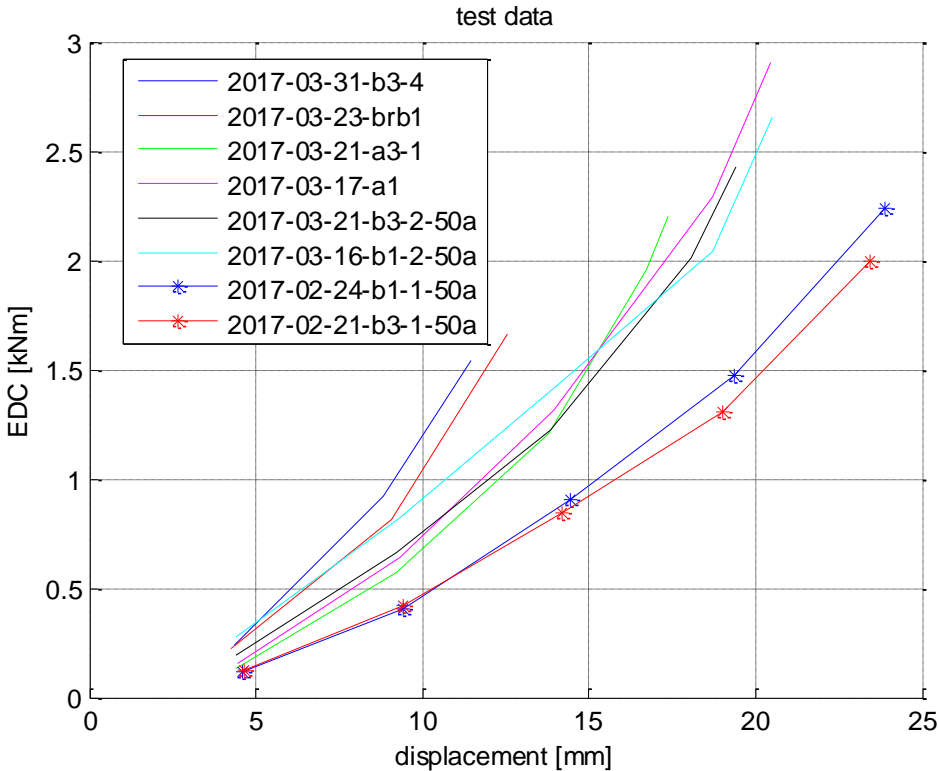


Figure 6-1. EDC vs displacement for test data of prototype II

Figure 6-1 clearly displays the relation between EDC and the input displacement for all configurations of Prototype II. At first glance, it can be noticed that the curves are clustered in three distinct groups. These correspond namely to the three different shear stiffness levels of EBs with the lowest one including B3-1 and B1-1. The next cluster covers the intermediate stiffness level of B1-2, B3-2, A1 and A3-1. The third cluster characterized with the highest EDC corresponds to the configurations with the largest

stiffness: BRB and B3-4. Thus, the EB shear stiffness determines the slope of the EDC vs displacement curve, i.e. they are directly proportional.

The two configurations in the utmost cluster (BRB and B3-4) have difference in horizontal stiffness similar to the stiffness difference between the lowest and the middle group. Yet, the curves are not as diverged as the lowest and middle cluster. This observation suggests about a possible saturation effect specific to the geometrical and mechanical properties of the damper design that may be dependent on interaction between design parameters.

Within the middle cluster there are EBs of different type (plain elastomer A and laminated rubber B). Yet, their response is quite similar. Therefore, it may be inferred that the type of EB is not a key parameter in design.

Yet, the curves within a cluster do not overlap but hold to a reasoned gradation defined by both the amplification ratio and EB rotational stiffness. The divergence becomes more obvious for increasing displacements. Similarly, the curves corresponding to B1-1 and B3-1 (lowest stiffness cluster) almost overlap till 15mm of displacement and hereafter they begin to diverge with B1-1 following a steeper curve. B1-1 has more than twice the rotational stiffness of B3-1 but its average amplification ratio is 1.73 compared to 1.83 for B3-1. This observation can be explained with the parallel increase in displacement and rotation. Thus, larger displacements generate larger angles of rotation where the rotation stiffness comes into play. Still, the rotational stiffness does not have as pronounced an effect as the horizontal stiffness.

Power function, as expressed with Equation (54), is fitted to each curve of Figure 6-1, the fits are summarized in Figure 6-2 and their constants are tabulated in Table 6-1.

$$EDC(d) = a * d^b \quad (54)$$

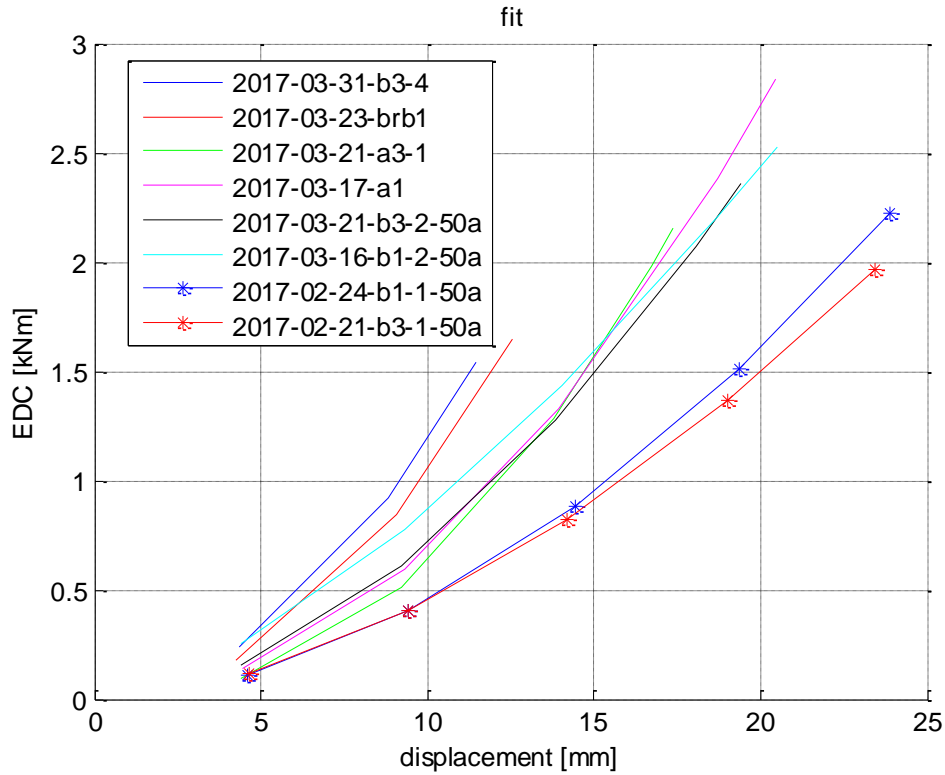


Figure 6-2. Power functions fitted to EDC vs displacement curves for Prototype II

Table 6-1. Coefficients of power functions fitted to the EDC vs displacement curves from test data

Test	EDC - a	EDC - b	EDC - rs
2017-03-31-b3-4	0.014	1.925	1.000
2017-03-23-brb1	0.009	2.081	0.997
2017-03-21-a3-1	0.003	2.254	0.996
2017-03-17-a1	0.007	1.987	0.997
2017-03-21-b3-2-50a	0.011	1.822	0.996
2017-03-16-b1-2-50a	0.028	1.493	0.987
2017-02-24-b1-1-50a	0.007	1.829	0.999
2017-02-21-b3-1-50a	0.008	1.739	0.997
Prototype I	0.028	1.339	0.981

All the R-square (rs) values listed in the fourth column of Table 6-1 are very close to 1.00, an indication that the selected power function is a very good representation of the test data.

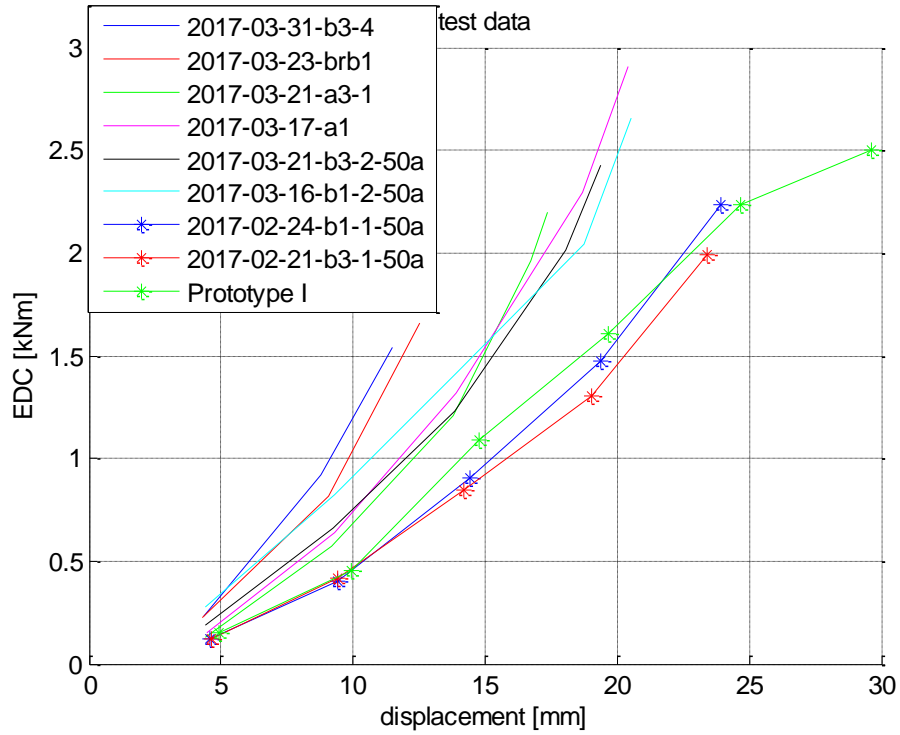


Figure 6-3. EDC vs displacement curves for all tests including prototype I

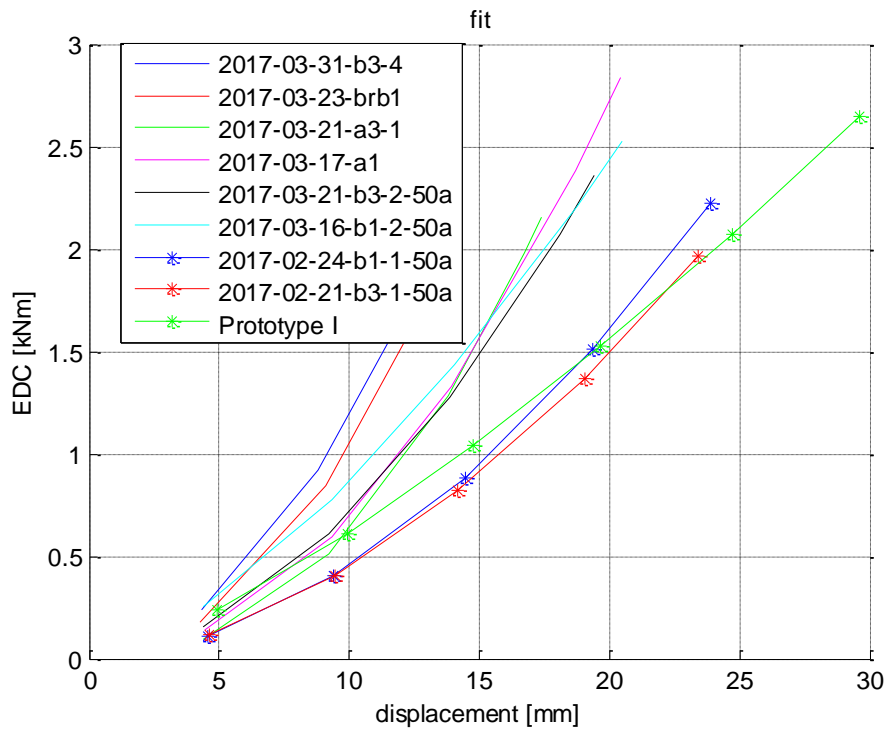


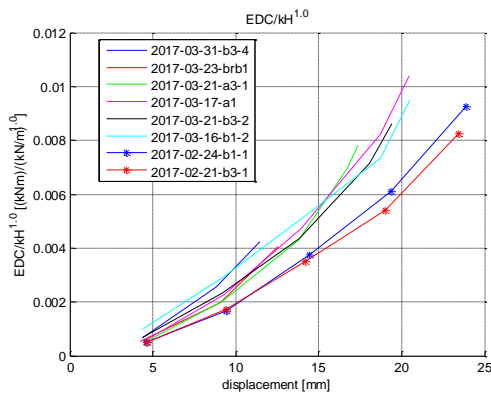
Figure 6-4. Power functions fitted to EDC vs displacement curves for all tests

The dependence of EDC on input displacement for all the tests including the prototype I is summarized in Figure 6-3, and the power functions fitted to the same curves are plotted in Figure 6-4. Although the horizontal stiffness of prototype I EB belongs to the second level, its curve falls within the first cluster and even below for displacements larger than 20mm. Its fitted power function illustrates the significantly smaller stiffness of the EDC curve. Moreover its EDC curve does not display as stable a character as the curves of prototype II. Therefore, prototype II is testified as a more successful design and the conclusions to follow on Backbone damper performance will be derived based on analyses and observations of prototype II.

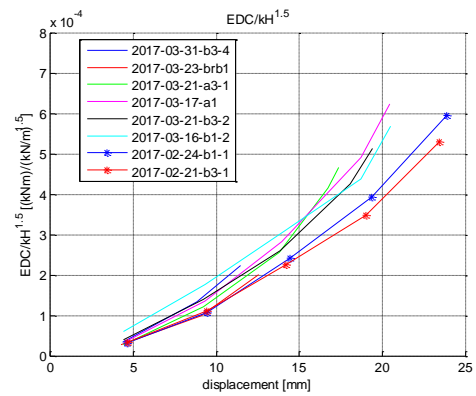
6.2.1.2 Upper and lower bound estimations

All the observations and conclusions thus far can be organized in a compact formulation.

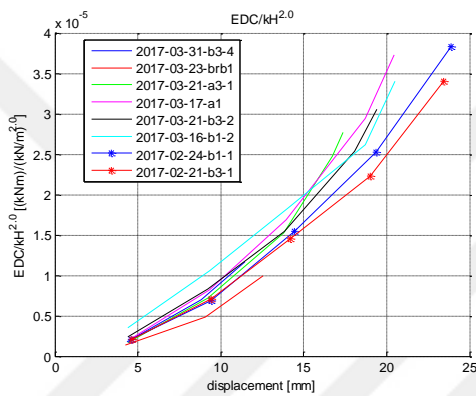
First, the EDC curves are normalized by a power of the K_h value of each EB. The candidate curves obtained for different powers (1.0, 1.5, 2.0 and 2.5) of K_h are shown in Figure 6-5.



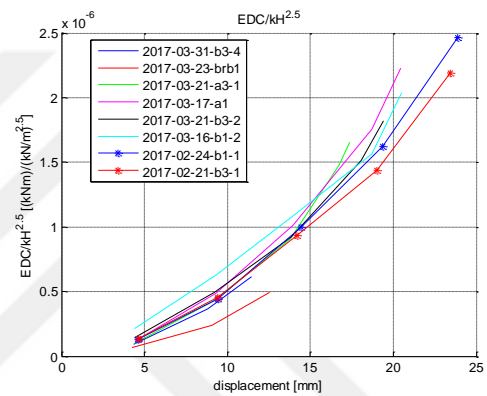
(a)



(b)



(c)



(d)

Figure 6-5. Candidate EDC curves normalized by (a) K_h ; (b) $K_h^{1.5}$; (c) K_h^2 and (d) $K_h^{2.5}$

The curves in Figure 6-5 (b) (with power of 1.5) are selected since they seem to form a more compact cluster. Later, the data in all these normalized curves are concentrated in three curves by determining the mean and standard deviation values as shown in Figure 6-6.

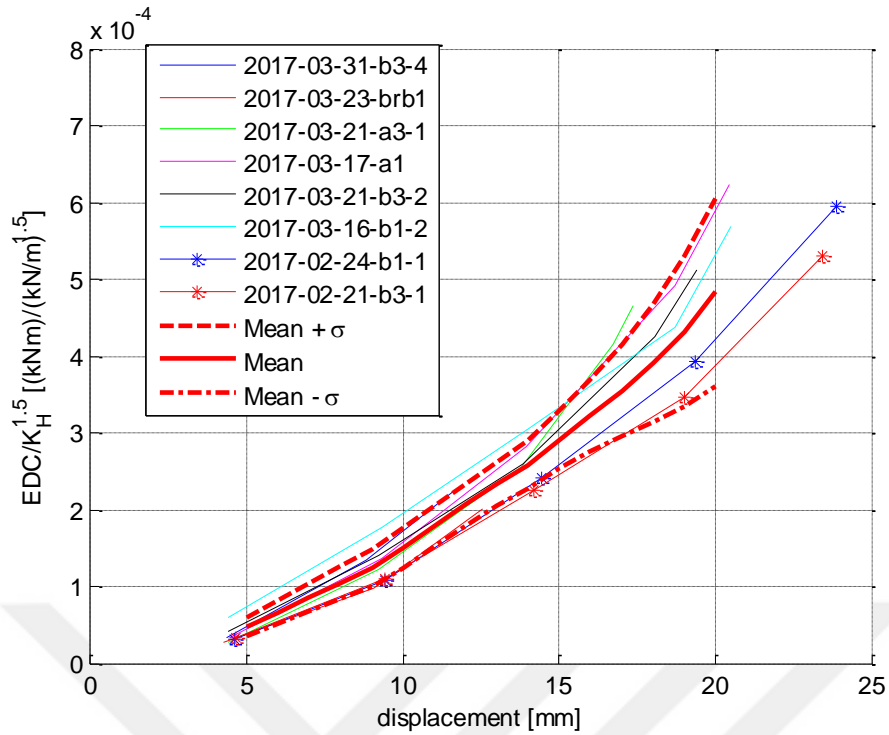


Figure 6-6. Formulation of EDC as a function of K_h and d , with mean and standard deviation curves

In the next step, power function (pow) and second order polynomial function (poly2) fits are applied to the three curves (mean+ σ , mean and mean- σ) as presented in Figure 6-7. It is observed that poly2 fits are better than pow fits, and these fits are used in the design formulations given in Figure 6-8.

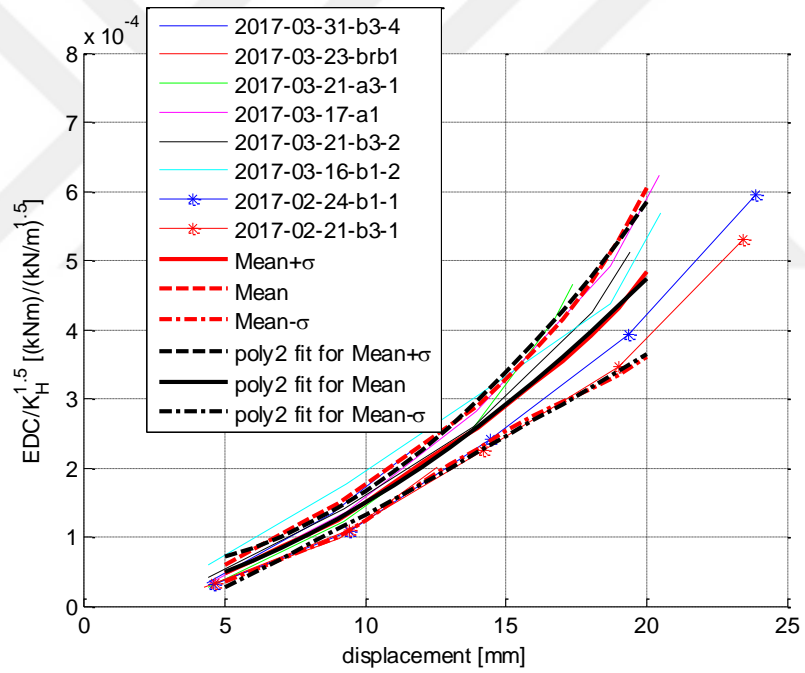
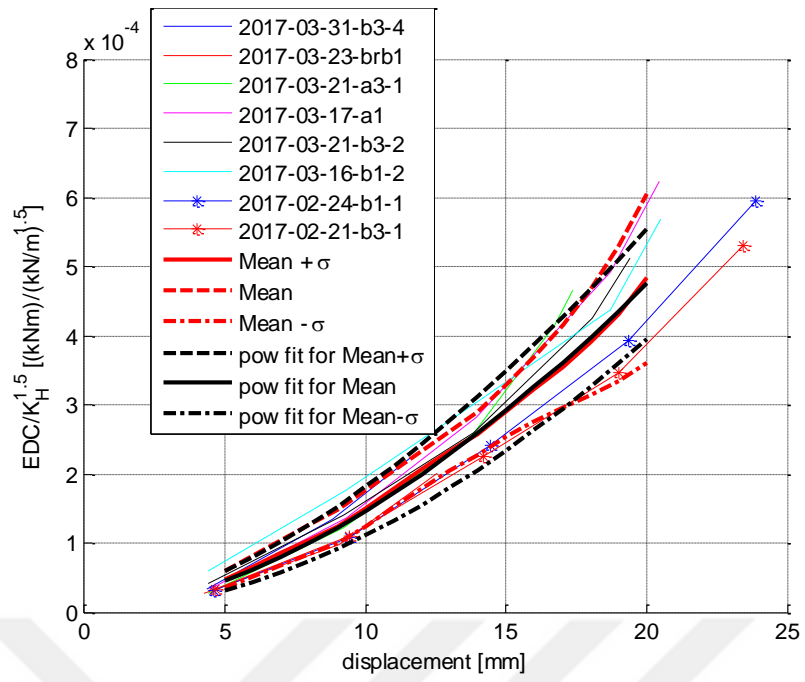


Figure 6-7. Formulation of EDC as a function of K_h and d , with pow (top) and poly2 (bottom) fits for mean and standard deviation curves

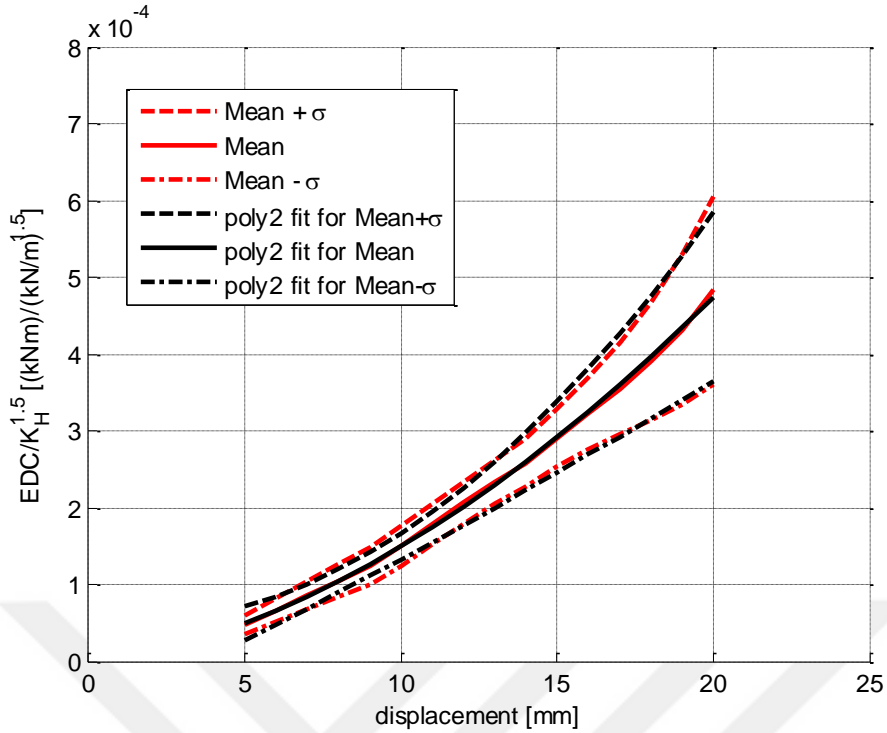


Figure 6-8. Formulation of EDC as a function of K_h and d , with poly2 fits for mean and standard deviation curves

The coefficients of second order polynomial fits used in design formulations are given in equations (55) to (57).

$$EDC(K_h, d) = K_h^{1.5} (1.5173 \cdot 10^{-6} \cdot d^2 - 3.7681 \cdot 10^{-6} \cdot d + 5.2637 \cdot 10^{-5}) \quad [r^2 = 0.99627, \text{mean} + \sigma] \quad (55)$$

$$EDC(K_h, d) = K_h^{1.5} (8.193 \cdot 10^{-7} \cdot d^2 + 7.8596 \cdot 10^{-6} \cdot d - 1.0681 \cdot 10^{-5}) \quad [r^2 = 0.99926, \text{mean}] \quad (56)$$

$$EDC(K_h, d) = K_h^{1.5} (1.213 \cdot 10^{-7} \cdot d^2 + 1.9487 \cdot 10^{-5} \cdot d - 7.3998 \cdot 10^{-5}) \quad [r^2 = 0.99686, \text{mean} - \sigma] \quad (57)$$

These formulations are an acceptable approximation for the device performance parameters.

6.2.2 Effective stiffness (K_{eff})

6.2.2.1 Analysis of experimental data

The second parameter of paramount importance is K_{eff} . Its values are plotted against displacement for all the test data in Figure 6-9.

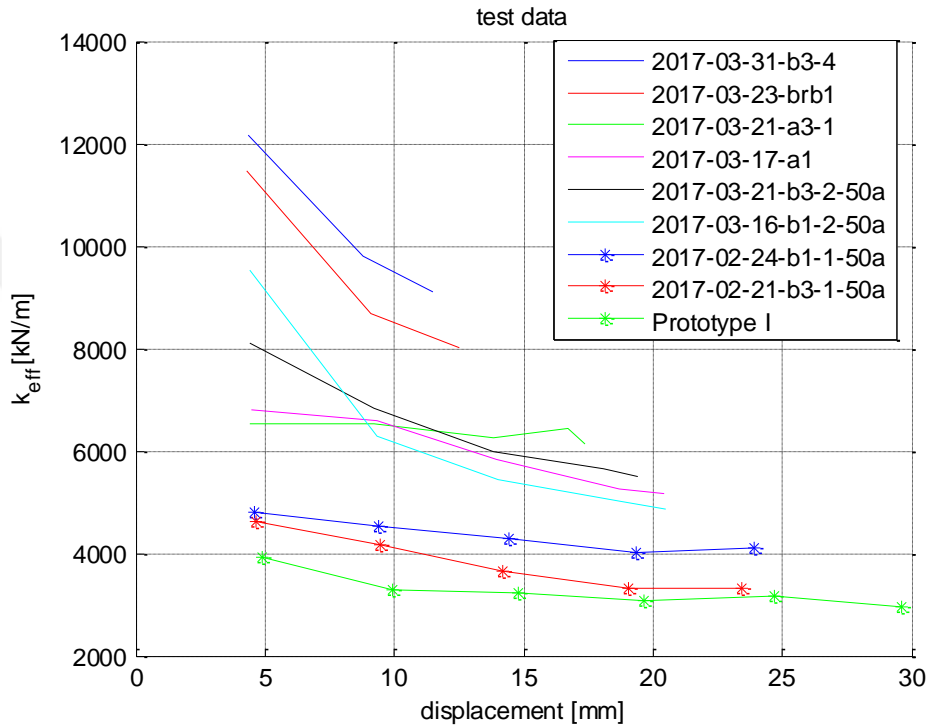


Figure 6-9. K_{eff} vs displacement

As expected, again the curves are grouped into three clusters corresponding to the EBs horizontal stiffness with the stiffest on top. Similar to EDC , K_{eff} is also directly proportional with EB's K_h . The Backbone damper effective stiffness decreases with increasing input displacement. This may be attributed to the decrease in EB's horizontal and vertical stiffness under increasing lateral displacements. Another observation from the plot is that for higher horizontal stiffness values of EB, the rate of decrease in damper effective stiffness is larger. The effective stiffness of BRB is much rapidly reduced under increasing displacement compared to B3-2 and even more compared to B3-1.

The decrease in stiffness has a beneficial effect on damper performance in the sense that the damper forces transferred to supporting structural members are reduced. And the reduction in K_{eff} under larger displacements limits the damper forces.

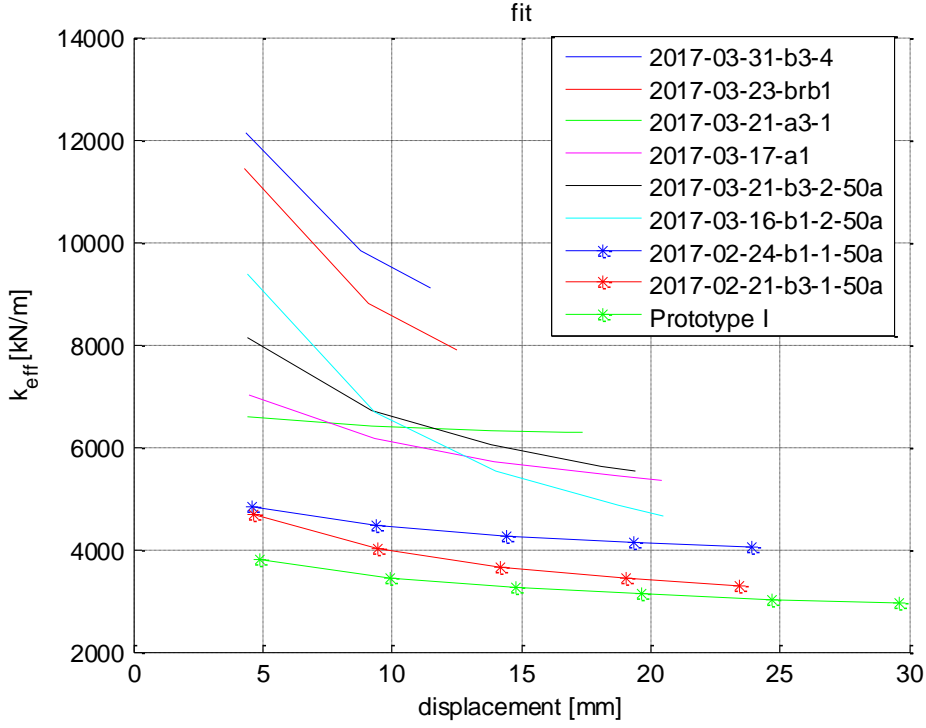


Figure 6-10. Power functions fitted to K_{eff} vs displacement curves

6.2.2.2 Upper and lower bound estimations

Similar to *EDC* estimations, K_{eff} curves for different EB configurations are normalized with powers of their shear stiffness (K_h) values as in Figure 6-11. The most compact form of normalized curves is observed for a power of 1.5 and this value is used in further estimation steps.

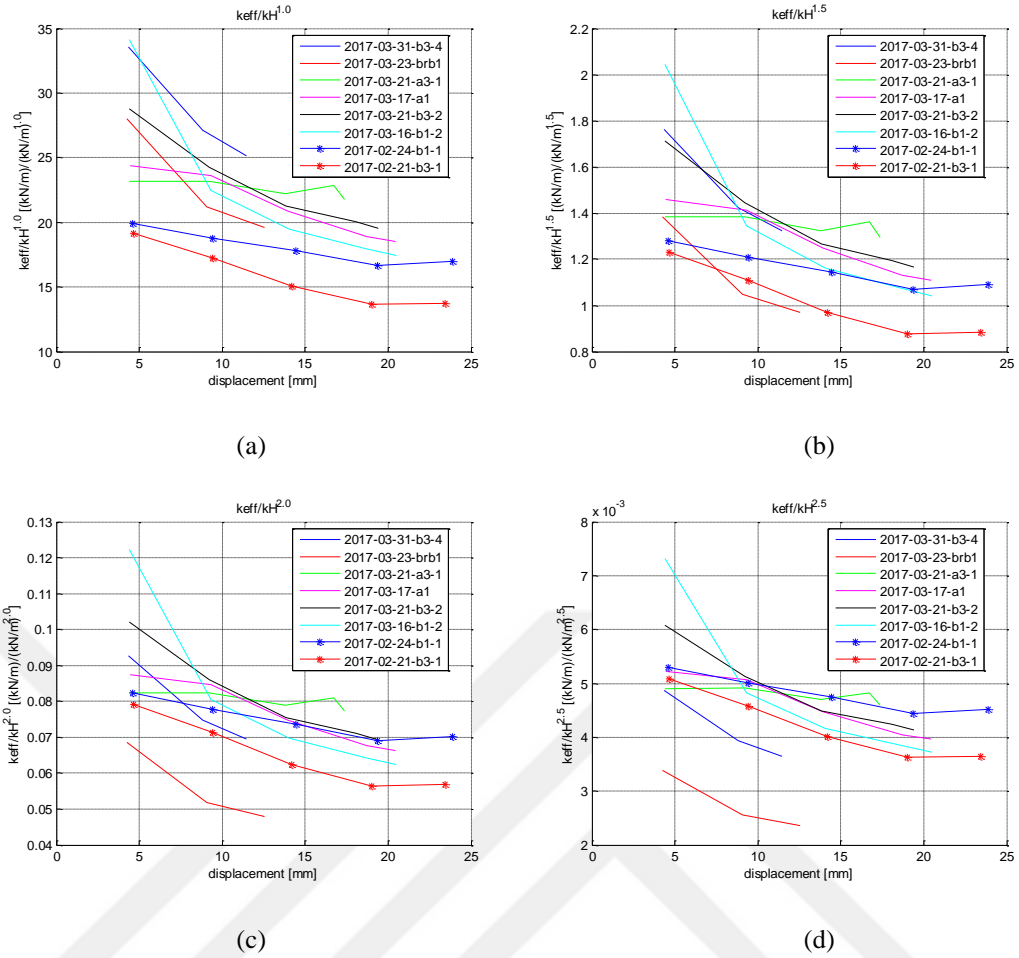


Figure 6-11. Candidate K_{eff} curves normalized by (a) K_h ; (b) $K_h^{1.5}$; (c) K_h^2 and (d) $K_h^{2.5}$

Mean and standard deviation curves are plotted on normalized K_{eff} curves as shown in Figure 6-12. Power fits and second order polynomial fits are performed for mean and standard deviation curves. It is observed that power fits represent the mean and standard deviation curves better than the poly2 fits. These fits are used in design formulations for K_{eff} .

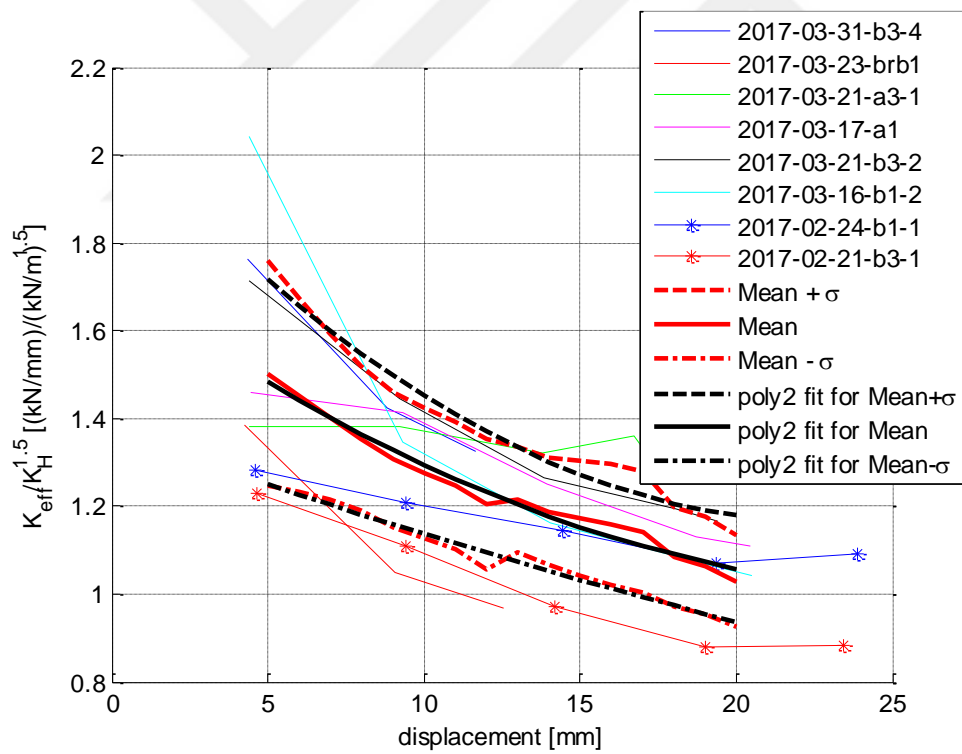
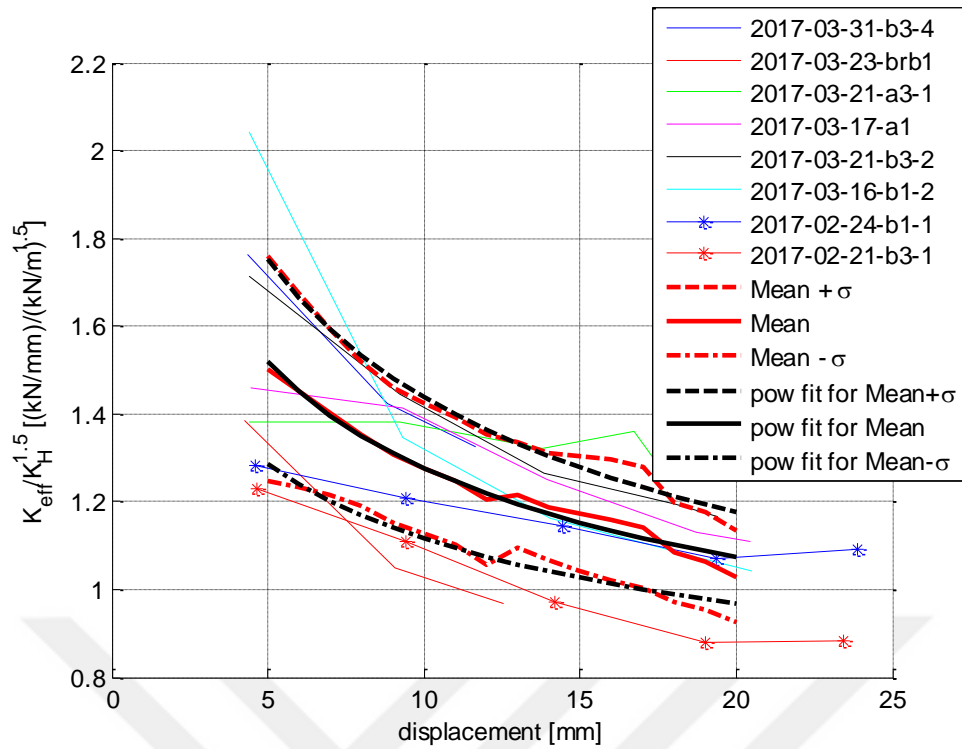


Figure 6-12. Formulation of K_{eff} as a function of K_h and d with pow (top) and poly2 (bottom) fits for mean and standard deviation curves

The equations with the power fits have been derived as follows:

$$K_{eff}(K_h, d) = K_h^{1.5}(2.7879 \cdot d^{-0.28786}) \quad (58)$$

$$[r^2 = 0.98252, mean + \sigma]$$

$$K_{eff}(K_h, d) = K_h^{1.5}(2.2771 \cdot d^{-0.25132}) \quad (59)$$

$$[r^2 = 0.98062, mean]$$

$$K_{eff}(K_h, d) = K_h^{1.5}(1.789 \cdot d^{-0.20496}) \quad (60)$$

$$[r^2 = 0.94715, mean - \sigma]$$

6.3 Summary and conclusions

Examining the results of experimental data, the dependence of two important performance parameters, EDC and K_{eff} , on design parameters and displacement input has been analyzed. Both EDC and K_{eff} are observed to be not clearly dependent on type of EB. Increase in EB's shear stiffness, K_h , results in a proportional increase in both performance parameters. This dependence is formulated with a power function of order 1.5. An increase in EDC is observed for an increase in input displacement. Second order polynomial functions have been proposed for upper and lower bounds as well as for the mean value estimation of EDC depending on input displacement. A decrease in K_{eff} is recorded for increasing input displacement. Power functions of input displacement have been derived for predicting both the upper and lower bounds and the mean value of K_{eff} .

CHAPTER 7

ANALYSIS OF A HOSPITAL BUILDING EQUIPPED WITH BACKBONE DAMPERS

7.1 Introduction

In the current chapter, modification of the seismic performance of a selected structural system after adding Backbone dampers is investigated under selected ground motion records. The structural system is a reinforced concrete frame system, typical of hospital buildings in Turkey. To study the response for different structural properties, the system is analyzed for changing story numbers with all the other system properties remaining unchanged. Thereby, the building story numbers vary as 2, 4, 6, 8 and 10. The response is evaluated with nonlinear time history analyses under an ensemble of three earthquake ground motion records scaled to a design response spectrum.

7.2 Building in analysis

The hospital building in analysis has a typical column spacing of 8 meters in plan. The story height of the structure is 4.5 meters and the number of stories is 10. The structure has a slab thickness of 200 mm, column size of 900 x 900 mm and beam size of 600 x 700 mm. The framing system of the hospital is very typical compared to hospitals in Isparta, Izmir, Kocaeli, Manisa and Eskisehir.



Figure 7-1. A typical urban hospital complex in Turkey

Following the weak beam strong column design philosophy, the beams have been expected to reach their plastic moment capacities during design earthquake. In all analysis models, hysteretic moment-rotation elements in LARSA 4D have been used to model the plastic end zones of the beams. The backbone curve of these hysteretic springs is shown in Figure 7-2. The structural model of the hospital represents a selected part of the complex as shown in Figure 7-1. The model has 7 bays in long direction and 4 bays of slab in short direction. The equivalent viscous damping is assumed to be 3% of critical in each mode of vibration and modelled as Rayleigh damping. Nonlinear geometric effects are included in the NLTHAs.

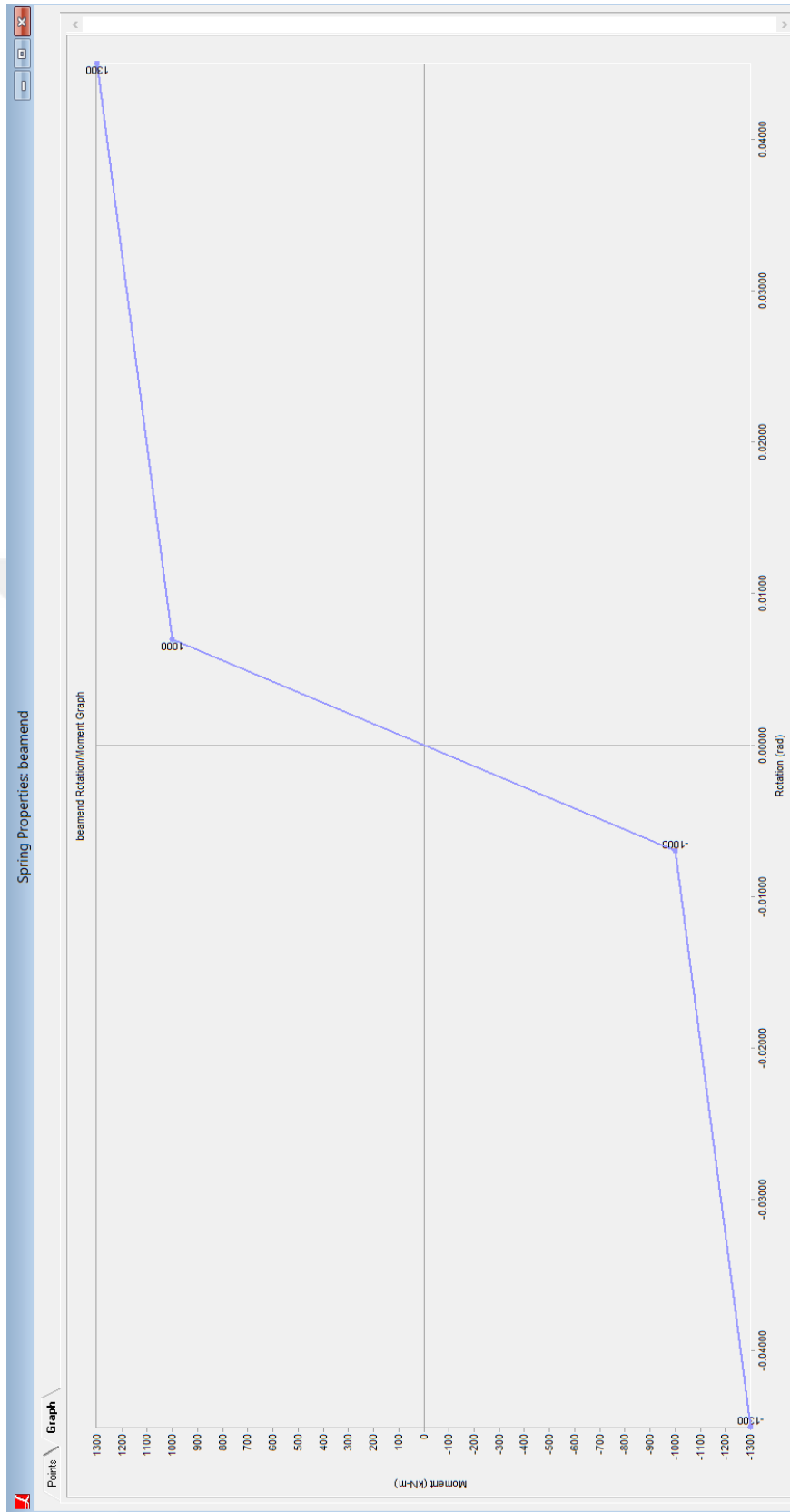


Figure 7-2. Moment vs rotation curve for beam end nonlinear (hysteretic) springs

All the analyses are run as staged construction analyses, i.e. first the gravity, then the live loads and finally the earthquake shaking is applied. This is to simulate the realistic way of loading on a building.

7.3 Backbone damper installation

The Backbone damper is modelled in LARSA4D interface as a hysteretic spring with the curve shown in Figure 7-3. The EDC and K_{eff} values are the parameters determining the points of the damper hysteretic curve. Their values are determined from the prediction formulae given in Chapter 6 for $K_h = 838kN/m$. In order to have an estimate of the needed damper strokes, the structure is first analyzed without any dampers installed. As a result, the damper stroke is set to 100mm and the corresponding EDC is calculated from the curves fitted to test data, as explained in Chapter 6.

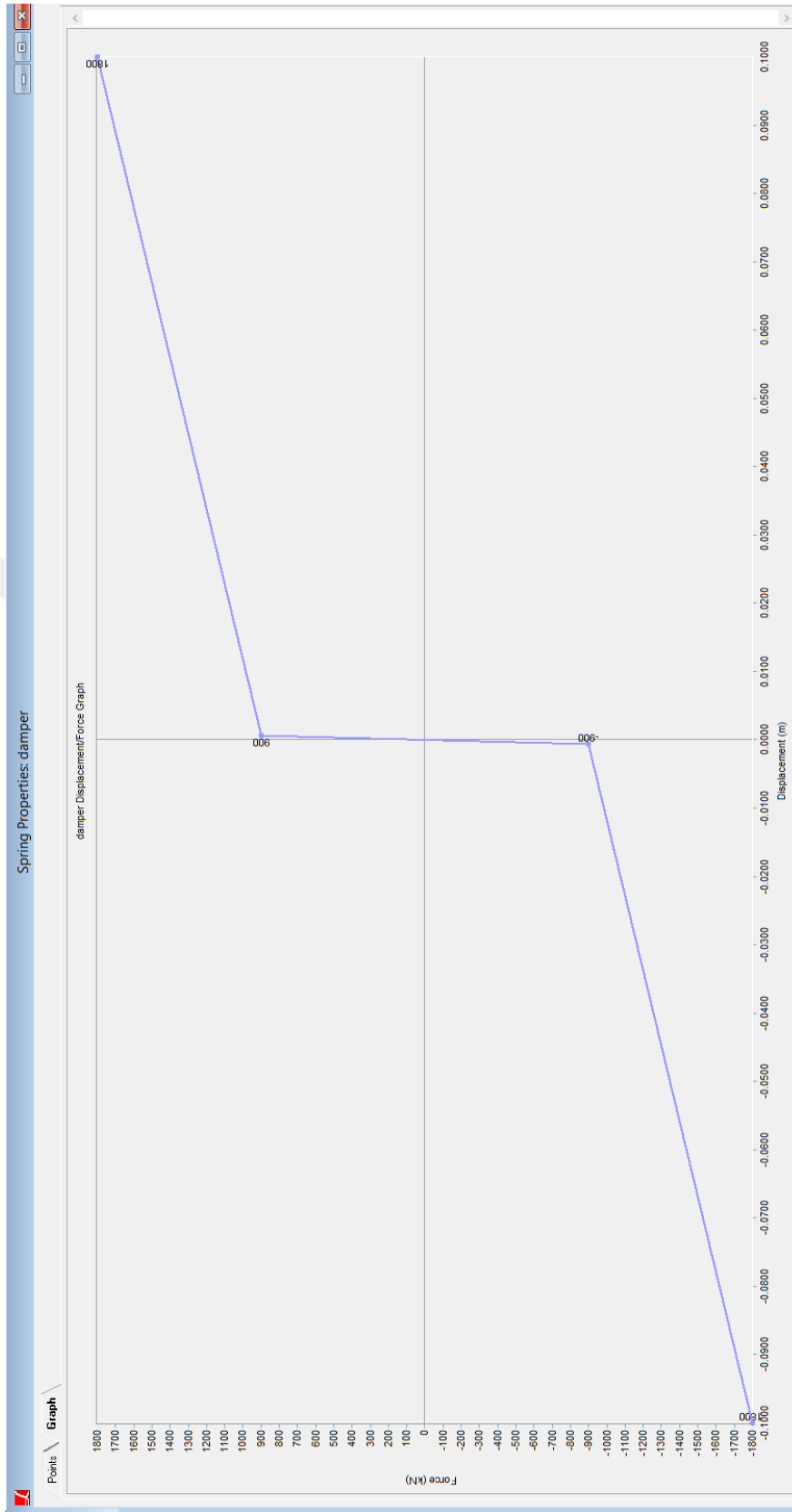
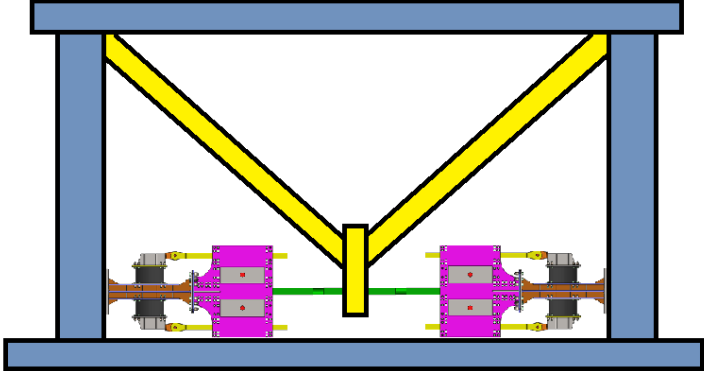


Figure 7-3. Backbone damper force-displacement curve as idealized in LARSA4D interface

Backbone dampers are installed in 4 bays in each direction of the building. The typical installation in a bay is shown in Figure 7-4. The damper-equipped buildings are presented against the original ones in Figure 7-5.



damper bay

Figure 7-4. Damper installation in a typical bay

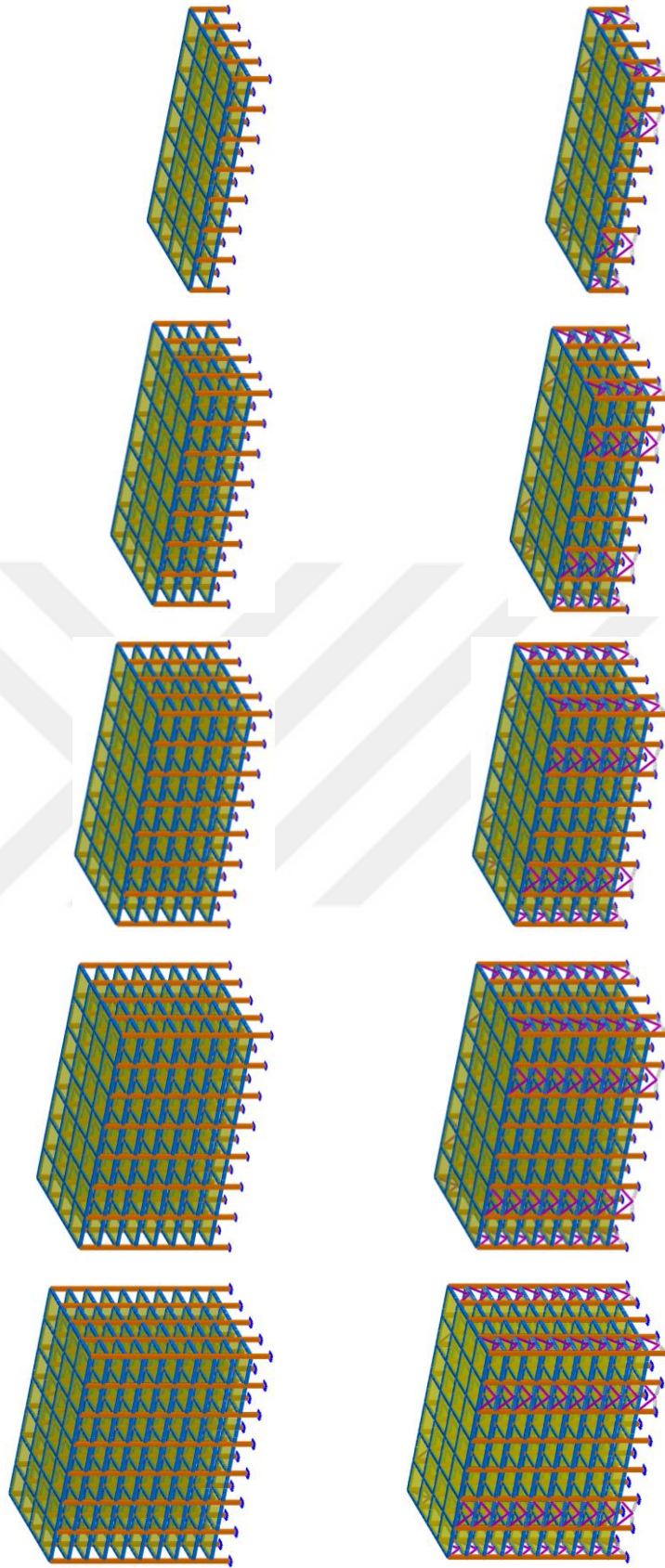


Figure 7-5. Analyzed building without (above) and with (below) dampers

7.4 Ground motion selection

Three earthquake records are selected for the nonlinear time history analyses. The results from the NLTHAs with these records are to illustrate the effect of Backbone damper on structural response depending on earthquake parameters without being able to draw on general conclusions. The aim is not to come up with general relations on damper performance and ground motion parameters but is rather to present the effect for selected cases. A detailed investigation covering more structural parameters and ground motion properties planned for a future research.

In the selection of the ground motions it is aimed to cover a larger band of possible parameters. In this sense, the three records differ in the distribution of their energy over the period band. Landers record has its energy distributed over a large period band, almost forming a plateau between 0.15s and 1.5s. El-Centro record also exhibits a fairly wide distribution of energy over the period axis, although not as pronounced as Landers. A “plateau” cannot be observed here, but yet the energy is not concentrated in a narrow period band. As for Kobe ground motion, it has a differentiated peak and its energy is distributed over a narrower band covering the lower end of the period spectrum. The difference between the characteristics of the ground motions can be seen from their SRSS spectra plotted in Figure 7-7.

They are all strong far-field earthquake motions selected from the far-field record set in FEMA P-695 [172], the smallest magnitude being 6.9. Their PGA values also differ, the ratio of Kobe/Landers being 2.0. The records’ summary is given in Table 7-1. Two perpendicular horizontal components for each record have been downloaded from PEER strong ground motion database [173].

Table 7-1. Records selected for the NLTHA

Record name	Magnitude	PGA _{max} (g)	Year	Recording station	Scale factor
Imperial Valley	6.95	0.28	1940	El Centro	1.36
Kobe	6.90	0.48	1995	Nishi-Akashi	1.33
Landers	7.28	0.24	1992	Yermo Fire Station	1.43

Each pair of motions is scaled as prescribed by Section 16.1.3.2 of ASCE 7-10 [174]. Hereby, the scale factors are determined such that in the period range from 0.2T to 1.5T, the average of the SRSS spectra of the selected earthquake ground motion records does not fall below the design response spectrum. Here, T is taken as the fundamental period of the 10-storey building. The parameters of the design response spectrum are determined per Section 11.4 of the same standard [174]. The calculation of the response spectrum parameters is explained in Appendix C and response spectrum is shown in Figure 7-6.

Seismic load combinations per [174] are created.

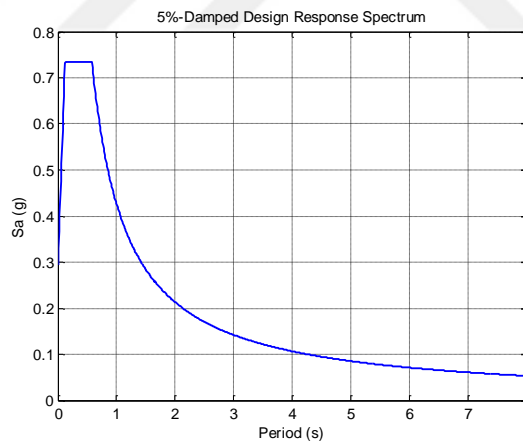


Figure 7-6. Target response spectrum

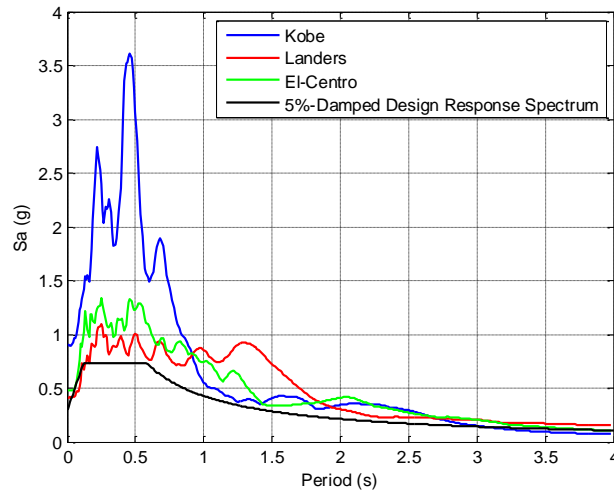


Figure 7-7. 5%-Damped SRSS spectra of selected ground motions (scaled)

7.5 Analysis results

The first step in system performance assessment is based on fundamental period estimation. Thereby, the dominant periods of the five buildings with and without dampers are calculated and tabulated in Table 7-2.

Table 7-2. Fundamental periods of investigated buildings with and without Backbone damper

	T_{1x} (s)		T_{1y} (s)		Reduction in T_1 (%)	
	no damper	with damper	no damper	with damper	X	Y
2-storey	0.368	0.224	0.365	0.215	39.16	41.10
4-storey	0.831	0.453	0.819	0.445	45.52	45.67
6-storey	1.325	0.730	1.304	0.718	44.88	44.94
8-storey	1.832	1.049	1.800	1.028	42.76	42.89
10-storey	2.345	1.400	2.300	1.364	40.31	40.70

The values in Table 7-2 show that the installation of dampers increases the system stiffness. The amount of reduction in period is significant, varying around 40% in average for all the cases. Re-centering dampers, like the one introduced through this study, provide recoverable damping while also contributing to system stiffness. With the increase in supporting (additional) stiffness, the equivalent damping ratio also

increases, i.e. the added dampers function [11]. Liang et al. [11] also report that every 10% of the damping added to the structure requires a supporting stiffness of about 100% of the structural stiffness. Thereby, the reported reduction in period is considered to be reasonable.

The three outstanding peaks of Kobe's SRSS spectrum are recorded at 0.22s, 0.46s and 0.7s. These correspond to the fundamental periods of the 2-, 4- and 6-storey buildings, respectively. This makes them more vulnerable under this record compared to the other structures. The buildings with more floors are less vulnerable under this earthquake record.

The peaks of El-Centro are not as pronounced as those of Kobe, yet the local peaks in the SRSS spectrum are at 0.17s, 0.25s, 0.46s, 0.8s, 1.2s. These may cause amplification in the response of 2-, 4- and 6-storey buildings.

The local peaks of Landers record are at 0.24s, 0.4s, 0.5s, 0.65s, 0.75s, 0.95s and 1.3s and thereby the record is expected to significantly excite all the analyzed buildings.

In this chapter, the detailed results for the 2- and 10-storey buildings under El-Centro record are presented. The detailed results of the remaining analyses are given in Appendix C. The findings from all the analyses are summarized and presented in a concise form at the end of this chapter so as to draw more general conclusions on the effect of Backbone dampers.

The peak values of response parameters are monitored to assess the change in response caused by installation of dampers. However, maximum displacement is not the only source of structural damage caused by earthquakes. Cumulative damage being the result of numerous inelastic cycles [175] can cause a low-cycle fatigue. This is expressed in failure of structural elements at deformation levels below the ultimate deformation capacity of the structure. This failure mode is caused by deterioration of the hysteretic behavior which is affected mainly by duration and referred to as cumulative damage. However, most current design methods do not consider effects of low-cycle fatigue. It provides a good estimate for the inelastic excursions and damage [176]. For the building without dampers, the response does not decay fast and the number of large-amplitude cycles is considerably high. To quantify this effect, root mean square values for the roof displacement, velocity and acceleration are calculated.

7.5.1 El-Centro earthquake ground motion

The acceleration-time plots of both orthogonal components of the record, as well as their Fourier amplitude spectra and elastic response spectra are summarized in Figure 7-8. The graphs show that the record's energy is spread over a comparatively wide frequency band.

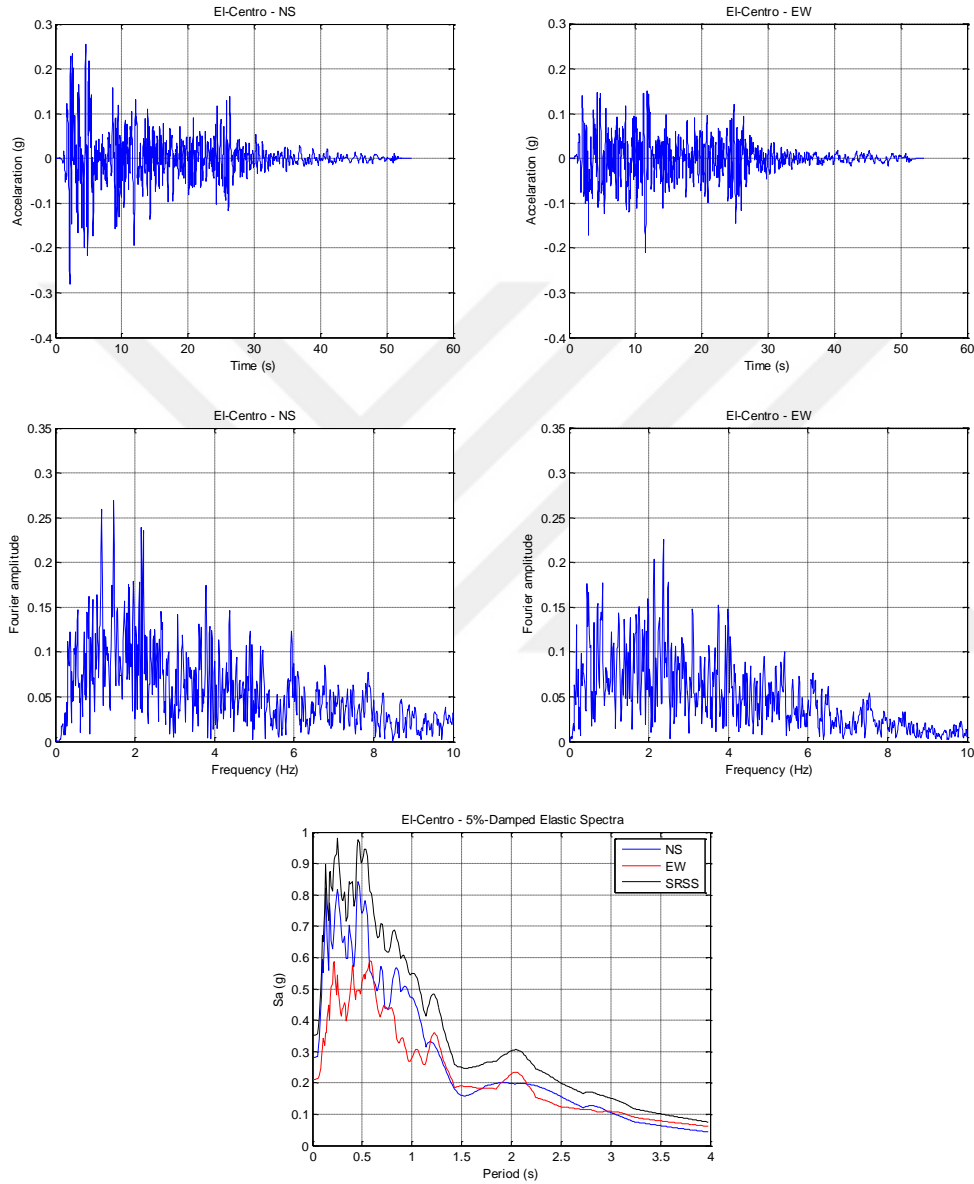


Figure 7-8. El-Centro earthquake record North-South (NS) and East-West (EW) components (unscaled)

The analyzed response parameters to illustrate the change in structure's response to seismic shaking after installation of Backbone dampers are the roof displacement, base shear vs roof displacement plot and interstory drifts.

7.5.1.1 2-storey building

Time histories of roof displacement are compared for the response with and without Backbone dampers. The graphs for both orthogonal directions are presented in Figure 7-9.

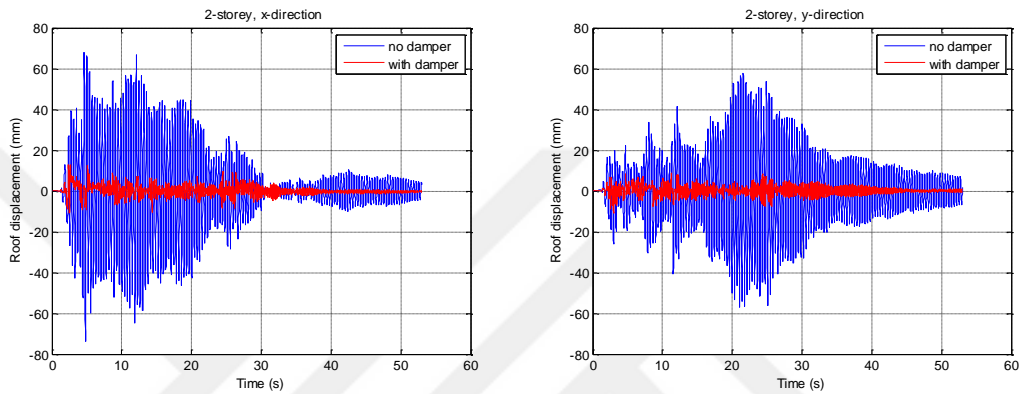


Figure 7-9. Roof displacement time histories in x and y directions of the 2-storey building under El-Centro earthquake record

In Figure 7-9, the level of reduction in displacement response can be clearly observed. The response of the damper-equipped structure is significantly mitigated both in terms of peak values and number of effective cycles.

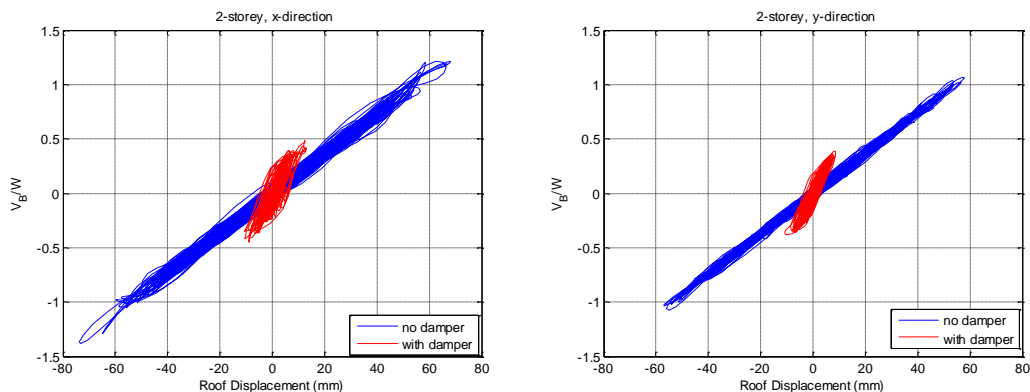


Figure 7-10. Base shear vs roof displacement plots in x and y directions of the 2-storey building under El-Centro earthquake record

In Figure 7-10, the base-shear (V_B) normalized by the system weight (W) is plotted against the roof displacement. The plots are indicative of the changes in the overall stiffness, displacement and base shear of the system with the installation of Backbone dampers. The graphs show the increase in stiffness which is reported from the decrease in period as well. Also, the significant reduction in base shear and roof displacement are underlined. The response curves of the damper-equipped structure are more stiff, concentrated and considerably shrunk.

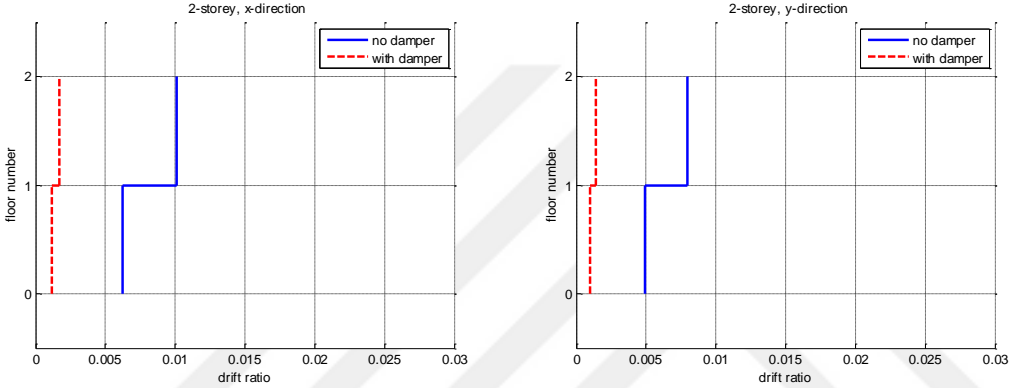


Figure 7-11. Drift ratio plots in x and y directions of the 2-storey building under El-Centro earthquake record

The accommodation of displacements within the structure is recorded with the plots of interstorey drift ratios given in Figure 7-11. The maximum interstorey drift ratio is the parameter most commonly related to the level of inelastic response and damage within the structure. Thereby, the reduction in IDR caused by dampers’ action can be interpreted as minimizing or even eliminating the inelastic performance of the structure. The maximum IDR plots of the damper-equipped building have considerably shifted to the left; moreover, the difference in the maximum IDR values of the floors has almost vanished, while being very prominent for the building without dampers.

All the above explained benefits are achieved with the small damper displacements given in Figure 7-12. Most probably it would not be the case if an amplification

mechanism were not integrated in the device. A common damper would maybe need twice the values presented in Figure 7-12 to provide the same effect as Backbone damper, which would reflect on the IDR ratios and other response parameters as well. This, emphasizes the advantage of the newly proposed damper.

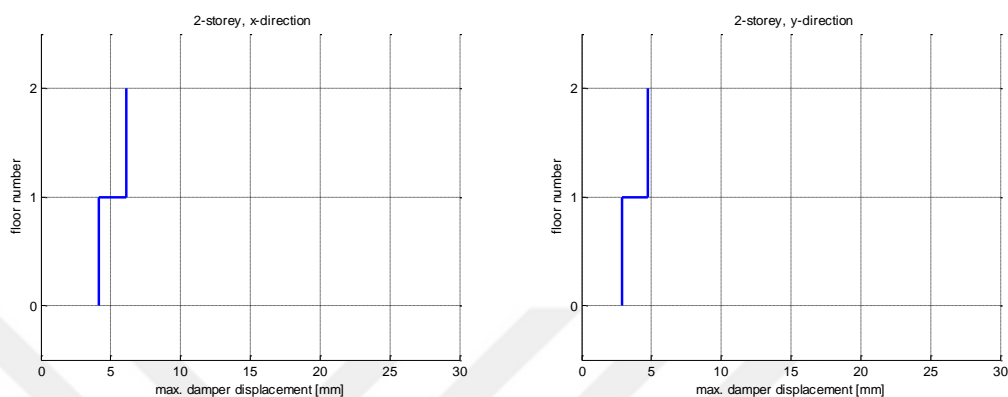


Figure 7-12. Plots of maximum damper displacement in x and y directions of the 2-storey building under El-Centro earthquake record

The reduction rates for displacement, velocity, acceleration and IDR are summarized in Table 7-3. The peak values of the response parameters are considered to estimate the maximum demand and root mean square is used to also include the time to decay in the response and the number of large cycles.

Table 7-3. Change in response parameters of the 2-storey building under El-Centro earthquake record

2-storey										
X-direction		no damper	with damper	reduction (%)		Y-direction		no damper	with damper	reduction (%)
disp (mm)	peak	73.70	12.93	82.5		disp (mm)	peak	57.76	10.66	81.5
disp (mm)	rms	20.40	2.57	87.4		disp (mm)	rms	18.31	2.32	87.3
disp (mm)	std	20.40	2.57	87.4		disp (mm)	std	18.31	2.31	87.4
vel (mm/s)	peak	1214.60	344.97	71.6		vel (mm/s)	peak	997.28	228.42	77.1
vel (mm/s)	rms	344.29	58.85	82.9		vel (mm/s)	rms	313.84	60.72	80.7
vel (mm/s)	std	344.29	58.85	82.9		vel (mm/s)	std	313.84	60.72	80.7
acc (mm/s ²)	peak	21053.47	13609.59	35.4		acc (mm/s ²)	peak	17668.03	9666.21	45.3
acc (mm/s ²)	rms	5858.70	2408.55	58.9		acc (mm/s ²)	rms	5416.97	2217.73	59.1
acc (mm/s ²)	std	5858.70	2408.55	58.9		acc (mm/s ²)	std	5416.97	2217.73	59.1
max idr		0.010	0.002	83.1		max idr		0.008	0.001	82.2
floor no		2	2			floor no		2	2	

The reduction in rms for each parameter is bigger than the reduction in peak value. This reflects the effective reduction in response over many cycles.

The forces developed by the dampers are accommodated by members of the parent structure. Therefore, the forces in the connected members need to be checked for the capacity not to be exceeded. To assess the effect of dampers on member forces, the maximum values of axial force, bending moments and shear forces in the connecting columns after the installation of dampers are normalized by their counterparts in the original structure. The ratios for all the columns are plotted in Figure 7-13. The forces are with respect to the global coordinate system.

It is observed from Figure 7-13 that the axial forces in columns increased by an order 40 to 90%. All the other force components are significantly reduced.

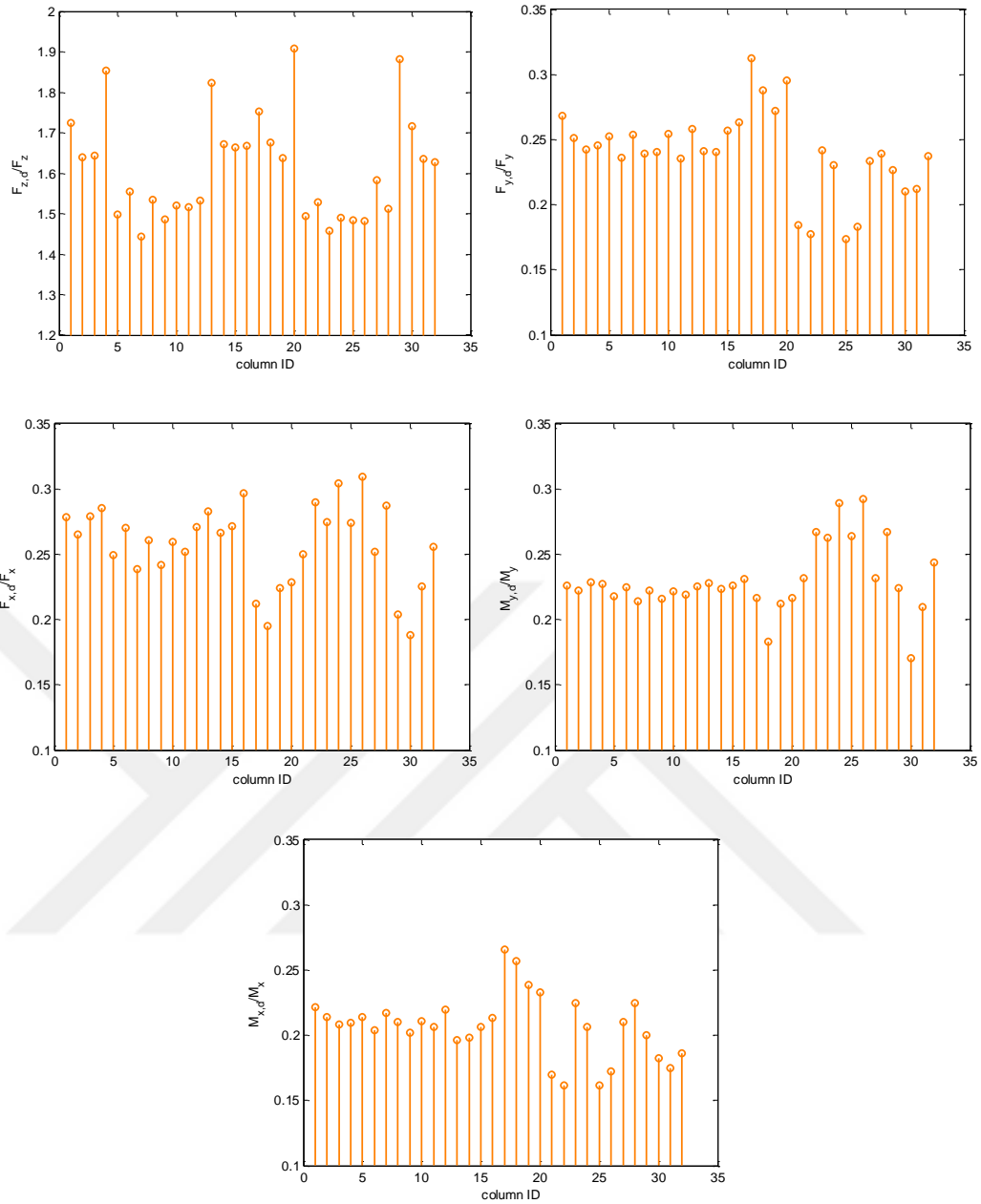


Figure 7-13. Forces in columns connected to dampers in the 2-storey building

In Figure 7-13:

F_z = column axial force (in global z direction) in the original structure

$F_{z,d}$ = column axial force (in global z direction) in the protected structure

F_x = column shear force in global x direction in the original structure

$F_{x,d}$ = column shear force in global x direction in the protected structure

F_y = column shear force in global y direction in the original structure

$F_{y,d}$ = column shear force in global y direction in the protected structure

M_x = column bending moment in global x direction in the original structure

$M_{x,d}$ = column bending moment in global x direction in the protected structure

M_y = column bending moment in global y direction in the original structure

$M_{y,d}$ = column bending moment in global y direction in the protected structure

7.5.1.2 10-storey building

The reduction in roof displacement with time can be seen from Figure 7-14. Again, the oscillations are effectively dampened out, but the reduction in peak response is smaller than for the 2-storey building.

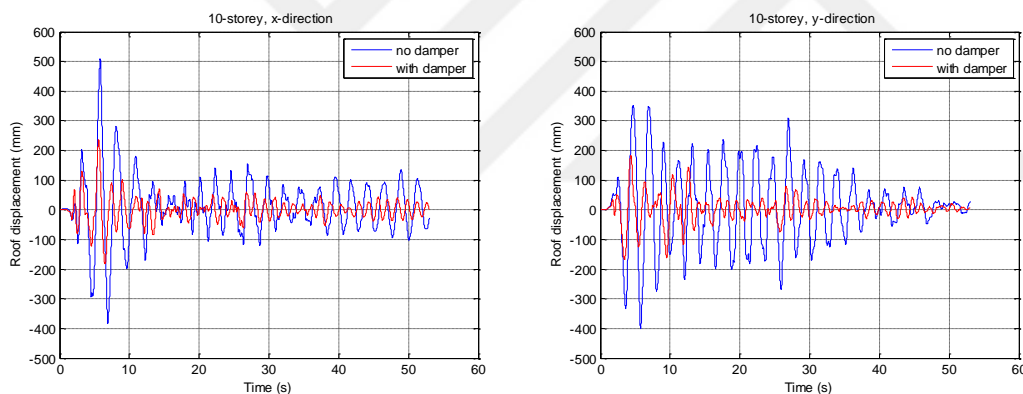


Figure 7-14. Roof displacement time histories in x and y directions of the 10-storey building under El-Centro earthquake record

Both the reduction in base shear and roof displacement can be observed from Figure 7-15. The plots are considerably different from their 2-storey counterparts. The difference is expressed in shape and reduction amount. The shapes imply the presence of nonlinearities in the system unlike the rather compact curve for the 2-storey case that recall of essentially elastic response. Yet, the curves of the damper-equipped building are characterized with less inelastic excursions.

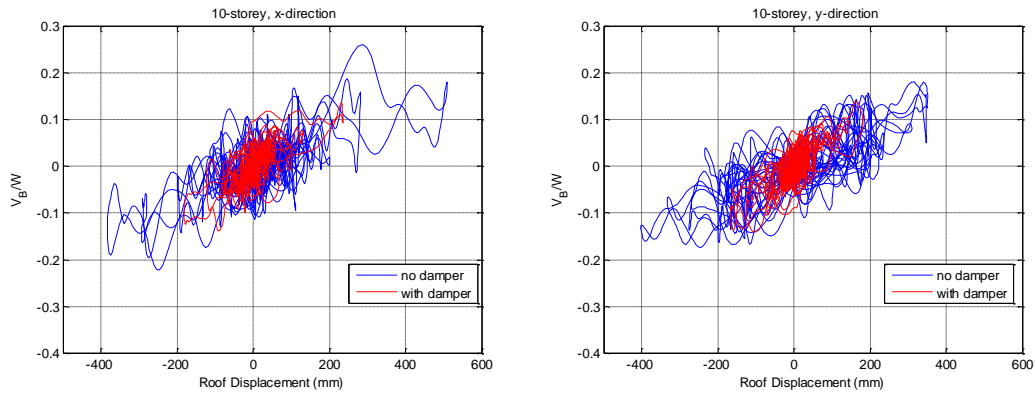


Figure 7-15. Base shear vs roof displacement plots in x and y directions of the 10-storey building under El-Centro earthquake record

The maximum interstory drift ratios are plotted in Figure 7-16. Again, a substantial reduction in values is expressed with a shift to the left, and not only. The pattern of the IDR plot is also changed with the installation of the dampers. The modified pattern is not as bulged as the initial one and the differences between the values of adjacent floors are reduced, which implies a more harmonic response. It should also be noted that that the reduction in maximum IDR is higher for the higher floors.

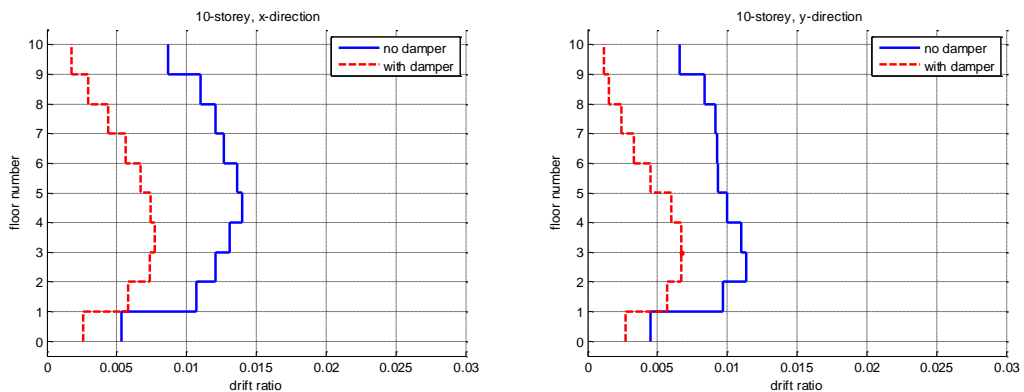


Figure 7-16. Drift ratio plots in x and y directions of the 10-storey building under El-Centro earthquake record

The patterns of the maximum IDR of Figure 7-16 repeat themselves in the maximum damper displacement graphs given in Figure 7-17, as expected. The largest damper displacements are observed at the lower floors. The biggest jump is predicted at the

second floor while the greatest displacement at the third one. After the third floor the damper displacements start decreasing. The pattern observed in Figure 7-17 is expected for the energy absorbed by dampers at each floor as well. The plot also shows the benefit from the dampers and their inclusion in the response control by floors. That is, the damper displacements of the last two floors are significantly smaller than the others and thus their contribution to the energy dissipation is limited. This analysis is very useful and necessary for the optimal placement and configuration of dampers.

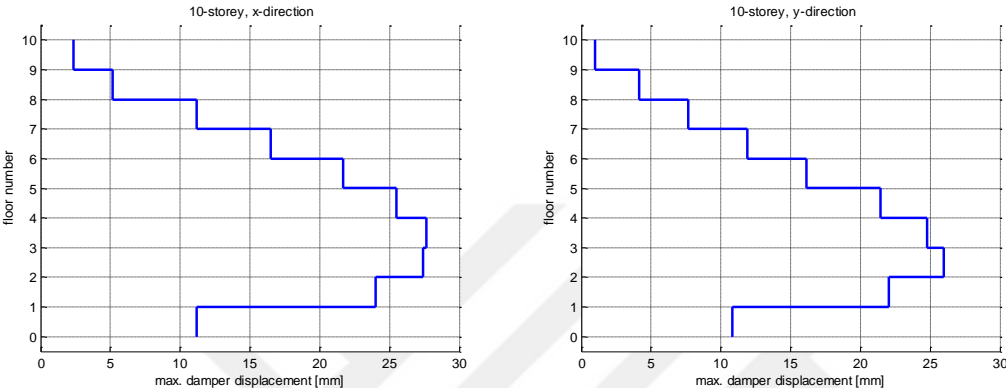


Figure 7-17. Plots of maximum damper displacement in x and y directions of the 10-storey building under El-Centro earthquake record

The change in system response induced by dampers is quantified with the response parameters summarized in Table 7-4. Again, a significant mitigation is predicted in terms of all parameters, the reduction being more pronounced for root mean square values of all the parameters.

Table 7-4. Change in response parameters of the 10-storey building under El-Centro earthquake record

10-storey									
X-direction		no damper	with damper	reduction %	Y-direction		no damper	with damper	reduction %
disp (mm)	peak	509.75	235.70	53.8	disp (mm)	peak	401.68	183.38	54.3
disp (mm)	rms	99.30	41.52	58.2	disp (mm)	rms	126.41	42.39	66.5
disp (mm)	std	98.77	41.52	58.0	disp (mm)	std	126.01	42.26	66.5
vel (mm/s)	peak	1439.46	757.97	47.3	vel (mm/s)	peak	1193.14	670.08	43.8
vel (mm/s)	rms	306.85	175.64	42.8	vel (mm/s)	rms	387.91	161.51	58.4
vel (mm/s)	std	306.85	175.64	42.8	vel (mm/s)	std	387.91	161.51	58.4
acc (mm/s ²)	peak	10521.66	9655.80	8.2	acc (mm/s ²)	peak	8979.22	7165.79	20.2
acc (mm/s ²)	rms	2529.80	1428.99	43.5	acc (mm/s ²)	rms	2356.84	1337.22	43.3
acc (mm/s ²)	std	2529.80	1428.99	43.5	acc (mm/s ²)	std	2356.84	1337.22	43.3
max idr		0.014	0.008	44.9	max idr		0.011	0.007	40.7
floor no		5	4		floor no		3	3	

7.5.1.3 Summary of analysis results for El-Centro record

Results from nonlinear time-history analyses of all the five buildings are summarized in Figure 7-18 and Figure 7-19.

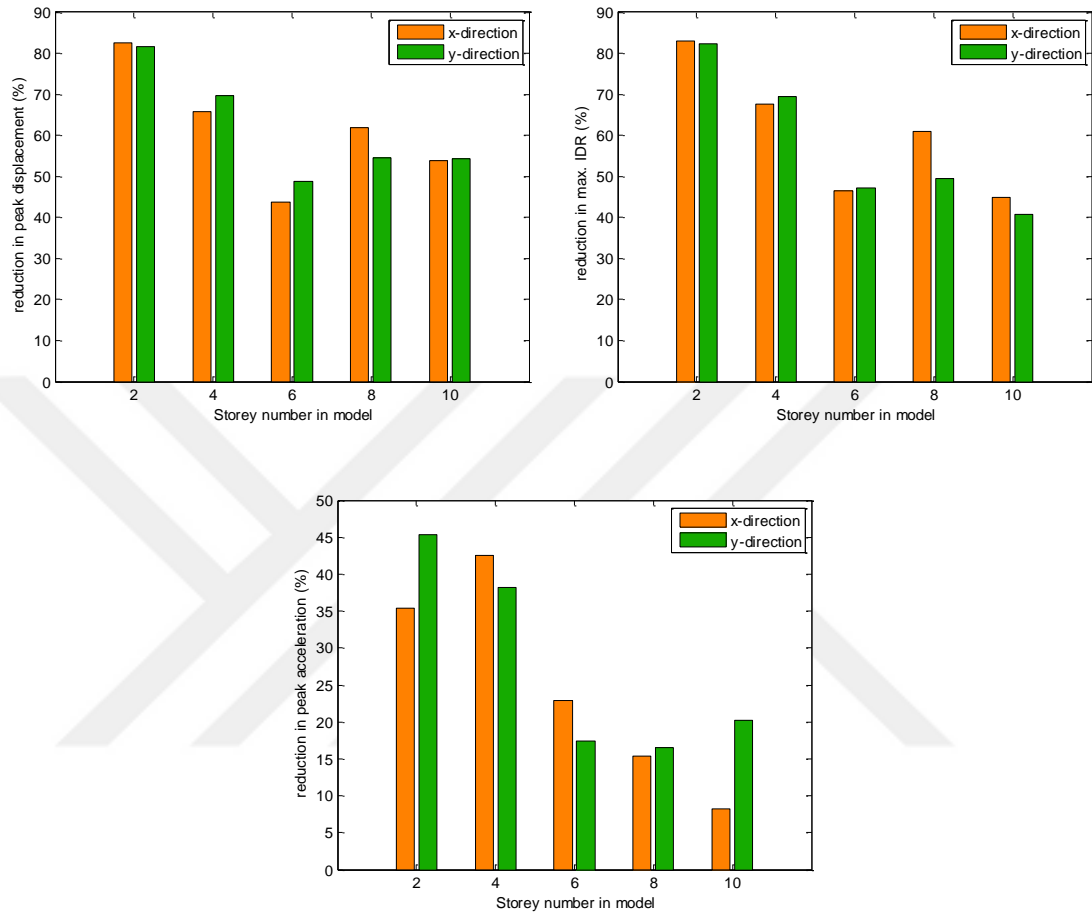


Figure 7-18. Reduction in peak response parameters for different models under El-Centro earthquake record after Backbone damper installation

The highest reduction in the peak values of displacement, IDR and acceleration is predicted for the 2- and 4-storey buildings. The smallest decrease in displacement and IDR is observed for the 6-storey building, where the reduction in peak displacement is 44% and 49% in x and y directions, respectively, which is still a significant improvement in response.

The drop in reduction rate is more pronounced for accelerations than for the other parameters.

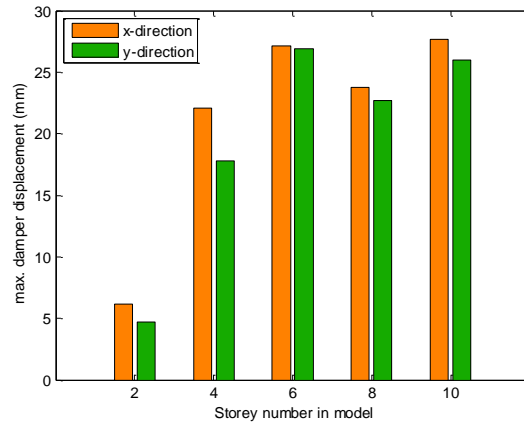


Figure 7-19. Maximum damper displacement for different models under El-Centro earthquake record

A general trend in the damper displacement cannot be concluded from Figure 7-19. The damper displaces proportionally to the number of stories (and consequently fundamental period) till the 6-storey building. The largest jump is predicted for the 4-storey building. These three buildings are in the resonance range of the earthquake frequencies.

The above-presented analysis findings indicate that the response modification caused by the damper is dependent on the initial structural properties. Yet, it is also dependent on the excitation record. To investigate the importance of ground motion parameters for the combined system performance, all the 5 structures are analyzed under Kobe and Landers records as well, and the results are presented next. The current installation of dampers, proven to provide satisfactory performance under El-Centro record, may not be the proper solution for earthquake protection under different seismic hazard conditions and might need an optimization.

7.5.2 Summary of all analysis results

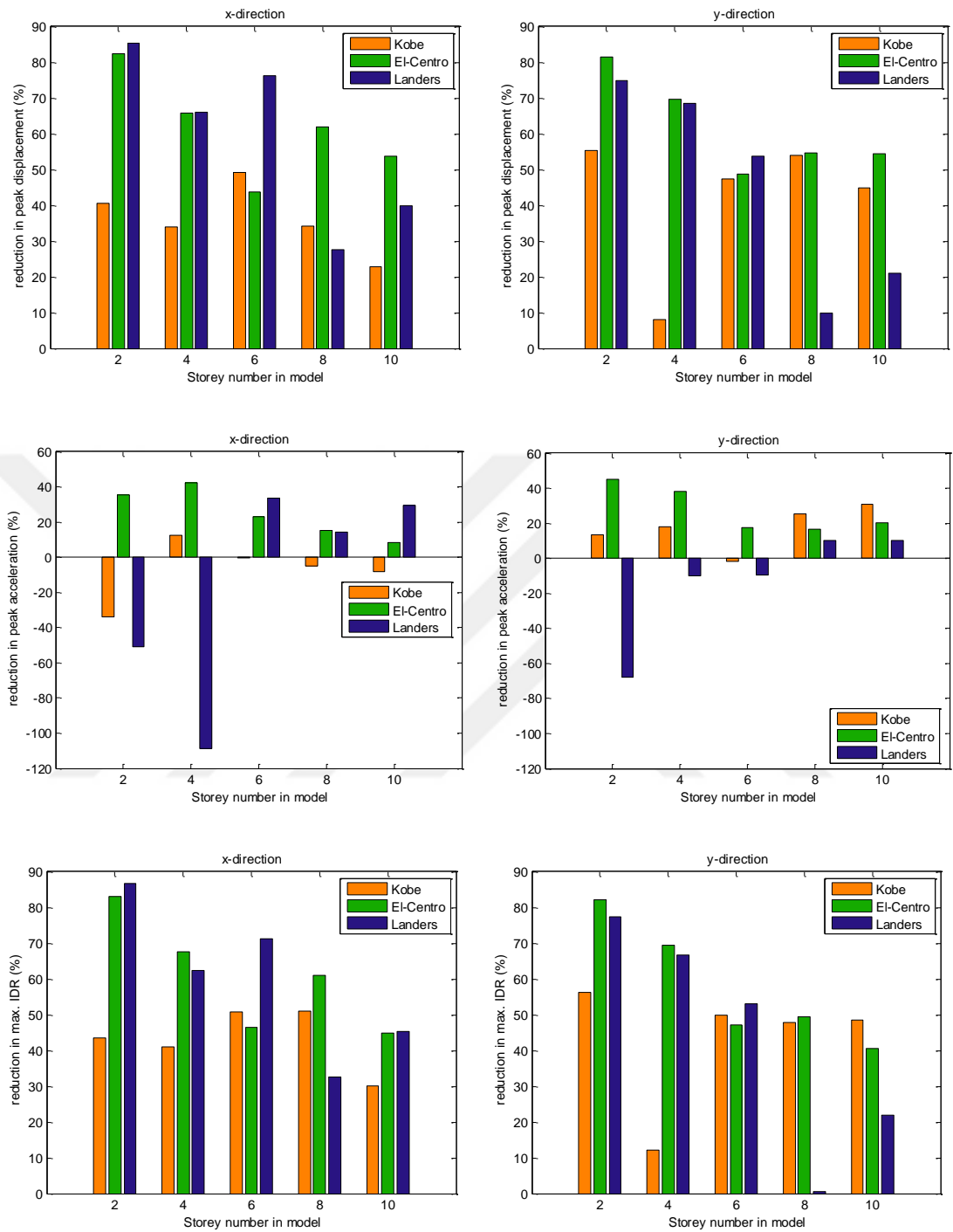


Figure 7-20. Reduction in peak response parameters under selected ground motions after Backbone damper installation

The effect of reduction in structural response is most pronounced in the resonance zone of the response. Therefore, the greatest reduction for 2-, 4- and 6-storey buildings is observed under Landers which excites all the systems.

Under El-Centro record, the damper is more effective in reducing the displacements rather than accelerations. In all the structures both response parameters are considerably reduced. The highest level of control is predicted for the 2- and 4-storey buildings, the reduction amount in each direction being more 70% for displacements and over 40% for accelerations. For the other buildings, reduction exceeds 50% for peak displacements and 10% for accelerations.

Under Kobe record, peak displacements are reduced but for some structures accelerations are amplified. This is most significant in the x direction of the 2-storey building, reaching almost 34%. This indicates that the ratio between the stiffness and damping added to the structure by the dampers is not optimal for the case and need to be further iterated. For the next iteration step, the added stiffness need to be reduced and damping increased. This can be achieved either through change in installation configuration or damper properties, or both.

As for Landers, reduction in displacements is too high for the 2-, 4- and 6-storey buildings but at the same time an increase in accelerations is predicted. Considering that both stiffness and damping are effective in displacement control while only the increase in damping is efficient in the mitigation of accelerations, it can be concluded that stiffness need to be reduced and damping increased to achieve more balanced response parameters, as in the case of Kobe. The same changes in supplemental damping system design can be made and if this cannot improve the performance, considering that the amplification in accelerations is more dramatic compared to Kobe, another seismic protection technology can be used. For the 8- and 10-storey buildings the decrease in displacements is smaller but accelerations are also reduced in both directions. The reduction of 10% in the y-direction peak displacement need to be increases as well. Therefore, damping may be further increased to improve the performance.

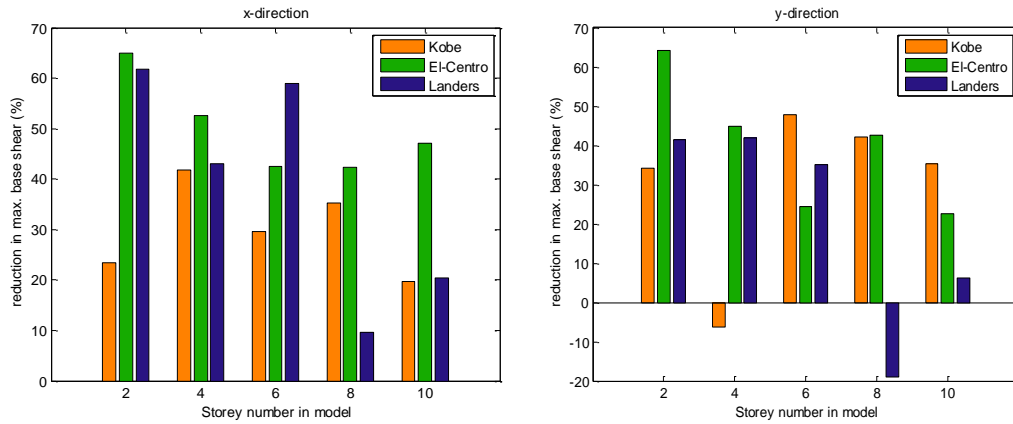


Figure 7-21. Reduction in maximum base shear under selected ground motions after Backbone damper installation

It is seen from Figure 7-21 that with the installation of Backbone dampers, the base shear is considerably reduced in almost all the analyzed cases. This is an indication of the significant energy absorption by the dampers, which also notably reduce the fundamental period.

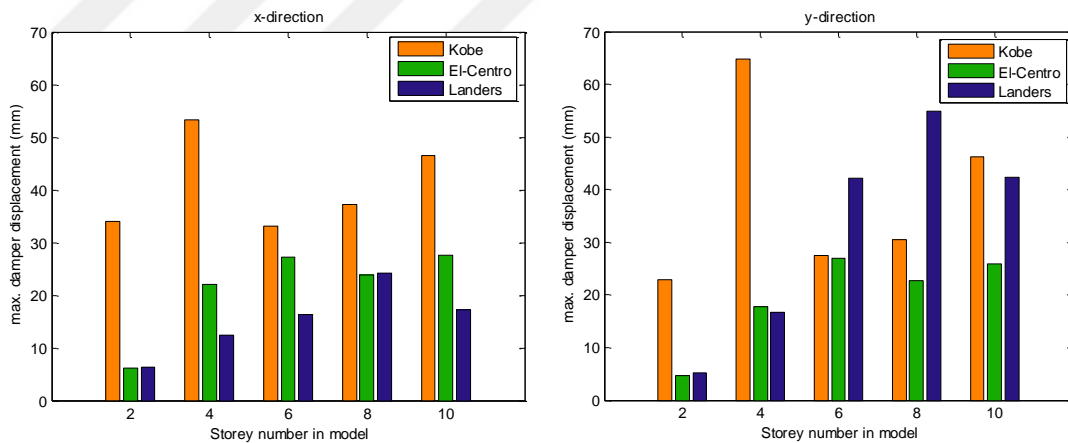


Figure 7-22. Maximum damper displacements under selected ground motions

The biggest damper displacements in x direction, as given Figure 7-22, are predicted for Kobe record. The peak in y direction being more than 60mm is expected again under Kobe ground motion. The installed dampers have the sufficient displacement capacity for all the buildings under the selected earthquake records.

7.6 Discussions and conclusions

The analysis results are limited by the small number of earthquake records. Therefore, the conclusions presented herein need to be verified with further analyses. Yet, based on the performed analyses, the following conclusions can be made:

The Backbone damper causes a significant reduction in the building period. Nevertheless, the base shear is reduced in all the analyzed cases. The damper can be an efficient tool for seismic structural control. It can effectively reduce the peak values of response parameters and the number of effective cycles, both determining the level of structural damage. The results indicate that the structural properties and the characteristics of the design ground motions need to be carefully assessed in the process of selecting the proper passive protection system. Although for a certain record it is possible to reduce all response parameters at the same time, for another record the reduction in displacements comes with an increase in acceleration. Optimization need to be performed including the seismic hazard, building properties, damper performance and the response objective. It should also be considered that reduction in more than one parameters can be contradicting objectives and a difficult task to realize.

CHAPTER 8

CONTRIBUTIONS, CONCLUSIONS AND RECOMMENDATIONS

8.1 Main contributions

A novel passive energy dissipation device for structural response control has been introduced. An application for the patent of the device has already been filed.

The device is innovative in manifold aspects:

- generation of displacement-dependent friction force easily scaled to structural application demands;
- integration of an internal displacement-dependent amplification mechanism;
- efficiently coupling multiple beneficial properties characterizing the most effective and advanced supplemental damping systems ((i) hybrid mechanism, (ii) re-centering capability and (iii) amplification of structural drift) into a single device at an affordable cost.

The device has a hybrid mechanism based on solid friction and dynamic straining of viscoelastic material. Therefore, it couples the advantages and exploits the potential of both friction and viscoelastic dampers. The advantages coming from friction dampers are:

- Increased energy dissipation;
- Properties not affected by excitation frequency and ambient temperature.

The strengths coming from viscoelastic dampers are:

- Effectiveness under all excitation levels;
- Re-centering force.

The frictional force component of the device is proportional to the input displacement. Here, it needs to be noted that a frictional force proportional to displacement is a highly desired yet very rarely achieved feature in the mechanical design of supplemental damping devices. Providing displacement-dependent frictional forces large enough to meet the force demands of civil engineering structures has been proposed, but not yet verified and implemented. Furthermore, the VE and frictional component are simultaneously activated, unlike other hybrid devices. This synchrony in behavior, together with both components being proportional to displacement, provides the re-centering capability of the damper.

Another innovative feature of Backbone damper is its integrated displacement amplification mechanism. The integration of the amplifier within the damper as its part has not been proposed before and brings some notable advantages:

- The device can be tested as a single unit and the effect of the amplification mechanism is included in the device performance parameters. In contrast, the complexity of the available amplifier configurations complicates the damper operation and introduces additional parameters affecting its performance. Thereby, the behavior of the Backbone damper can be predicted and controlled with a higher level of reliability compared to the response of dampers installed within available amplifier configurations.
- Ease of modelling - no need to model a complex bracing configuration.
- Ease of installation. The device is a compact apparatus with mechanically simple design that can easily be installed with conventional bracings.
- Low-cost production and installation. The Backbone damper can be produced and installed for less than the sources needed just for the amplifier brace configuration.

The integrated amplification mechanism can provide a displacement-dependent magnification ratio, which is another powerful feature of the introduced damper.

With all its novelties and advantages, the Backbone damper is considered as a contribution to the state-of-the-art and state-of-the-practice of passive structural control.

8.2 Conclusions

The novel Backbone damper has been investigated through experimental testing and numerical simulations. Full-size prototypes of the device have been produced and subjected to displacement-controlled dynamic tests with sinusoidal input. Eight different configurations of the viscoelastic unit have been tested, which enables investigating the relation between different design parameters. A detailed three-dimensional numerical model of the Backbone damper has been created in ABAQUS finite element software for the numerical simulations. The overall findings can be concluded as:

- The damper is characterized with a stable hysteretic behavior. Neither strength nor stiffness degradation is observed.
- The device EDC and K_{eff} are essentially independent of excitation frequency.
- The primary control parameters of the damper are the input displacement d and the horizontal stiffness of the elastomeric block K_h .
- Increase in displacement corresponds to an increase in EDC but decrease in K_{eff} .
- Larger K_h generates both larger EDC and K_{eff} . The coefficient of friction is expected to have the same effect.
- The behavior does not change and the device does not experience any damage after many fully reversed sinusoidal cycles. The number of cycles is around 100 for each EB and 800 for the amplification mechanism.
- Analytical formulations for EDC and K_{eff} depending on the main control parameters have been derived and can be used as a design guideline.
- The numerical model of the device is highly successful in predicting the damper behavior. The simulation result for K_{eff} matches the experimentally measured value while the EDC is underestimated by 7%.
- The Backbone damper is a mechanically simple device manufactured from readily available materials. Thereby, it can be produced at a relatively low cost.

- The Backbone damper can effectively improve the structural response to dynamic excitations. Optimization need to be performed considering the targeted response, the seismic hazard, building properties and damper features.

The final aim and contribution of the presented research can be divided in three main bodies: (1) development of a new patented passive supplemental damping device; (2) validation of its performance and (3) identification of design parameters and derivation of relationships to predict its response. These are considered as successfully completed within the framework and limitations of the presented doctoral research with recommendations for future studies on the topic.

8.3 Future work

All the conclusions presented herein are valid for the current tested geometry. The effect of variation in geometry in terms of

- tolerances between the case supports and the amplification mechanism components;
- moment arm values of the top adapter;
- change in the top adapter connection detailing

can be further investigated either through prototype testing or numerical simulations with the validated model.

Further topics for future research are:

- Preparation of a more detailed design guideline.
- Formulation of a constitutive relation for the hysteretic behavior of the device so as for it to be modelled more accurately.
- Experimental work covering testing a full-scale prototype installed on two- or three-dimensional frame structure.
- Estimation of device performance with high-damping rubber used for the elastomeric block.
- Optimization of device installation configurations.

- Development of a simplified model of the Backbone damper to facilitate its modelling in commonly used structural analysis programs.
- Inclusion of friction coefficient and EB's vertical stiffness within the relations for predicting device performance.
- Performing a detailed cost analysis of the device
- Detailed assessment regarding the effect of strong motion parameters on the seismic response of building with Backbone dampers.
- Further experimental testing under increased number of repeated reversed cycles.
- Further experimental testing under larger displacement magnitudes.



REFERENCES

- [1] Takagi, J., Tamura, K., and Wada, A., “Seismic Design of Big Cities,” in *Proc. 2017 NZSEE Conference, Wellington, New Zealand*, 2017.
- [2] Hare, J., Oliver, S., and Galloway, B., “Performance Objectives for Low Damage Seismic Design of Buildings,” in *Proc. 2012 NZSEE Conference*, 2012.
- [3] Mander, J. B. and Cheng, C. T., “Seismic Resistance of Bridge Piers Based on Damage Avoidance Design,” NCEER-97-0014, New York, 1997.
- [4] Erochko, J., Christopoulos, C., and Tremblay, R., “Design and Testing of an Enhanced-Elongation Telescoping Self-Centering Energy-Dissipative Brace,” *J. Struct. Eng.*, 141(6), pp. 1–11, 2015.
- [5] Kasai, K., Nakai, M., Nakamura, Y., Asai, H., Suzuki, Y., and Ishii, M., “Current Status of Building Passive Control in Japan,” in *Proc. 14th World Conference on Earthquake Engineering*, 2008.
- [6] Liu, R. and Palermo, A., “Low Damage Design and Seismic Isolation : What’s the difference?,” in *Proc. 2015 NZSEE Conference*, 2015.
- [7] Priestley, M. J. N., Calvi, G. M., and Kowalsky, M. J., *Displacement Based Seismic Design of Structures*. IUSS Press, Pavia, Italy, 2007.
- [8] Cheng, F., Jiang, H., and Lou, K., *Smart Structures: Innovative Systems for Seismic Response Control*. Taylor & Francis, Boca Raton, 2008.
- [9] Christopoulos, C. and Filiatrault, A., *Principles of Passive Supplemental Damping and Seismic Isolation*. IUSS Press, Pavia, Italy, 2006.
- [10] Takewaki, I., *Building Control with Passive Dampers: Optimal Performance-Based Design for Earthquakes*. John Wiley & Sons, Ltd, 2009.
- [11] Liang, Z., Lee, G. C., Dargush, G. F., and Song, J., *Structural Damping: Applications in Seismic Response Modification*. Taylor & Francis, Boca Raton,

- 2011.
- [12] Soong, T. T. and Dargush, G. F., *Passive Energy Dissipation Systems in Structural Engineering*. New York: John Wiley & Sons, Ltd, 1997.
- [13] Symans, M. D. *et al.*, “Energy Dissipation Systems for Seismic Applications: Current Practice and Recent Developments,” *J. Struct. Eng.*, 134(1), pp. 3–21, 2008.
- [14] Soong, T. T. and Spencer, B. F., “Supplemental energy dissipation: state-of-the-art and state-of-the-practice,” *Eng. Struct.*, 24(3), pp. 243–259, 2002.
- [15] Beards, C. F., *Structural Vibration: Analysis and Damping*. John Wiley & Sons, Inc., 1996.
- [16] Ribakov, Y. and Reinhorn, A. M., “Design of Amplified Structural Damping Using Optimal Considerations,” *J. Struct. Eng.*, 129(10), pp. 1422–1427, 2003.
- [17] Ahmed, A. M. A. S., Zasso, A., and Resta, F., “Proposed Configurations for the Use of Smart Dampers with Bracings in Tall Buildings,” *Smart Mater. Res.*, 2012, pp. 1–16, 2012.
- [18] Berton, S. and Bolander, J. E., “Amplification System for Supplemental Damping Devices in Seismic Applications,” *J. Struct. Eng.*, 131(6), pp. 979–983, 2005.
- [19] Elnashai, A. S. and Di Sarno, L., *Fundamentals of Earthquake Engineering: From Source to Fragility*, Second Edi. John Wiley & Sons, Ltd, 2015.
- [20] Pampanin, S., Christopoulos, C., and Nigel Priestley, M. J., “Performance-Based Seismic Response of Frame Structures Including Residual Deformations. Part II: Multi-Degree of Freedom Systems,” *J. Earthq. Eng.*, 7(1), pp. 119–147, 2003.
- [21] Ruiz-Garcia, J. and Miranda, E., “Residual Displacement Ratios for Assessment of Existing Structures,” *Earthq. Eng. Struct. Dyn.*, 35(3), pp. 315–336, 2006.
- [22] Bazzurro, P., Cornell, C. A., Menun, C., and Motahari, M., “Guidelines for Seismic Assessment of Damaged Buildings,” in *Proc. 13th World Conference on Earthquake Engineering*, 2004.

- [23] McCormick, J., Aburano, H., Ikenaga, M., and Nakashima, M., “Permissible Residual Deformation Levels for Building Structures Considering Both Safety and Human Elements,” in *Proc. 14th World Conference on Earthquake Engineering*, 2008.
- [24] Erochko, J., Christopoulos, C., Tremblay, R., and Choi, H., “Residual Drift Response of SMRFs and BRB Frames in Steel Buildings Designed according to ASCE 7-05,” *J. Struct. Eng.*, 137(5), pp. 589–599, 2011.
- [25] Pettinga, D., Christopoulos, C., Pampanin, S., and Priestley, N., “Effectiveness of Simple Approaches in Mitigating Residual Deformations in Buildings,” *Earthq. Eng. Struct. Dyn.*, 36(12), pp. 1763–1783, 2007.
- [26] Kasai, K., Mita, A., Kitamura, H., Matsuda, K., Morgan, T. A., and Taylor, A. W., “Performance of Seismic Protection Technologies during the 2011 Tohoku-Oki Earthquake,” *Earthq. Spectra*, 29(1), pp. 265–293, 2013.
- [27] Matta, E., “Effectiveness of Tuned Mass Dampers against Ground Motion Pulses,” *J. Struct. Eng.*, 139(2), pp. 188–198, 2013.
- [28] Lavan, O., “A Methodology for the Integrated Seismic Design of Nonlinear Buildings with Supplemental Damping,” *Struct. Control Heal. Monit.*, 22(3), pp. 484–499, 2015.
- [29] Ibrahim, Y. E., “A New Visco-Plastic Device for Seismic Protection of Structures,” Virginia Polytechnic Institute and State University, Blacksburg, VA, 2005.
- [30] Heysami, A., “Types of Dampers and Their Seismic Performance during an Earthquake,” *Curr. World Environ.*, 10(1), pp. 1002–1015, 2015.
- [31] Beheshti-Aval, S. B., Mahbanouei, H., and Zareian, F., “A Hybrid Friction-Yielding Damper to Equip Centrally Braced Steel Frames,” *Int. J. Steel Struct.*, 13(4), pp. 577–587, 2013.
- [32] Kim, J. and Shin, H., “Seismic Loss Assessment of a Structure Retrofitted with Slit-Friction Hybrid Dampers,” *Eng. Struct.*, 130, pp. 336–350, 2017.
- [33] Whittaker, A., Bertero, V., Alonso, J., and Thompson, C., “Earthquake Simulator Testing of Steel Plate Added Damping and Stiffness Elements,”

UCB/EERC-89/02, Berkeley, California, 1989.

- [34] Whittaker, A. S., Bertero, V. V., Thompson, C., and Alonso, J., “Seismic Testing of Steel Plate Energy Dissipation Devices,” *Earthq. Spectra*, 7(4), pp. 563–604, 1991.
- [35] Tsai, K. C., Chen, H. W., Hong, C. P., and Su, Y. F., “Design of Steel Triangular Plate Energy Absorbers for Seismic-Resistant Construction,” *Earthq. Spectra*, 9(3), pp. 505–528, 1993.
- [36] Basu, D. and Reddy, P. R. M., “A New Metallic Damper for Seismic Resilience: Analytical Feasibility Study,” *Structures*, 7, pp. 165–183, 2016.
- [37] Lee, M., Lee, J., and Kim, J., “Seismic Retrofit of Structures Using Steel Honeycomb Dampers,” *Int. J. Steel Struct.*, 17(1), pp. 215–229, 2017.
- [38] Nakashima, M., “Strain-Hardening Behavior of Shear Panels Made of Low-Yield Steel. I: Test,” *J. Struct. Eng.*, 121(12), pp. 1742–1749, 1995.
- [39] Foti, D., Diaferio, M., and Nobile, R., “Optimal Design of a New Seismic Passive Protection Device Made in Aluminium and Steel,” *Struct. Eng. Mech.*, 35(1), pp. 119–122, 2010.
- [40] Teruna, D. R., Majid, T. A., and Budiono, B., “Experimental Study of Hysteretic Steel Damper for Energy Dissipation Capacity,” *Adv. Civ. Eng.*, 2015, pp. 1–12, 2015.
- [41] Li, G. and Li, H., “Earthquake-Resistant Design of RC Frame with ‘Dual Functions’ Metallic Dampers,” in *Proc. 14th World Conference on Earthquake Engineering*, 2008.
- [42] Lee, H. M., Oh, H. S., Huh, C., Oh, S. Y., Yoon, H. M., and Moon, S. T., “Ultimate Energy Absorption Capacity of Steel Plate Slit Dampers Subjected to Shear Force,” *Steel Struct.*, 12, pp. 71–79, 2002.
- [43] Oh, S.-H., Kim, Y.-J., and Ryu, H.-S., “Seismic Performance of Steel Structures with Slit Dampers,” *Eng. Struct.*, 31(9), pp. 1997–2008, 2009.
- [44] Watanabe, A., Hitomi, Y., Saeki, E., Wada, A., and Fujimoto, M., “Properties of Brace Encased in Buckling-Restraining Concrete and Steel Tube,” in *Proc.*

- 9th World Conference on Earthquake Engineering, Tokyo-Kyoto, Japan, 1988.*
- [45] Iwata, M., “Application Design of Buckling Restrained Braces in Japan,” in *13th World Conference on Earthquake Engineering, 2004.*
- [46] Iwata, M. and Murai, M., “Buckling-Restrained Brace Using Steel Mortar Planks; Performance Evaluation as a Hysteretic Damper,” *Earthq. Eng. Struct. Dyn.*, 35(14), pp. 1807–1826, 2006.
- [47] Benavent-Climent, A., “A Brace-Type Seismic Damper Based on Yielding the Walls of Hollow Structural Sections,” *Eng. Struct.*, 32(4), pp. 1113–1122, 2010.
- [48] Atlayan, O. and Charney, F. A., “Hybrid Buckling-Restrained Braced Frames,” *J. Constr. Steel Res.*, 96(5), pp. 95–105, 2014.
- [49] Abebe, D. Y., Kim, J. W., and Choi, J. H., “Hysteresis Characteristic of Circular Pipe Steel Damper Using LYP 225,” in *Proc. Steel Innovation Conference, 2013.*
- [50] Suzuki, K., Watanabe, A., and Saeki, E., “Development of U-shaped Steel Damper for Seismic Isolation System,” NIPPON STEEL Technical Report No. 92, 2005.
- [51] Takayama, M. and Morita, K., “Ultimate Capacity of U-Shaped Lead Damper Used in Seismic Isolation System,” *AIJ J. Technol. Des.*, 2(3), pp. 48–52, 1996.
- [52] Bowden, F. P. and Tabor, D., *Friction: An Introduction to Tribology*. Anchor Press, Garden City, New York, USA, 1973.
- [53] Bhushan, B., *Introduction to Tribology*, Second Edi. John Wiley & Sons, Ltd, 2013.
- [54] Constantinou, M. C., Tsepelas, P., Kasalanati, A., and Wolff, E. D., “Property Modification Factors for Seismic Isolation Bearings,” Report No. MCEER-99-0012, Multidisciplinary Center for Earthquake Engineering Research, Buffalo, NY, 1999.
- [55] Pall, A. S. and Marsh, C., “Response of Friction Damped Braced Frames,” *J. Struct. Division, ASCE*, 108(ST6), pp. 1313–1323, 1982.
- [56] Filiatrault, A. and Cherry, S., “Performance Evaluation of Friction Damped

- Braced Steel Frames Under Simulated Earthquake Loads,” *Earthq. Spectra*, 3(1), pp. 57–78, 1987.
- [57] Aiken, I. D., Kelly, J. M., and Pall, A. S., “Seismic Response of a Nine-Story Steel Frame with Friciton Damped Cross-Bracing,” in *Proc. 9th World Conference on Earthquake Engineering*, 1988.
- [58] Wu, B., Zhang, J., Williams, M. S., and Ou, J., “Hysteretic Behavior of Improved Pall-Typed Frictional Dampers,” *Eng. Struct.*, 27(8), pp. 1258–1267, 2005.
- [59] FitzGerald, T. F., Anagnos, T., Goodson, M., and Zsutty, T., “Slotted Bolted Connections in Aseismic Design for Concentrically Braced Connections,” *Earthq. Spectra*, 5(2), pp. 383–391, 1989.
- [60] Grigorian, C. E., Yang, T. S., and Popov, E. P., “Slotted Bolted Connection Energy Dissipators,” *Earthq. Spectra*, 9(3), pp. 491–504, 1993.
- [61] Aiken, I. D. and Kelly, J. M., “Earthquake Simulator Testing and Analytical Studies of Two Energy-Absorbing Systems for Multistory Structures,” UCB/EERC-90/03, California, Berkeley, 1990.
- [62] Aiken, I. D., Nims, D. K., and Kelly, J. M., “Comparative Study of Four Passive Energy Dissipation Systems,” *Bull. New Zeal. Soc. Earthq. Eng.*, 25(3), pp. 175–192, 1992.
- [63] Nims, D. K., Richter, P. J., and Bachman, R. E., “The Use of the Energy Dissipating Restraint for Seismic Hazard Mitigation,” *Earthq. Spectra*, 9(3), pp. 467–489, 1993.
- [64] Xiyuan, Z. and Lingyun, P., “A New Type of Damper with Friction-Variable Characteristics,” *Earthq. Eng. Eng. Vib.*, 8(4), pp. 507–520, 2009.
- [65] Karr, R., Rainer, J. H., and Lefrancois, A. C., “Dynamic Properties of a Circuit Braker with Friction-Based Seismic Dampers,” *Earthq. Spectra*, 12(2), pp. 297–314, 1996.
- [66] Filiatrault, A., Tremblay, R., and Kar, R., “Performance Evaluation of Friciton Spring Seismic Damper,” *J. Struct. Eng.*, 126(4), pp. 491–499, 2000.

- [67] Christopoulos, C., Tremblay, R., Kim, H., and Lacerte, M., “Self-Centering Energy Dissipative Bracing System for the Seismic Resistance of Structures : Development and Validation,” *J. Struct. Eng.*, 134(1), pp. 96–107, 2008.
- [68] “Design and Testing of an Enhanced-Elongation Telescoping Self-Centering Energy-Dissipative Brace,” *J. Struct. Eng.*, 141(6), pp. 1–11, 2015.
- [69] Mualla, I. H. and Belev, B., “Performance of Steel Frames with a New Friction Damper Device under Earthquake Excitation,” *Eng. Struct.*, 24(3), pp. 365–371, 2002.
- [70] Cho, C. G. and Kwon, M., “Development and Modeling of a Frictional Wall Damper and Its Applications in Reinforced Concrete Frame Structures,” *Earthq. Eng. Struct. Dyn.*, 33(7), pp. 821–838, 2004.
- [71] Morgen, B. G. and Kurama, Y. C., “A Friction Damper for Post-Tensioned Precast Concrete Moment Frames,” *PCI J.*, 49(4), pp. 122–133, 2004.
- [72] Martínez, C. A. and Curadelli, O., “Testing and Performance of a New Friction Damper for Seismic Vibration Control,” *J. Sound Vib.*, 399(7), pp. 60–74, 2017.
- [73] Shen, S., Pan, P., Sun, J., Gong, R., and Wang, H., “Development of a Double-Sliding Friction Damper (DSFD),” *Smart Struct. Syst.*, 20(2), pp. 151–162, 2017.
- [74] Constantinou, M. C., Symans, M. D., Tsepelas, P., and Taylor, D. P., “Fluid Viscous Dampers in Applications of Seismic Energy Dissipation and Seismic Isolation,” in *Proc. ATC 17-1 on Seismic Isolation, Energy Dissipation and Active Control*, 1993, pp. 581–591.
- [75] Constantinou, M. C. and Symans, M. D., “Experimental Study of Seismic Response of Buildings with Supplemental Fluid Dampers,” *Struct. Des. Tall Build.*, 2(2), pp. 93–132, 1993.
- [76] Seleemah, A. A. and Constantinou, M. C., “Investigation of Seismic Response of Buildings with Linear and Nonlinear Fluid Viscous Dampers,” Report No. NCEER 97–0004, National Center for Earthquake Engineering Research, State Univ. of New York at Buffalo, Buffalo, N.Y., 1997.
- [77] Narkhede, D. I. and Sinha, R., “Shock Vibration Control of Structures Using

- Fluid Viscous Dampers,” in *Proc. 15th World Conference on Earthquake Engineering*, 2012.
- [78] Martinez-Rodrigo, M. and Romero, M. L., “An Optimum Retrofit Strategy for Moment Resisting Frames with Nonlinear Viscous Dampers for Seismic Applications,” *Eng. Struct.*, 25(7), pp. 913–925, 2003.
- [79] Banazadeh, M. and Ghanbari, A., “Seismic Performance Assessment of Steel Moment-Resisting Frames Equipped with Linear and Nonlinear Fluid Viscous Dampers with the Same Damping Ratio,” *J. Constr. Steel Res.*, 136, pp. 215–228, 2017.
- [80] Halperin, I., Ribakov, Y., and Agranovich, G., “Optimal Viscous Dampers Gains for Structures Subjected to Earthquakes,” *Struct. Control Heal. Monit.*, 23(3), pp. 458–469, 2016.
- [81] Arima, F., Miyazaki, M., Tanaka, H., and Yamazaki, Y., “A Study on Buildings with Large Damping Using Viscous Damping Walls,” in *Proc. 9th World Conference on Earthquake Engineering*, Tokyo, 1988.
- [82] Miyazaki, M. and Mitsusaka, Y., “Design of a Building with 20% or Greater Damping,” in *Proc. 10th World Conference on Earthquake Engineering*, 1992.
- [83] Zhang, R.-H., Soong, T. T., and Mahmoodi, P., “Seismic Response of Steel Frame Structures with Added Viscoelastic Dampers,” *Earthq. Eng. Struct. Dyn.*, 18(3), pp. 389–396, 1989.
- [84] Chang, K. C., Soong, T. T., Lai, M. L., and Nielsen, E. J., “Viscoelastic Dampers as Energy Dissipation Devices for Seismic Applications,” *Earthq. S.*, 9(3), pp. 371–387, 1993.
- [85] Higgins, C. and Kasai, K., “Experimental and Analytical Simulation of Wind Response for a Full-Scale VE-Damped Steel Frame,” *J. Wind Eng. Ind. Aerodyn.*, 77–8, pp. 297–313, 1998.
- [86] Lai, M. L., Chang, K. C., Soong, T. T., Hao, D. S., and Yeh, Y. C., “Full-Scale Viscoelastically Damped Steel Frame,” *J. Struct. Eng.*, 121(10), pp. 1443–1447, 1995.
- [87] Mazza, F. and Vulcano, A., “Control of the Earthquake and Wind Dynamic

- Response of Steel-Framed Buildings by Using Additional Braces and/or Viscoelastic Dampers,” *Earthq. Eng. Struct. Dyn.*, 40(2), pp. 155–174, 2011.
- [88] Samali, B. and Kwok, K. C. S., “Use of Viscoelastic Dampers in Reducing Wind- and Earthquake- Induced Motion of Building Structures,” *Eng. Struct.*, 17(9), pp. 639–654, 1995.
- [89] Nielsen, E. J., Lai, M. L., Soong, T. T., and Kelly, J. M., “Viscoelastic Damper Overview for Seismic and Wind Applications,” in *Proc. SPIE 2720, Smart Structures and Materials 1996: Passive Damping and Isolation*, pp. 138–144.
- [90] Kitagawa, Y. and Midorikawa, M., “Seismic Isolation and Passive Response-Control Buildings in Japan,” *Smart Mater. Struct.*, 7(5), pp. 581–587, 1998.
- [91] Munshi, J. A., “Effect of Viscoelastic Dampers on Hysteretic Response of Reinforced Concrete Elements,” *Eng. Struct.*, 19(11), pp. 921–935, 1997.
- [92] Montgomery, M. and Christopoulos, C., “Experimental Validation of Viscoelastic Coupling Dampers for Enhanced Dynamic Performance of High-Rise Buildings,” *J. Struct. Eng.*, 141(5), pp. 1–11, 2015.
- [93] Christopoulos, C. and Montgomery, M., “Viscoelastic Coupling Dampers (VCDs) for Enhanced Wind and Seismic Performance of High-Rise Buildings,” *Earthq. Eng. Struct. Dyn.*, 42(15), pp. 2217–2233, 2013.
- [94] Gong, S., Zhou, Y., and Ge, P., “Seismic Analysis for Tall and Irregular Temple Buildings: A Case Study of Strong Nonlinear Viscoelastic Dampers,” *Struct. Des. Tall Spec. Build.*, 26(7), pp. 1–9, 2017.
- [95] Gong, S. and Zhou, Y., “Experimental Study and Numerical Simulation on a New Type of Viscoelastic Damper with Strong Nonlinear Characteristics,” *Struct. Control Heal. Monit.*, 24(4), pp. 1–18, 2017.
- [96] Yamamoto, M. and Sone, T., “Damping Systems that Are Effective over a Wide Range of Displacement Amplitudes Using Metallic Yielding Component and Viscoelastic Damper in Series,” *Earthq. Eng. Struct. Dyn.*, 43(14), pp. 2097–2114, 2014.
- [97] Zhou, Y., Wu, C. X., Deng, X. S., and Wu, Y., “Research and Application of Lead Viscoelastic Damper,” in *Proc. 14th World Conference on Earthquake*

Engineering, 2008.

- [98] Derham, C. J., Kelly, J. M., and Thomas, A. G., “Nonlinear Natural Rubber Bearings for Seismic Isolation,” *Nucl. Eng. Des.*, 84(3), pp. 417–428, 1985.
- [99] Fuller, K. N. G., Gogh, J., Pond, T. J., and Ahmadi, H. R., “High Damping Natural Rubber Seismic Isolators,” *J. Struct. Control*, 4(2), pp. 19–40, 1997.
- [100] Teramoto, T., Kitamura, H., Ozaki, H., Furuya, O., Morikawa, S., and Suzuki, S., “Practical Application of High Damping Rubber Damper to a Slender Building,” in *Proc. 11th World Conference on Earthquake Engineering*, 1996.
- [101] Dall’Asta, A. and Ragni, L., “Experimental Tests and Analytical Model of High Damping Rubber Dissipating Devices,” *Eng. Struct.*, 28(13), pp. 1874–1884, 2006.
- [102] Dall’Asta, A. and Ragni, L., “Nonlinear Behavior of Dynamic Systems with High Damping Rubber Devices,” *Eng. Struct.*, 30(12), pp. 3610–3618, 2008.
- [103] Xu, Z. D., Xin Liao, Y., Ge, T., and Xu, C., “Experimental and Theoretical Study of Viscoelastic Dampers with Different Matrix Rubbers,” *J. Eng. Mech.*, 142(8), pp. 1–12, 2016.
- [104] Amadio, C., Clemente, I., Macorini, L., and Fragiaco, M., “Seismic Behaviour of Hybrid Systems Made of PR Composite Frames Coupled with Dissipative Bracings,” *Earthq. Eng. Struct. Dyn.*, 37(6), pp. 861–879, 2008.
- [105] Vargas, R. and Bruneau, M., “Effect of Supplemental Viscous Damping on the Seismic Response of Structural Systems with Metallic Dampers,” *J. Struct. Eng.*, 133(10), pp. 1434–1444, 2007.
- [106] Uetani, K., Tsuji, M., and Takewaki, I., “Application of an Optimum Design Method to Practical Building Frames with Viscous Dampers and Hysteretic Dampers,” *Eng. Struct.*, 25, pp. 579–592, 2003.
- [107] Murthy, K., “Application of Visco-Hyperelastic Devices in Structural Response Control,” Virginia Polytechnic Institute and State University, 2005.
- [108] Marshall, J. D. and Charney, F. A., “A Hybrid Passive Control Device for Steel Structures, I: Development and Analysis,” *J. Constr. Steel Res.*, 66, pp. 1278–

1286, 2010.

- [109] Marshall, J. D. and Charney, F. A., “Seismic Response of Steel Frame Structures with Hybrid Passive Control Systems,” *Earthq. Eng. Struct. Dyn.*, 41(4), pp. 715–733, 2012.
- [110] Guo, J. W. W. and Christopoulos, C., “Response Prediction, Experimental Characterization and P-Spectra Design of Frames with Viscoelastic–Plastic Dampers,” *Earthq. Eng. Struct. Dyn.*, 45(11), pp. 1855–1874, 2016.
- [111] Kasai, K., Teramoto, M., and Watanabe, Y., “Behavior of a Passive Control Damper Combining Visco-Elastic and Elasto-Plastic Devices in Series,” *J. Struct. Constr. Eng.*, 556, pp. 51–58, 2002.
- [112] Seo, C.-Y. and Sause, R., “Ductility Demands on Self-Centering Systems under Earthquake Loading,” *ACI Struct. J.*, 102(2), pp. 275–285, 2005.
- [113] Christopoulos, C., Filiatrault, A., and Folz, B., “Seismic Response of Self-Centering Hysteretic SDOF Systems,” *Earthq. Eng. Struct. Dyn.*, 31(5), pp. 1131–1150, 2002.
- [114] Choi, H., Erochko, J., Christopoulos, C., and Tremblay, R., “Comparison of the Seismic Response of Steel Buildings Incorporating Self-Centering Energy Dissipative Braces , Buckling Restrained Braced and Moment Resisting Frames,” in *Proc. 14th World Conference on Earthquake Engineering*, 2008.
- [115] Tremblay, R., Lacerte, M., and Christopoulos, C., “Seismic Response of Multistory Buildings with Self-Centering Energy Dissipative Steel Braces,” *J. Struct. Eng.*, 134(1), pp. 108–120, 2008.
- [116] MacRae, G. A., “P-Delta Effects on Single-Degree-of-Freedom Structures in Earthquakes,” *Earthq. Spectra*, 10(3), pp. 539–568, 1994.
- [117] MacRae, G. A. and Kawashima, K., “Post-Earthquake Residual Displacements of Bilinear Oscillators,” *Earthq. Eng. Struct. Dyn.*, 26(7), pp. 701–716, 1997.
- [118] Rahgozar, N., Moghadam, A. S., and Aziminejad, A., “Inelastic Displacement Ratios of Fully Self-Centering Controlled Rocking Systems Subjected to Near-Source Pulse-like Ground Motions,” *Eng. Struct.*, 108, pp. 113–133, 2016.

- [119] Blebo, F. C. and Roke, D. A., “Seismic-Resistant Self-Centering Rocking Core System,” *Eng. Struct.*, 101, pp. 193–204, 2015.
- [120] Sarti, F., Palermo, A., and Pampanin, S., “Quasi-Static Cyclic Testing of Two-Thirds Scale Unbonded Posttensioned Rocking Dissipative Timber Walls,” *J. Struct. Eng.*, 142(2008), pp. 1–14, 2015.
- [121] Dowden, D. M. *et al.*, “Full-Scale Pseudodynamic Testing of Self-Centering Steel Plate Shear Walls,” *J. Struct. Eng.*, 142(1), 2016.
- [122] Eatherton, M. R., Deierlein, G. G., Ma, X., Krawinkler, H., and Hajjar, J., “Towards a Performance-Based Design Framework for Self-Centering Rocking Braced-Frame Spine Systems,” *Proc. 15th World Conf. Earthq. Eng.*, 2012.
- [123] Rojas, P., Ricles, J. M., and Sause, R., “Seismic Performance of Post-tensioned Steel Moment Resisting Frames With Friction Devices,” *J. Struct. Eng.*, 131(4), pp. 529–540, 2005.
- [124] Eatherton, M. R., Fahnestock, L. A., and Miller, D. J., “Computational Study of Self-Centering Buckling-Restrained Braced Frame Seismic Performance,” *Earthq. Eng. Struct. Dyn.*, 43(13), pp. 1897–1914, 2014.
- [125] Kafeikivi, M., Roke, D. A., and Huang, Q., “Seismic Performance Assessment of Self-Centering Dual Systems with Different Configurations,” *Structures*, 5, pp. 88–100, 2016.
- [126] Pollino, M., “Seismic Design for Enhanced Building Performance Using Rocking Steel Braced Frames,” *Eng. Struct.*, 83, pp. 129–139, 2015.
- [127] Dyanati, M., Huang, Q., and Roke, D., “Seismic Demand Models and Performance Evaluation of Self-Centering and Conventional Concentrically Braced Frames,” *Eng. Struct.*, 84, pp. 368–381, 2015.
- [128] Iwashita, K., Kimura, H., Kasuga, Y., and Suzuki, N., “Shaking Table Test of a Steel Frame Allowing Uplift,” *J. Struct. Constr. Eng.*, 67(561), pp. 47–54, 2002.
- [129] Midorikawa, M., Azuhata, T., Ishihara, T., and Wada, A., “Shaking Table Tests on Seismic Response of Steel Braced Frames with Column Uplift,” *Earthq. Eng. Struct. Dyn.*, 35(14), pp. 1767–1785, 2006.

- [130] Garlock, M. M., Ricles, J. M., and Sause, R., “Experimental Studies of Full-Scale Posttensioned Steel Connections,” *J. Struct. Eng.*, 131(3), pp. 438–448, 2005.
- [131] Kam, W. Y., Pampanin, S., Palermo, A., and Carr, A. J., “Self-Centering Structural Systems with Combination of Hysteretic and Viscous Energy Dissipations,” *Earthq. Eng. Struct. Dyn.*, 39(10), pp. 1083–1108, 2010.
- [132] Garlock, M. M., Sause, R., and Ricles, J. M., “Behavior and Design of Posttensioned Steel Frame Systems,” *J. Struct. Eng.*, 133(3), pp. 389–399, 2007.
- [133] Ricles, J. M., Sause, R., Garlock, M. M., and Zhao, C., “Posttensioned Seismic-Resistant Connections for Steel Frames,” *J. Struct. Eng.*, 127(2), 2001.
- [134] Chou, C.-C., Chen, J.-H., Chen, Y.-C., and Tsai, K.-C., “Evaluating Performance of Post-Tensioned Steel Connections with Strands and Reduced Flange Plates,” *Earthq. Eng. Struct. Dyn.*, 35(9), pp. 1167–1185, 2006.
- [135] Tang, W. and Lui, E. M., “Hybrid Recentering Energy Dissipative Device for Seismic Protection,” *J. Struct.*, 2014, pp. 1–17, 2014.
- [136] Yang, C.-S. W., DesRoches, R., and Leon, R. T., “Design and Analysis of Braced Frames with Shape Memory Alloy and Energy-Absorbing Hybrid Devices,” *Eng. Struct.*, 32(2), pp. 498–507, 2010.
- [137] Hu, J. W., “Seismic Analysis and Evaluation of Several Recentering Braced Frame Structures,” *J. Mech. Eng. Sci.*, 228(5), pp. 781–798, 2014.
- [138] Dolce, M., Cardone, D., and Marnetto, R., “Implementation and Testing of Passive Control Devices Based on Shape Memory Alloys,” *Earthq. Eng. Struct. Dyn.*, 29(7), pp. 945–968, 2000.
- [139] Dolce, M., Cardone, D., Ponzo, F. C., and Valente, C., “Shaking Table Tests on Reinforced Concrete Frames without and with Passive Control Systems,” *Earthq. Eng. Struct. Dyn.*, 34(14), pp. 1687–1717, 2005.
- [140] Zhu, S. and Zhang, Y., “Seismic Analysis of Concentrically Braced Frame Systems with Self-Centering Friction Damping Braces,” *J. Struct. Eng.*, 134(1), pp. 121–131, 2008.

- [141] DesRoches, R., McCormick, J., and Delemont, M., “Cyclic Properties of Superelastic Shape Memory Alloy Wires and Bars,” *J. Struct. Eng.*, 130(1), pp. 38–46, 2004.
- [142] DesRoches, R. and Syith, B., “Shape Memory Alloys in Seismic Resistant Desing and Retrofit: a Critical Review of their Potential and Limitations,” *J. Earthq. Eng.*, 8(3), pp. 415–429, 2004.
- [143] Erochko, J., Christopoulos, C., and Tremblay, R., “Design, Testing, and Detailed Component Modeling of a High-Capacity Self-Centering Energy-Dissipative Brace,” *J. Struct. Eng.*, 141(8), pp. 1–12, 2015.
- [144] Constantinou, M. C., Tsopeles, P., Hammel, W., and Sigaher, A. N., “Toggle-Brace-Damper Seismic Energy Dissipation Systems,” *J. Struct. Eng.*, 127(2), pp. 105–112, 2001.
- [145] Sigaher, A. N. and Constantinou, M. C., “Scissor-Jack-Damper Energy Dissipation,” *Earthq. Spectra*, 19(1), pp. 133–158, 2003.
- [146] Sarlis, A. A., Pasala, D. T. R., Constantinou, M. C., Reinhorn, A. M., Nagarajaiah, S., and Taylor, D. P., “Negative Stiffness Device for Seismic Protection of Structures,” *J. Struct. Eng.*, 139(7), pp. 1124–1133, 2013.
- [147] Constantinou, M. C., Tsopeles, P., and Hammel, W., “Testing and Modeling of an Improved Damper Configuration for Stiff Structural Systems,” Center for Industrial Effectiveness and Taylor Devices, Inc, 1997.
- [148] Londoño, J. M., Neild, S. A., and Wagg, D. J., “Using a Damper Amplification Factor to Increase Energy Dissipation in Structures,” *Eng. Struct.*, 84, pp. 162–171, 2015.
- [149] Gluck, J. and Ribakov, Y., “Active Viscous Damping System with Amplifying Braces for Control of MDOF Structures,” *Earthq. Eng. Struct. Dyn.*, 31(9), pp. 1735–1751, 2002.
- [150] Huang, H. C. and McNamara, R. J., “The Efficiency of the Motion Amplification Device with Viscous Dampers,” *Earthq. Eng. Eng. Vib.*, 8(4), pp. 521–536, 2009.
- [151] Mosqueda, J. S. B., Almazan, J. L., and Tapia, N. F., “Amplification System for

- Concentrated and Distributed Energy Dissipation Devices,” *Earthq. Eng. Struct. Dyn.*, 45(6), pp. 935–956, 2016.
- [152] Zasso, A., Aly, A., and Resta, F., “MR Dampers with Lever Mechanism for Response Reduction in High-Rise Buildings under Wind Loads,” in *Proc. 5th European & African Conference on Wind Engineering, Florence*, 2009.
- [153] Kang, J. and Tagawa, H., “Experimental Evaluation of Dynamic Characteristics of Seesaw Energy Dissipation System for Vibration Control of Structures,” *Earthq. Eng. Struct. Dyn.*, 43(12), pp. 1889–1895, 2014.
- [154] Sui, J. and Liu, W., “Research on a New Type of Energy Dissipation Brace,” *Appl. Mech. Mater.*, 71–78, pp. 3816–3820, 2011.
- [155] Polat, E. and Constantinou, M. C., “Open Space Damping System Theory and Experimental Validation,” MCEER-16-0007, New York, 2016.
- [156] Almazan, J. L., Tapia, N., and Baquero, J., “Eccentric Lever Arm Amplification System For Frictional Energy Dissipation Devices,” in *Proc. 16th World Conference on Earthquake Engineering, Santiago*, 2017.
- [157] Burgos, M., “Influence of Layout of Fluid Viscous Dampers in Their Effectiveness For Seismic Protection of Buildings,” in *Proc. 16th World Conference on Earthquake Engineering, Santiago*, 2017.
- [158] Saito, T. *et al.*, “New Seismic Response Control System Using Block And Tackle,” in *Proc. 16th World Conference on Earthquake Engineering, Santiago*, 2017.
- [159] Ishii, M., Oyama, T., and Udagawa, T., “Proposal For New Deformation Amplification System,” in *Proc. 16th World Conference on Earthquake Engineering, Santiago*, 2017.
- [160] Chalhoub, M. S. and Kelly, J. M., “Effect of Bulk Compressibility on the Stiffness of Cylindrical Base Isolation Bearings,” *Int. J. Solids Struct.*, 26(7), pp. 743–760, 1990.
- [161] Kelly, J. M. and Konstantinidis, D. A., *Mechanics of Rubber Bearings for Seismic and Vibration Isolation*. Chichester, U.K.: John Wiley & Sons, Ltd, 2011.

- [162] Naeim, F. and Kelly, J. M., *Design of Seismic Isolated Structures: From Theory to Practice*. New York: John Wiley & Sons, Inc., 1999.
- [163] Warn, G. P. and Whittaker, A. S., “A Study of the Coupled Horizontal-Vertical Behavior of Elastomeric and Lead-Rubber Seismic Isolation Bearings,” MCEER-06-0011, 2006.
- [164] Warn, G. P., Whittaker, A. S., and Constantinou, M. C., “Vertical Stiffness of Elastomeric and Lead–Rubber Seismic Isolation Bearings,” *J. Struct. Eng.*, 133(9), pp. 1227–1236, 2007.
- [165] He, W. F., Liu, W. G., Yang, Q. R., and Feng, D. M., “Nonlinear Rotation and Shear Stiffness Theory and Experiment Research on Rubber Isolators,” *J. Eng. Mech.*, 138(5), pp. 441–449, 2012.
- [166] Ishii, K., Kikuchi, M., Nishimura, T., and Black, C. J., “Coupling Behavior of Shear Deformation and End Rotation of Elastomeric Seismic Isolation Bearings,” *Earthq. Eng. Struct. Dyn.*, 46(4), pp. 677–694, 2017.
- [167] American Association of State Highway and Transportation Officials (AASHTO), *AASHTO LRFD Bridge Design Specifications*. 2012.
- [168] Stanton, J., Roeder, C., Mackenzie-Helnwein, P., White, C., Kuester, C., and Craig, B., “Rotation Limits for Elastomeric Bearings,” NCHRP Report No 596, WA, 2008.
- [169] Özkaya, C., “Development of A New Seismic Isolator Named ‘Ball Rubber Bearing,’” Middle East Technical University, Ankara, 2010.
- [170] Thompson, A. C. T., Whittaker, A. S., Fenves, G. L., and Mahin, S. A., “Property Modification Factors for Elastomeric Seismic Isolation Bearings,” in *Proc. 12th World Conference on Earthquake Engineering*, 2000.
- [171] Building Seismic Safety Council (FEMA 450), *NEHRP Recommended Provisions for Seismic Regulations for New Buildings and Other Structures (Fema 450)*. 2003.
- [172] Federal Emergency Management Agency, *Quantification of Building Seismic Performance Factors (FEMA P-695)*. 2009.

- [173] “PEER Ground Motion Database - PEER Center.” [Online]. Available: <https://ngawest2.berkeley.edu/>. [Accessed: 06-Nov-2017].
- [174] ASCE, “Minimum Design Loads for Buildings and Other Structures, ASCE/SEI 7-10.” American Society of Civil Engineers, 2013.
- [175] Fajfar, P. and Vidic, T., “Consistent Inelastic Design Spectra: Hysteretic and Input Energy,” *Earthq. Eng. Struct. Dyn.*, 23(5), pp. 523–537, 1994.
- [176] Deger, Z. T. and Sutcu, F., “Evaluation of Earthquake Input Energy Distribution in an RC Building for an Energy-Based Seismic Design Approach,” in *Proc. 16th World Conference on Earthquake Engineering, Santiago, Chile, 2017*.



APPENDIX A

TEST RESULTS

A.1 A1 results

The EB of configuration A1 is plain elastomer. Its mechanical properties are summarized in Table A-1.

Table A-1. Mechanical properties of configuration A1

Configuration	K_h , [kN/m]	E_c , [MPa]	K_{v0} , [kN/m]	K_v , [kN/m]
A1	279.25	1.48	516.75	260.22

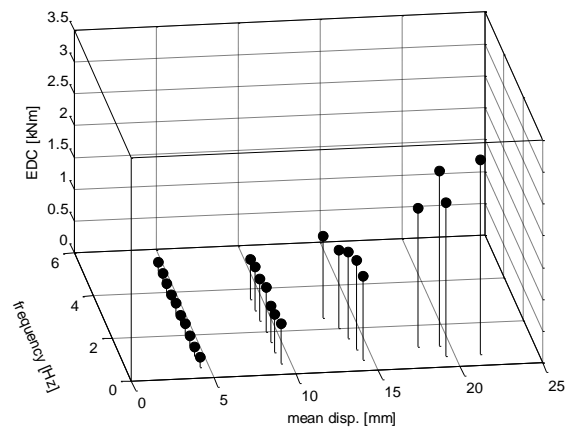


Figure A-1. Device EDC vs input frequency and displacement for A1

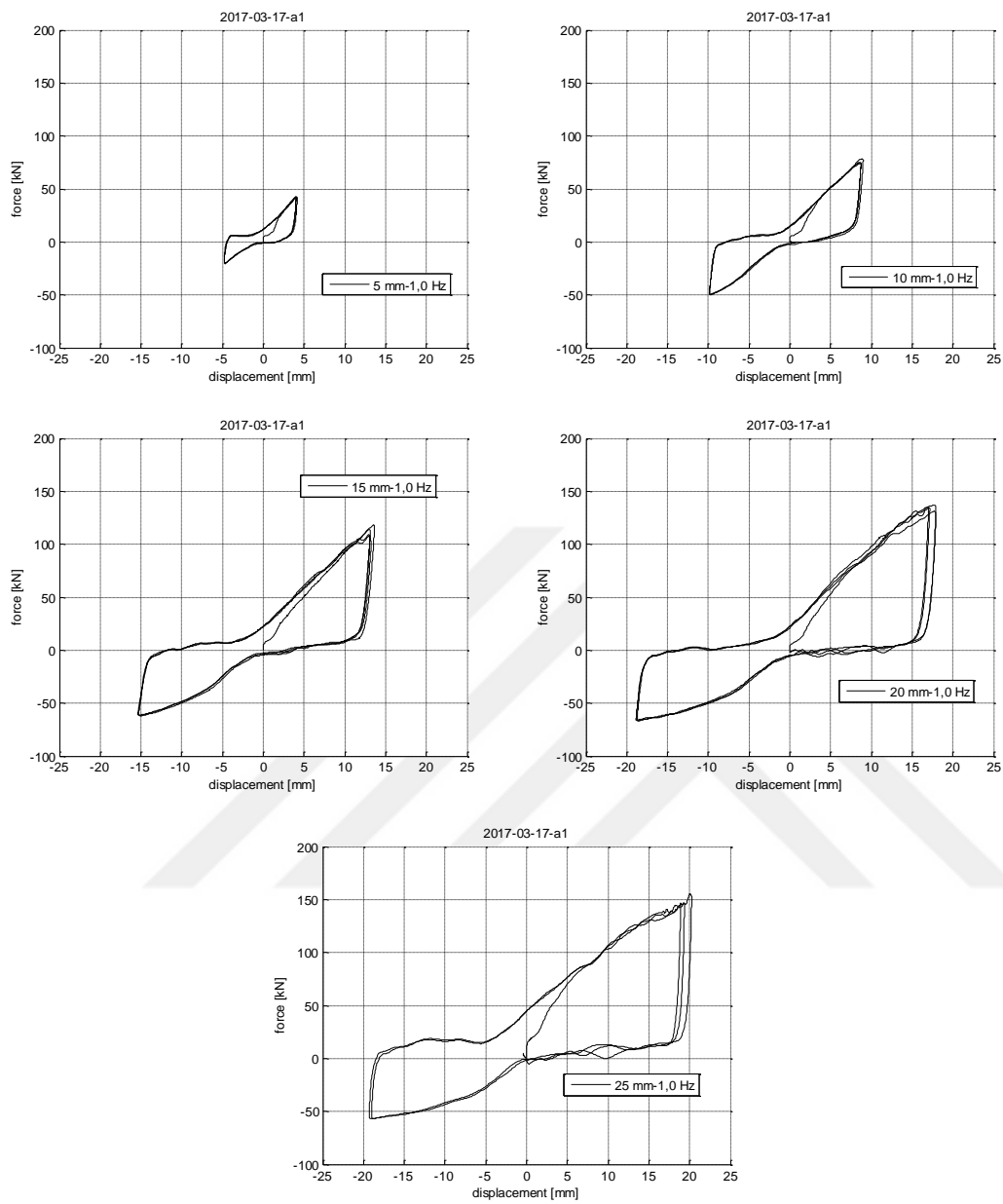


Figure A-2. Hysteresis loops of configuration A1 at 1.0Hz frequency and different displacement amplitudes

Table A-2. Results for A1 tests

d [mm]	f [Hz]	d ⁺ [mm]	d ⁻ [mm]	F ⁺ [kN]	F ⁻ [kN]	EDC [kNm]	k _{eff} [kN/m]	c _{eq} [kNs/m]	ξ_{eff}	AR at d ⁺	AR at d ⁻
5	0,5	4.05	-4.91	41.79	-19.52	0.154	6844.10	0.778	0.22	1.90	1.20
5	1,0	4.04	-4.82	41.67	-19.49	0.157	6904.20	0.405	0.22	1.62	1.38
5	1,5	3.97	-4.83	41.75	-20.02	0.157	7017.71	0.274	0.23	1.80	1.24
5	2,0	4.04	-4.84	39.22	-17.62	0.184	6400.66	0.236	0.28	1.71	1.29
5	2,5	4.07	-4.83	42.48	-18.62	0.145	6864.29	0.149	0.20	1.63	1.40
5	3,0	3.94	-4.98	42.56	-16.87	0.166	6658.65	0.141	0.26	1.86	1.19
5	3,5	3.88	-5.00	45.18	-20.01	0.138	7344.82	0.101	0.20	1.78	1.21
5	4,0	3.98	-4.99	42.56	-18.83	0.148	6845.22	0.093	0.22	1.86	0.98
5	4,5	4.12	-4.93	40.10	-18.46	0.140	6469.69	0.077	0.20	1.84	0.96
5	5,0	4.29	-4.79	40.56	-20.93	0.141	6774.77	0.069	0.18	1.52	1.28
10	0,5	8.79	-9.99	73.65	-50.38	0.619	6606.17	0.712	0.19	2.11	1.81
10	1,0	8.73	-9.89	73.13	-49.14	0.609	6565.80	0.356	0.19	1.99	1.91
10	1,5	8.70	-10.07	74.62	-50.04	0.565	6643.10	0.217	0.18	2.04	1.81
10	2,0	8.48	-10.23	76.08	-48.45	0.689	6655.72	0.200	0.23	2.04	1.78
10	2,5	8.51	-10.03	74.33	-46.94	0.665	6543.12	0.157	0.22	2.00	1.86
10	3,0	8.44	-10.06	79.20	-47.05	0.689	6824.39	0.136	0.23	1.93	1.90
10	3,5	8.15	-10.36	72.92	-44.77	0.628	6357.74	0.106	0.24	2.15	1.67
15	0,5	13.59	-15.22	107.34	-60.94	1.320	5844.60	0.646	0.20	2.18	1.95
15	1,0	13.22	-15.33	101.20	-60.54	1.396	5664.91	0.347	0.22	2.19	1.98
15	1,5	13.19	-14.98	106.86	-59.36	1.357	5901.14	0.231	0.21	2.07	2.00
15	2,0	12.96	-14.65	100.36	-60.16	1.225	5813.71	0.163	0.20	2.04	1.96
15	2,5	12.25	-13.95	96.54	-58.76	1.291	5927.15	0.152	0.23	2.09	1.95
20	0,5	18.37	-20.46	131.17	-62.47	2.414	4988.23	0.649	0.23	2.11	2.05
20	1,0	17.16	-18.85	134.17	-65.71	2.172	5550.56	0.339	0.21	2.10	2.03
25	0,5	21.03	-22.03	154.92	-67.42	3.062	5168.13	0.671	0.21	2.10	2.03
25	1,0	19.35	-19.31	145.63	-54.47	2.749	5175.89	0.373	0.23	2.03	2.02

A.2 B1-1 results

The EB of configuration B1-1 is laminated rubber. Its mechanical properties are summarized in Table A-3.

Table A-3. Mechanical properties of configuration B1-1

Configuration	K_h , [kN/m]	E_c , [MPa]	K_{v0} , [kN/m]	K_v , [kN/m]
B1-1	241.53	98.40	3300.92	1542.61

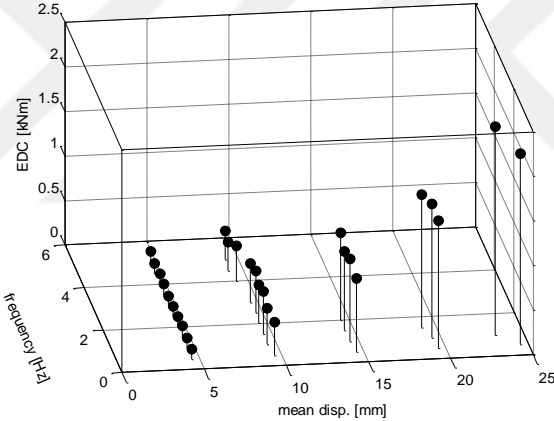


Figure A-3. Device EDC vs input frequency and displacement for B1-1

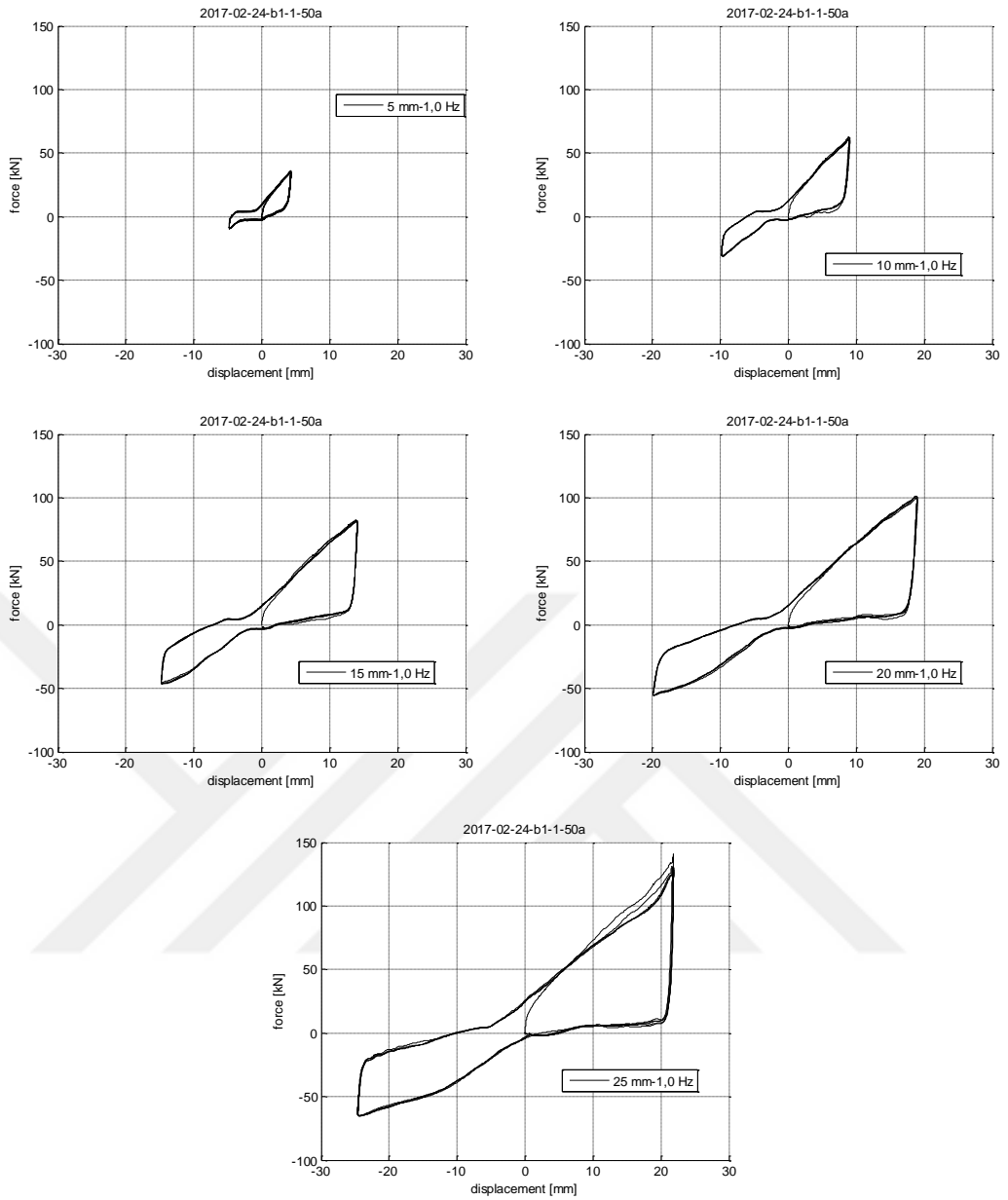


Figure A-4. Hysteresis loops of configuration B1-1 at 1.0Hz frequency and different displacement amplitudes

Table A-4. Results for B1-1 tests

d [mm]	f [Hz]	d ⁺ [mm]	d ⁻ [mm]	F ⁺ [kN]	F ⁻ [kN]	EDC [kNm]	k _{eff} [kN/m]	c _{eq} [kNs/m]	ξ_{eff}	AR at d ⁺	AR at d ⁻
5	0,5	4.70	-4.39	31.72	-11.61	0.108	4773.47	0.530	0.16	2.27	0.67
5	1,0	4.28	-4.80	35.41	-8.91	0.117	4877.49	0.287	0.21	2.17	0.84
5	1,5	4.31	-4.79	35.41	-9.39	0.133	4923.31	0.217	0.23	2.14	0.83
5	2,0	4.30	-4.84	34.08	-8.65	0.122	4675.19	0.149	0.23	2.14	0.82
5	2,5	4.33	-4.82	35.56	-9.20	0.117	4892.05	0.113	0.20	2.13	0.78
5	3,0	4.29	-4.84	36.25	-8.07	0.111	4853.09	0.090	0.20	2.18	0.73
5	3,5	4.26	-4.91	35.74	-8.92	0.123	4873.31	0.085	0.22	2.23	0.67
5	4,0	4.32	-4.90	36.95	-9.16	0.120	4997.67	0.071	0.21	2.27	0.63
5	4,5	4.36	-4.88	34.96	-7.89	0.114	4639.45	0.060	0.21	2.34	0.64
5	5,0	4.37	-4.96	35.28	-7.38	0.131	4574.45	0.061	0.24	2.21	0.64
10	0,5	9.26	-9.83	59.32	-30.40	0.372	4700.57	0.414	0.15	2.23	1.61
10	1,0	9.00	-9.85	60.46	-30.64	0.411	4833.51	0.234	0.17	2.24	1.60
10	1,5	9.15	-9.80	57.58	-29.46	0.475	4597.54	0.179	0.20	2.18	1.62
10	2,0	9.13	-9.88	58.27	-30.46	0.432	4667.98	0.121	0.18	2.20	1.60
10	2,5	9.18	-9.97	57.47	-30.21	0.473	4576.80	0.105	0.20	2.21	1.56
10	3,0	9.27	-9.87	57.59	-28.49	0.429	4495.33	0.079	0.18	2.18	1.48
10	4,0	8.85	-9.76	55.04	-25.60	0.392	4334.39	0.057	0.18	2.51	1.14
10	4,5	8.43	-9.73	54.42	-25.60	0.321	4406.78	0.044	0.16	2.63	1.08
10	5,0	9.01	-9.41	51.71	-26.41	0.328	4241.60	0.039	0.15	2.34	0.78
15	0,5	14.73	-14.31	73.62	-48.74	0.824	4212.54	0.396	0.14	2.25	1.79
15	1,0	14.09	-14.79	79.77	-45.17	0.924	4326.00	0.224	0.17	2.23	1.82
15	1,5	13.93	-14.82	83.66	-44.39	0.892	4454.09	0.146	0.16	2.24	1.81
15	2,0	14.01	-14.88	76.47	-44.75	0.978	4195.96	0.119	0.19	2.22	1.84
20	0,5	19.20	-19.86	93.83	-56.09	1.433	3838.17	0.381	0.16	2.22	1.93
20	1,0	19.02	-19.91	98.34	-54.92	1.498	3937.89	0.200	0.17	2.22	1.91
20	1,5	18.56	-19.64	109.41	-54.42	1.491	4288.44	0.138	0.16	2.20	1.91
25	0,5	23.84	-25.23	135.47	-67.65	2.141	4140.79	0.361	0.15	2.18	1.91
25	1,0	21.90	-24.65	126.06	-62.86	2.331	4058.86	0.218	0.19	2.17	1.91

A.3 B1-2 results

The EB of configuration B1-2 is laminated rubber. Its mechanical properties are summarized in Table A-5.

Table A-5. Mechanical properties of configuration B1-2

Configuration	K_h , [kN/m]	E_c , [MPa]	K_{v0} , [kN/m]	K_v , [kN/m]
B1-2	279.25	112.80	4374.96	2203.08

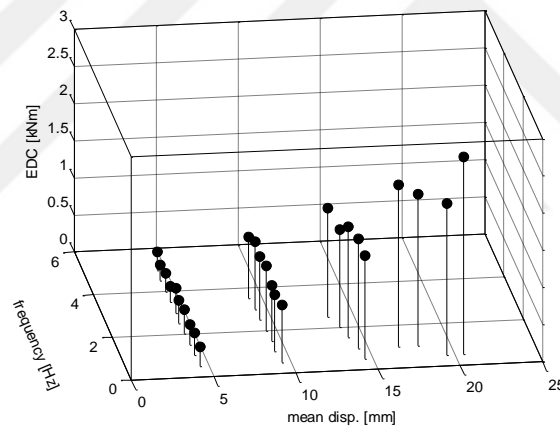


Figure A-5. Device EDC vs input frequency and displacement for B1-2

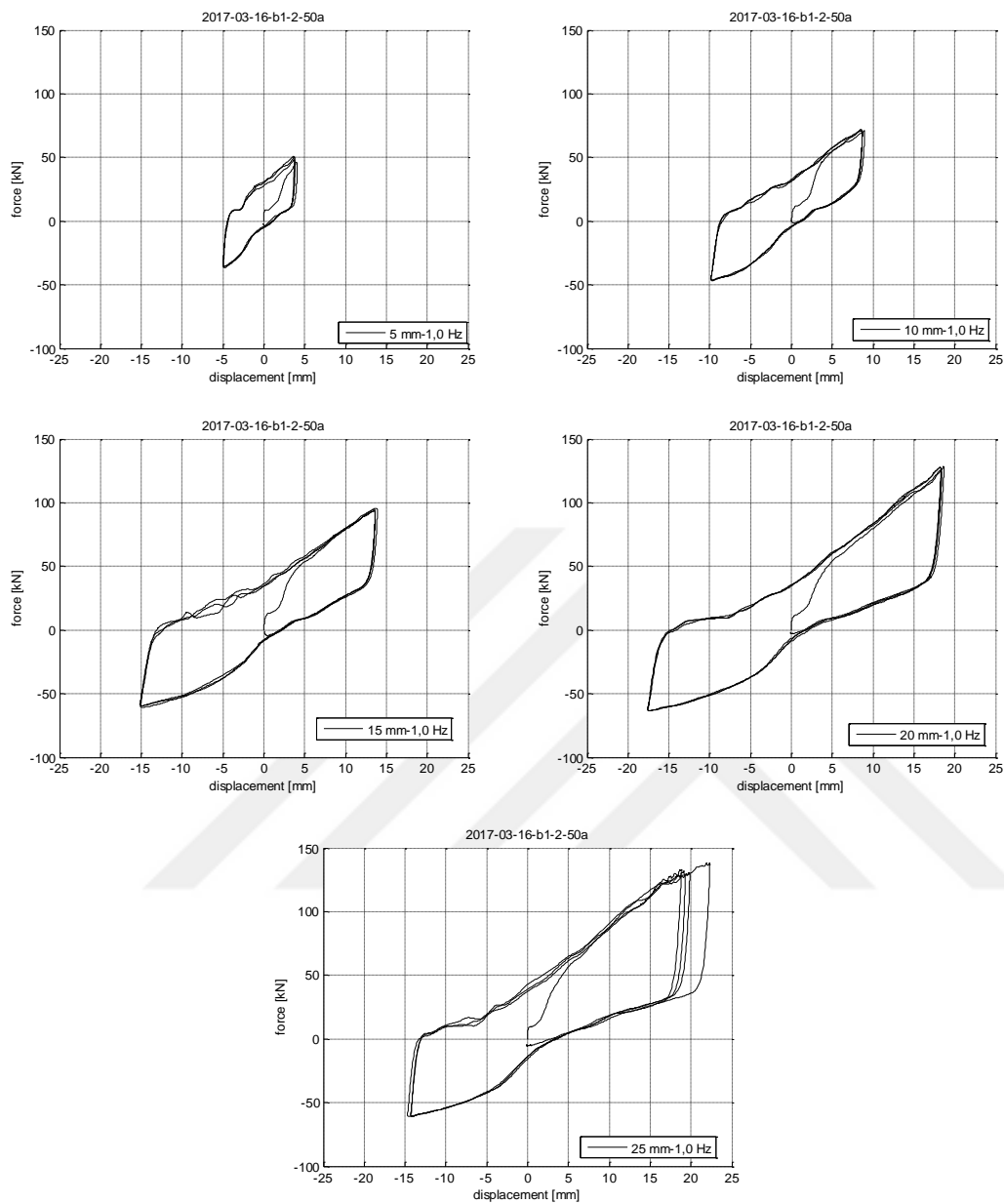


Figure A-6. Hysteresis loops of configuration B1-2 at 1.0Hz frequency and different displacement amplitudes

Table A-6. Results for B1-2 tests

d [mm]	f [Hz]	d ⁺ [mm]	d ⁻ [mm]	F ⁺ [kN]	F ⁻ [kN]	EDC [kNm]	k _{eff} [kN/m]	c _{eq} [kNs/m]	ξ_{eff}	AR at d ⁺	AR at d ⁻
5	0,5	3.94	-5.00	51.38	-34.57	0.262	9619.87	1.331	0.28	1.16	1.71
5	1,0	3.77	-5.01	48.88	-36.10	0.308	9677.03	0.810	0.36	1.15	1.67
5	1,5	3.85	-4.95	49.24	-35.54	0.274	9638.31	0.479	0.31	1.14	1.68
5	2,0	3.85	-4.92	44.19	-34.16	0.333	8934.98	0.439	0.40	1.15	1.68
5	2,5	3.72	-4.96	48.37	-36.17	0.314	9765.17	0.340	0.37	1.15	1.69
5	3,0	3.78	-5.10	50.01	-35.06	0.329	9584.29	0.282	0.38	1.21	1.62
5	3,5	3.71	-5.16	48.49	-37.59	0.220	9713.02	0.162	0.26	1.30	1.58
5	4,0	3.85	-4.98	44.39	-40.33	0.252	9587.68	0.163	0.28	1.39	1.52
5	4,5	3.87	-4.85	46.22	-36.18	0.223	9463.44	0.132	0.25	1.39	1.59
5	5,0	3.82	-5.13	47.55	-36.67	0.248	9407.76	0.125	0.29	1.66	1.45
10	0,5	8.82	-10.03	68.07	-46.97	0.770	6103.72	0.879	0.26	1.86	2.02
10	1,0	8.73	-9.87	69.62	-46.17	0.771	6227.65	0.452	0.26	1.82	2.05
10	1,5	8.81	-9.97	72.47	-48.80	0.751	6459.33	0.288	0.24	1.80	1.98
10	2,0	8.76	-10.00	68.02	-46.96	0.874	6129.80	0.252	0.30	1.81	1.96
10	2,5	8.45	-10.12	69.06	-49.06	0.851	6360.60	0.200	0.30	1.84	1.94
10	3,0	8.77	-9.73	68.32	-47.92	0.914	6285.79	0.181	0.30	1.79	1.94
10	3,5	8.32	-10.06	68.61	-49.03	0.827	6401.31	0.142	0.30	1.99	1.81
15	0,5	13.63	-15.31	92.68	-56.32	1.384	5148.75	0.670	0.23	2.02	2.06
15	1,0	13.68	-15.12	91.98	-60.19	1.477	5285.08	0.361	0.24	1.98	2.01
15	1,5	13.39	-14.79	96.30	-59.34	1.494	5524.31	0.254	0.24	1.96	1.96
15	2,0	13.39	-14.31	94.82	-57.87	1.322	5510.74	0.174	0.21	1.94	1.96
15	2,5	13.05	-13.72	95.70	-56.35	1.467	5679.35	0.166	0.24	1.87	1.97
20	0,5	18.74	-20.20	121.85	-64.36	2.044	4781.11	0.546	0.19	2.00	2.07
20	1,0	18.39	-17.61	125.15	-63.45	2.043	5239.22	0.320	0.18	2.01	2.00
25	0,5	23.76	-17.27	130.00	-69.35	2.657	4858.74	0.640	0.15	2.04	2.01

A.4 B3-1 results

The EB of configuration B3-1 is laminated rubber. Its mechanical properties are summarized in Table A-7.

Table A-7. Mechanical properties of configuration B3-1

Configuration	K_h , [kN/m]	E_c , [MPa]	K_{v0} , [kN/m]	K_v , [kN/m]
B3-1	241.94	66.91	3372.60	1245.98

The effects of both frequency and displacement on the prototype EDC are summarized with the 3D plot of Figure A-7. The plot clearly shows the predominant effect of displacement rather than frequency on the device EDC.

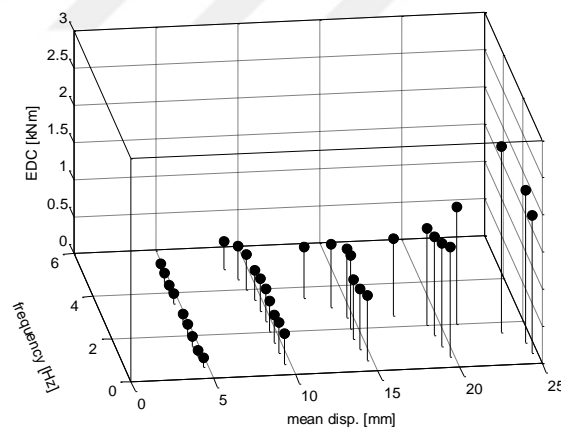


Figure A-7. Effect of frequency and displacement on the device EDC for B3-1

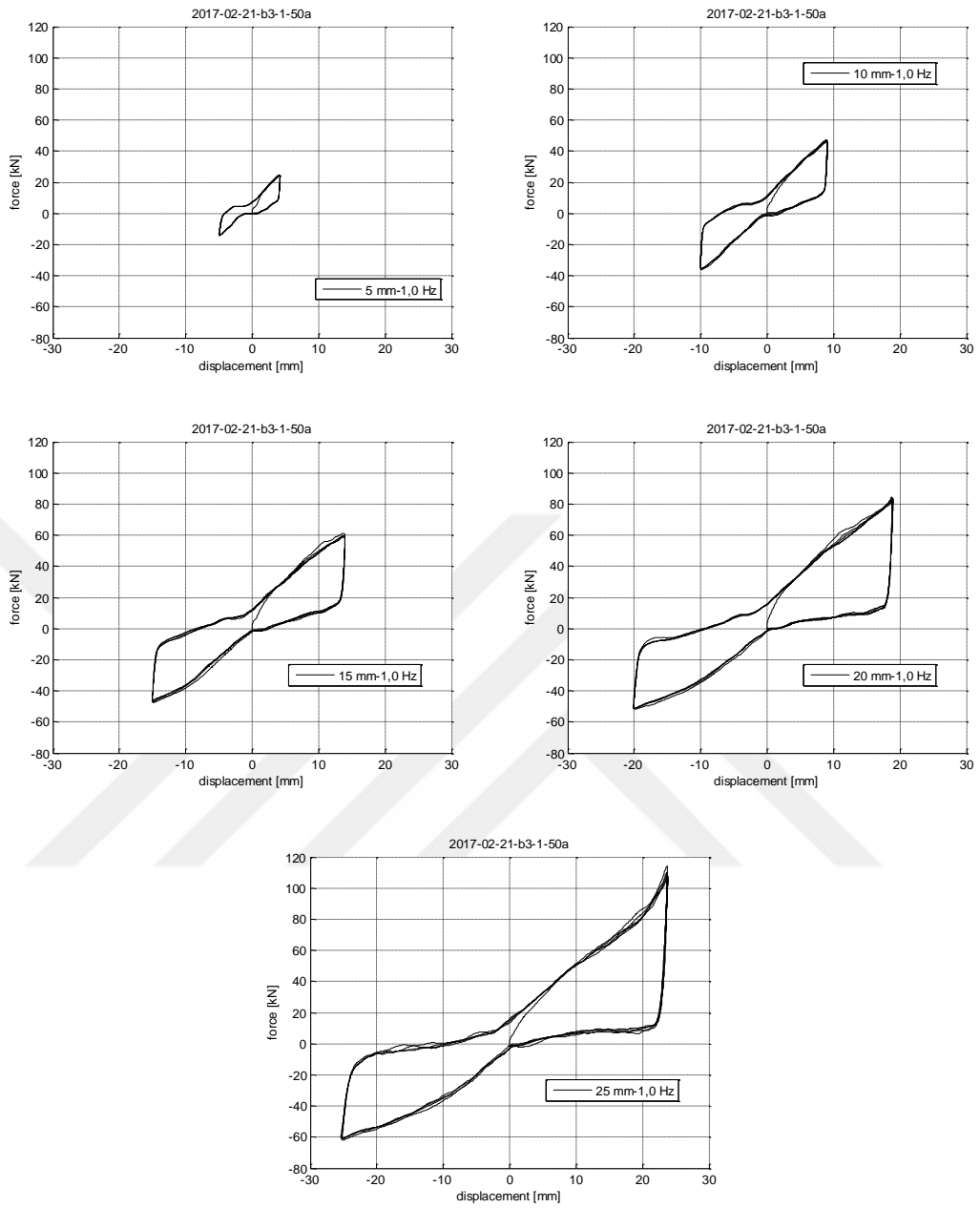


Figure A-8. Hysteresis loops of configuration B3-1 at 1.0Hz frequency and different displacement amplitudes

Table A-8. Results for B3-1 tests

d [mm]	f [Hz]	d ⁺ [mm]	d ⁻ [mm]	F ⁺ [kN]	F ⁻ [kN]	EDC [kNm]	k _{eff} [kN/m]	c _{eq} [kNs/m]	ξ_{eff}	AR at d ⁺	AR at d ⁻
5	0,5	4.38	-4.96	28.66	-14.62	0.125	4629.65	0.581	0.22	1.88	1.35
5	1,0	4.26	-5.00	24.40	-13.83	0.089	4129.85	0.211	0.19	1.91	1.34
5	1,5	4.26	-4.94	24.44	-16.00	0.135	4396.45	0.215	0.27	1.86	1.33
5	2,0	4.20	-5.04	26.54	-16.04	0.155	4605.02	0.184	0.30	1.86	1.32
5	2,5	4.23	-5.04	29.64	-18.58	0.152	5202.51	0.143	0.26	1.62	1.49
5	3,5	4.26	-5.02	27.72	-18.62	0.132	4989.45	0.089	0.23	1.54	1.60
5	4,0	4.20	-5.03	26.94	-17.11	0.103	4774.43	0.062	0.20	1.86	1.29
5	4,5	4.28	-5.05	27.76	-16.32	0.128	4724.31	0.066	0.23	1.99	1.19
5	5,0	4.29	-5.10	24.09	-15.27	0.109	4193.72	0.050	0.23	2.43	0.73
10	0,5	9.34	-9.94	44.22	-37.98	0.409	4264.57	0.446	0.18	2.11	1.90
10	1,0	9.07	-10.04	45.20	-34.70	0.419	4181.01	0.233	0.19	2.13	1.88
10	1,5	9.16	-10.03	46.01	-35.58	0.375	4251.49	0.137	0.17	2.10	1.87
10	2,0	9.35	-9.88	44.16	-34.55	0.416	4092.69	0.114	0.19	2.06	1.89
10	2,5	9.21	-10.07	41.09	-33.83	0.441	3885.38	0.096	0.21	2.10	1.93
10	3,0	9.26	-9.90	42.37	-33.97	0.428	3983.29	0.079	0.20	2.11	1.88
10	3,5	9.13	-9.96	41.84	-33.88	0.398	3965.70	0.063	0.19	2.15	1.75
10	4,0	8.81	-9.93	52.37	-32.98	0.473	4556.44	0.068	0.21	1.94	1.78
10	4,5	8.48	-9.81	46.40	-29.44	0.443	4144.74	0.060	0.24	2.56	1.56
10	5,0	8.04	-9.09	38.77	-36.46	0.367	4392.97	0.051	0.21	2.33	1.35
15	0,5	14.76	-14.55	52.83	-53.03	0.873	3611.18	0.412	0.18	2.10	2.10
15	1,0	13.97	-15.07	58.22	-46.44	0.817	3603.59	0.196	0.19	2.19	2.02
15	1,5	13.93	-14.91	62.22	-44.09	0.807	3685.37	0.131	0.18	2.21	2.02
15	2,0	14.15	-14.91	61.99	-43.76	0.978	3638.90	0.117	0.21	2.19	2.03
15	2,5	14.09	-15.06	58.73	-44.13	0.924	3528.62	0.088	0.21	2.20	2.05
15	3,0	13.41	-14.43	59.16	-41.41	0.856	3611.89	0.075	0.21	2.22	1.86
15	3,5	12.30	-12.86	53.31	-44.65	0.684	3893.21	0.063	0.19	2.23	1.51
20	0,5	19.66	-19.72	69.10	-58.34	1.476	3236.31	0.386	0.19	2.15	2.11
20	1,0	18.95	-20.08	81.71	-50.41	1.385	3384.90	0.184	0.18	2.20	2.06
20	1,5	18.84	-19.86	80.73	-50.94	1.327	3402.89	0.120	0.18	2.23	2.06
20	2,0	18.83	-19.54	74.82	-52.96	1.308	3330.48	0.090	0.18	2.20	2.08
20	2,5	16.86	-18.01	63.10	-47.50	1.038	3171.41	0.069	0.18	2.21	2.08
25	0,5	24.47	-24.90	96.84	-65.29	1.859	3284.23	0.309	0.15	2.15	2.07
25	1,0	23.82	-25.39	106.70	-60.55	2.043	3398.46	0.171	0.17	2.18	2.03
25	1,5	22.59	-24.25	103.48	-56.08	2.511	3406.99	0.155	0.23	2.26	1.96
25	2,0	19.42	-22.58	83.27	-51.62	1.567	3211.21	0.090	0.21	2.25	2.03

A.5 B3-2 Results

The EB of configuration B3-2 is laminated rubber. Its mechanical properties are summarized in Table A-9.

Table A-9. Mechanical properties of configuration B3-2

Configuration	K_h , [kN/m]	E_c , [MPa]	K_{v0} , [kN/m]	K_v , [kN/m]
B3-2	281.65	77.43	4543.59	1842.38

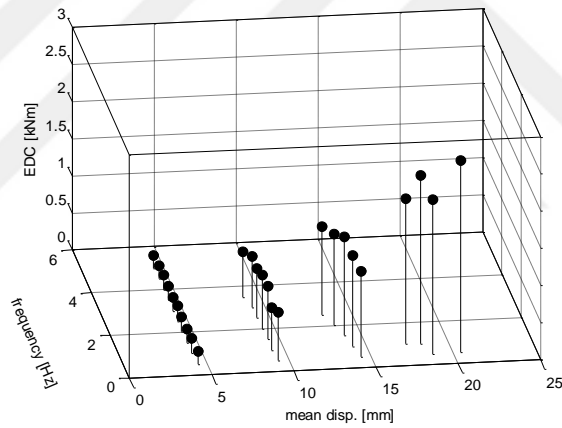


Figure A-9. Device EDC vs input frequency and displacement for B3-2

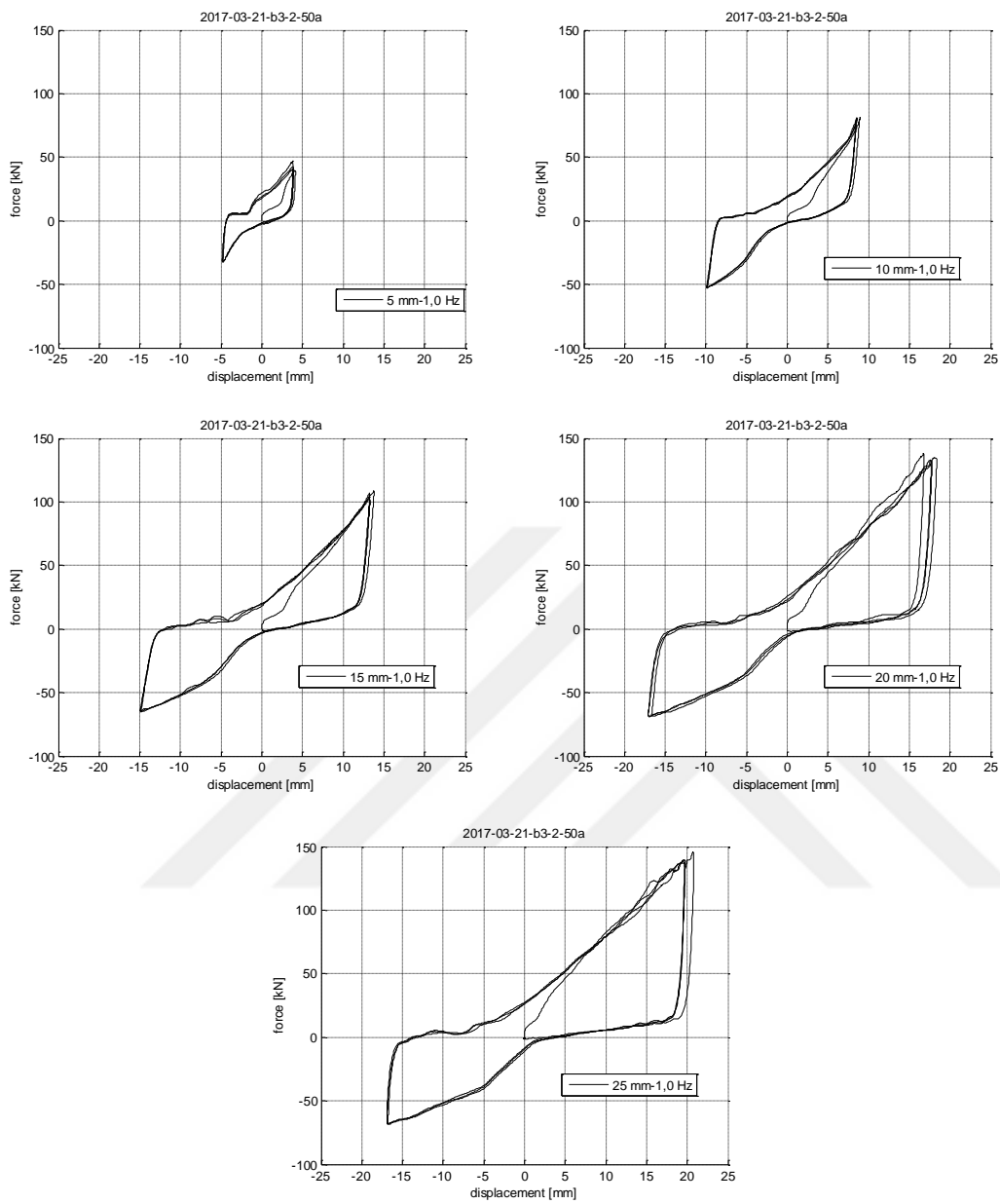


Figure A-10. Hysteresis loops of configuration B3-2 at 1.0Hz frequency and different displacement amplitudes

Table A-10. Results for B3-2 tests

d [mm]	f [Hz]	d ⁺ [mm]	d ⁻ [mm]	F ⁺ [kN]	F ⁻ [kN]	EDC [kNm]	k _{eff} [kN/m]	c _{eq} [kNs/m]	ξ_{eff}	AR at d ⁺	AR at d ⁻
5	0,5	3.84	-5.08	40.67	-32.32	0.168	8181.96	0.858	0.22	1.97	0.93
5	1,0	3.88	-4.84	42.23	-32.53	0.209	8572.04	0.556	0.26	1.44	1.28
5	1,5	3.78	-4.97	44.82	-30.17	0.192	8568.90	0.338	0.25	1.31	1.35
5	2,0	3.80	-4.89	41.89	-29.93	0.202	8266.94	0.271	0.27	1.42	1.31
5	2,5	3.88	-4.94	38.97	-29.05	0.210	7716.28	0.219	0.29	1.46	1.32
5	3,0	3.75	-5.04	42.96	-30.41	0.188	8349.49	0.164	0.26	1.49	1.30
5	3,5	3.70	-5.15	42.01	-28.21	0.189	7937.44	0.140	0.28	1.56	1.21
5	4,0	3.84	-4.95	42.54	-28.80	0.196	8114.11	0.129	0.26	1.88	1.21
5	4,5	3.92	-4.91	39.29	-28.46	0.181	7678.77	0.105	0.25	2.07	1.15
5	5,0	4.02	-4.78	39.07	-28.17	0.177	7641.18	0.092	0.23	2.18	0.96
10	0,5	8.95	-9.78	75.53	-53.93	0.651	6913.87	0.753	0.19	1.93	1.77
10	1,0	8.58	-9.90	80.67	-52.45	0.568	7204.19	0.337	0.17	1.86	1.80
10	1,5	8.62	-10.03	78.38	-50.22	0.708	6896.45	0.275	0.22	1.87	1.76
10	2,0	8.39	-10.06	77.26	-48.94	0.722	6842.19	0.215	0.24	1.92	1.75
10	2,5	8.51	-9.92	76.52	-49.29	0.671	6827.37	0.160	0.22	1.87	1.79
10	3,0	8.43	-9.98	71.58	-47.58	0.683	6470.69	0.136	0.24	1.94	1.60
10	3,5	8.25	-9.61	72.30	-46.73	0.612	6668.52	0.111	0.22	2.65	1.69
15	0,5	13.41	-15.39	108.25	-64.67	1.150	6005.65	0.562	0.17	2.08	1.85
15	1,0	13.36	-14.99	103.65	-64.73	1.224	5939.05	0.309	0.18	2.04	1.91
15	1,5	13.15	-14.73	98.82	-62.98	1.331	5801.73	0.231	0.21	2.06	1.87
15	2,0	13.13	-14.07	103.04	-62.59	1.236	6089.24	0.169	0.19	2.00	1.84
15	2,5	12.49	-13.83	99.01	-60.91	1.193	6076.47	0.140	0.20	2.03	1.86
20	0,5	18.45	-19.01	136.75	-70.05	2.067	5521.58	0.597	0.18	2.07	1.93
20	1,0	17.72	-17.11	131.97	-68.62	1.959	5759.59	0.327	0.17	2.06	1.89
25	0,5	22.04	-18.88	151.81	-70.69	2.587	5437.59	0.626	0.16	2.10	1.90
25	1,0	19.75	-16.90	138.24	-65.89	2.263	5569.76	0.341	0.17	2.07	1.89

A.6 B3-4 results

The EB of configuration B3-4 is laminated rubber. Its mechanical properties are summarized in Table A-11.

Table A-11. Mechanical properties of configuration B3-4

Configuration	K_h , [kN/m]	E_c , [MPa]	K_{v0} , [kN/m]	K_v , [kN/m]
B3-4	362.29	98.40	5988.20	2634.45

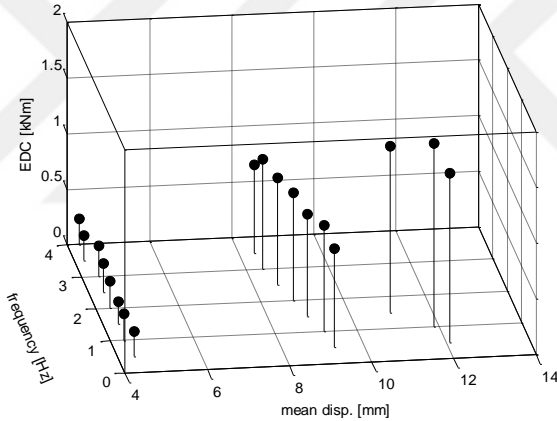


Figure A-11. Device EDC vs input frequency and displacement for B3-4

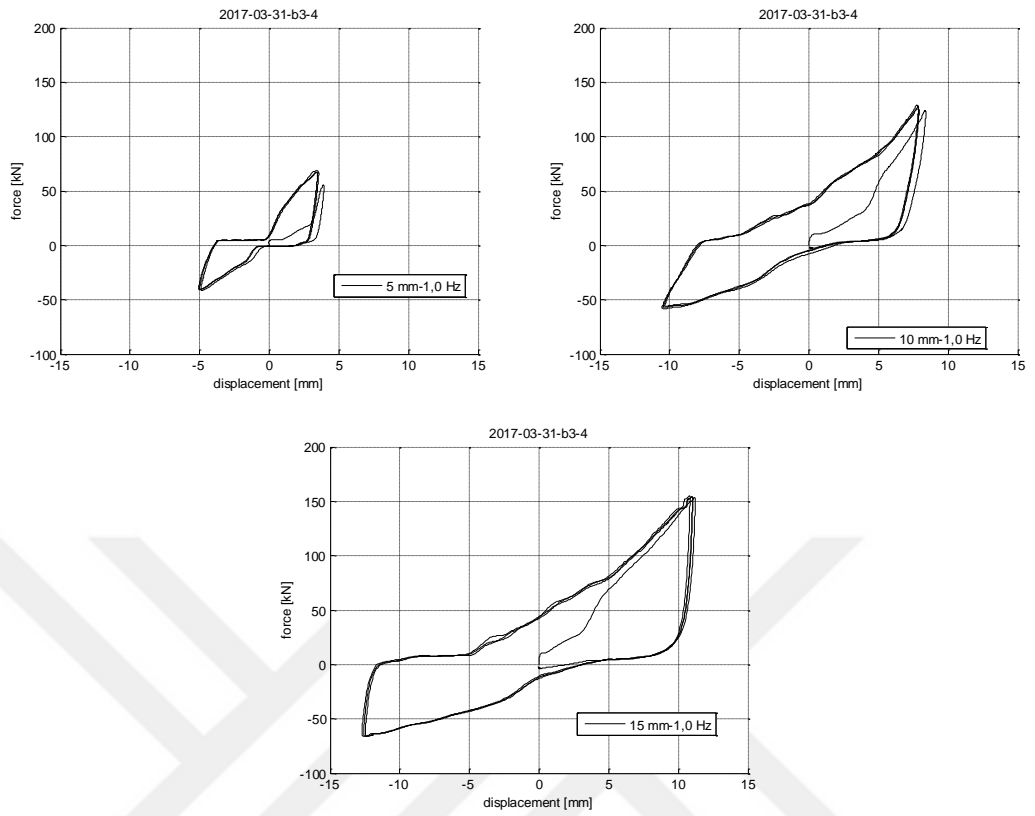


Figure A-12. Hysteresis loops of configuration B3-4 at 1.0Hz frequency and different displacement amplitudes

Table A-12. Results for B3-4 tests

d [mm]	f [Hz]	d ⁺ [mm]	d ⁻ [mm]	F ⁺ [kN]	F ⁻ [kN]	EDC [kNm]	k _{eff} [kN/m]	c _{eq} [kNs/m]	ξ_{eff}	AR at d ⁺	AR at d ⁻
5	0,5	3.75	-5.01	70.58	-41.44	0.219	12781.99	1.157	0.19	0.72	1.06
5	1,0	3.50	-5.14	67.68	-41.22	0.237	12602.55	0.643	0.25	0.55	0.98
5	1,5	3.48	-5.23	67.67	-39.35	0.200	12284.48	0.356	0.21	0.59	0.94
5	2,0	3.31	-5.33	67.56	-39.58	0.245	12392.46	0.332	0.29	0.62	0.92
5	2,5	3.78	-4.89	68.61	-35.65	0.257	12021.22	0.277	0.24	0.58	1.04
5	3,0	3.61	-5.22	64.62	-32.85	0.277	11031.31	0.239	0.31	0.53	1.04
5	3,5	3.23	-5.22	65.49	-36.78	0.223	12098.34	0.181	0.28	0.79	0.88
5	4,0	3.49	-5.09	65.69	-37.56	0.233	12038.15	0.161	0.25	0.58	0.83
10	0,5	9.06	-9.48	129.48	-65.19	0.883	10500.50	1.042	0.16	1.51	1.69
10	1,0	7.90	-10.48	123.54	-56.79	0.954	9815.65	0.573	0.25	1.22	1.76
10	1,5	7.86	-10.05	124.08	-55.11	0.918	10008.27	0.387	0.24	0.95	2.01
10	2,0	7.78	-9.83	119.46	-55.03	0.963	9907.32	0.314	0.26	1.19	1.81
10	2,5	7.20	-9.98	117.51	-52.67	0.956	9907.48	0.263	0.30	1.29	1.74
10	3,0	7.37	-9.44	107.33	-49.78	0.988	9350.56	0.236	0.31	1.44	1.61
10	3,5	7.45	-9.29	105.53	-48.88	0.790	9222.94	0.163	0.25	2.29	1.66
15	0,5	10.29	-13.85	156.93	-66.26	1.520	9246.76	1.057	0.25	1.52	1.64
15	1,0	11.02	-12.73	150.88	-65.45	1.645	9108.53	0.591	0.24	1.43	1.77
15	1,5	10.32	-11.64	136.91	-61.82	1.495	9048.98	0.419	0.25	1.38	1.84

A.7 BRB results

The EB of configuration BRB is ball rubber composite. Its mechanical properties are summarized in Table A-13.

Table A-13. Mechanical properties of configuration BRB

Configuration	K_h , [kN/m]	E_c , [MPa]	K_{v0} , [kN/m]	K_v , [kN/m]
BRB	327.25	-	-	-

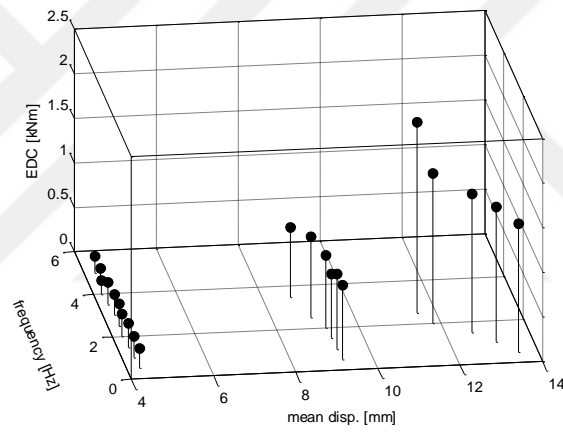


Figure A-13. Device EDC vs input frequency and displacement for BRB

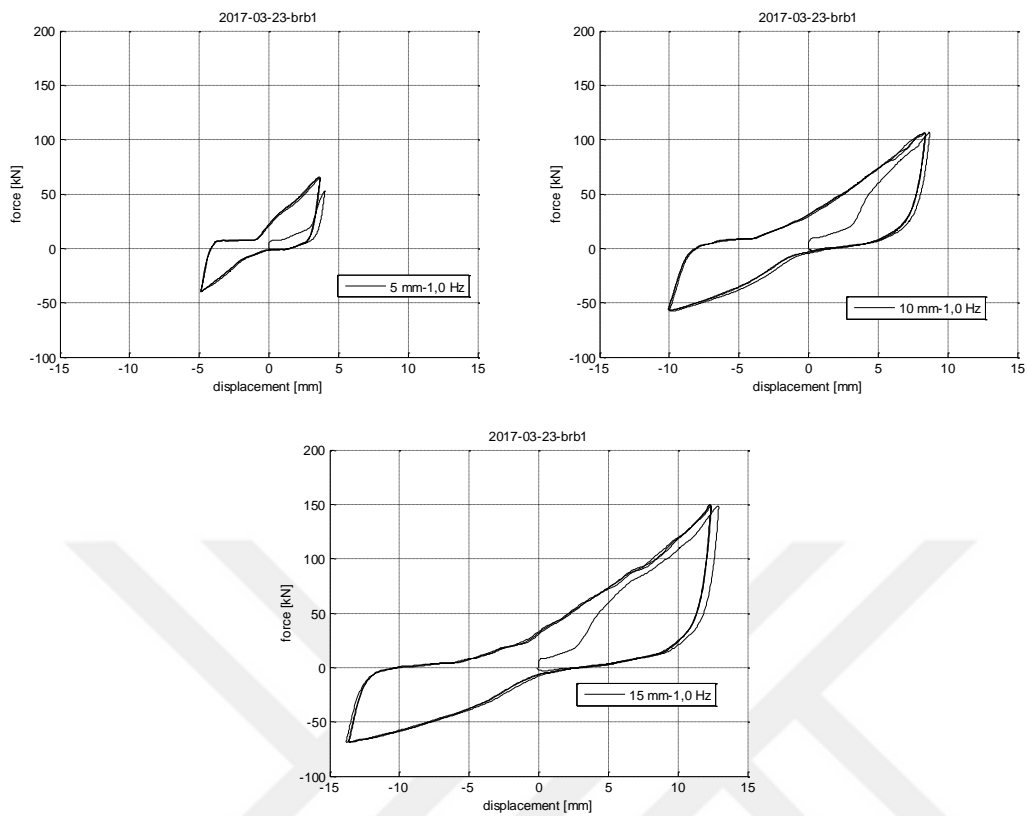


Figure A-14. Hysteresis loops of configuration BRB at 1.0Hz frequency and different displacement amplitudes

Table A-14. Results for BRB tests

d [mm]	f [Hz]	d ⁺ [mm]	d ⁻ [mm]	F ⁺ [kN]	F ⁻ [kN]	EDC [kNm]	k _{eff} [kN/m]	c _{eq} [kNs/m]	ξ_{eff}	AR at d ⁺	AR at d ⁻
5	0,5	3.70	-4.93	63.44	-39.26	0.222	11899.93	1.208	0.22	0.73	1.40
5	1,0	3.69	-4.89	63.51	-39.39	0.244	11994.89	0.671	0.24	0.71	1.36
5	1,5	3.64	-4.89	61.75	-37.71	0.267	11648.54	0.494	0.28	0.72	1.35
5	2,0	3.51	-4.95	61.80	-38.76	0.254	11882.50	0.359	0.28	0.72	1.36
5	2,5	3.71	-4.84	61.29	-37.70	0.253	11590.50	0.281	0.25	0.73	1.38
5	3,0	3.59	-4.99	59.46	-38.01	0.236	11359.44	0.217	0.26	0.80	1.35
5	3,5	3.36	-5.11	59.91	-34.90	0.249	11199.11	0.201	0.31	0.95	1.29
5	4,0	3.57	-4.84	59.72	-38.35	0.155	11661.67	0.111	0.17	0.94	1.26
5	4,5	3.80	-4.80	54.99	-39.10	0.170	10979.69	0.104	0.17	0.84	1.16
5	5,0	4.04	-4.53	47.60	-41.23	0.180	10368.51	0.100	0.17	1.34	1.27
10	0,5	8.70	-9.82	101.41	-60.82	0.830	8759.21	0.980	0.20	1.56	1.80
10	1,0	8.40	-10.08	104.75	-56.81	0.838	8744.13	0.497	0.22	1.50	1.80
10	1,5	8.41	-10.04	104.41	-57.98	0.725	8800.59	0.288	0.19	1.48	1.77
10	2,0	8.42	-9.99	101.62	-57.26	0.810	8632.75	0.242	0.21	1.47	1.75
10	2,5	8.04	-9.85	96.38	-56.50	0.901	8545.77	0.228	0.26	1.46	1.81
10	3,5	8.54	-8.82	90.23	-58.28	0.778	8554.95	0.149	0.20	2.47	1.64
15	0,5	12.97	-14.10	151.75	-69.83	1.440	8188.04	0.797	0.17	1.74	1.81
15	1,0	12.40	-13.83	145.52	-68.51	1.515	8165.09	0.447	0.19	1.70	1.83
15	1,5	12.21	-13.09	138.42	-65.57	1.545	8064.64	0.326	0.21	1.62	1.84
15	2,0	11.08	-12.53	134.34	-64.45	1.679	8425.02	0.305	0.26	1.61	1.74
15	2,5	10.79	-12.30	108.03	-58.09	2.133	7195.75	0.324	0.41	1.70	1.82

APPENDIX B

NUMERICAL ANALYSES

B.1 Unfiltered and filtered results

ABAQUS loops have some slight oscillations. These oscillations are based on numerical solution with explicit dynamic analysis. To eliminate the oscillations, all the numerical results reported from ABAQUS are filtered with the same cut-off frequency to keep to the consistency and so as to be able to compare the parameters without introducing any shift due to the filter. The effect of filter on the results can be observed from Figure B-1. It is seen that the filter changes neither the character of the hysteresis loop nor the EDC. Therefore, it can be concluded that the numerical oscillations do not affect the validity of FEA solution. The oscillations can be considered as a numerical noise, a “chatter”, which is like the noise present in the experimental measurements.

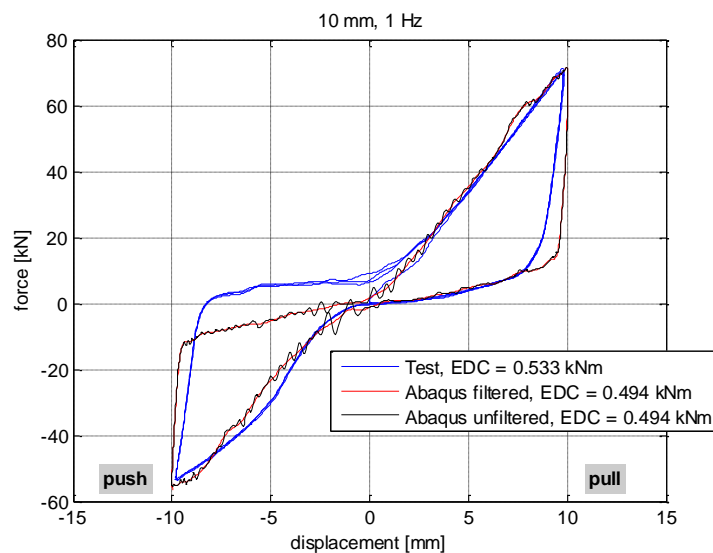


Figure B-1. Comparison of ABAQUS result (unfiltered) against test result for A3-1, 10 mm 1.0 Hz

B.2 Free-body diagrams for configuration A3-1 under 10mm at 1.0 Hz

B.2.1 Top elastomeric block

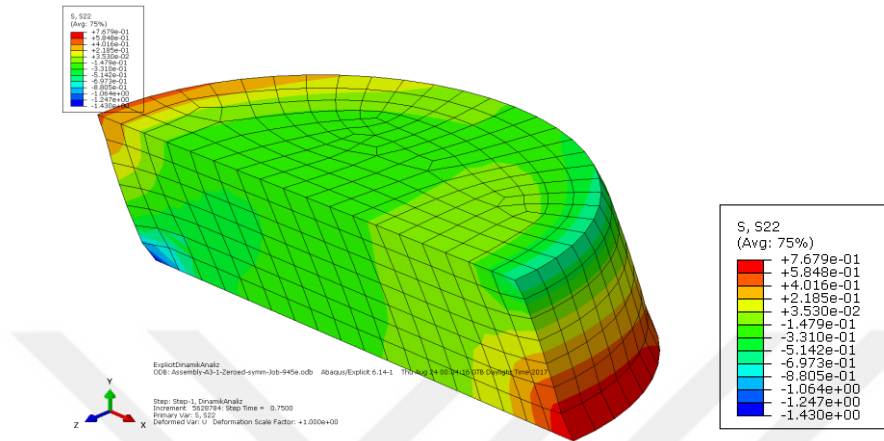


Figure B-2. S22 contour plot of top EB at maximum pull

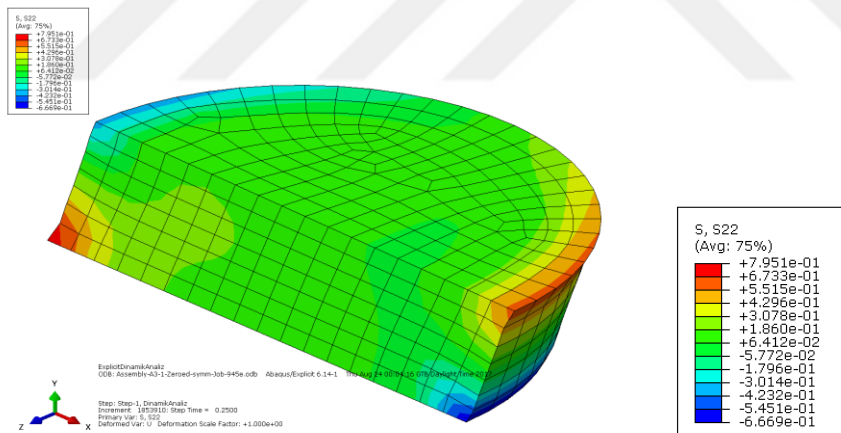


Figure B-3. S22 contour plot of top EB at maximum push

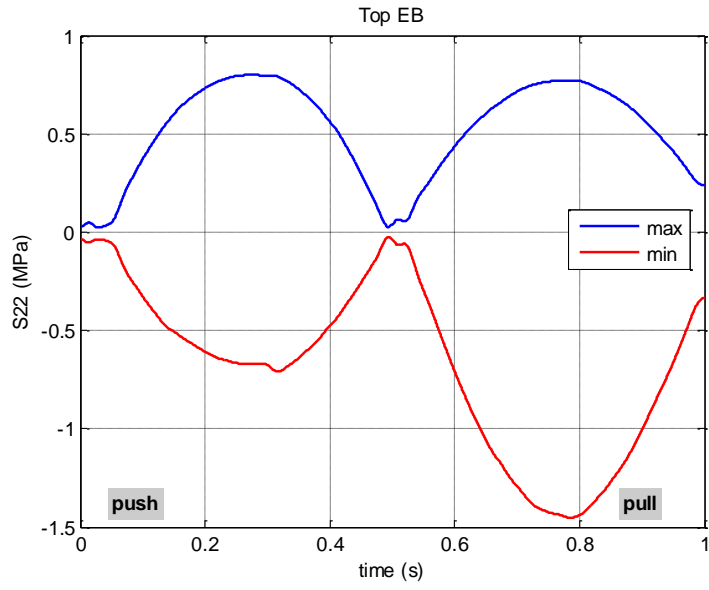


Figure B-4. Envelope curve of S22 of top EB

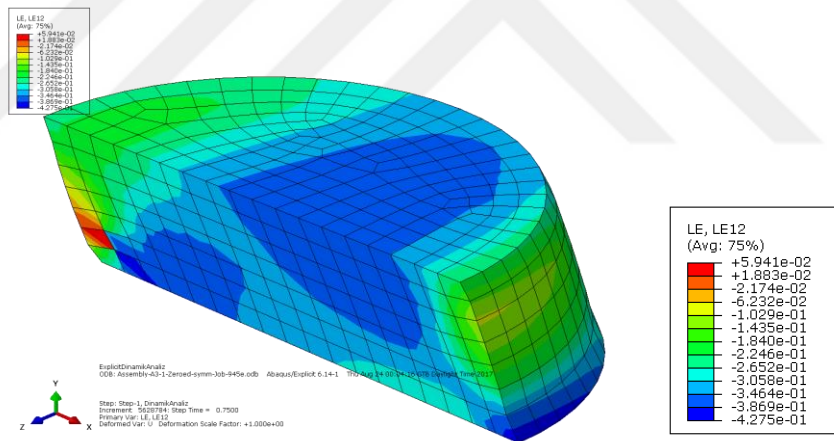


Figure B-5. LE12 contour plot of top EB at maximum pull

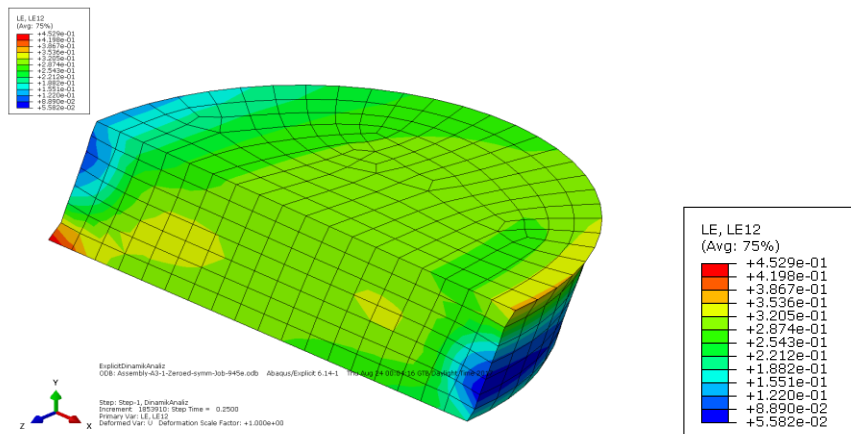


Figure B-6. LE12 contour plot of top EB at maximum push

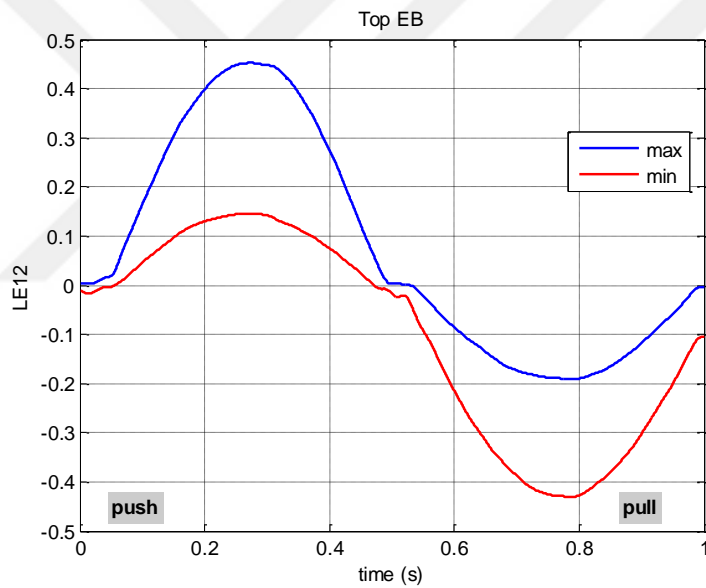


Figure B-7. Envelope curve of LE12 of top EB

B.2.2 Top driven bar

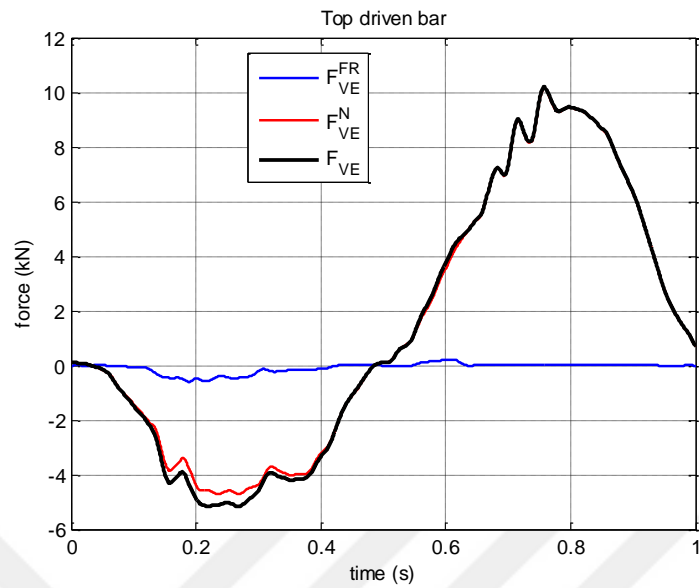


Figure B-8. U1-direction force components transferred from VE unit to top driven bar

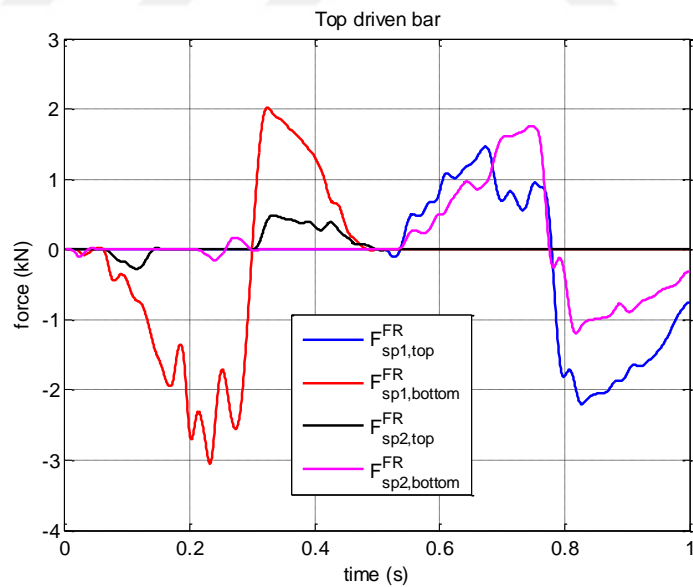


Figure B-9. U1-direction friction forces acting on top driven bar generated from its sliding on the supports

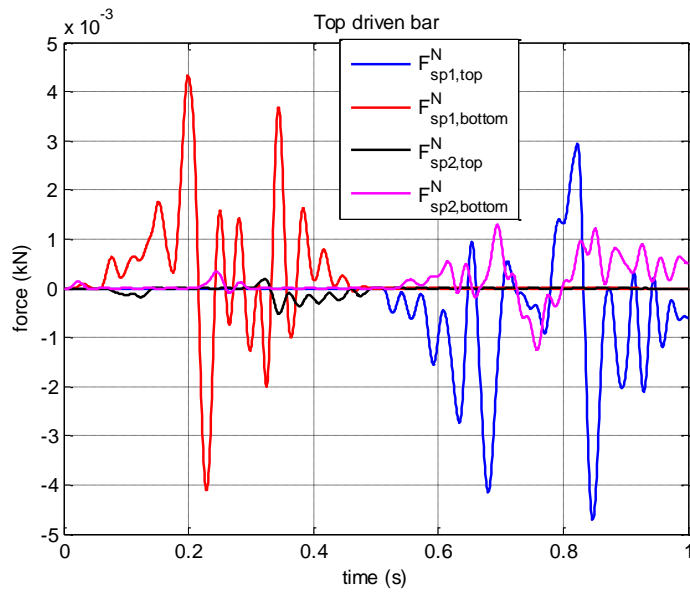


Figure B-10. U1-direction normal forces acting on top driven bar generated from its sliding on the supports

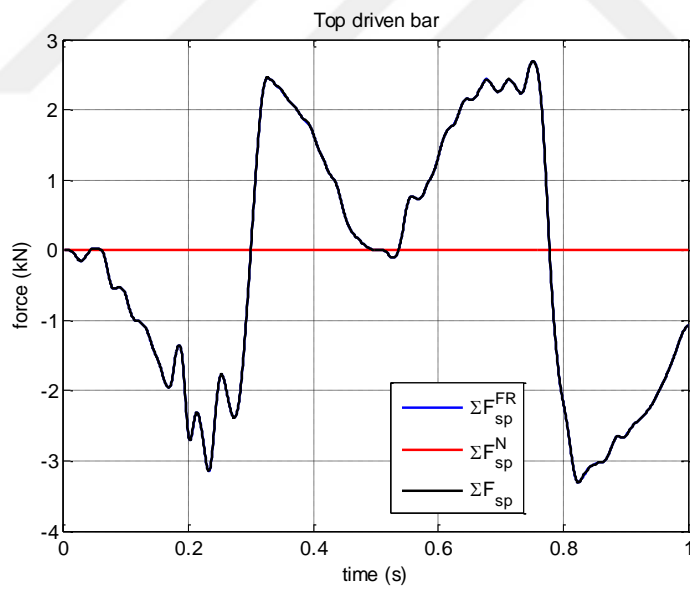


Figure B-11. U1-direction total forces acting on top driven bar generated from its sliding on the supports

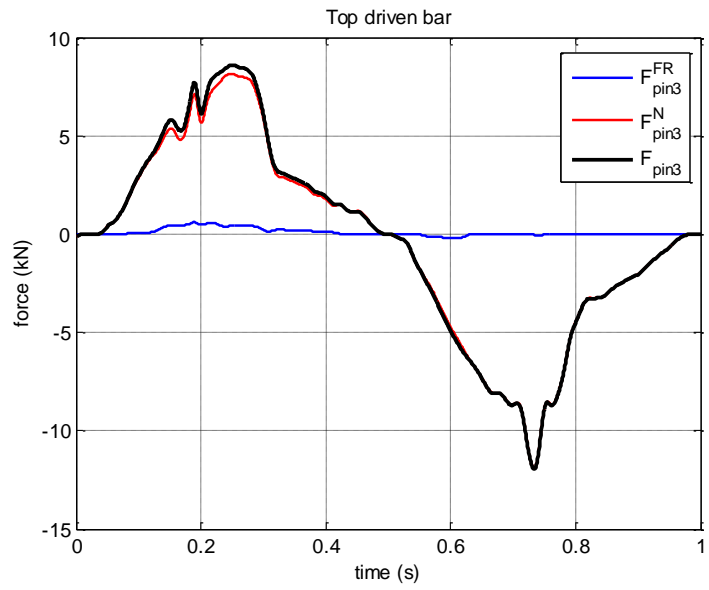


Figure B-12. U1-direction contact forces transferred from Pin3 to top driven bar

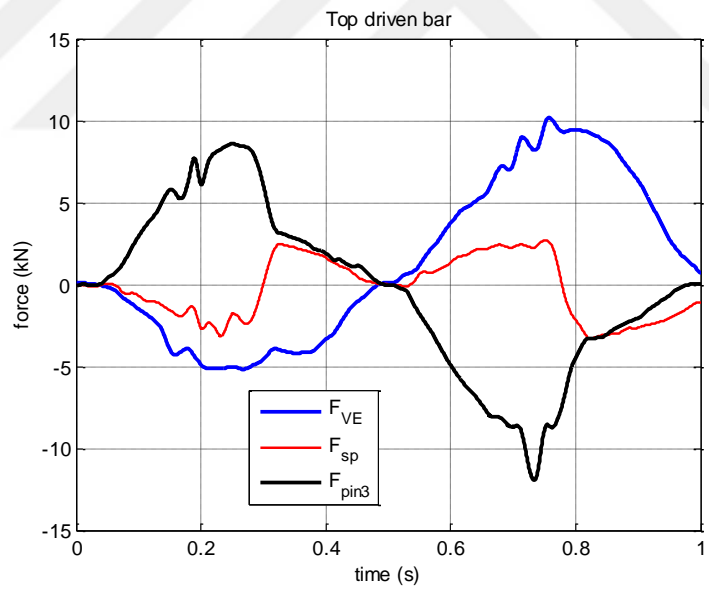


Figure B-13. U1-direction forces acting on top driven bar

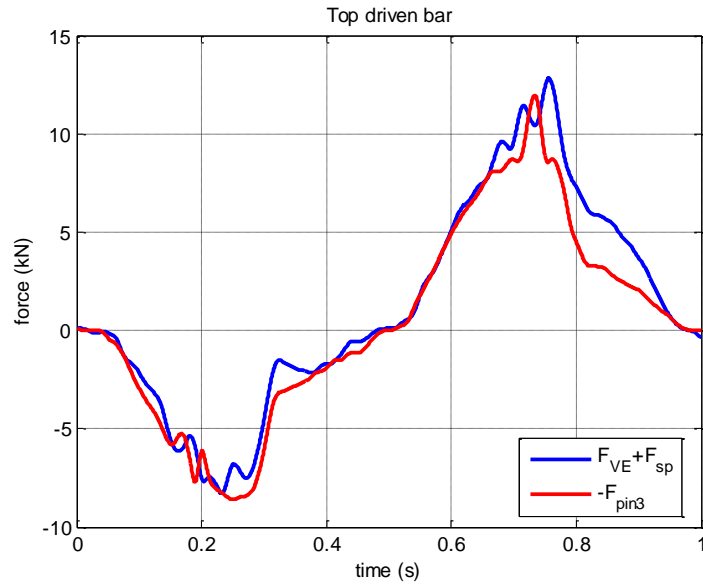


Figure B-14. Magnitude comparison of U1-direction forces acting on top driven bar

The discrepancy is due to the inertial forces which are not included in the dynamic force balance.

B.2.3 Top asymmetric disk

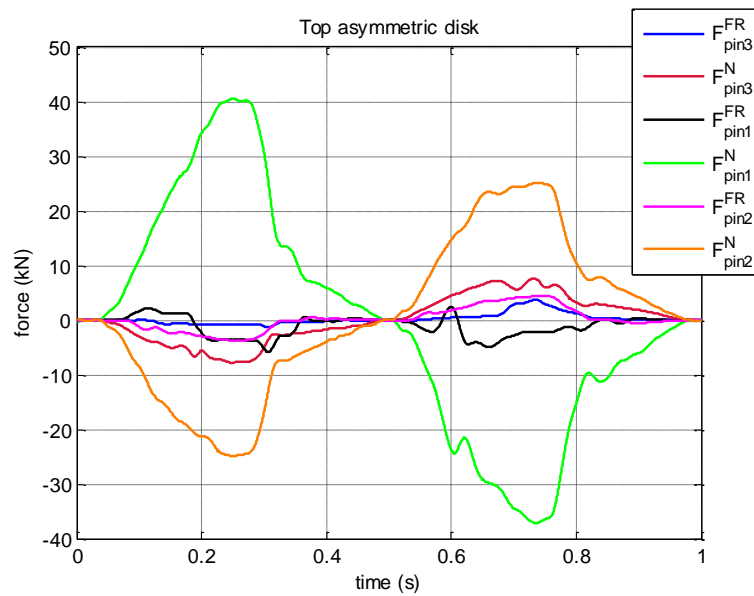


Figure B-15. U1-direction force components transferred from Pin1, Pin2 and Pin3 to top asymmetric disk

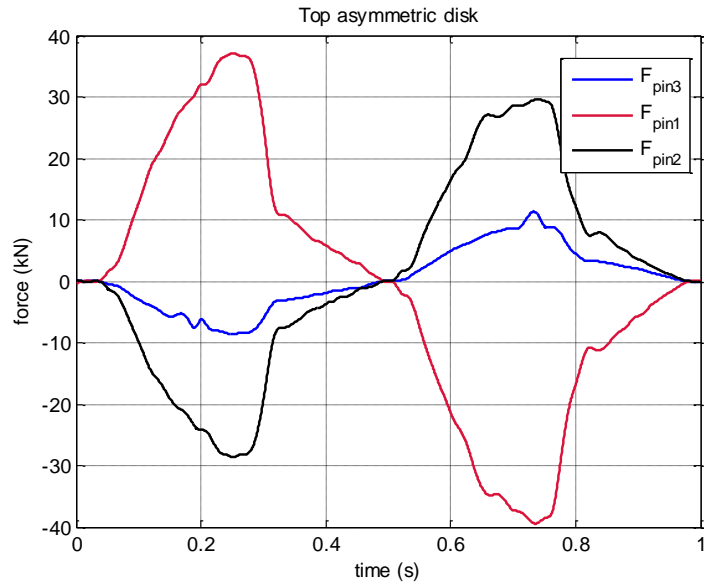


Figure B-16. U1-direction forces transferred from Pin1, Pin2 and Pin3 to top asymmetric disk

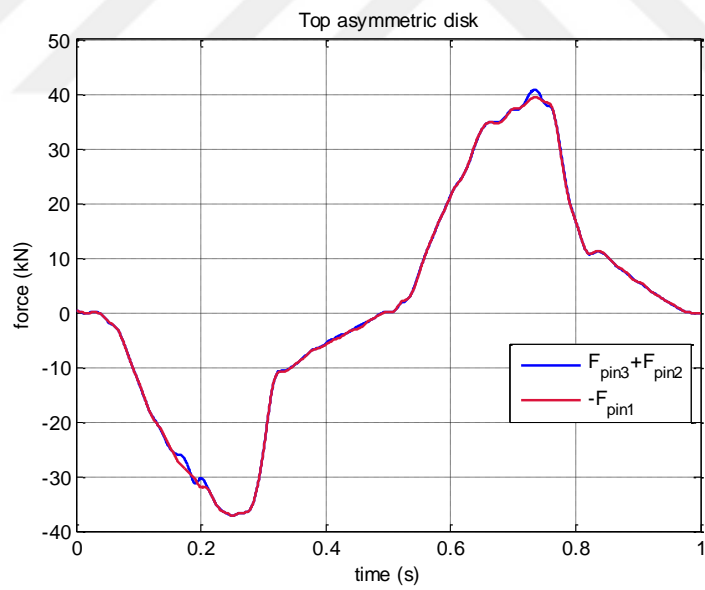


Figure B-17. Magnitude comparison of U1-direction forces acting on top asymmetric disk

APPENDIX C

BUILDING ANALYSES

C.1 Response spectrum parameters

The parameters of the response spectra are calculated as:

$$S_{MS} = F_a S_S$$

$$S_{M1} = F_v S_1$$

where

S_{MS} = the MCE_R , 5% damped, spectral response acceleration parameter at short periods adjusted for site effects as defined in Section 11.4.3

S_S = mapped MCE_R , 5% damped, spectral response acceleration parameter at short periods as defined in Section 11.4.1

S_{M1} = the MCE_R , 5 % damped, spectral response acceleration parameter at a period of 1 s adjusted for site class effects as defined in Section 11.4.3

S_1 = mapped MCE_R , 5% damped, spectral response acceleration parameter at a period of 1 s as defined in Section 11.4.1

The map of ground motion parameters for Turkey is currently in test phase and not verified yet, therefore the mapped acceleration parameters S_S and S_1 are determined for a selected region in the United States from the maps shown in Figure C-1 and Figure C-2.

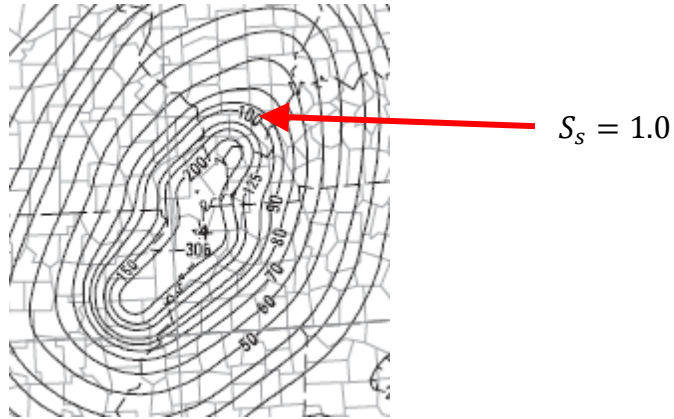


Figure C-1. “ S_s Risk-Targeted Maximum Considered Earthquake (MCE_R) [174]

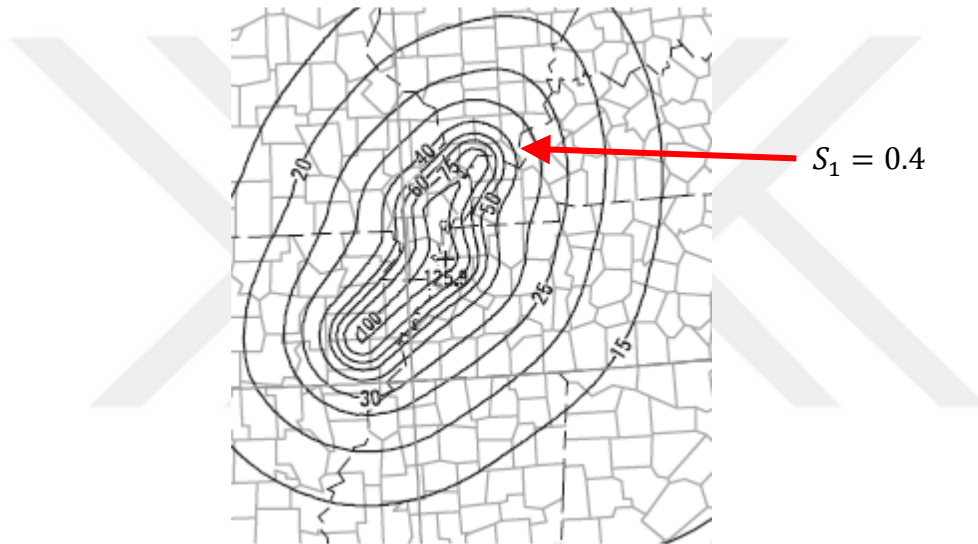


Figure C-2. “ S_1 Risk-Targeted Maximum Considered Earthquake (MCE_R) [174]

$$S_s = 1.0 \quad \text{and} \quad S_1 = 0.4$$

F_a and F_v are site coefficients

$$\text{For } S_s = 1.0 \quad \text{and site class D} \quad F_a = 1.1$$

$$\text{For } S_1 = 0.4 \quad \text{and site class D} \quad F_v = 1.6$$

$$S_{MS} = F_a S_s = 1.1 * 1 = 1.1$$

$$S_{M1} = F_v S_1 = 1.6 * 0.4 = 0.64$$

S_{DS} = the design spectral response acceleration parameter at short periods

S_{D1} = the design spectral response acceleration parameter at 1-s period

T_L = long period transition period

$$S_{DS} = \frac{2}{3} S_{MS} = \frac{2.2}{3}$$

$$S_{D1} = \frac{2}{3} S_{M1} = \frac{1.28}{3}$$

$$T_0 = \frac{0.2 S_{D1}}{S_{DS}} = 0.116s$$

$$T_s = \frac{S_{D1}}{S_{DS}} = 0.58s$$

$$T_L = 12s$$

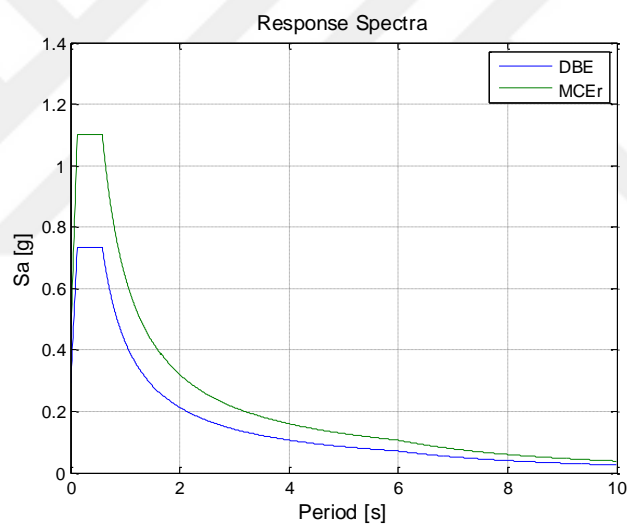


Figure C-3. Response spectra for analyses

C.2 El-Centro earthquake ground motion

C.2.1 4-storey building

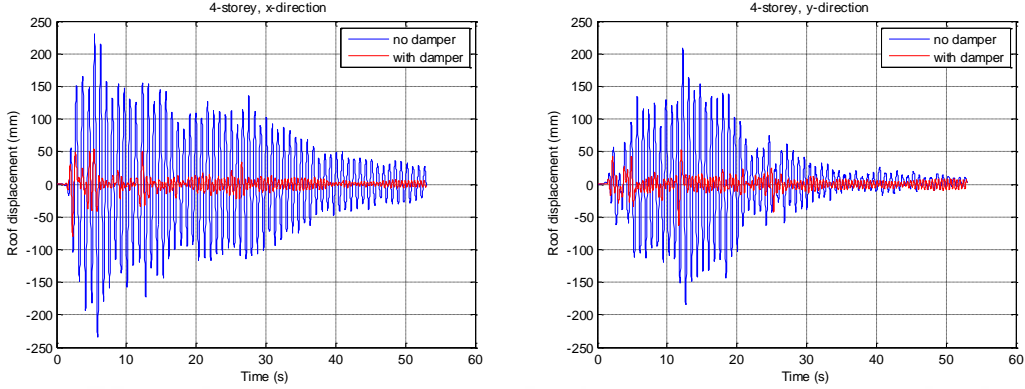


Figure C-4. Roof displacement time histories in x and y directions of the 4-storey building under El-Centro earthquake record

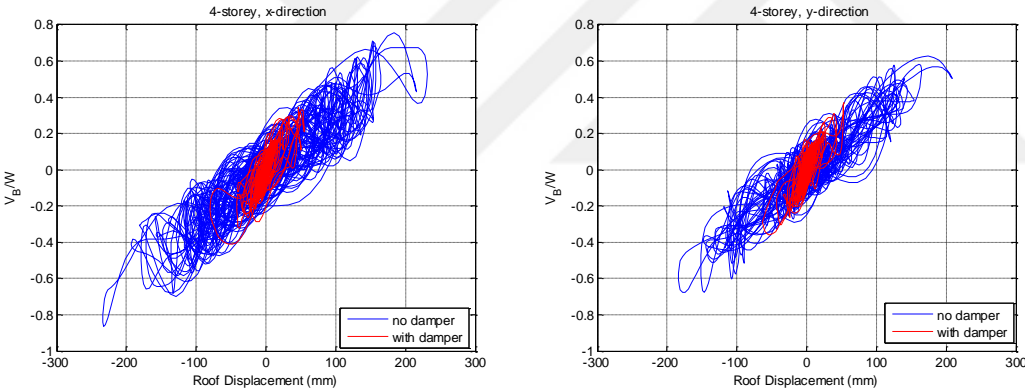


Figure C-5. Base shear vs roof displacement plots in x and y directions of the 4-storey building under El-Centro earthquake record

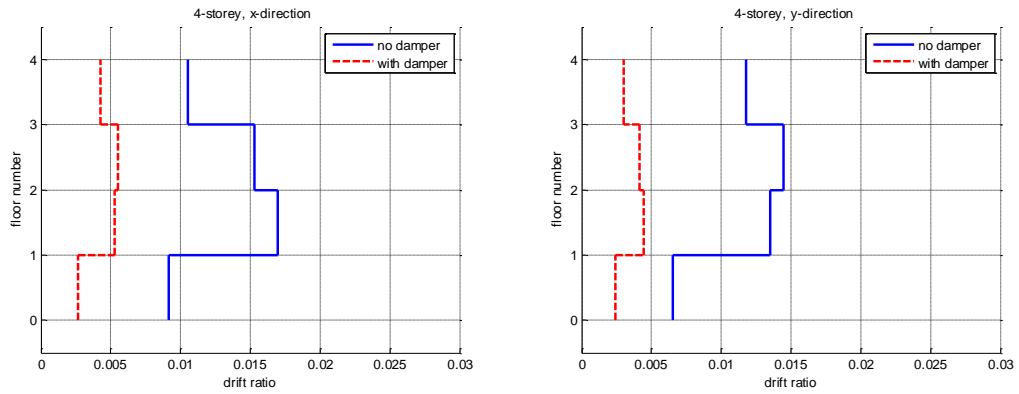


Figure C-6. Drift ratio plots in x and y directions of the 4-storey building under El-Centro earthquake record

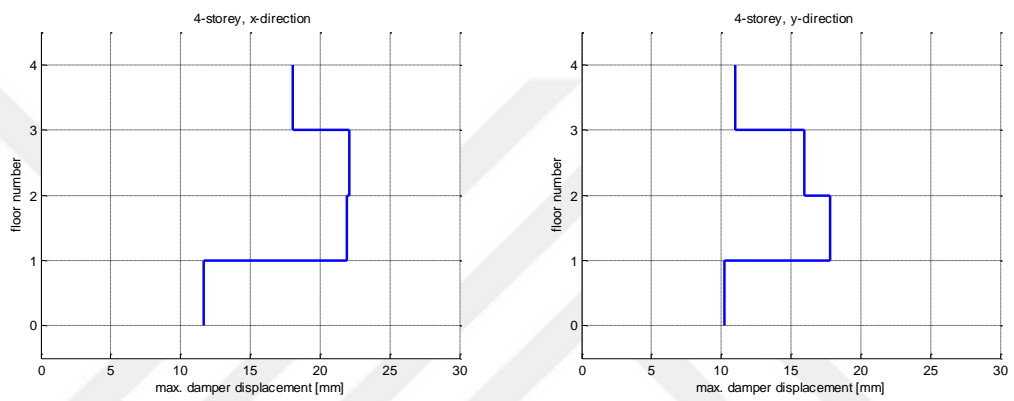


Figure C-7. Plots of maximum damper displacement in x and y directions of the 4-storey building under El-Centro earthquake record

C.2.2 6-storey building

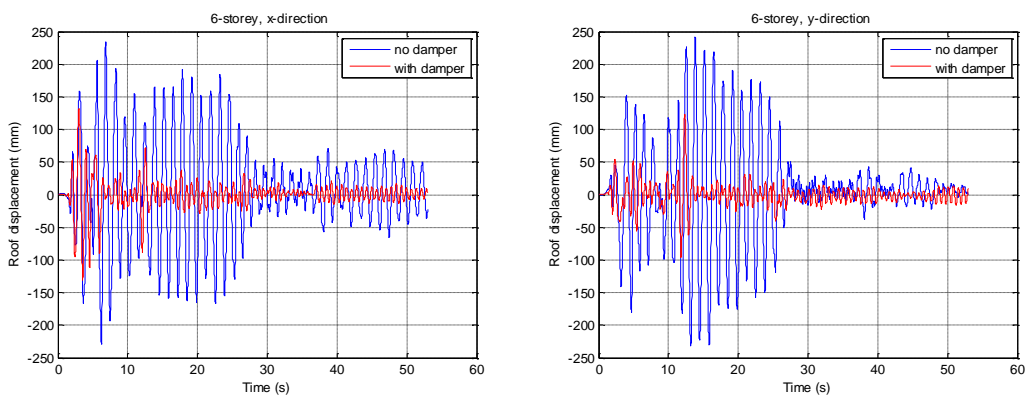


Figure C-8. Roof displacement time histories in x and y directions of the 6-storey building under El-Centro earthquake record

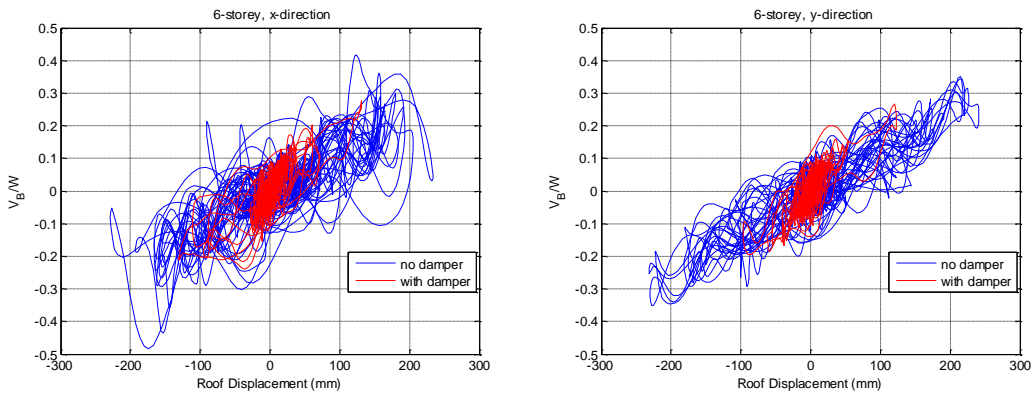


Figure C-9. Base shear vs roof displacement plots in x and y directions of the 6-storey building under El-Centro earthquake record

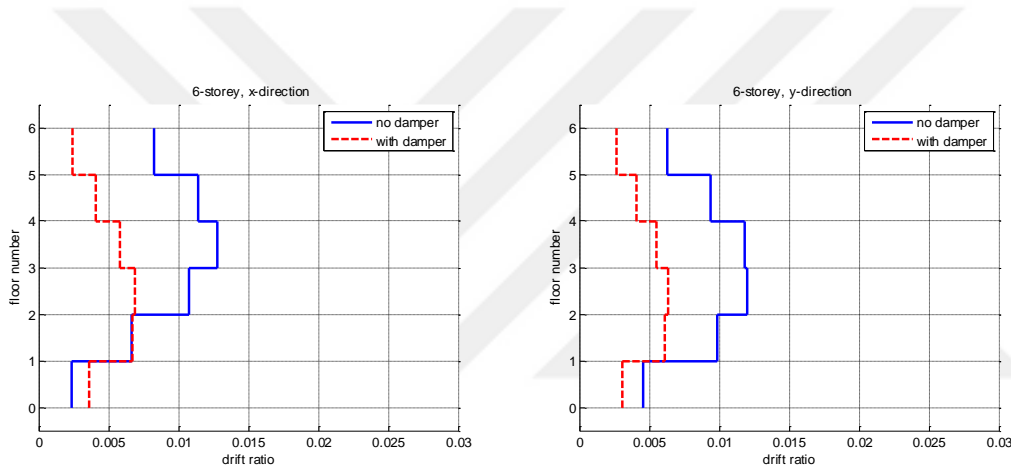


Figure C-10. Drift ratio plots in x and y directions of the 6-storey building under El-Centro earthquake record

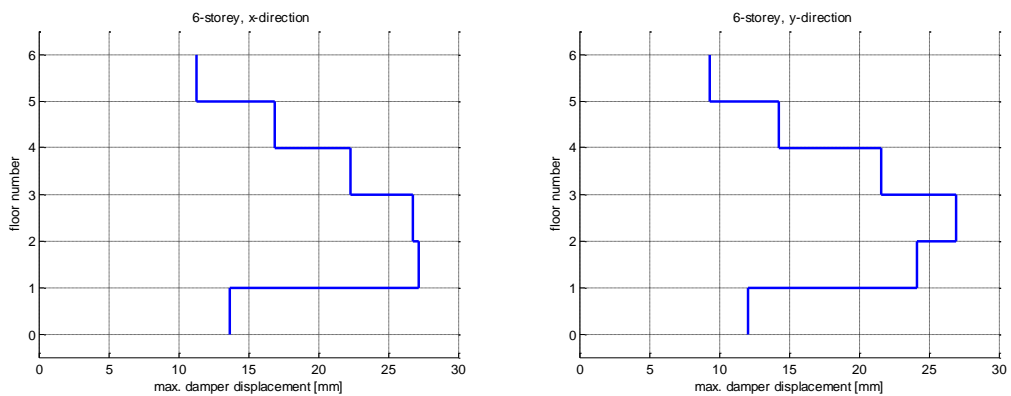


Figure C-11. Plots of maximum damper displacement in x and y directions of the 6-storey building under El-Centro earthquake record

C.2.3 8-storey building

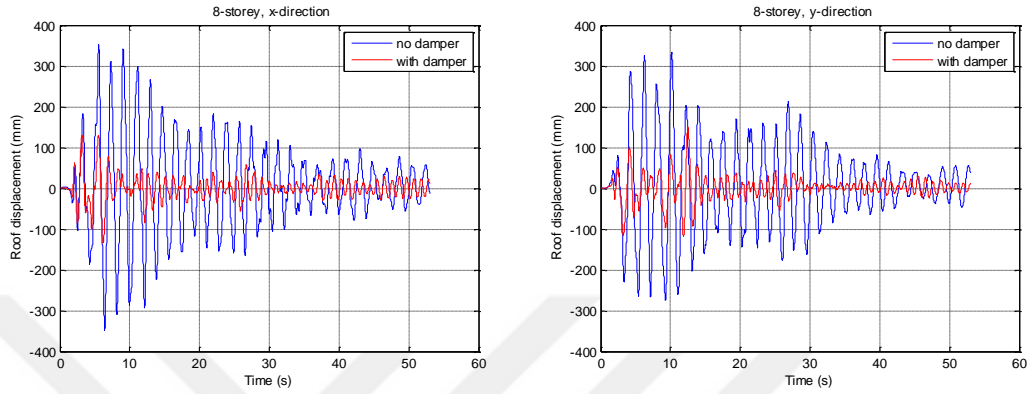


Figure C-12. Roof displacement time histories in x and y directions of the 8-storey building under El-Centro earthquake record

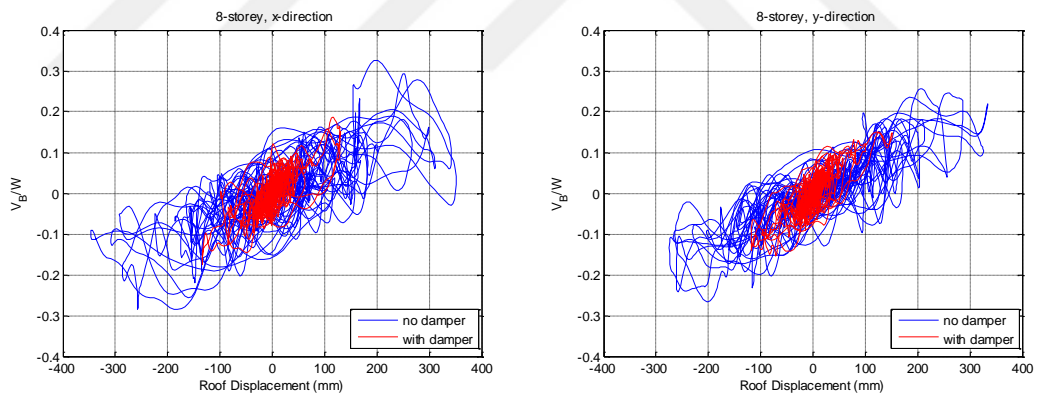


Figure C-13. Base shear vs roof displacement plots in x and y directions of the 8-storey building under El-Centro earthquake record

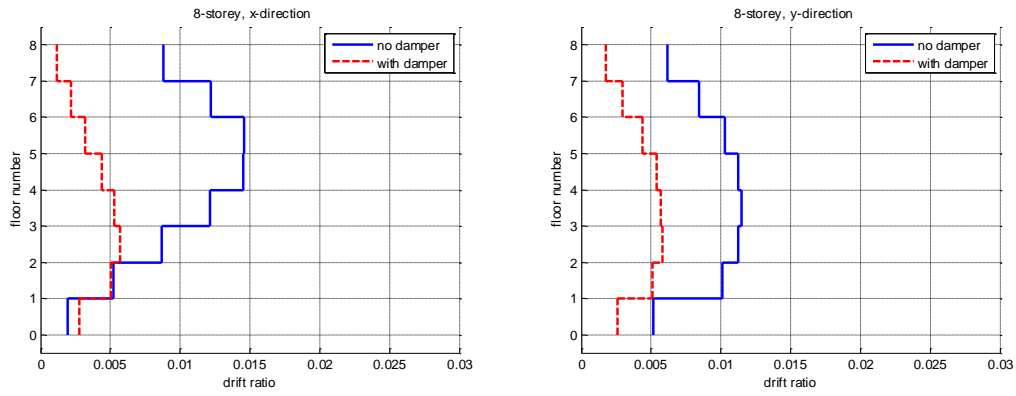


Figure C-14. Drift ratio plots in x and y directions of the 8-storey building under El-Centro earthquake record

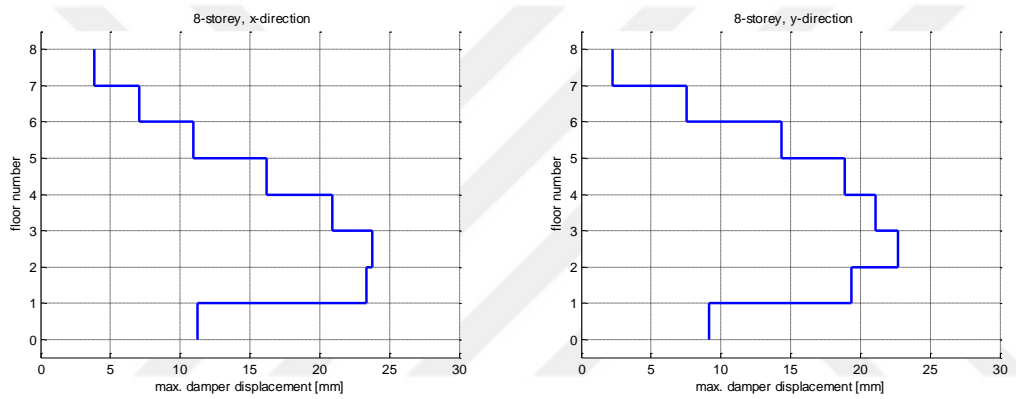


Figure C-15. Plots of maximum damper displacement in x and y directions of the 8-storey building under El-Centro earthquake record

C.3 Kobe earthquake ground motion

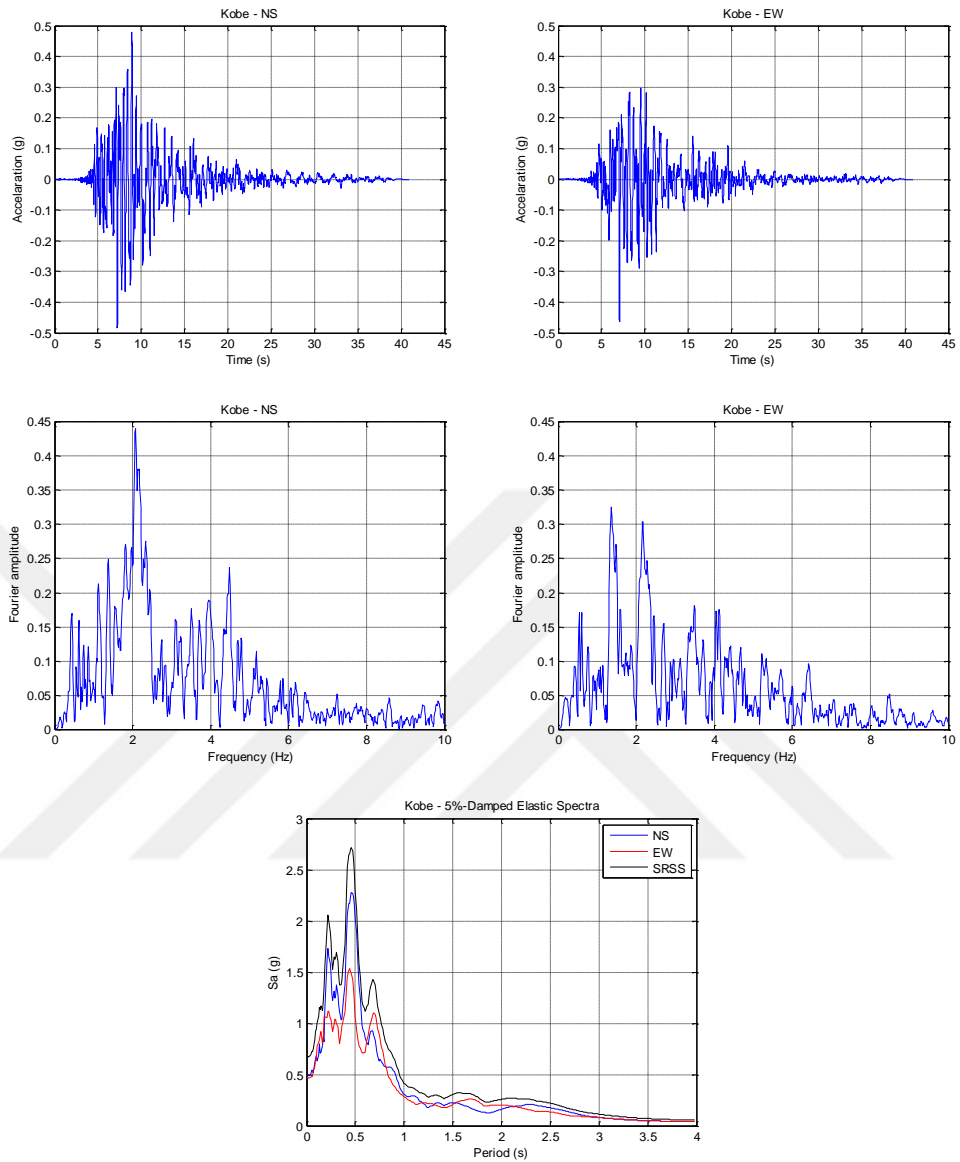


Figure C-16. Kobe earthquake record North-South (NS) and East-West (EW) components

C.3.1 2-storey building

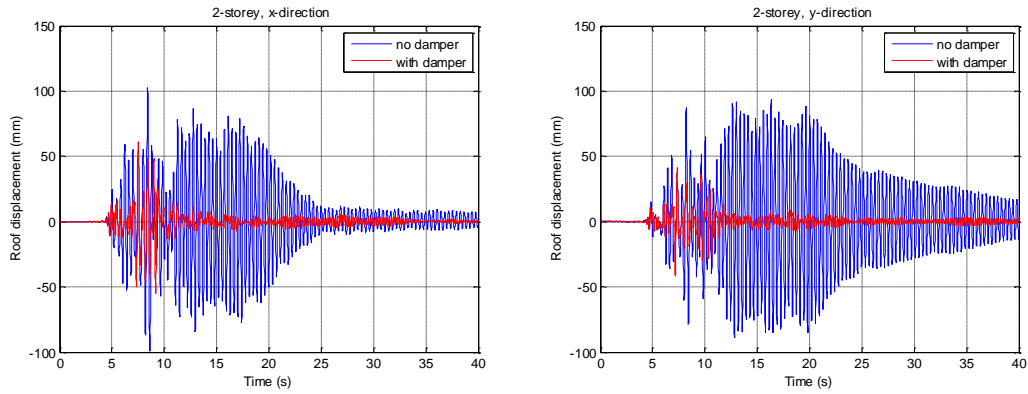


Figure C-17. Roof displacement time histories in x and y directions of the 2-storey building under Kobe earthquake record

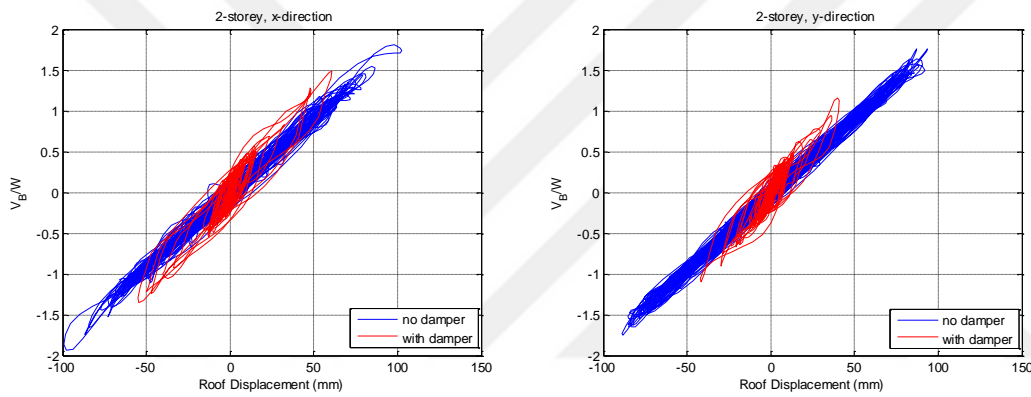


Figure C-18. Base shear vs roof displacement plots in x and y directions of the 2-storey building under Kobe earthquake record

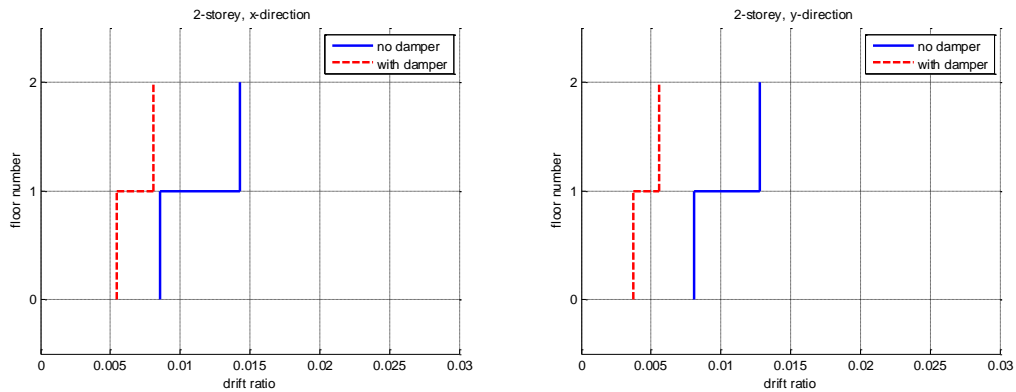


Figure C-19. Drift ratio plots in x and y directions of the 2-storey building under Kobe earthquake record

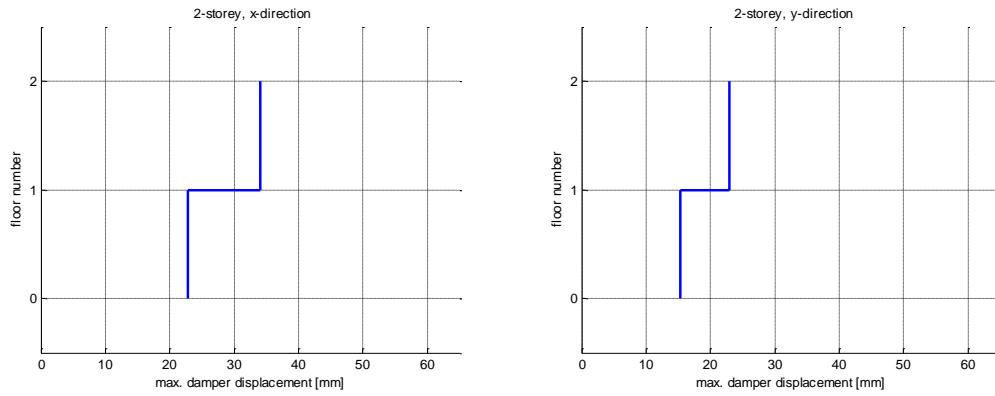


Figure C-20. Plots of maximum damper displacement in x and y directions of the 2-storey building under Kobe earthquake record

C.3.2 4-storey building

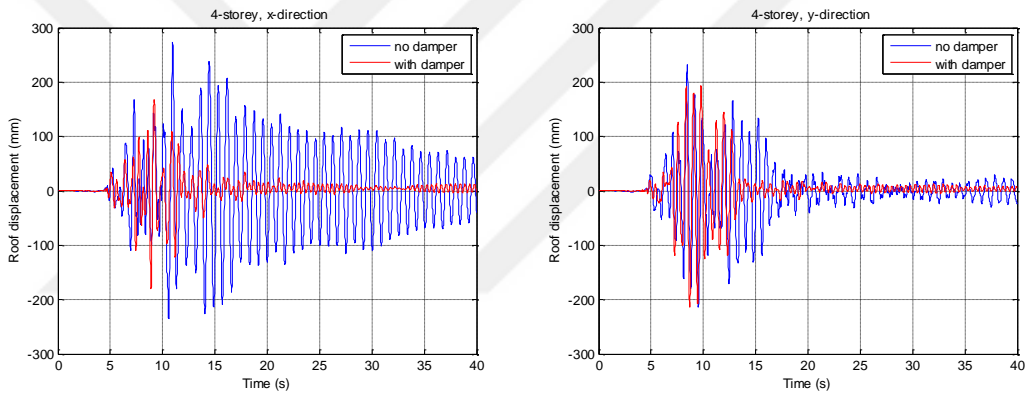


Figure C-21. Roof displacement time histories in x and y directions of the 4-storey building under Kobe earthquake record

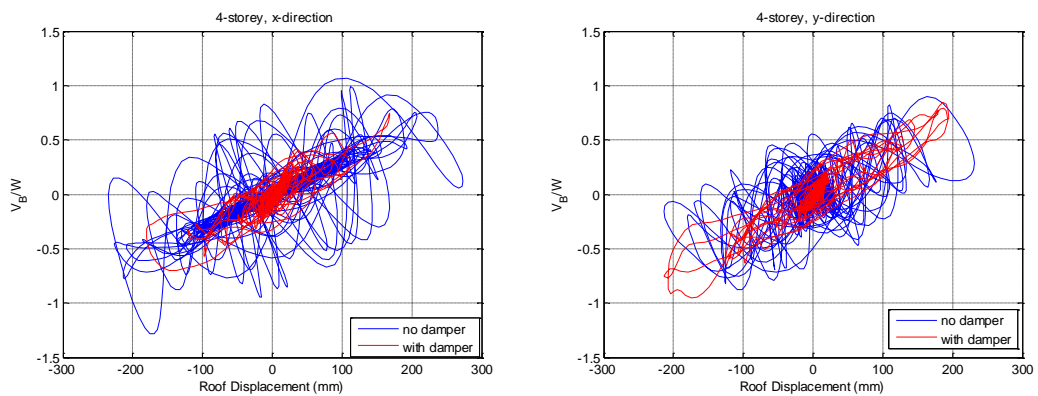


Figure C-22. Base shear vs roof displacement plots in x and y directions of the 4-storey building under Kobe earthquake record

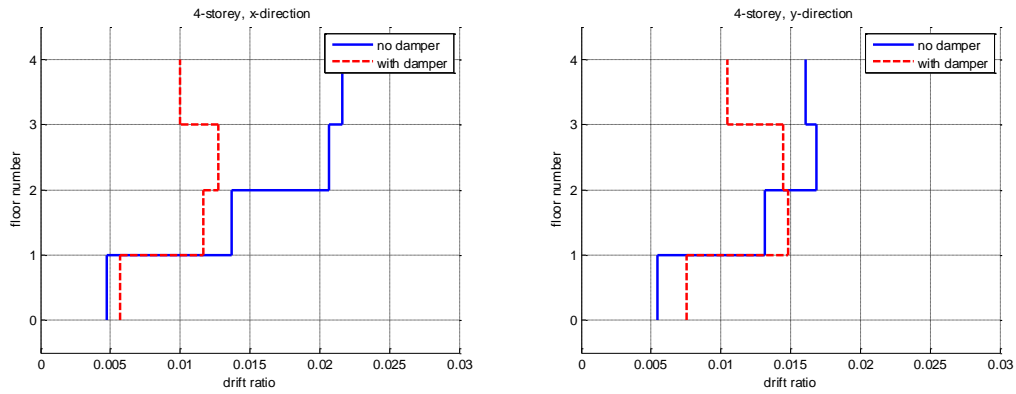


Figure C-23. Drift ratio plots in x and y directions of the 4-storey building under Kobe earthquake record

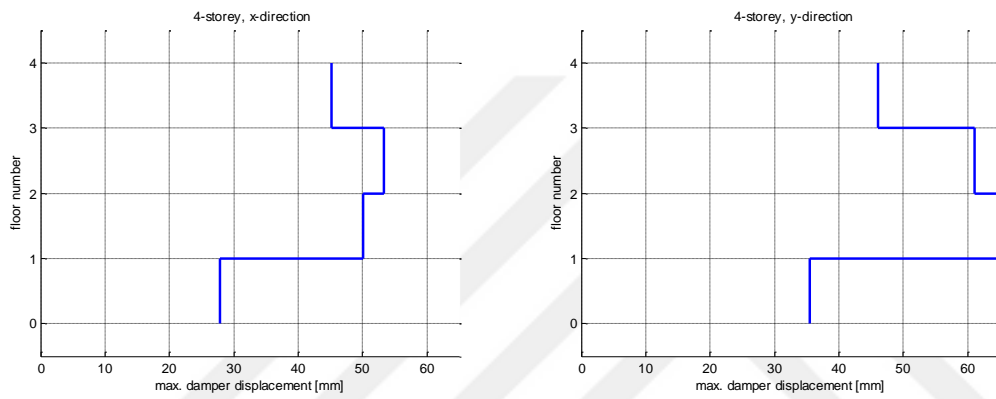


Figure C-24. Plots of maximum damper displacement in x and y directions of the 4-storey building under Kobe earthquake record

C.3.3 6-storey building

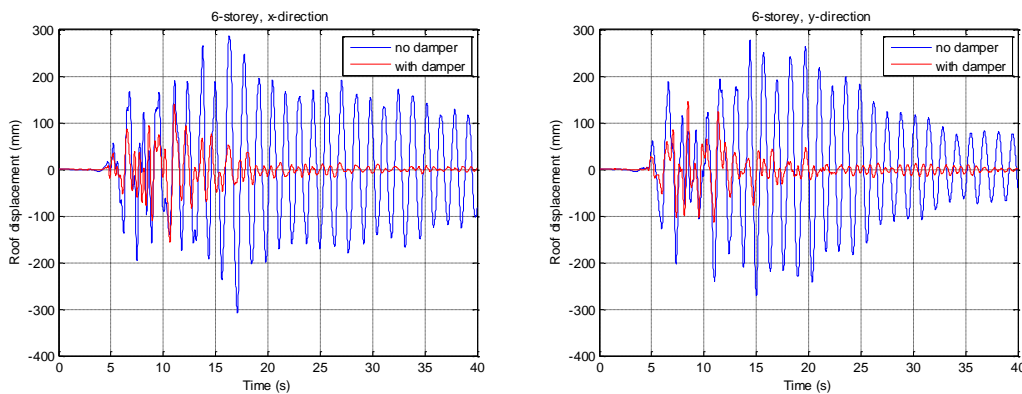


Figure C-25. Roof displacement time histories in x and y directions of the 6-storey building under Kobe earthquake record

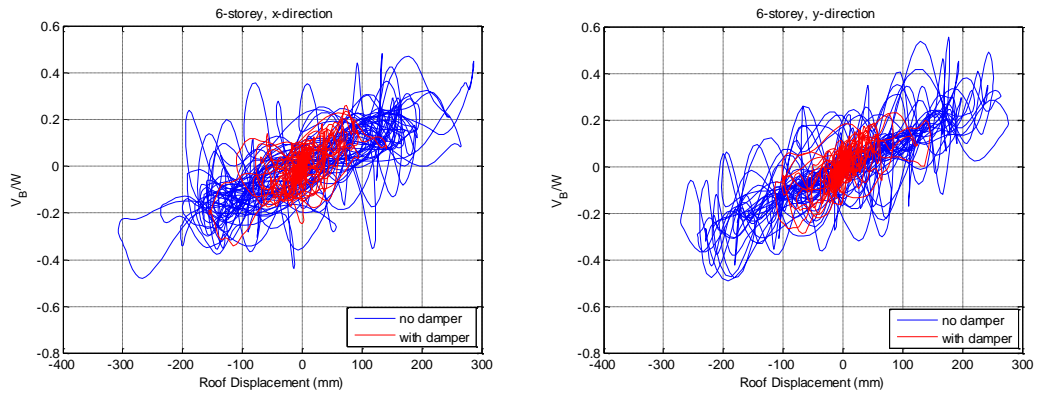


Figure C-26. Base shear vs roof displacement plots in x and y directions of the 6-storey building under Kobe earthquake record

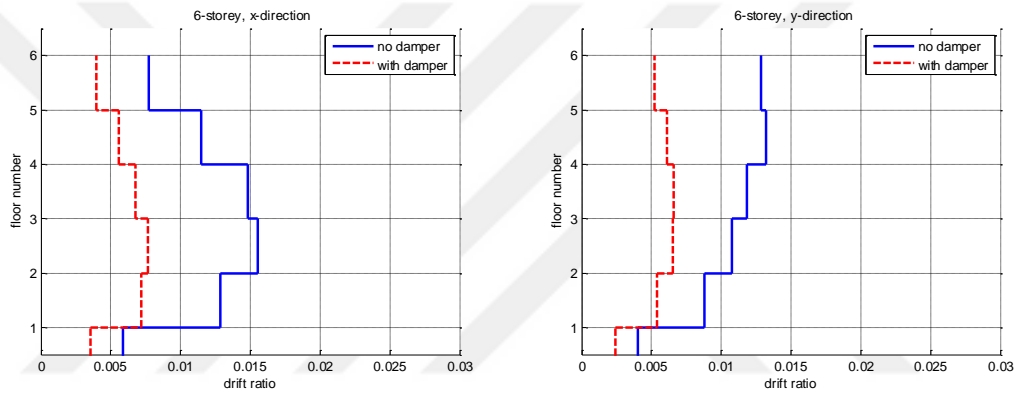


Figure C-27. Drift ratio plots in x and y directions of the 6-storey building under Kobe earthquake record

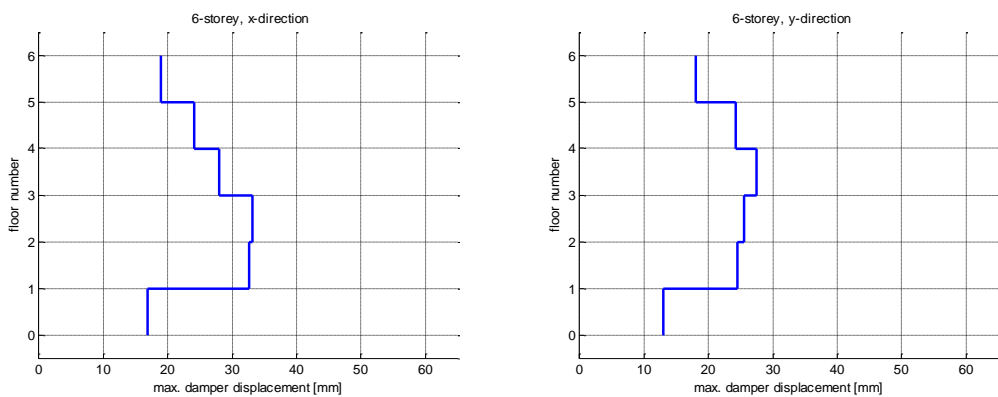


Figure C-28. Plots of maximum damper displacement in x and y directions of the 6-storey building under Kobe earthquake record

C.3.4 8-storey building

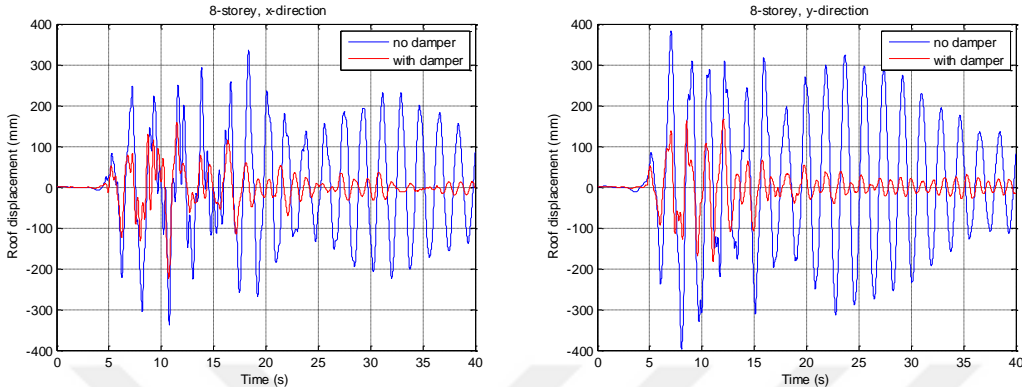


Figure C-29. Roof displacement time histories in x and y directions of the 8-storey building under Kobe earthquake record

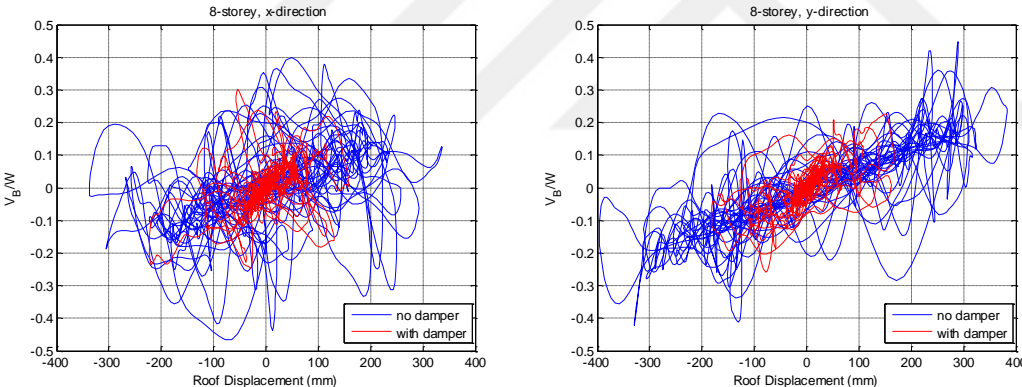


Figure C-30. Base shear vs roof displacement plots in x and y directions of the 8-storey building under Kobe earthquake record

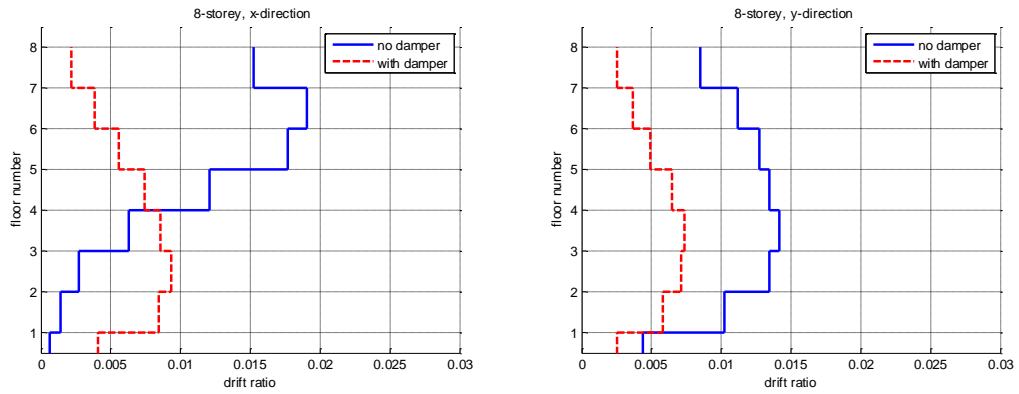


Figure C-31. Drift ratio plots in x and y directions of the 8-storey building under Kobe earthquake record

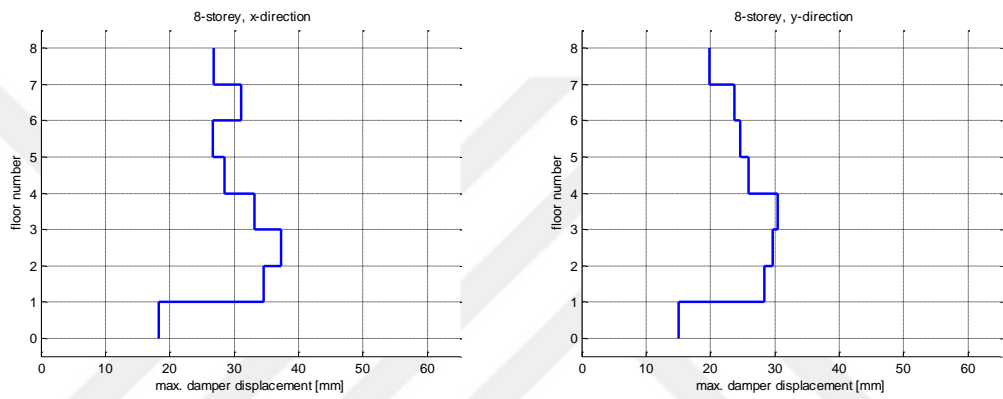


Figure C-32. Plots of maximum damper displacement in x and y directions of the 8-storey building under Kobe earthquake record

C.3.5 10-storey building

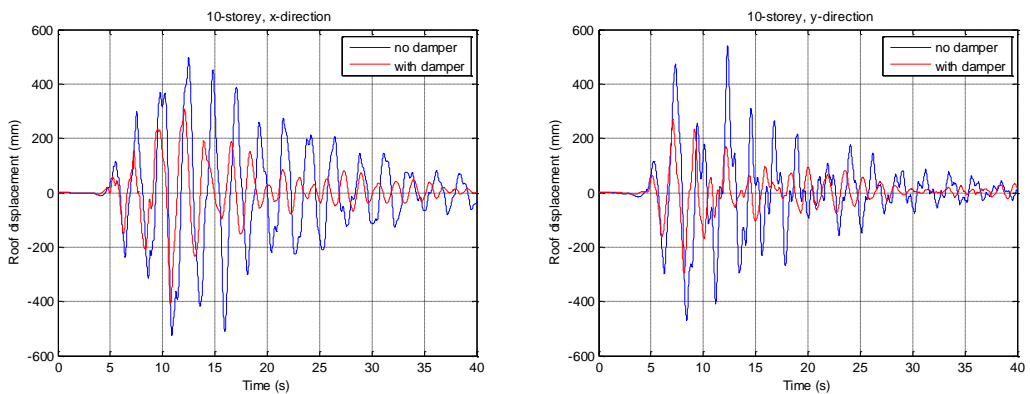


Figure C-33. Roof displacement time histories in x and y directions of the 10-storey building under Kobe earthquake record

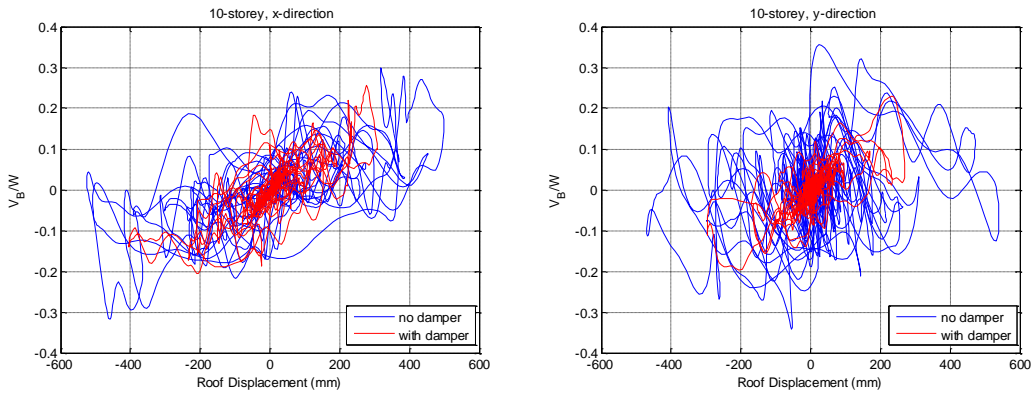


Figure C-34. Base shear vs roof displacement plots in x and y directions of the 10-storey building under Kobe earthquake record

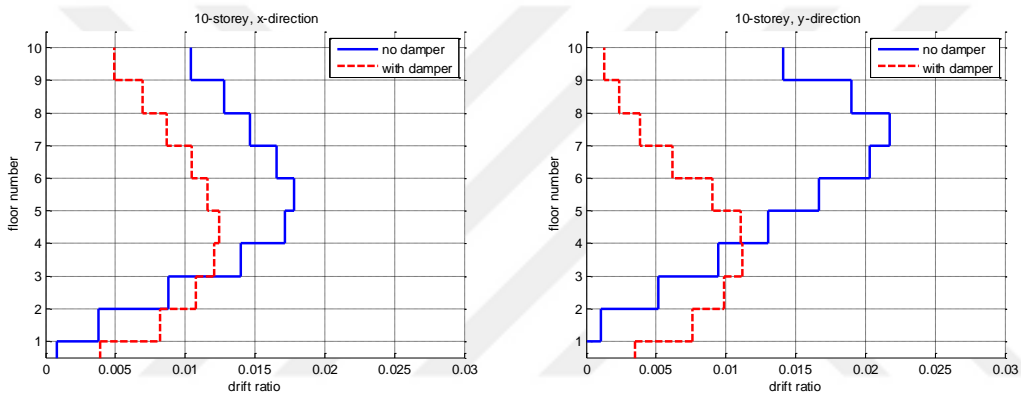


Figure C-35. Drift ratio plots in x and y directions of the 10-storey building under Kobe earthquake record

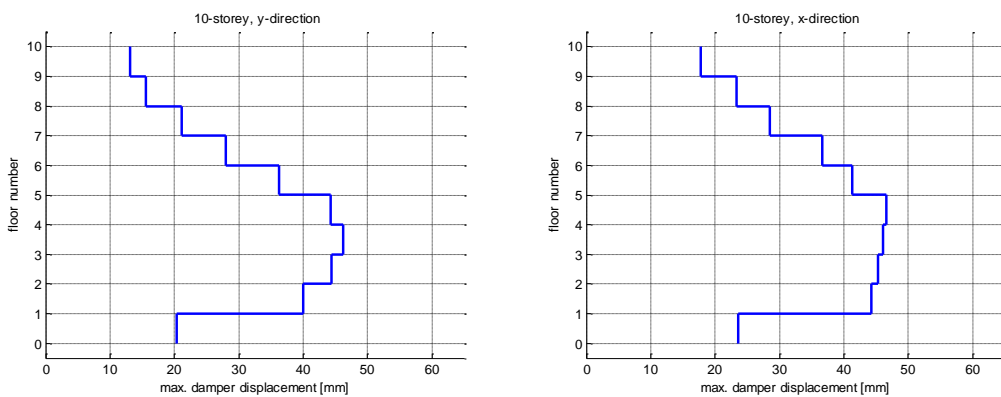


Figure C-36. Plots of maximum damper displacement in x and y directions of the 10-storey building under Kobe earthquake record

C.3.6 Summary

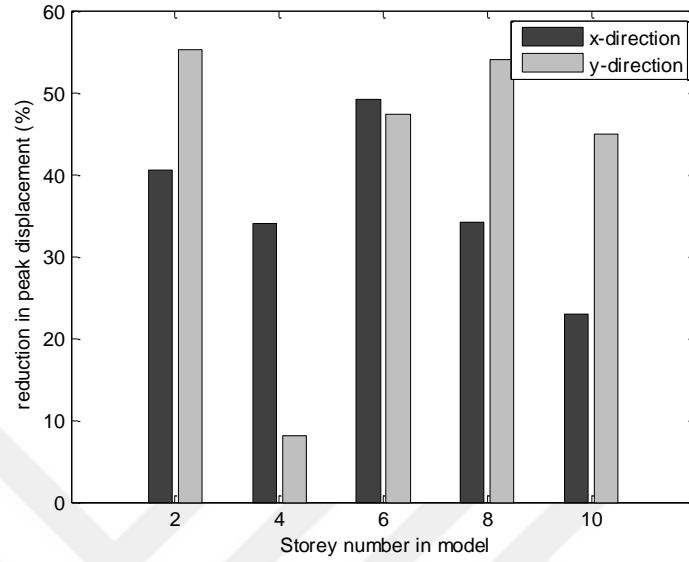


Figure C-37. Reduction in peak displacement for different models under Kobe earthquake record

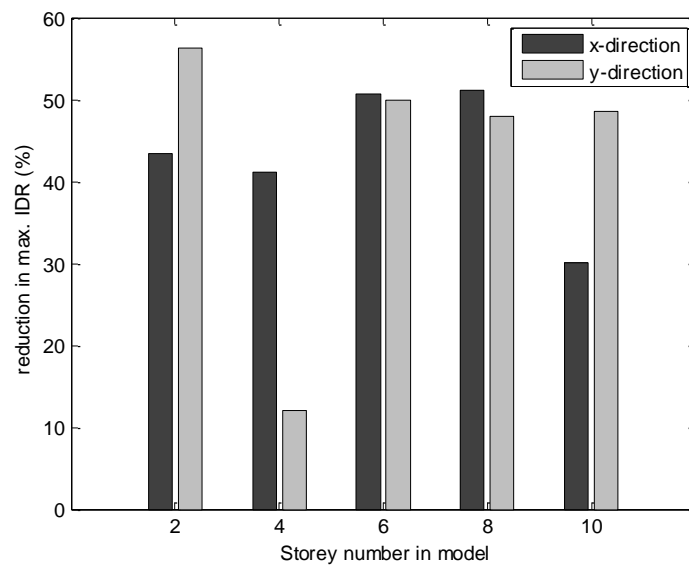


Figure C-38. Reduction in max. IDR for different models under Kobe earthquake record

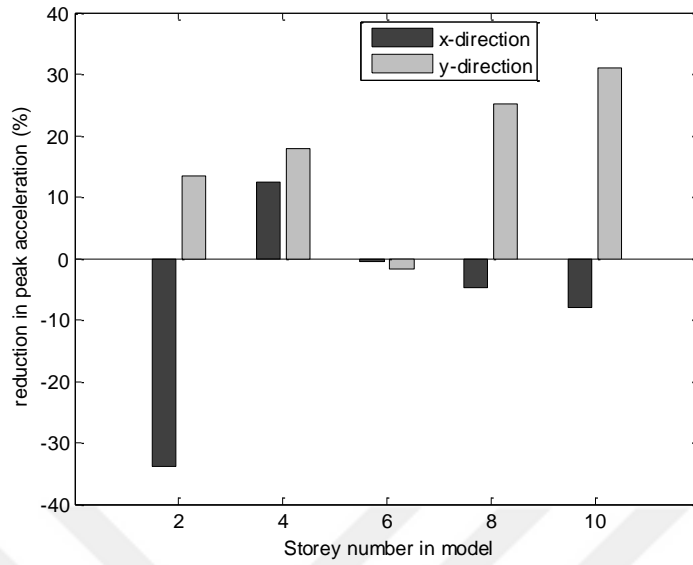


Figure C-39. Reduction in peak acceleration for different models under Kobe earthquake record

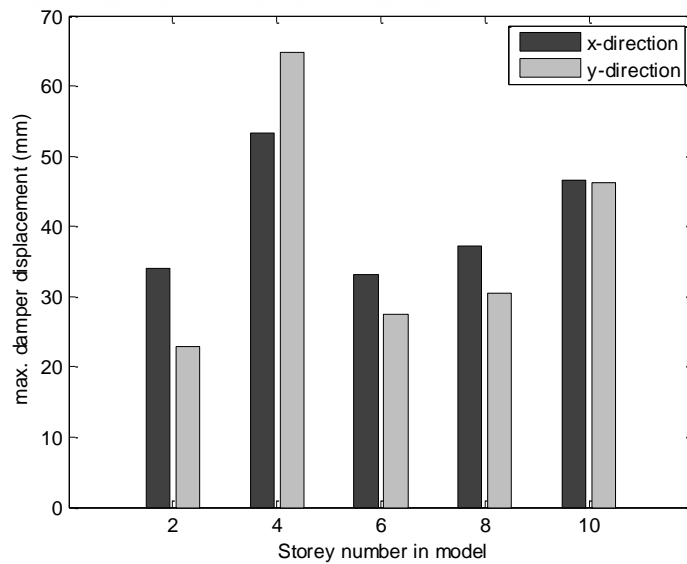


Figure C-40. Maximum damper displacement for different models under Kobe earthquake record

C.4 Landers earthquake ground motion

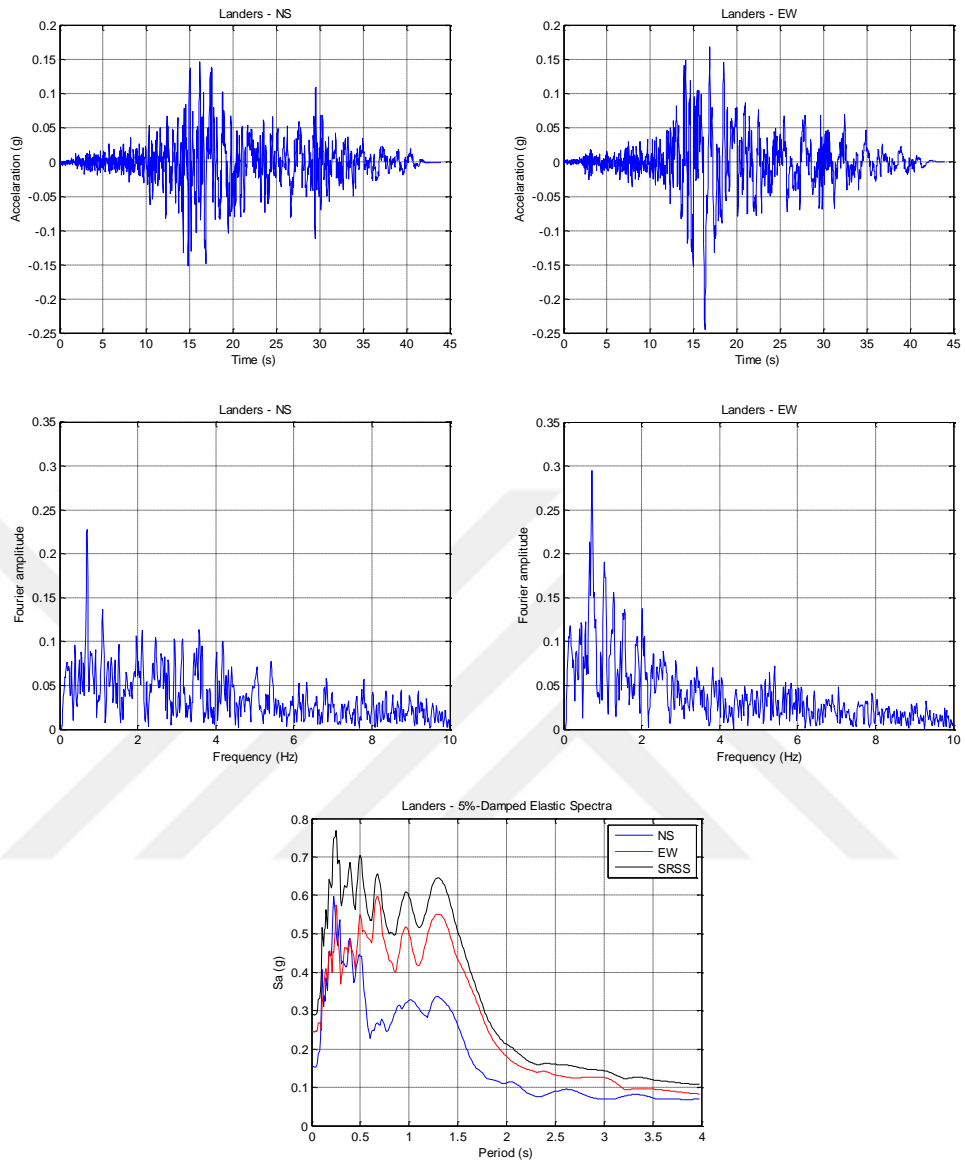


Figure C-41. Landers earthquake record North-South (NS) and East-West (EW) components

C.4.1 2-storey building

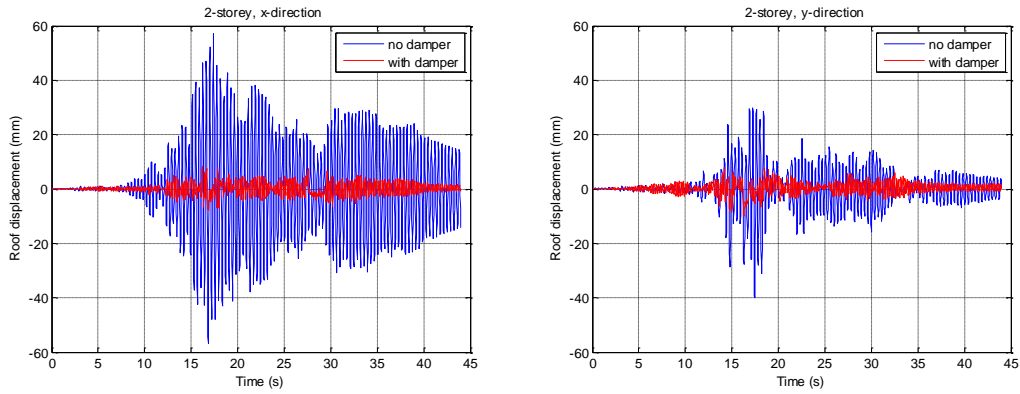


Figure C-42. Roof displacement time histories in x and y directions of the 2-storey building under Landers earthquake record

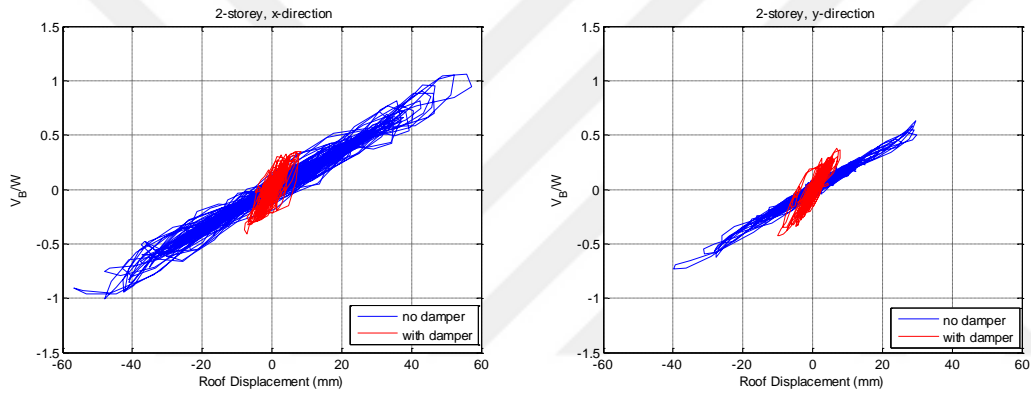


Figure C-43. Base shear vs roof displacement plots in x and y directions of the 2-storey building under Landers earthquake record

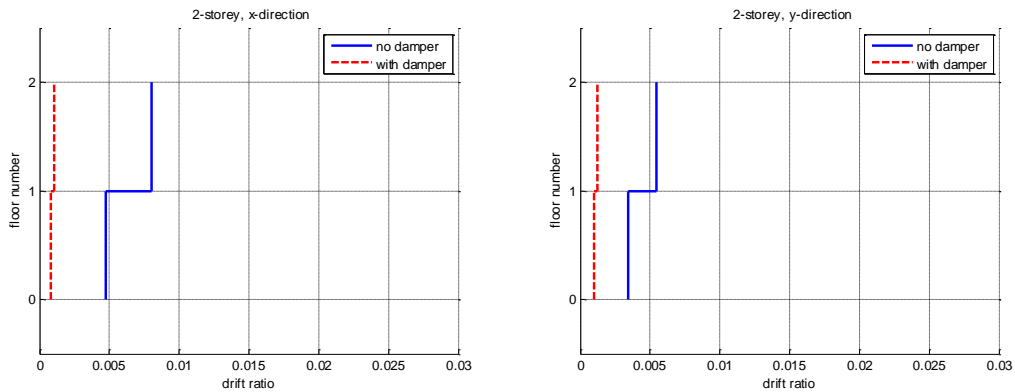


Figure C-44. Drift ratio plots in x and y directions of the 2-storey building under Landers earthquake record

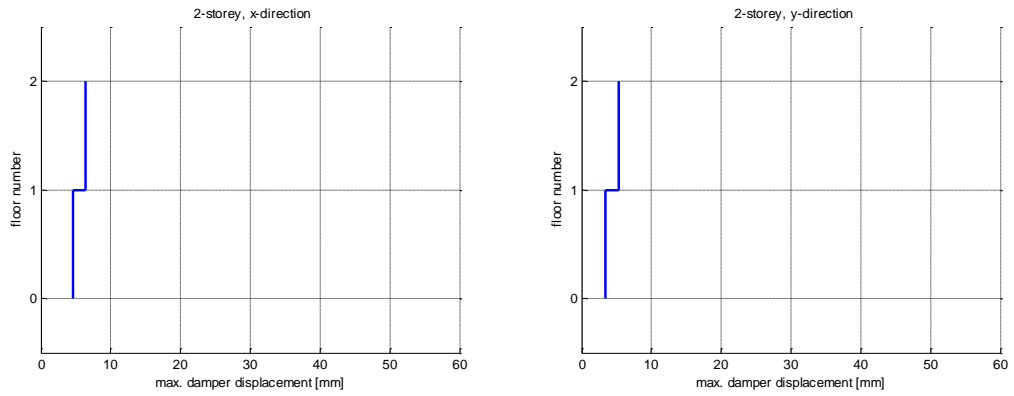


Figure C-45. Plots of maximum damper displacement in x and y directions of the 2-storey building under Landers earthquake record

C.4.2 4-storey building

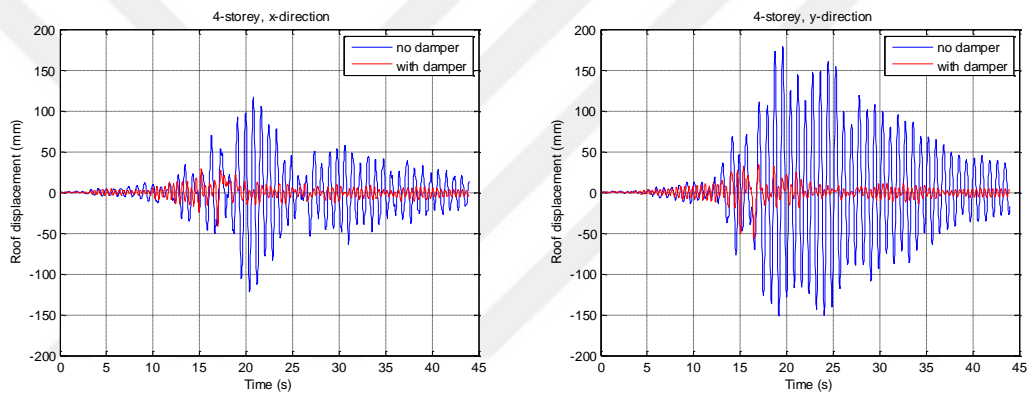


Figure C-46. Roof displacement time histories in x and y directions of the 4-storey building under Landers earthquake record

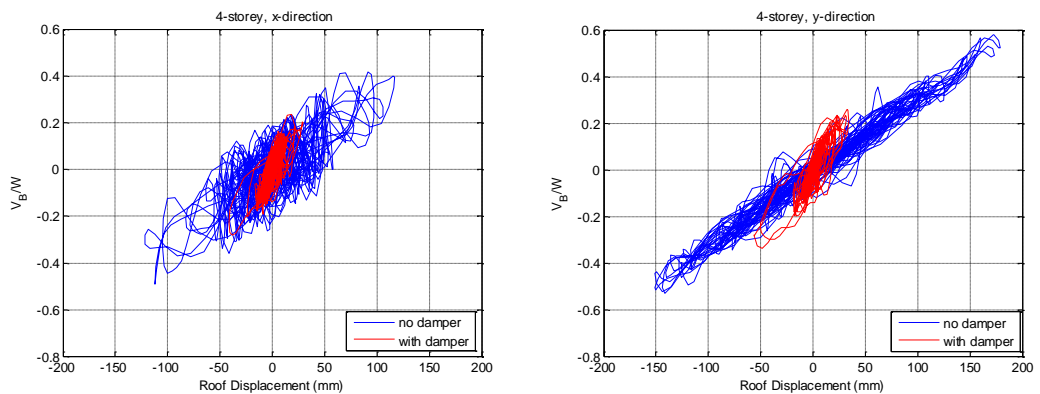


Figure C-47. Base shear vs roof displacement plots in x and y directions of the 4-storey building under Landers earthquake record

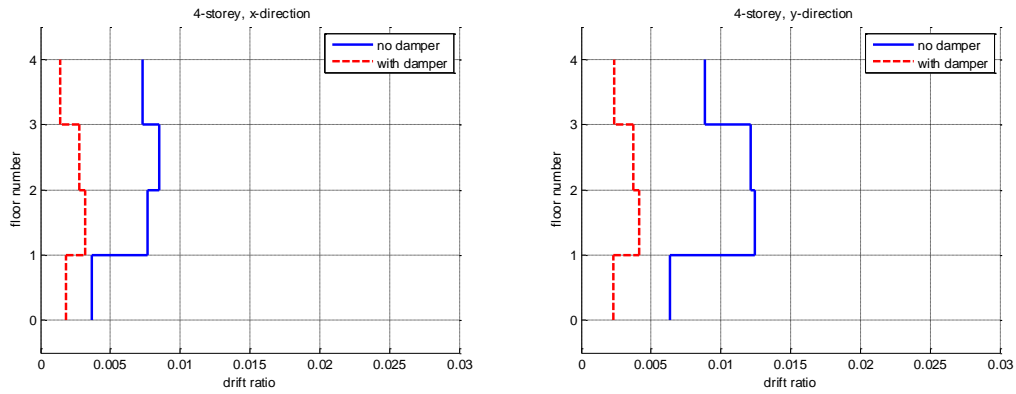


Figure C-48. Drift ratio plots in x and y directions of the 4-storey building under Landers earthquake record

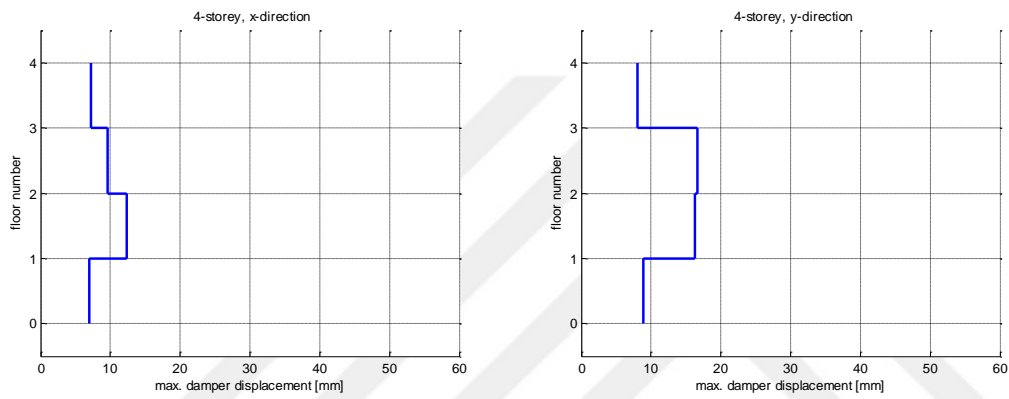


Figure C-49. Plots of maximum damper displacement in x and y directions of the 4-storey building under Landers earthquake record

C.4.3 6-storey building

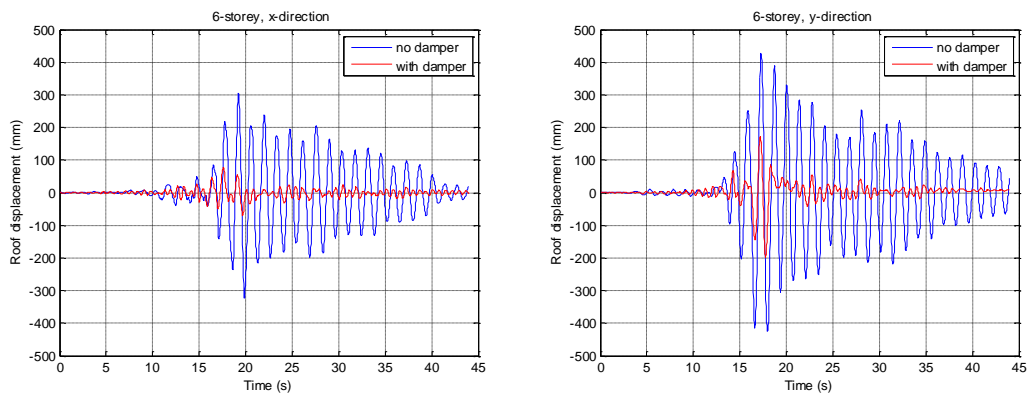


Figure C-50. Roof displacement time histories in x and y directions of the 6-storey building under Landers earthquake record

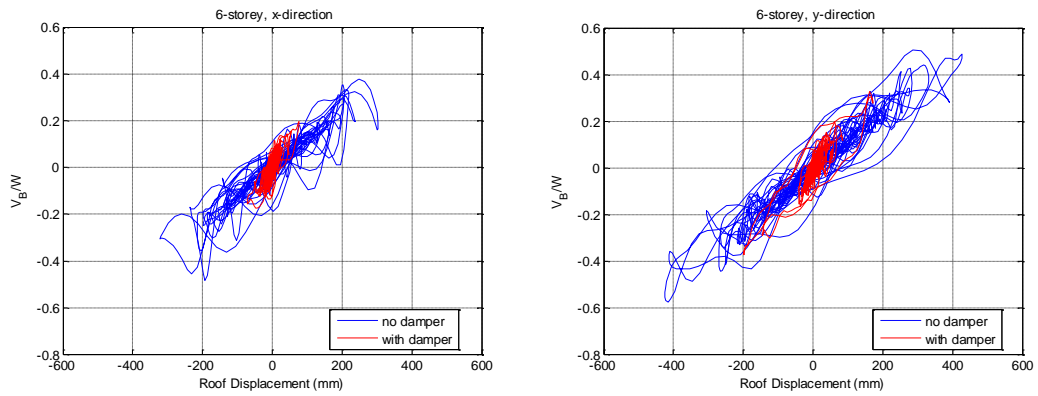


Figure C-51. Base shear vs roof displacement plots in x and y directions of the 6-storey building under Landers earthquake record

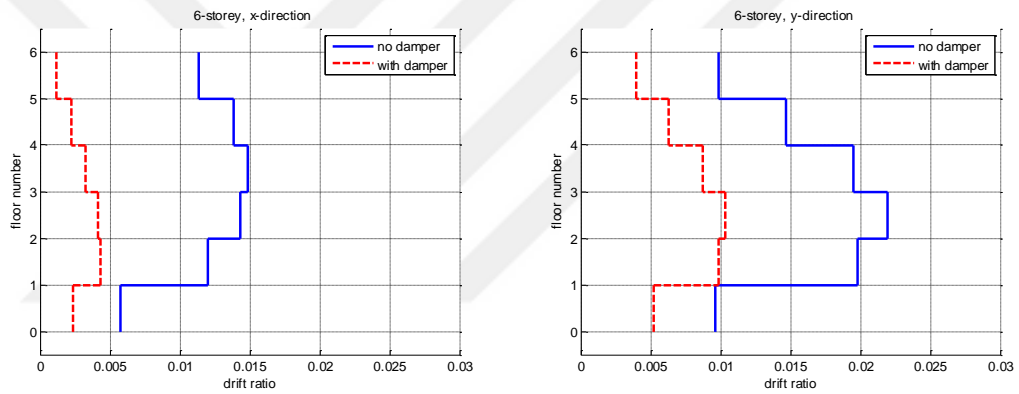


Figure C-52. Drift ratio plots in x and y directions of the 6-storey building under Landers earthquake record

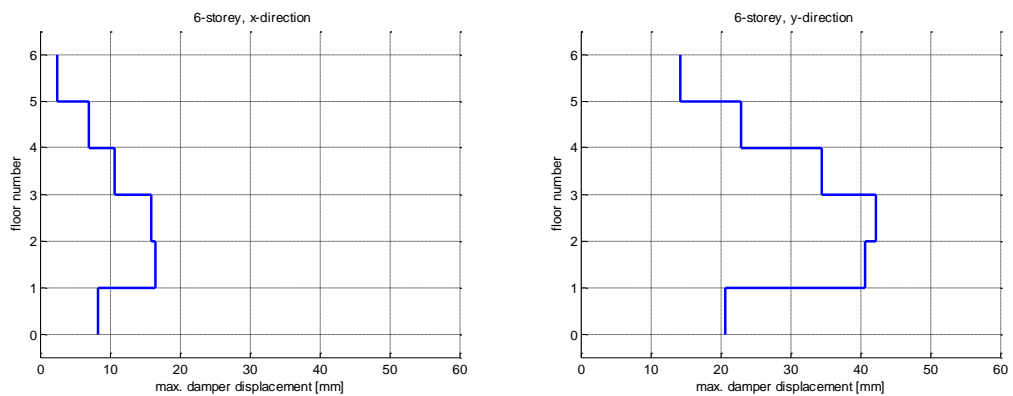


Figure C-53. Plots of maximum damper displacement in x and y directions of the 6-storey building under Landers earthquake record

C.4.4 8-storey building

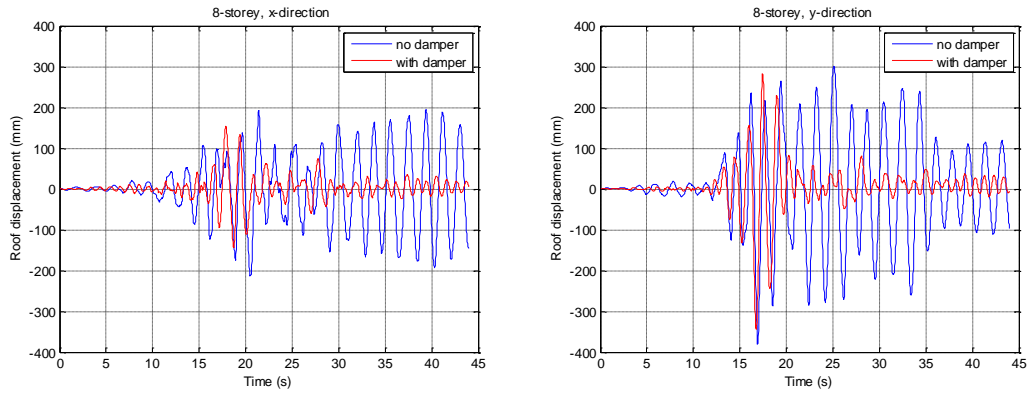


Figure C-54. Roof displacement time histories in x and y directions of the 8-storey building under Landers earthquake record

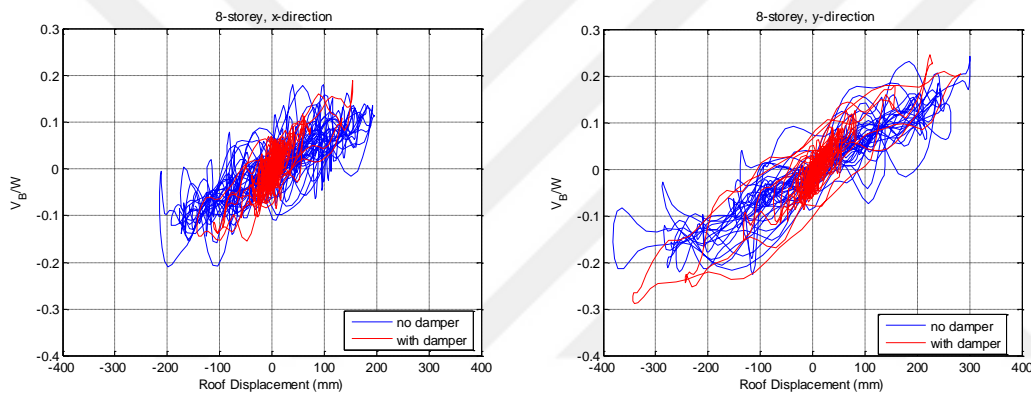


Figure C-55. Base shear vs roof displacement plots in x and y directions of the 8-storey building under Landers earthquake record

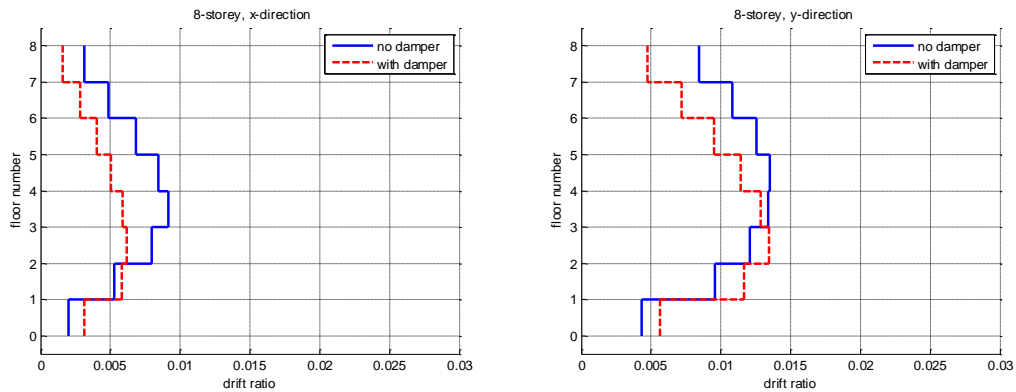


Figure C-56. Drift ratio plots in x and y directions of the 8-storey building under Landers earthquake record

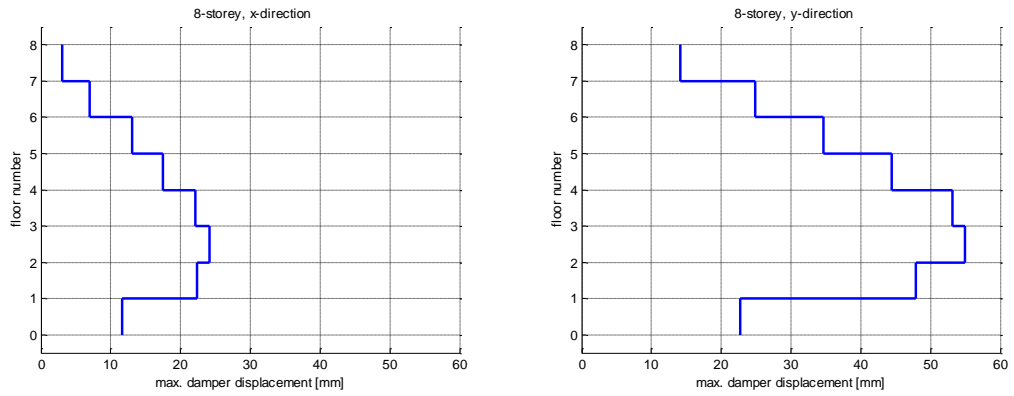


Figure C-57. Plots of maximum damper displacement in x and y directions of the 8-storey building under Landers earthquake record

C.4.5 10-storey building

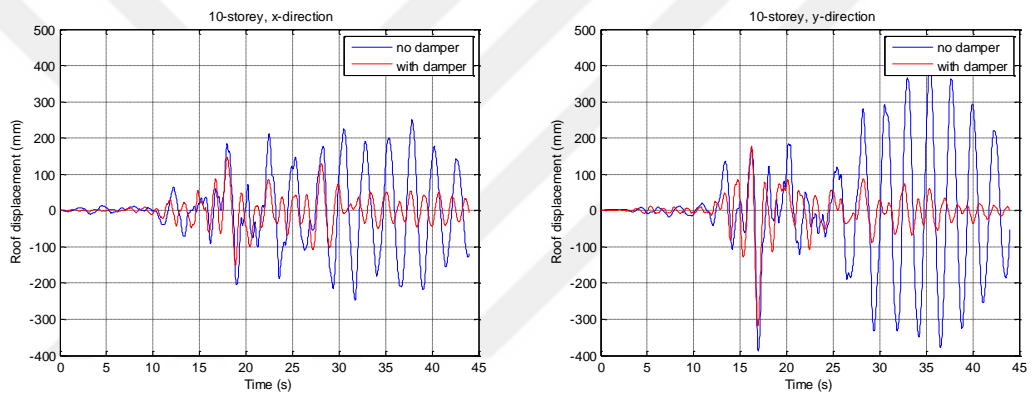


Figure C-58. Roof displacement time histories in x and y directions of the 10-storey building under Landers earthquake record

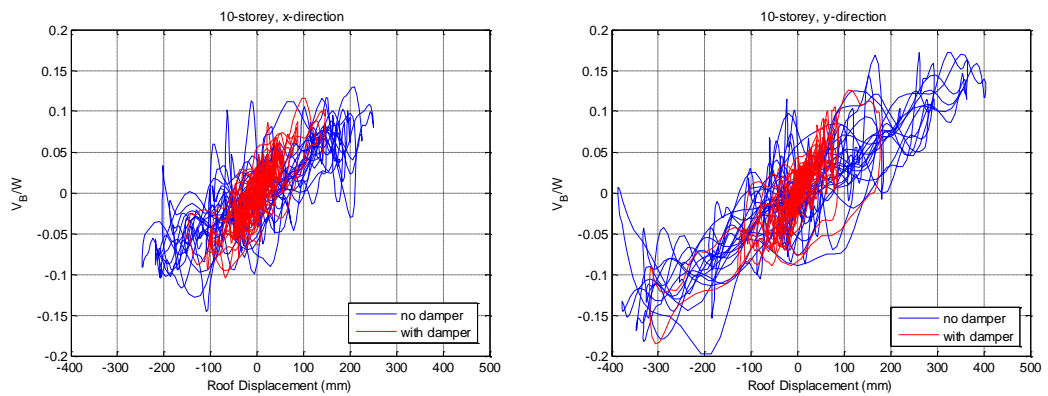


Figure C-59. Base shear vs roof displacement plots in x and y directions of the 10-storey building under Landers earthquake record

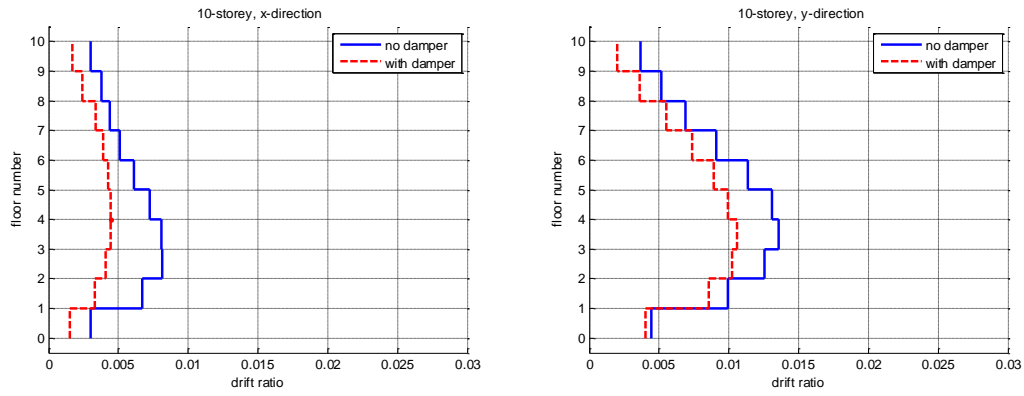


Figure C-60. Drift ratio plots in x and y directions of the 10-storey building under Landers earthquake record

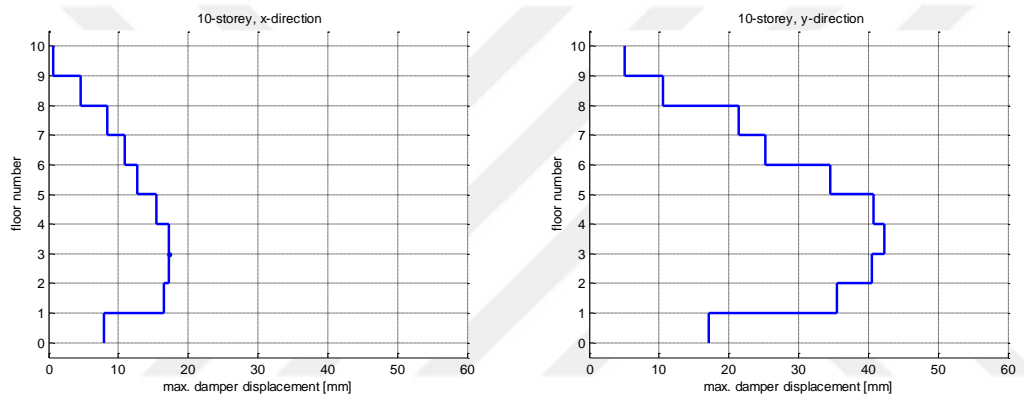


Figure C-61. Plots of maximum damper displacement in x and y directions of the 10-storey building under Landers earthquake record

C.4.6 Summary

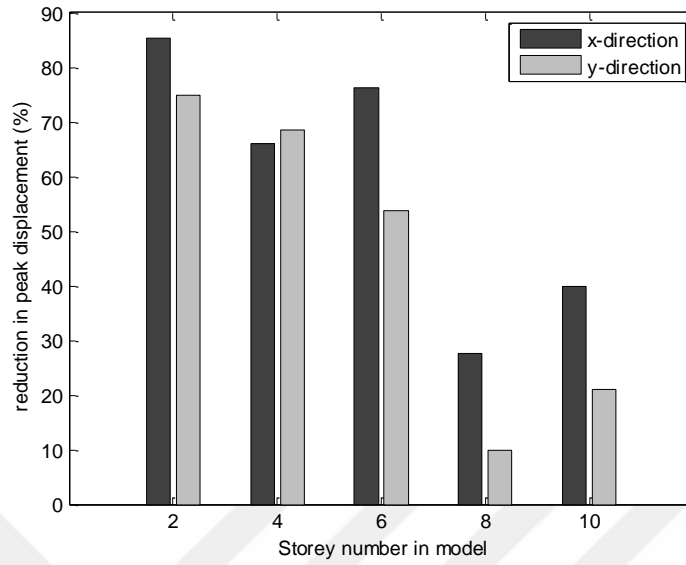


Figure C-62. Reduction in peak displacement for different models under Landers earthquake record

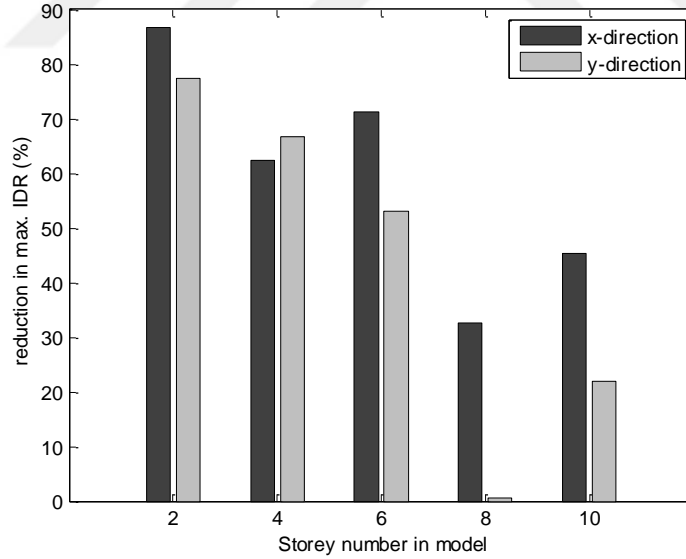


Figure C-63. Reduction in max. IDR for different models under Landers earthquake record

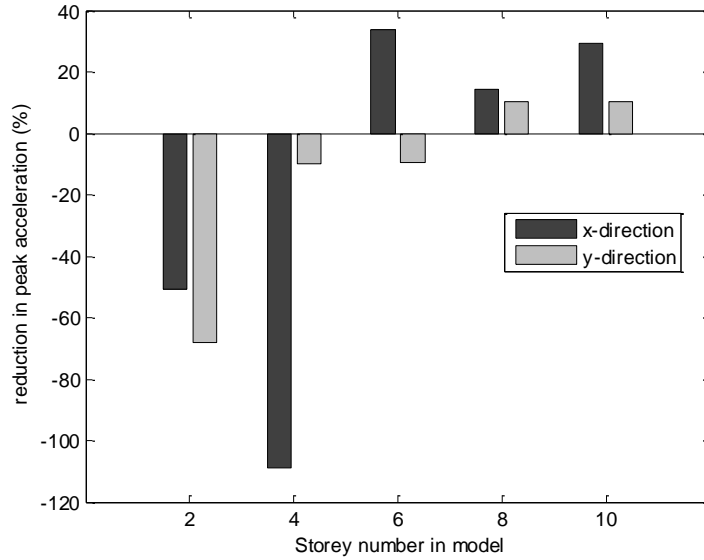


Figure C-64. Reduction in peak acceleration for different models under Landers earthquake record

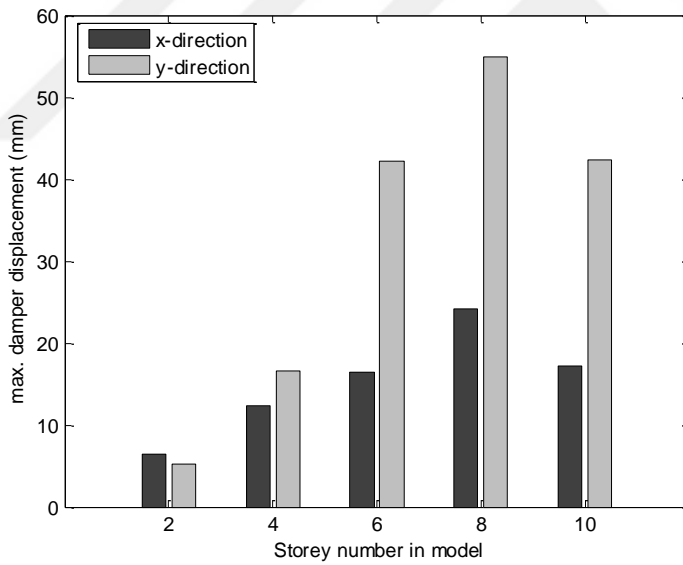


Figure C-65. Maximum damper displacement for different models under Landers earthquake record

CURRICULUM VITAE

PERSONAL INFORMATION

Surname, Name: Shaban, Nefize

Nationality: Bulgarian

Date and Place of Birth: 8 July 1987, Kardzhali

Marital Status: Single

Phone: +90 312 210 24 34

e-mail: nefishaban@gmail.com

EDUCATION

Degree	Institution	Year of Graduation
BSc and MSc	Univ. of Arch., Civil Eng. and Geodesy, Sofia	2010
High School	English Lang. School "Hristo Botev", Kardzhali	2005

LANGUAGES

Turkish, Bulgarian, English, German, Japanese, Spanish

PUBLICATIONS

Journal Papers

1. N. Shaban, A. Caner, A. Yakut, A. Askan Gundogan, A. Karimzadeh Naghshineh, A. Domanic and G. Can. (2014). "Vehicle Effects on Seismic Response of a Simple-Span Bridge during Shake Tests", *Earthquake Engineering and Structural Dynamics*, 44(6), 889-905.

2. N. Shaban and A. Caner, (2016) “Prototype Testing of a New Passive Energy Dissipation Device for Seismic Retrofit of Bridges”, *Frontiers in Built Environment*, doi: 10.3389/fbuil.2016.00023.
3. N. Shaban, O. Avsar and A. Caner. “Integration of Practical Supplemental Measurements into Bridge Condition Visual Inspection Grading”, under review
4. N. Shaban and A. Caner, “Shake Table Tests of Different Seismic Isolation Systems on a Large Scale Structure Subjected to Low to Moderate Earthquakes”, under review.

Conference Papers

1. K. Mladenov, A. Doicheva, N. Shaban. “Stressed and Deformed Shape of Eccentrically Supported Beams with Special Attention to The Different Shapes of Loss of Stability”, *International Scientific Conference in UACEG 2009*, paper 77, Sofia.
2. S. Lilkova-Markova, N. Shaban. “Influence of Shear Forces on The Elastic Line”, *International Scientific Conference in UACEG 2009*, paper 98, Sofia.
3. N. Shaban, A. Caner. “Development of a New Re-Centering Damper with Cables”, *11th International Congress on Advances in Civil Engineering*, 2014, Istanbul.
4. N. Shaban, A. Caner. “Diagrid Structures: An Innovative and Promising Approach to Bridge Design”, *Steel Bridges: Innovation and New Challenges 2015*, Istanbul.
5. N. Shaban, A. Caner, E. Baran. “Application of New Turkish Bridge Design Guidelines: Composite Steel Girder Highway Bridge”, *Steel Bridges: Innovation and New Challenges 2015*, Istanbul.
6. N. Shaban, A. Caner, A. I. Yilmaz. “Seismic Retrofit of Old Bridges with Seismic Isolation”, *16th World Conference on Earthquake Engineering*, 16WCEE 2017, Santiago Chile, Paper № 3788.
7. N. Shaban, S. Ozdemir, A. Caner and U. Akyuz. “Seismic Retrofit of Buildings with Backbone Dampers”, *COMPDYN 2017, 6th ECCOMAS Thematic Conference on Computational Methods in Structural Dynamics and Earthquake Engineering*, Rhodes Island, Greece, 15-17 June 2017.

8. O. T. Turan, N. E. Kesici, N. Shaban, M. A. Ersoylu, H. G. Oztekin, I. Senol, A. I. Yilmaz. “A Conceptual Design of a Footbridge over Kizilirmak River that Allows Pedestrian Induced Vibrations”, 2017 New York City Bridge Conference, August 21st-22nd.
9. N. Shaban, A. Caner, E. Baran. “Modelling and Experimental Investigation of the Construction Stage of a Composite Steel Bridge”, 5th National Symposium on Steel Structures, 2013, Istanbul, in Turkish.
10. N. Shaban, A. Caner. “Investigation of Vehicle Effect on Bridge Dynamic Behaviour”, 3rd Symposium on Bridges and Viaducts, 08-09-10 May 2015, Bursa, in Turkish.
11. N. Shaban and A. Caner. “The Effect of Damping Models on the Reliability of Structural Dynamic Analyses”, 3rd National Conference on Earthquake Engineering and Seismology, 14-16 October 2015, Izmir, in Turkish.